

RICE UNIVERSITY

**NMR Oil Well Logging: Diffusional Coupling and
Internal Gradients in Porous Media**

by

Vivek Anand

A THESIS SUBMITTED
IN PARTIAL FULFILLMENT OF THE
REQUIREMENTS FOR THE DEGREE

Doctor of Philosophy

APPROVED, THESIS COMMITTEE

George J. Hirasaki, A. J. Hartsook Professor, Chair
Chemical and Biomolecular Engineering

Walter G. Chapman, William W. Akers Chair,
Chemical and Biomolecular Engineering

Andreas Luttge, Associate Professor
Earth Science and Chemistry

HOUSTON, TEXAS

APRIL 2007

ABSTRACT

NMR Oil Well Logging:

Diffusional Coupling and Internal Gradients in Porous Media

by

Vivek Anand

The default assumptions used for interpreting NMR measurements with reservoir rocks fail for many sandstone and carbonate formations. This study provides quantitative understanding of the mechanisms governing NMR relaxation of formation fluids for two important cases in which default assumptions are not valid. The first is diffusional coupling between micro and macropore, the second is susceptibility-induced magnetic field inhomogeneities. Understanding of governing mechanisms can aid in better estimation of formation properties such as pore size distribution and irreducible water saturation.

The assumption of direct correspondence between relaxation time and pore size distribution of a rock fails if fluid in different sized pores is coupled by diffusion. Pore scale simulations of relaxation in coupled micro and macropores are done to analyze the effect of governing parameters such as surface relaxivity, pore geometry and fluid diffusivity. A new coupling parameter (α) is introduced which quantifies the extent of coupling by comparing the rate of relaxation in a coupled pore to the rate of diffusional transport. Depending on α , the pores can communicate through total, intermediate or

decoupled regimes of coupling. This work also develops a new technique for accurate estimation of irreducible saturation, an approach that is applicable in all coupling regimes. The theory is validated for representative cases of sandstone and carbonate formations.

Another assumption used in NMR formation evaluation is that the magnetic field distribution corresponds to the externally applied field. However, strong field inhomogeneities can be induced in the presence of paramagnetic minerals such as iron on pore surfaces of sedimentary rocks. A generalized relaxation theory is proposed which identifies three asymptotic relaxation regimes of motionally averaging, localization and free diffusion. The relaxation characteristics of the asymptotic regimes such as T_1/T_2 ratio and echo spacing dependence are quantitatively illustrated by random walk simulations and experiments with paramagnetic particles of several sizes. The theory can aid in better interpretation of diffusion measurements in porous media as well as imaging experiments in Magnetic Resonance Imaging (MRI).

ACKNOWLEDGEMENTS

First and foremost, I would like to acknowledge my advisor Dr. George J. Hirasaki for his continuous support and inspiration. I will remain indebted to him throughout my life for the things he has taught me.

I would also like to thank Dr. Walter G. Chapman and Dr. Andreas Lutge for serving on my thesis committee.

I am very thankful to William Knowles, Jie Yu and Shyam Benegal for their help with the BET, DLS and Coulter Counter measurements.

I am also thankful to Dr. Vicki L. Colvin's Lab for providing magnetite nanoparticles and TEM measurements.

Many thanks go to Jim Howard at Conoco Phillips for providing North Burbank cores and Chuck Devier at PTS labs for making mercury porosimetry and permeability measurements.

I greatly appreciate Dr. Marc Fluery at French Institute of Petroleum (IFP) for sharing his carbonate NMR measurements at high temperatures.

I would like to acknowledge Department of Energy (grant number DE-PS26-04NT15515) and consortium for processes in porous media for the financial support.

Most importantly, I would like to thank my parents, my family members for their love and support.

TABLE OF CONTENTS

TITLE PAGE.....	i
ABSTRACT.....	ii
ACKNOWLEDGEMENTS.....	iv
TABLE OF CONTENTS.....	v
LIST OF TABLES.....	ix
LIST OF FIGURES.....	xi
Chapter 1. Introduction.....	1
Chapter 2. Diffusional Coupling	4
2.1 Literature Review.....	4
2.1.1 Nuclear Magnetism.....	4
2.1.2 Pulse tipping and Free Induction Decay.....	5
2.1.3 Longitudinal relaxation.....	6
2.1.4 Transverse relaxation.....	7
2.1.5 NMR formation evaluation.....	8
2.1.6 Diffusional coupling.....	10
2.1.7 Spectral BVI and tapered $T_{2,cutoff}$	12
2.2 Diffusional coupling between micro and macropore.....	13
2.2.1 Mathematical modeling.....	14
2.2.2 Magnetization decay in coupled pore.....	17
2.2.3 Coupling Parameter.....	19
2.2.3.1 Micropore relaxation.....	22
2.2.3.2 Macropore relaxation.....	25
2.2.4 Estimation of irreducible saturation and α	26
2.2.5 Unification of spectral and sharp $T_{2,cutoff}$ theory.....	28
2.3 Diffusional coupling between pore lining clays and pore body.....	31
2.3.1 Pore size distribution of North Burbank sandstone.....	32

2.3.2	Numerical solution of Bloch equation in pore size distribution	34
2.3.3	Simulated T_2 distributions	36
2.3.4	Coupling regimes in North Burbank sandstone	37
2.3.5	Estimation of surface relaxivity.....	41
2.4	Effect of clay distribution on diffusional coupling	42
2.4.1	Synthesis of model shaly sands with laminated and dispersed clays.....	43
2.4.2	T_2 distribution of shaly sands.....	45
2.4.3	Estimation of irreducible water saturation in shaly sands.....	49
2.5	Diffusional coupling in microporous grainstones.....	52
2.5.1	Coupling parameter for grainstones.....	53
2.5.2	Experimental validation of grain size dependence on pore coupling.....	55
2.5.3	Estimation of irreducible saturation for the sandstone and grainstone systems.....	62
2.6	Effect of temperature on diffusional coupling.....	63
2.6.1	Temperature dependence of α	64
2.6.2	Temperature dependence of T_2 distributions of silica gels and carbonate core	65
2.6.3	Discussion.....	69
2.7	Conclusions.....	71

Chapter 3. Paramagnetic Relaxation in Sandstones: Generalized Relaxation

Theory	73
3.1 Introduction and Literature Review.....	73
3.2 Generalized secular relaxation theory.....	77
3.2.1 Characteristic time scales for secular relaxation.....	77
3.2.1.1 Characteristic time scale for restricted diffusion in a constant gradient.....	78
3.2.1.2 Characteristic time scale for relaxation in field induced by paramagnetic sphere.....	78
3.2.2 Asymptotic regimes of secular relaxation.....	80
3.2.2.1 Motionally averaging regime.....	81
3.2.2.2 Free diffusion regime.....	83

3.2.2.3	Localization regime.....	85
3.2.3	Parametric representation of asymptotic regimes.....	87
3.3	Relaxation regimes in sedimentary rocks.....	88
3.3.1	Paramagnetic particles at dilute surface concentration.....	89
3.3.2	Paramagnetic particles at high surface concentration.....	91
3.4	Random walk simulations.....	96
3.4.1	Non-dimensionalization of Bloch equations.....	97
3.4.2	Algorithm.....	99
3.4.3	Validation of numerical solution.....	101
3.4.3.1	Unrestricted diffusion in constant gradient.....	101
3.4.3.2	Restricted diffusion in constant gradient.....	102
3.4.4	Results.....	105
3.5	Conclusions.....	117
 Chapter 4. Paramagnetic Relaxation in Sandstones: Experiments.....		119
4.1	Paramagnetic particles in aqueous dispersions.....	119
4.1.1	Ferric Ion.....	119
4.1.2	Polymer coated magnetite nanoparticles.....	120
4.1.3	Magnetite nanoparticles coated with citrate ion.....	125
4.1.4	Characteristic time scales for paramagnetic particles in dispersion.....	129
4.2	Paramagnetic particles on silica surface.....	132
4.2.1	Fine sand coated with ferric ions.....	132
4.2.2	Fine sand coated with magnetite nanoparticles.....	136
4.2.3	Fine sand with dispersed 2.4 μm magnetite.....	140
4.2.4	Coarse sand coated with magnetite nanoparticles.....	142
4.3	Paramagnetic relaxation in sandstones.....	144
4.3.1	Motionally averaging regime.....	144
4.3.2	Free diffusion regime.....	145
4.3.3	Localization regime.....	148
4.4	Parametric representation of asymptotic regimes in experimental systems.....	153
4.5	Conclusions.....	159

Chapter 5. Conclusions	161
Chapter 6. Future Work	166
REFERENCES	168
Appendix A. Numerical solution of Bloch equations in coupled pore model.....	174
Appendix B. Relaxation time of micropore in coupled pore model.....	181
Appendix C. Characteristic parameters for the sandstones and grainstone systems.....	185
Appendix D. Characteristic parameters for the experimental systems of Chapter 4. ...	187

LIST OF TABLES

Table 2.1: Characteristic parameters for the simulations for three NB cores.....	39
Table 2.2: Physical Properties of Fine Sand, Kaolinite and Bentonite clays.....	44
Table 2.3: Physical properties of the grainstone systems.....	55
Table 4.1: Characteristic Time scales for the ferric ions and magnetite nanoparticles...131	131
Table 4.2: Longitudinal and transverse relaxation times of water-saturated fine sand coated with ferric ions at different surface concentrations (area/ferric ion).....	134
Table 4.3: Longitudinal and transverse relaxation times of water-saturated fine sand coated with 25 nm magnetite at different surface concentrations.....	137
Table 4.4: Longitudinal and transverse relaxation times of water-saturated fine sand coated with 110 nm magnetite at different surface concentrations.....	137
Table 4.5: Longitudinal and transverse relaxation times of water-saturated fine sand with dispersed 2.4 μm magnetite.....	140
Table 4.6: Longitudinal and transverse relaxation times of water-saturated coarse sand coated with 25 nm magnetite at different surface concentrations.....	144
Table 4.7: Characteristic time scales for relaxation in coarse sand coated with 25nm ($7 \cdot 10^2 \text{ nm}^2/\text{particle}$) and fine sand coated with 110nm magnetite ($1.5 \cdot 10^6 \text{ nm}^2/\text{particle}$)	147
Table 4.8: Characteristic time scales for relaxation in fine sand coated with 25 nm and 110 nm magnetite at high surface concentrations.	149
Table 4.9: Characteristic time scales for relaxation in fine with dispersed 2.4 μm magnetite.....	149
Table 4.10: Logmean longitudinal and transverse relaxation times of water saturated North Burbank cores.....	151
Table A.1: Model parameters for magnetization decay simulations.....	179
Table C.1: Characteristic parameters for North Burbank sandstone	185
Table C.2: Characteristic parameters for chalk.....	185
Table C.3: Characteristic parameters for silica gels.....	185

Table C.4: Characteristic parameters for molecular sieves.....	186
Table C.5: Characteristic parameters for silica gels at 30, 50, 75 and 95°C	186
Table C.6: Characteristic parameters for reservoir carbonate core at 25, 50, 80°C.....	186
Table D.1: Characteristic parameters for fine sand coated with 25 nm magnetite at different surface concentrations. Φ and $1/T_{2,\text{sec}}^D$ are dimensionless.....	187
Table D.2: Characteristic parameters for fine sand coated with 110 nm magnetite at different surface concentrations. Φ and $1/T_{2,\text{sec}}^D$ are dimensionless.....	188
Table D.3: Characteristic parameters for coarse sand coated with 25 nm magnetite at different surface concentrations. Φ and $1/T_{2,\text{sec}}^D$ are dimensionless.....	188
Table D.4: Characteristic parameters for fine sand with dispersed 2.4 μm magnetite at different concentrations. Φ and $1/T_{2,\text{sec}}^D$ are dimensionless.....	189
Table D.5: Characteristic parameters for North-Burbank sandstones. Φ and $1/T_{2,\text{sec}}^D$ are dimensionless.....	189

LIST OF FIGURES

Figure 2.1: Conceptual model of pore coupling in clay-lined pores in sandstones (Straley et al., 1995) (a) at 100% water saturation (b) at irreducible saturation.....	12
Figure 2.2: Physical model of coupled pore geometry. Fluid molecules relax at the micropore surface while diffusing between micro and macropore.....	14
Figure 2.3: Contour plots of magnetization at $t=1$ in coupled pores with $\beta = 0.5$ and $\eta = 10$ and different values of μ . The gradients along the longitudinal direction for larger μ imply that micropore is relaxing faster compared to macropore.....	18
Figure 2.4: Contour plots of magnetization at $t=1$ in coupled pores with $\beta = 0.5$ and $\mu = 0.1$ and different values of η . For comparison, the aspect ratios are <i>not</i> drawn to scale. Note the difference in contour plots for systems with same μ	19
Figure 2.5: Simulated T_2 distributions of coupled pores with $\beta = 0.5$ and $\eta = 10$ and different values of μ . The systems transition from unimodal to bimodal distribution with increase in α	21
Figure 2.6: Simulated T_2 distributions of coupled pores with $\beta = 0.5$ and $\mu = 0.1$ and different values of η . The T_2 distributions transition from unimodal to bimodal distribution with increase in α even though μ remains same	22
Figure 2.7: Plot of independent microporosity fraction (ψ/β) with α for different simulation parameters. The inset shows plot of (ψ/β) with μ for same simulation parameters.....	24
Figure 2.8: Plot of dimensionless relaxation time of macropore with $(1 - \beta)\sqrt{\alpha}$	26
Figure 2.9: Contour plots of correlations for ψ and $T_{2,\text{macro}}/T_{2,\mu}$ in the α and β parameter space.....	28
Figure 2.10: Plot of Θ vs. $T_{2,\text{macro}}/T_{2,\mu}$ for different α . A spectral or tapered cutoff is required for the estimation of irreducible saturation in the intermediate coupling regime. A sharp cutoff is applicable for decoupled regime.....	30
Figure 2.11: (a) Model of a clay-lined pore showing micropores opening to a macropore (Straley et al., 1995) (b) Simplified model with rectangular clays arranged along macropore wall.....	31
Figure 2.12: Pore throat distribution of the North Burbank sandstone obtained from mercury porosimetry. The bimodal distribution arises due to pore-lining chlorite.....	32

Figure 2.13: Lognormal pore size distribution simulated to approximate the distribution of macropores. Also shown are the pores with changing proportion of pore volume occupied by the clay flakes.....	33
Figure 2.14: Simulated T_2 distributions for $\beta_c = 0.3$ and $\eta_c = 100$ showing transition from unimodal to bimodal distribution with increase in $\bar{\alpha}$	37
Figure 2.15: Comparison of simulated and experimental T_1 distributions for three water saturated North Burbank cores.	39
Figure 2.16: (a) Independent microporosity fraction agrees with the lognormal relationship (Equation 2.25) for the three North Burbank cores (b) Normalized macropore relaxation time also agrees with the cubic relationship (Equation 2.27).....	40
Figure 2.17: Comparison of simulated and experimental distributions for two hexane saturated North Burbank cores.....	41
Figure 2.18: T_2 distributions of dispersed kaolinite-sand systems for different clay weight fractions.	46
Figure 2.19: T_2 distributions of laminated kaolinite-sand systems for different clay weight fractions.....	46
Figure 2.20: T_2 distributions of dispersed bentonite-sand systems for different clay weight fractions.....	47
Figure 2.21: T_2 distributions of laminated bentonite-sand systems for different clay weight fractions.....	47
Figure 2.22: Linear dependence of the relaxation rates of dispersed clay-sand systems with the clay content.....	48
Figure 2.23: Comparison of the irreducible water saturation calculated using the inversion technique and measured experimentally for dispersed systems.....	51
Figure 2.24: Pore coupling model in grainstone systems. The three-dimensional model (Ramakrishan et al., 1999) can be mapped to a two-dimensional model of periodic array of microporous grains separated by macropores.....	52
Figure 2.25: T_2 distributions of microporous chalk as a function of grain radius. The transition from decoupled ($R_g = 335 \mu\text{m}$) to total coupling regime ($R_g = 11 \mu\text{m}$) is predicted by the values of α	58
Figure 2.26: T_2 distributions of silica gels as a function of grain radius. The transition from almost decoupled ($R_g = 168 \mu\text{m}$) to total coupling regime ($R_g = 28 \mu\text{m}$) is predicted by the values of α	59

Figure 2.27: T_2 distributions of alumino-silicate molecular sieves as a function of grain radius.....	60
Figure 2.28: The lognormal and cubic relationships of Equations (2.25) and (2.27) hold for the grainstone systems.....	61
Figure 2.29: Comparison of calculated and experimentally measured values of microporosity fraction (β) for the grainstone and sandstone systems. The values are estimated within 4% average absolute error.....	62
Figure 2.30: Comparison of calculated and experimentally measured values of α for the grainstone and sandstone systems. The values are estimated within 11% error for all coupling regimes.....	63
Figure 2.31: T_2 distributions of silica gels at 100% water saturation and at 30, 50, 75 and 95°C.....	66
Figure 2.32: T_2 distribution of medium coarse silica gel at irreducible saturation and at 30, 50, 75 and 95°C.....	66
Figure 2.33: T_2 distributions of the Thamama formation carbonate core at 100% water (upper panel) and irreducible water saturation (lower panel) at 25, 50 and 80°C (Fleury, 2006)	69
Figure 2.34: Plot of independent microporosity fraction (ψ/β) with α for grainstone systems and carbonate core	70
Figure 2.35: Comparison of the microporosity fraction calculated using the inversion technique and measured experimentally for silica gels and carbonate core.....	71
Figure 3.1: Magnetic field lines in the presence of a paramagnetic sphere with magnetic susceptibility 10^6 times that of the surrounding medium. The field lines concentrate in their passage through the sphere.....	76
Figure 3.2: Contour plots of z component of internal magnetic field (dimensionless) induced by a unit paramagnetic sphere in a vertical plane passing through the center of the sphere. The external magnetic field is applied in the vertical z direction.....	80
Figure 3.3: Schematic diagram of asymptotic relaxation regimes in $(\delta\omega\tau_R, \delta\omega\tau_E)$ parameter space.....	88
Figure 3.4: (a) Contour plots of dimensionless magnetic field (Equation 3.12) in the outer region of a silica grain coated with paramagnetic spheres at dilute concentrations(No. of particles per unit area ~ 3). Radial distance is normalized with respect to the radius of the grain. The ratio of radius of the silica grain to that of paramagnetic particles is 10. (b) Contour plots in a quadrant at higher magnification.....	90

Figure 3.5: (a) Contour plots of dimensionless magnetic field (Equation 3.12) in the outer region of a silica grain coated with paramagnetic spheres at high concentrations (No. of particles per unit area ~ 30). Radial distance is normalized with respect to the radius of the grain. The ratio of radius of the silica grain to that of paramagnetic particles is 10. (b) Contour plots in a quadrant at higher magnification.....93

Figure 3.6: Contour plots of dimensionless magnetic field (Equation 3.12) in the outer region of a paramagnetic shell around a unit sphere. The thickness of the shell is calculated such the volume of the shell is same as the total volume of paramagnetic particles in Figure 3.5.....94

Figure 3.7 Schematic diagram of a tetrahedral pore between four touching silica grains of radius R_g . The length scale of field inhomogeneity is equal to the dimension of the tetrahedral pore when the paramagnetic particles are present at high concentration on the surface of the grains.....96

Figure 3.8: Comparison of analytical and simulated echo decay for **unrestricted diffusion in a constant gradient**. The parameters used in the simulations are $g = 100$ G/cm, $\tau_E = 2$ ms, $N_w = 10,000$ and $dt = 0.1$ μ s. The simulated echo decay matches within 0.1% of the analytical decay.....102

Figure 3.9: Comparison of simulated and analytical echo decays for **restricted diffusion in a sphere** with a constant gradient. The parameters used in the simulations are $L_g^* = 1.2$ and $L_d^* = 2$ (upper panel) and $L_d^* = 3$ (lower panel). Lesser number of points in the lower figure is due to smaller sampling rate with larger L_d^* . The analytical rate is given by Equation (3.54) normalized by $1/t_c$104

Figure 3.10: Comparison of simulated and analytical echo decays for **restricted diffusion in a sphere** with a constant gradient. The parameters used in the simulations are $L_g^* = 1.5$ and $L_d^* = 2$ (upper panel) and $L_d^* = 3$ (lower panel). Lesser number of points in the lower figure is due to smaller sampling rate with larger L_d^* . The analytical rate is given by Equation (3.54) normalized by $1/t_c$105

Figure 3.11: Plot of simulated secular relaxation rate (dimensionless) with $\delta\omega\tau_R$ as a function of $\delta\omega\tau_E$. The parameters used in the simulations are $\Phi = 1.25 \cdot 10^{-4}$, $k = 1.2$, $B_0 = 496$ Gauss. The solid, dotted and dash-dotted line are the theoretically estimated secular relaxation rates according to the outer sphere theory (Equation 3.60), mean gradient diffusion theory (Equation 3.61) and modified mean gradient diffusion theory (Equation 3.62) plotted in the respective regimes of validity. The dashed lines are the boundaries $\delta\omega\tau_R = 1$ and $\delta\omega\tau_E = 1$ that delineate the asymptotic regimes.....107

Figure 3.12: Contour plots of dimensionless secular relaxation rate in the $(\delta\omega\tau_R, \delta\omega\tau_E)$ parameter space. Contours differ by a factor of $\sqrt{10}$. The parameters used in the simulations are $\Phi = 1.25 \cdot 10^{-4}$, $k = 1.2$, $B_0 = 496$ Gauss. The dotted lines are the

corresponding plots for the theoretically predicted relaxation rates given by Equations (3.60), (3.61) and (3.62). The bold dashed lines are the boundaries between asymptotic regimes. The contours are invariant for dilute volume fractions ($\Phi \leq 1.25 \cdot 10^{-4}$).....112

Figure 3.13: Plot of secular relaxation rates (dimensionless) with dimensionless echo spacing $\delta\omega\tau_E$ for $\delta\omega\tau_R \leq 1$. The parameters used in the simulations are $\Phi = 1.25 \cdot 10^{-4}$, $k = 1.2$, $B_0 = 496$ Gauss. The dotted lines are the plots of theoretically predicted relaxation rates in the motionally averaging regime given by Equation (3.60). The bold dashed line is the boundary $\delta\omega\tau_E = \delta\omega\tau_R$ delineating free diffusion and motionally averaging regimes. The relaxation rates are almost independent of the echo spacing in the motionally averaging regime.....113

Figure 3.14: Plot of secular relaxation rates (dimensionless) with dimensionless echo spacing $\delta\omega\tau_E$ for $\delta\omega\tau_R \gg 1$. The parameters used in the simulations are $\Phi = 1.25 \cdot 10^{-4}$, $k = 1.2$, $B_0 = 496$ Gauss. The dotted and dash-dotted lines are the theoretically predicted relaxation rates in the free diffusion and the localization regime given by Equations (3.61) and (3.62) respectively. The bold dashed line is the boundary $\delta\omega\tau_E = 1$ delineating free diffusion and localization regimes. The dependence of the relaxation rates on echo spacing is less than quadratic in the localization regime.....114

Figure 3.15: Contour plots of dimensionless secular relaxation rate in the $(\delta\omega\tau_R, \delta\omega\tau_E)$ parameter space for $\Phi = 0.6$. A paramagnetic shell with susceptibility 0.2 (SI units) and $3\varepsilon/R_g = 10^{-3}$ is assumed for the simulations. Contours differ by a factor of $\sqrt{10}$. The dotted lines are the corresponding plots for the theoretical relaxation rates given by Equations (3.60), (3.61) and (3.62). The bold dashed lines are the boundaries between asymptotic regimes.....116

Figure 3.16: Plot of average absolute deviation (%) of simulations with higher volume fractions from the simulations with $\Phi = 1.25 \cdot 10^{-4}$. The deviation is less than 10% for $\Phi < 0.001$117

Figure 4.1: Longitudinal and Transverse relaxation rates ($\tau_E = 0.2$ ms) of ferric chloride solutions as a function of the concentration of the solution. No echo spacing dependence of T_2 relaxation was observed and T_1/T_2 ratio is equal to unity.....120

Figure 4.2: TEM images of magnetite nanoparticles. (a) 4 nm magnetite (b) 9 nm magnetite (c) 16 nm magnetite (Agarwal, 2007).....122

Figure 4.3: Plots of transverse, longitudinal and secular relaxation rates with the concentration of aqueous dispersions of polymer-coated nanoparticles of three different sizes. The average diameter of the nanoparticles (D_p) and slopes of the linear best fits are also mentioned.....123

- Figure 4.4: T_1 and T_2 distributions of aqueous dispersions of ferric ions and polymer coated magnetite nanoparticles. The T_2 distributions are independent of the echo spacing and T_1/T_2 ratio increases with the particle size.....124
- Figure 4.5: T_1/T_2 ratio of the aqueous dispersions of paramagnetic particles as a function of the particle size. The T_1/T_2 ratio increases with the particle size in the motionally averaging regime.....125
- Figure 4.6: Particle size distribution of magnetite dispersions synthesized using Massart's method (1981). The average diameters of the particles are 25 nm (upper panel) and 110 nm (lower panel) respectively.....127
- Figure 4.7: Plots of transverse, longitudinal and secular relaxation rates with the concentration of aqueous dispersions of magnetite nanoparticles synthesized using Massart's Method (1981). The average diameters of the nanoparticles (D_p) and slopes of the linear best fits are also mentioned.....128
- Figure 4.8: T_1 and T_2 distributions of aqueous dispersions of ferric ions and citrate coated magnetite nanoparticles. The T_2 distributions are independent of the echo spacing and T_1/T_2 ratio increases with the particle size.....129
- Figure 4.9: T_1 and T_2 distributions of fine sand coated with ferric ions at different surface concentrations.....135
- Figure 4.10: T_1 and T_2 distribution of water-saturated fine sand coated with 25 nm magnetite nanoparticles at various concentrations.....138
- Figure 4.11: T_1 and T_2 distribution of water-saturated fine sand coated with 110 nm magnetite nanoparticles at various concentrations.....139
- Figure 4.12: T_1 and T_2 distributions of fine sand with dispersed 2.4 μm magnetite at two concentrations. A large T_1/T_2 ratio and echo spacing dependence of transverse relaxation is observed.....141
- Figure 4.13: T_1 and T_2 distributions of coarse sand coated with 25 nm magnetite at different surface concentrations.....143
- Figure 4.14: Plot of the secular relaxation rate of water-saturated coated sand with τ_E for cases in which free diffusion regime is observed. The surface concentrations are $1.5 \cdot 10^6 \text{ nm}^2/110 \text{ nm}$ particle (fine sand) and $7 \cdot 10^2 \text{ nm}^2/25 \text{ nm}$ particle (coarse sand) respectively. The vertical lines are the boundary $\delta\omega\tau_E = 1$ at which the two systems transition from the free diffusion to the localization regime. The solid lines are the regression lines for the power-law fits in the two relaxation regimes. Relaxation rates show almost quadratic dependence on echo spacing in the free diffusion regime and less than linear dependence in the localization regime.....147

Figure 4.15: T_1 and T_2 distributions of water saturated North Burbank sandstone cores 1 and 2.....150

Figure 4.16: Plot of secular relaxation rate with half echo spacing for the several cases of the localization regime. The solid lines are the regression lines for the power law fits to the data. The exponents of the power law fits are less than unity for all cases.....153

Figure 4.17: Parametric representation of dimensionless secular relaxation rates for experimental systems in the $(\delta\omega\tau_R, \delta\omega\tau_E)$ parameter space. The symbols are the experimental systems: (+) aqueous dispersion of 4nm, 9nm, 16nm particles, (*) fine and coarse sand coated with dilute concentrations of 25nm, (\times) fine sand coated with dilute surface concentration of 110nm magnetite, (Δ) fine sand coated with 25nm magnetite Conc. = $7 \cdot 10^3$ nm²/part, (\blacktriangle) fine sand coated with 25nm magnetite Conc. = $3 \cdot 10^3$ nm²/part., (\blacklozenge) coarse sand coated with 25nm magnetite Conc. = $7 \cdot 10^2$ nm²/part., (\square) fine sand coated with 110nm magnetite Conc. = $1.5 \cdot 10^6$ nm²/part., (\blacksquare) fine sand coated with 110nm magnetite Conc. = $3 \cdot 10^5$ nm²/part, (∇) fine sand with dispersed 2.4 μ m magnetite, (\bullet) North Burbank sandstone. (a) Comparison with contour plots for $\Phi \leq 1.25 \cdot 10^{-4}$ (b) Comparison with contours for $\Phi = 0.6$156

Figure 4.18: Plot of secular relaxation rates with $\delta\omega\tau_E$ for experimental systems in free diffusion and localization regimes. The relaxation rates show nearly quadratic dependence on echo spacing in the free diffusion regime and less than linear dependence in the localization regime.....158

Figure 4.19: T_1/T_2 ratio for experimental systems. The ratio ranges from 1.1 to 13 and is echo spacing dependent for several systems.....159

Figure A.1: Finite difference approximation scheme along the $x=0$ boundary.....177

Figure B.1: Plot of micropore relaxation time with α for different simulation parameters. Micropore appears to relax faster when coupled with macropore.....182

Figure B.2: Simulated relaxation data for $\alpha=10$ ($\beta=0.5, \eta=100$ and $\mu=0.2$). The black dashed line is an exponential decay with relaxation time of 1. The solid line is a bi-exponential fit ($0.26\exp(-t/0.4) + 0.74\exp(-t/2.2)$) of the data.....184

Chapter 1. Introduction

Nuclear Magnetic Resonance (NMR) well logging has become an important tool for formation evaluation. NMR measurements provide useful information about formation properties such as porosity, permeability, irreducible water saturation, oil saturation and viscosity. Interpretation of NMR measurements with fluid-saturated rocks is usually based on default assumptions about fluid and rock properties. However, in several scenarios, the default assumptions are not valid. For example, application of a sharp $T_{2,cutoff}$ to partition the T_2 spectrum at 100% water saturation in free fluid and bound volume fractions is not valid if micro and macropores are coupled by diffusion. The objective of this work is to develop analytical and experimental techniques for the interpretation of NMR measurements when the default assumptions are not satisfied.

Two important cases are elucidated in which the default assumptions fail. First is diffusional coupling between micro and macropores, second is magnetic field inhomogeneities induced due to susceptibility differences between the solid matrix and the pore fluid. A brief description of the two cases is mentioned below.

The estimation of pore size distribution from NMR T_2 measurements assumes that pores of different sizes relax independently of each other. Provided that the pores remain in the fast diffusion regime, relaxation rate of a fluid in an isolated pore is related to the surface-to-volume ratio of the pore (Brownstein et al., 1979). Thus, the T_2 distribution of a fluid-saturated rock provides a signature of the pore size distribution. However, this interpretation fails if the fluid in micro and macropores is coupled through diffusion. In such cases, the relaxation rate of the fluid is influenced by the surface-to-volume ratio of both the micro and macropores and thus, the correspondence between T_2 and pore size

distribution is lost. The estimation of formation properties such as permeability and irreducible water saturation using the traditional $T_{2,cutoff}$ method would give erroneous results.

Another assumption usually employed in NMR formation evaluation is that the magnetic field distribution in pore spaces corresponds to the externally applied field. However, magnetic field inhomogeneities are often induced when a fluid-saturated rock is placed in an external magnetic field due to susceptibility differences between the solid matrix and the pore fluid. The presence of the field inhomogeneities can influence NMR measurements in various ways. Diffusion of spins in the inhomogeneous field leads to additional transverse relaxation (Bloch, 1946). The inhomogeneities can also interfere and cause distortions in imaging or diffusion measurements (Hürlimann, 1998).

The thesis is organized as follows. Chapter 2 provides a theoretical and experimental understanding of NMR relaxation in systems with diffusionally coupled micro and macropores. Relaxation is modeled such that the fluid molecules relax at the surface of the micropore and simultaneously diffuse between the two pore types. The governing parameters are combined in a single coupling parameter (α) which provides a quantitative estimate of pore coupling. The theoretical models are validated for representative cases of pore coupling in microporous grainstones and clay-lined pores in sandstones.

Chapter 3 proposes a generalized relaxation theory of transverse relaxation due to diffusion in inhomogeneous magnetic fields. Three characteristic time scales are defined which characterize transverse relaxation in inhomogeneous fields: time for significant dephasing, diffusional correlation time, and half echo spacing for Carr-Purcell-Meiboom-

Gill (CPMG) pulse sequence. Depending on the shortest characteristic time scale, T_2 relaxation in inhomogeneous fields is classified in three asymptotic regimes. Random walk simulations of T_2 relaxation in an inhomogeneous field induced by paramagnetic spheres illustrate the relaxation characteristics of the asymptotic regimes.

In Chapter 4, asymptotic regimes in porous media are experimentally analyzed. A series of model sandstones are synthesized by coating coarse and fine sand with paramagnetic particles of known sizes and concentrations. The experimental results illustrate the transition of the asymptotic regimes as a function of the governing parameters.

Chapter 5 concludes the important findings of this study and Chapter 6 suggests possible directions for future work.

Chapter 2. Diffusional Coupling

Interpretation of NMR measurements with fluid-saturated rocks assumes that the T_1 or T_2 distribution is directly related to the pore size distribution. However, this assumption fails if the fluid in different sized pores is coupled through diffusion. In such cases, estimation of formation properties such as permeability and irreducible water saturation using the traditional $T_{2,cutoff}$ method would give erroneous results. This chapter develops a theoretical understanding of NMR relaxation in systems with diffusional coupled micro and macropores. The theoretical framework is applied to interpret NMR measurements in microporous grainstones and clay-lined pores in sandstones.

2.1. Literature Review

NMR relaxation measurements provide useful information about formation properties such as porosity, permeability, pore size distribution, oil saturation and viscosity. This section reviews the phenomenological relaxation process of atomic nuclei in external magnetic fields and its application in formation evaluation. In addition, the effect of diffusional coupling and the techniques of Spectral BVI (Coates et al., 1998) and Tapered $T_{2,cutoff}$ (Kleinberg et al., 1997) that have been introduced to account for diffusional coupling are also described.

2.1.1. Nuclear magnetism

Nuclear Magnetic Resonance refers to the response of atomic nuclei to external magnetic fields (Coates et al., 1999). When the spins of the protons and/or neutrons comprising a nucleus are not paired, the overall spin of the nucleus generates a magnetic

moment along the spin axis. In presence of an external magnetic field, \vec{B}_0 , the individual magnetic moments align parallel or antiparallel to the field. There is a slight preponderance of nuclei aligned parallel with the magnetic field giving rise to a net magnetization (M_0) along the direction of the applied magnetic field.

The macroscopic magnetization (\vec{M}) is not collinear with the external field but precesses about an angle. The equation of motion is given by equating the torque due to the external field with the rate of change of \vec{M} shown below.

$$\frac{d\vec{M}}{dt} = \vec{M} \times (\gamma \vec{B}_0) \quad (2.1)$$

The parameter γ is called the gyromagnetic ratio. Equation (2.1) says that the changes in \vec{M} are perpendicular to both \vec{M} and \vec{B}_0 . Thus, the angle between \vec{M} and \vec{B}_0 does not change and the magnetization precesses around the magnetic field with an angular frequency $f = \frac{\gamma B_0}{2\pi}$ called the Larmor frequency.

2.1.2. Pulse tipping and Free Induction Decay

\vec{M} remains in equilibrium state until perturbed. If a magnetic field rotating at Larmor frequency is applied in the plane perpendicular to the static field, the magnetization tips from the longitudinal (z) direction to the transverse plane. The angle θ through which the magnetization is tipped is given as

$$\theta = \gamma B_1 t_p \quad (2.2)$$

where t_p is the time over which the oscillating field is applied and B_1 is the amplitude of applied magnetic field. In NMR measurements, usually a π ($\theta=180^\circ$) or $\pi/2$ ($\theta=90^\circ$) Radio frequency (RF) pulse is applied. When the RF pulse is removed, relaxation mechanisms

(Fukushima et al., 1981) cause the magnetization to return to equilibrium condition and at the same time the transverse components to decay to zero. If a coil of wire is set up around an axis perpendicular to \vec{B}_0 , oscillation of \vec{M} induces a sinusoidal current in the coil called the Free Induction Decay (FID).

2.1.3. Longitudinal relaxation

The relaxation of the longitudinal magnetization after the application of the RF pulse is exponential in simplest cases. The time constant of the exponential response is called the longitudinal or spin-lattice relaxation time (T_1). The equation describing the longitudinal relaxation is given as

$$\frac{dM_z}{dt} = -\frac{[M_z - M_0]}{T_1} \quad (2.3)$$

where M_0 is the equilibrium magnetization and M_z is the z component of the magnetization. A common pulse sequence used to measure T_1 relaxation time is the Inversion-Recovery (IR) pulse sequence. The IR sequence starts with a 180° pulse which flips the magnetization in the negative z direction. After a fixed amount of time t , a 90° pulse is applied which brings the magnetization to the x-y plane. Free induction decay of the magnetization after the 90° pulse induces a sinusoidal voltage which is detected by the receiver coil. The amplitude of the FID immediately after the 90° pulse gives the value of M_z after the wait time t . A series of such experiments are performed for a range of values of t which gives the values of M_z increasing from $-M_0$ to $+M_0$. The T_1 relaxation time is determined by fitting an exponential fit to the measured values of M_z given as

$$M_z(t) = M_0 \left(1 - 2 \exp\left(\frac{-t}{T_1}\right) \right) \quad (2.4)$$

2.1.4. Transverse relaxation

After the application of the RF pulse, \vec{M} also has transverse components which relax to the equilibrium value of zero by redistributing energy among spins. This process is referred to as the transverse or spin-spin relaxation. Bloch (1946) showed that in simplest cases, the transverse components of magnetization (M_x and M_y) relax exponentially with characteristic time T_2 called the spin-spin relaxation time. The equation describing transverse relaxation is given as

$$\frac{dM_{x,y}}{dt} = -\frac{M_{x,y}}{T_2} \quad (2.5)$$

Transverse relaxation is additionally influenced by the inhomogeneity of the static magnetic field as described below. The transverse magnetization is the sum of small magnetization vectors in different parts of the sample called isochromats which are experiencing a homogeneous static field (Fukushima et al., 1981). After the application of the 90° pulse, isochromats which are experiencing larger magnetic field precess faster than those experiencing smaller magnetic fields. Thus, the isochromats get out of phase with each other resulting in additional transverse relaxation due to loss of phase coherence. This transverse relaxation rate in inhomogeneous magnetic field is denoted by $1/T_2^*$ and is given as

$$\frac{1}{T_2^*} = \frac{1}{T_2} + \gamma\Delta B_0 \quad (2.6)$$

where ΔB_0 is the inhomogeneity of the magnetic field. Carr-Purcell-Meiboom-Gill (CPMG) pulse sequence (Carr et al., 1954; Meiboom et al., 1958) was designed to partially offset this effect of the inhomogeneous field. A CPMG spin echo train starts with a 90° RF pulse along the x' -axis in the rotating frame (Fukushima et al., 1981) that

tips the magnetization onto the y' axis. After the initial 90° pulse, the spin isochromats dephase due to the inhomogeneity of the field. Then, after a time τ (half echo spacing), a 180° pulse is applied along the y' axis. The 180° pulse rephases the spin isochromats on y' axis at time 2τ to form a “spin echo”. Subsequent 180° pulses are applied at 3τ , 5τ , $7\tau\dots$ and the spin echoes are formed at time 4τ , 6τ , $8\tau\dots$. The amplitudes of the spin echoes are recorded to yield the decay curve from which the effect of the inhomogeneous dephasing has been partially removed. The decay, if single exponential, can be expressed as

$$M_{x,y}(t) = M_0 \exp\left(-\frac{t}{T_2}\right) \quad (2.7)$$

where $t = [2\tau, 4\tau, 6\tau\dots]$.

2.1.5. NMR formation evaluation

NMR logging tools measure the relaxation of hydrogen nuclei in pore fluids such as water and hydrocarbons. These measurements can provide useful information about the formation such as porosity, pore size distribution and fraction of producible fluids as described below.

1. **Porosity** - The estimation of porosity from NMR is based on the fact that low field measurements are only sensitive to the signal from protons in pore fluids. Thus, the initial amplitude of the decay curve is directly proportional to the number of polarized protons within the sensitive region of the tool. Porosity is given as the ratio of this amplitude to the tool response in a tank of water divided by the hydrogen index of the formation fluid. Hydrogen index is defined as the ratio of the number of hydrogen nuclei per unit volume of a fluid to the number of

hydrogen nuclei per unit volume of pure water at standard temperature and pressure (Coates et al., 1999).

2. **Pore size distribution** - The NMR response of protons in pore spaces of rocks is usually different from that in the bulk due to interactions with the pore surfaces. Provided that the pores remain in the fast-diffusion regime (i.e. relaxation at the surface of pores is much slower compared to the diffusional transport of spins to the surface), T_2 of a fluid in a single pore is related to the surface-to-volume $(S/V)_{\text{pore}}$ ratio of the pore (Brownstein et al., 1979) as

$$\frac{1}{T_2} = \rho_2 \left(\frac{S}{V} \right)_{\text{pore}} \quad (2.8)$$

The parameter ρ_2 called the T_2 surface relaxivity, measures the T_2 relaxing strength of the grain surface. Hence for a 100% water saturated rock, the decay curve can be fitted to a sum of exponentials to obtain a T_2 distribution. Each component of the T_2 distribution represents a pore with surface-to-volume ratio given by Equation (2.8). An inherent assumption in this interpretation is that the pores of different sizes are relaxing independently.

3. **Free fluid index** - The T_2 spectrum of fluid-saturated rocks can also be used to estimate the fraction of fluids that will flow under normal reservoir conditions called free fluid index (FFI). The estimation of FFI assumes that movable fluids are present in larger pores and have long relaxation times, while bound fluids are present in smaller pores and have short relaxation times (Coates et al., 1999). A $T_{2,\text{cutoff}}$ value can be chosen which partitions the T_2 spectrum in two components: (a) the component with T_2 greater than $T_{2,\text{cutoff}}$ corresponds to the movable fluids in the larger pores and (b) the component with T_2 shorter than $T_{2,\text{cutoff}}$ corresponds

to the immovable fluids in the smaller pores. Hence, the T_2 spectrum can be divided into the free fluid index porosity and the bound fluid porosity or bulk volume irreducible (BVI).

The value of $T_{2,cutoff}$ is lithology specific and is usually determined in the laboratory from NMR measurements on representative core samples. The technique for the determination of $T_{2,cutoff}$ is as follows. T_2 distributions of core samples are obtained from NMR measurements at 100% water saturation and at irreducible saturation. Irreducible saturation can be achieved by using the centrifuge technique or the porous plate technique at a specified capillary pressure. The two T_2 distributions are displayed on a cumulative porosity plot. The cumulative porosity at which the sample is at irreducible saturation is horizontally projected on the cumulative porosity plot for 100% water saturation. The T_2 value of the intersection point between the projection and the cumulative porosity plot for 100% water saturation is the $T_{2,cutoff}$.

2.1.6. Diffusional Coupling

As was described earlier, NMR T_2 measurements are often used to estimate pore size distribution of fluid-saturated rocks. NMR pore size estimation assumes that in the fast diffusion limit, T_2 of a fluid in a single pore is given by Equation (2.8). For a rock sample with a pore size distribution, each pore is assumed to be associated with a T_2 component and the net magnetization relaxes as a multiexponential decay.

$$M(t) = \sum_j f_j \exp\left(-\frac{t}{T_{2,j}}\right) \quad (2.9)$$

where f_j is the amplitude of each T_{2j} . Such interpretation of NMR measurements assumes that pores of different sizes relax independently of each other. However, the assumption breaks down if the fluid molecules in different sized pores are coupled with each other through diffusion. This is especially true for shaly sandstones and carbonates such as grainstones and packstones. Ramakrishnan et al. (1999) demonstrated that T_2 spectrum of peloidal grainstones having pore spaces with widely separated length scales may consist of single peak indicating that the direct link between T_2 and pore size is lost. They explained that the failure could be understood by considering the diffusion of fluid molecules between inter (macro) and intragranular (micro) pores. In an isolated pore, relaxation rate of the fluid is proportional to the surface-to-volume ratio of the pore (Equation 2.8). When the fluid in macropores diffuses into micropores, it relaxes faster than that predicted by Equation (2.8) due to larger surface-to-volume ratio of the micropores. Similarly, diffusion of fluid from micropores to macropores causes it to decay slower. Thus, the relaxation rate of fluid is influenced by an average surface-to-volume ratio of micro and macropores and the direct correspondence between pore size and T_2 distribution is lost. In such cases, the estimation of formation properties such as permeability and irreducible water saturation using the traditional $T_{2,cutoff}$ method would give erroneous results.

The effect of diffusional coupling on accurate estimation of irreducible saturation can be illustrated for the case of clay-lined pores in sandstones. Figure 2.1 shows the schematic diagram of a clay-lined pore (Straley et al., 1995) (a) at 100% water saturation and (b) at irreducible saturation after capillary drainage of the macropore. First consider the case of the pore at irreducible saturation in Figure 2.1(b). Since the macropore is

drained, there is no diffusional exchange between fluids in micro and macropore. Thus, the fluid in micropores relaxes with a rate proportional to the surface-to-volume ratio of the micropores. Now consider the case of 100% water-saturated pore in Figure 2.1(a). If the fluid in micropores is in diffusional exchange with that in macropore, its apparent volume is larger but the surface area for relaxation remains same. Thus, the fluid in micropores relaxes with a smaller relaxation rate at 100% saturation than at irreducible saturation. If a sharp $T_{2,cutoff}$ based on the relaxation rate of fluid in micropores at irreducible saturation is employed, then it may under-predict the irreducible saturation because a fraction of fluid in micropores may be relaxing slower than $T_{2,cutoff}$.

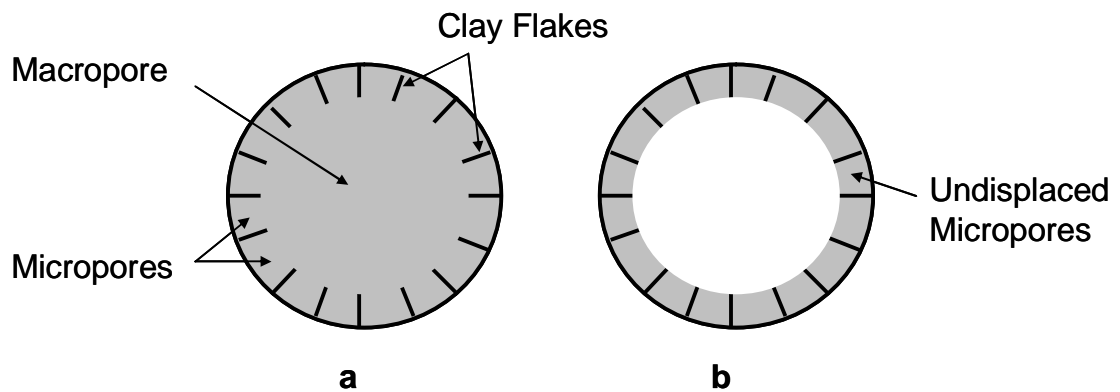


Figure 2.1: Conceptual model of pore coupling in clay-lined pores in sandstones (Straley et al., 1995) (a) at 100% water saturation (b) at irreducible saturation.

2.1.7. Spectral BVI and tapered $T_{2,cutoff}$

Straley et al. (1995) found that the T_1 spectrum of some sandstones showed a build up in short T_1 components after reduction of water saturation by centrifuging, implying that some water remains in the large pores. Thus, application of fixed cutoff to the 100% water saturated spectra would under-predict the irreducible water saturation in

such cases. The concept of spectral BVI was introduced by Coates et al. (1998) to take into account the diffusional coupling of bulk pore fluids with fluid in regions of high radius of curvature. The method is based on the premise that each pore size has its own inherent irreducible water saturation. The fraction of bound water associated with each pore size is defined by a weighting function $W(T_{2,i})$, where $0 \leq W(T_{2,i}) \leq 1$. The spectral BVI (SBVI) is given as

$$SBVI = \sum_{i=1}^n W_i \phi_i \quad (2.10)$$

where n is the number of bins in the T_2 distribution and ϕ_i is the porosity associated with each bin. The weighting factors are usually determined from core analysis or using empirical permeability models or cylindrical pore models in cases where core data are not available. The irreducible water saturations predicted using SBVI were found to correlate better with core measurements than the usual fixed cutoff method.

Kleinberg et al. (1997) considered the effect of diffusional coupling in estimating BVI by considering a layer of water remaining on the surface of cylindrical pores after centrifugation. The thickness of this layer depends on the capillary pressure generated by centrifugation and the interfacial tension between the wetting and non-wetting fluids. A tapered cutoff was introduced in which the bound water was found from a weighted sum of amplitudes in the T_2 distribution. The tapered cutoff was found to give better estimation of BVI in formations that are substantially water saturated.

2.2 Diffusional coupling between micro and macropores

The techniques of spectral BVI or tapered $T_{2,cutoff}$ usually provide better estimates of formation properties when diffusional coupling between pores of different sizes is

significant. However, a theoretical basis for application of these techniques needs to be established. This section describes pore scale simulations of NMR relaxation in coupled pores that provide a theoretical understanding of the effect of governing parameters on diffusional coupling. A new coupling parameter is introduced which provides a quantitative basis for the application of spectral or sharp cutoffs.

2.2.1. Mathematical modeling

NMR relaxation is modeled in a coupled pore geometry consisting of a micropore in physical proximity to a macropore as shown in Figure 2.2. The fluid molecules relax at the surface of the micropore and simultaneously diffuse between the two pore types. As a result, T_2 distribution of the pore is determined by several parameters such as micropore surface relaxivity, diffusivity of the fluid and geometry of the pore system. The simple model helps to keep the analysis tractable and also captures the essential features of more complicated pore coupling models (Toumelin et al., 2003).

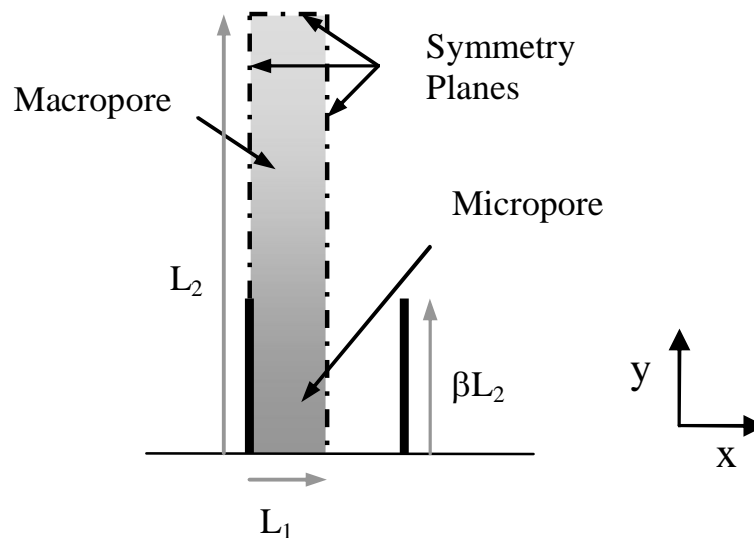


Figure 2.2: Physical model of coupled pore geometry. Fluid molecules relax at the micropore surface while diffusing between micro and macropore.

The coupled pore is defined by three geometrical parameters: half-length of the pore (L_2), half-width of the pore (L_1) and microporosity fraction (β). The decay of magnetization per unit volume (M) in the pore is given by the Bloch-Torrey equation

$$\frac{\partial M}{\partial t} = D\nabla^2 M - \frac{M}{T_{2B}} \quad (2.11)$$

where D is the diffusivity of the fluid and T_{2B} is the fluid bulk relaxation time. The boundary conditions are

$$D\vec{n} \cdot \nabla M + \rho M = 0 \text{ at micropore surface} \quad (2.12)$$

$$\vec{n} \cdot \nabla M = 0 \text{ at symmetry planes} \quad (2.13)$$

where \vec{n} is the unit normal pointing outwards from the pore surface and ρ is the surface relaxivity. A uniform magnetization is assumed in the entire pore initially. In addition, bulk relaxation is assumed to be very small in comparison to surface relaxation and is neglected.

The governing Equations (2.11-2.13) can be made dimensionless by introducing characteristic parameters. The spatial variables are, thus, non-dimensionalized with respect to the half-length of the pore (L_2), magnetization with respect to initial magnetization and time with respect to a characteristic relaxation time, $T_{2,c}$ defined as

$$T_{2,c} = \frac{V_{\text{total}}}{\rho S_{\text{active}}} = \frac{L_1 L_2}{\rho \beta L_2} = \frac{L_1}{\rho \beta} \quad (2.14)$$

In the above equation, S_{active} refers to the surface area of the micropore at which relaxation is taking place and V_{total} refers to the total volume of the pore. An analogous relaxation time of the micropore, $T_{2,\mu}$, can be defined as

$$T_{2,\mu} = \frac{1}{\rho} \left(\frac{V}{S} \right)_{\mu} = \frac{\beta L_2 L_1}{\rho \beta L_2} = \frac{L_1}{\rho} \quad (2.15)$$

where $(V/S)_{\mu}$ refers to the volume-to-surface ratio of the micropore. The characteristic relaxation time $T_{2,c}$ can be related to $T_{2,\mu}$ by comparing Equations (2.14) and (2.15)

$$\Rightarrow T_{2,c} = \frac{T_{2,\mu}}{\beta} \quad (2.16)$$

Equation (2.16) is used to normalize relaxation time for the experimental systems shown in the later sections.

Three dimensionless groups are next introduced: aspect ratio of the pore η , Brownstein number μ (Brownstein et al., 1979) and coupling parameter α , defined as

$$\eta = \frac{L_2}{L_1} \quad (2.17)$$

$$\mu = \frac{\rho L_2}{D} \quad (2.18)$$

$$\alpha = \beta \eta \mu = \frac{\rho \beta L_2^2}{D L_1} \quad (2.19)$$

η is the ratio of the characteristic dimension of the macropore to that of micropore. μ and α are the ratios of relaxation rate to diffusion rate but μ treats the system as a single macropore while α includes the contribution of the micropore to the total surface-to-volume ratio. The physical significance of the parameters is detailed in the next sections. The governing equations can, thus, be expressed in terms of above mentioned dimensionless parameters as shown in Appendix A. A finite difference Alternation Direction Implicit technique (Peaceman et al., 1955) is employed for the numerical

solution of the dimensionless equations. The details of the numerical technique are also mentioned in Appendix A.

2.2.2. Magnetization decay in coupled pore

The decay of magnetization in the coupled pore is characterized by three parameters: aspect ratio of the pore (η), microporosity fraction (β) and Brownstein number (μ). Depending on the value of μ , defined as

$$\mu = \frac{\text{Relaxation rate}}{\text{Diffusion rate}} = \frac{\rho/L_2}{D/L_2^2} = \frac{\rho L_2}{D} \quad (2.20)$$

the decay can be classified into fast, intermediate and slow diffusion regimes. In the fast diffusion regime ($\mu \ll 1$), the lowest eigen value of the diffusion Equation (2.11) completely dominates, and the decay curve is mono-exponential. However, in the slow diffusion regime ($\mu \gg 10$), the higher modes also contribute to the relaxation and the decay curve is multi-exponential (Brownstein et al., 1979). These diffusion regimes can be visualized with the help of snapshots of magnetization in the pore at intermediate decay times. Figure 2.3 shows the contour plots of magnetization for $\beta = 0.5$ and $\eta = 10$ at dimensionless time $t = 1$ for various values of μ . For μ small compared to 1 ($\mu = 0.1$), fast diffusion leads to nearly homogeneous magnetization in the entire pore. With the increase in the value of μ , gradients in magnetization along the longitudinal direction become substantial. The gradients imply that the micropore is relaxing much faster than the macropore.

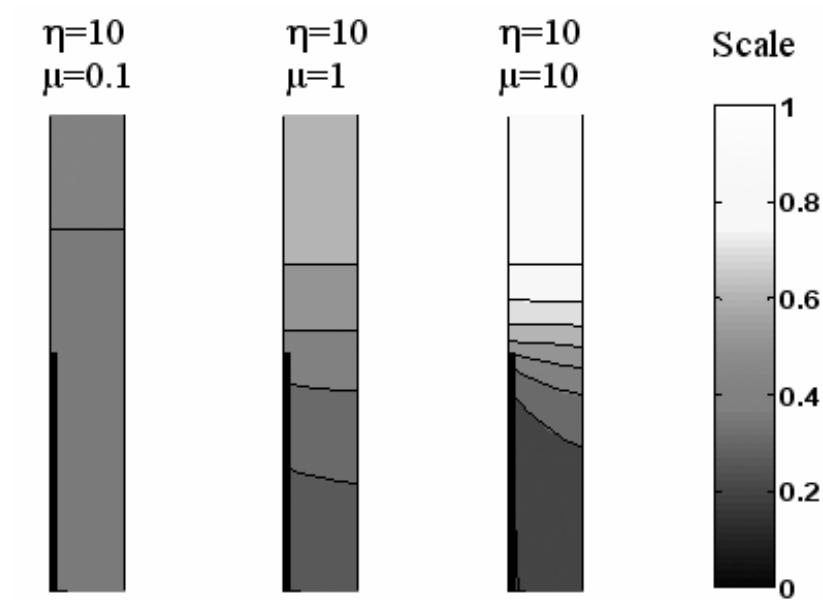


Figure 2.3: Contour plots of magnetization at $t = 1$ in coupled pores with $\beta = 0.5$ and $\eta = 10$ and different values of μ . The gradients along the longitudinal direction for larger μ imply that micropore is relaxing faster compared to macropore.

Note that μ is based on an analysis for a one-dimensional pore with a single characteristic length (L_2). For a one dimensional pore, μ can also be expressed as the square of the ratio of pore length to diffusion length as shown

$$\mu = \frac{\rho L_2}{D} = \frac{L_2^2}{DL_2/\rho} = \left(\frac{L_2}{\sqrt{DT_{2,1-D}}} \right)^2 \quad (2.21)$$

where $1/T_{2,1-D}$ is the relaxation rate of the one-dimensional pore given as

$$\frac{1}{T_{2,1-D}} = \rho \left(\frac{S}{V} \right)_{\text{pore}} = \frac{\rho}{L_2} \quad (2.22)$$

The assumption of a single surface-to-volume ratio inherent in the definition of μ fails for a system of coupled micropore and macropore with different surface-to-volume ratios. Figure 2.4 shows the contour plots of magnetization at dimensionless time $t = 1$ for three coupled pore systems with $\beta = 0.5$ and $\mu = 0.1$ but with increasing aspect ratios. Even

though μ remains same, the systems with larger η show larger gradients in magnetization. This increase in gradients is because as η increases, the dimension of micropore decreases ($\eta = L_2/L_1$) and thus, the relaxation rate of micropore increases. Since μ is independent of the micropore dimension, it can *not* characterize relaxation regimes in coupled pore systems.

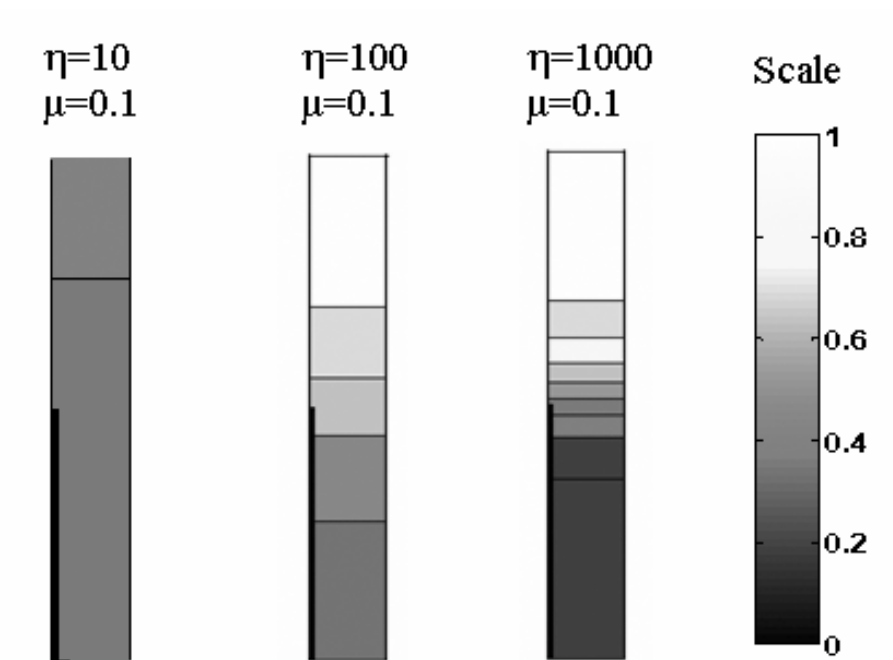


Figure 2.4: Contour plots of magnetization at $t = 1$ in coupled pores with $\beta = 0.5$ and $\mu = 0.1$ and different values of η . For comparison, the aspect ratios are *not* drawn to scale. Note the difference in contour plots for systems with same μ .

2.2.3. Coupling parameter

Two processes characterize the decay of magnetization in the coupled geometry: relaxation of spins at the micropore surface and diffusion of spins between the micro and macropore. If the relaxation of spins in the micropore is much faster than the inter-pore diffusion, coupling between the two pore types is small. On the other hand, if the

diffusion rate is much greater than the relaxation rate, the two pores are significantly coupled with each other. Thus, the extent of coupling can be characterized with the help of a coupling parameter (α) which is defined as the ratio of the characteristic relaxation rate of the pore to the rate of diffusional mixing of spins between micro and macropore, i.e.

$$\alpha = \frac{1/T_{2c}}{D/L_2^2} = \frac{\rho\beta/L_1}{D/L_2^2} = \frac{\rho\beta L_2^2}{DL_1} = \beta\eta\mu \quad (2.23)$$

The physical significance of α can be illustrated with the help of simulated T_2 distributions for the previously mentioned case of $\beta = 0.5$ and $\eta = 10$ as shown in Figure 2.5. For small α ($= 0.5$), relaxation at micropore surface is small compared to diffusional mixing between the two pore types. Thus, the micro and macropore relax at the same rate and the T_2 distribution shows a single peak. As the value of α increases ($\alpha = 5$), some spins in the micropore are able to relax faster than they can diffuse into the macropore. This results in the appearance of a peak at short relaxation times (micropore peak). In addition, the spins in the macropore diffuse to the micropore slowly and thus, the macropore peak shifts towards longer relaxation times. As a still weaker coupling regime is approached ($\alpha = 50$), the inter-pore diffusion becomes negligible and the entire micropore relaxes independent of the macropore. Thus, the amplitude of the micropore peak in the T_2 distribution approaches the true microporosity fraction β .

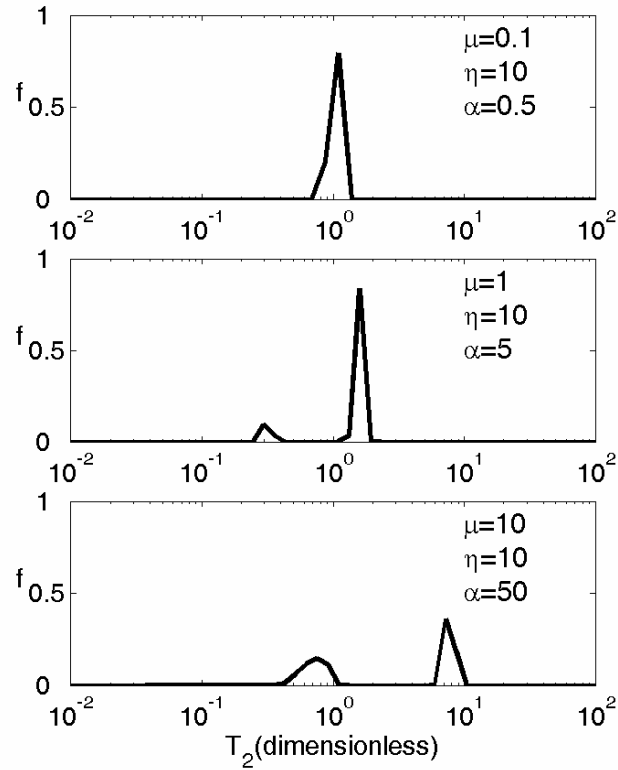


Figure 2.5: Simulated T_2 distributions of coupled pores with $\beta = 0.5$ and $\eta = 10$ and different values of μ . The systems transition from unimodal to bimodal distribution with increase in α .

α can also be expressed as the square of the ratio of the pore length to the diffusion distance in characteristic relaxation time $T_{2,c}$ (Equation 2.14) as shown below

$$\alpha = \frac{\rho\beta L_2^2}{DL_1} = \frac{L_2^2}{D(L_1 / \rho\beta)} = \left(\frac{L_2}{\sqrt{DT_{2,c}}} \right)^2 \quad (2.24)$$

Thus, if the macropore length is much larger than the diffusion distance in characteristic time (i.e. $L_2 \gg \sqrt{DT_{2,c}} \Rightarrow \alpha \gg 1$), the pores are decoupled and vice versa. Since the characteristic relaxation time takes into account the effective surface-to-volume ratio of the coupled pore, α provides a better metric than μ to quantify coupling between the

micro and macropore. Figure 2.6 shows the simulated T_2 distributions of systems with $\beta = 0.5$ and $\mu = 0.1$ but with increasing η . The systems progressively transition from unimodal to bimodal distribution as η increases even though μ remains same. The decrease in coupling is, however, quantified by increasing values of α .

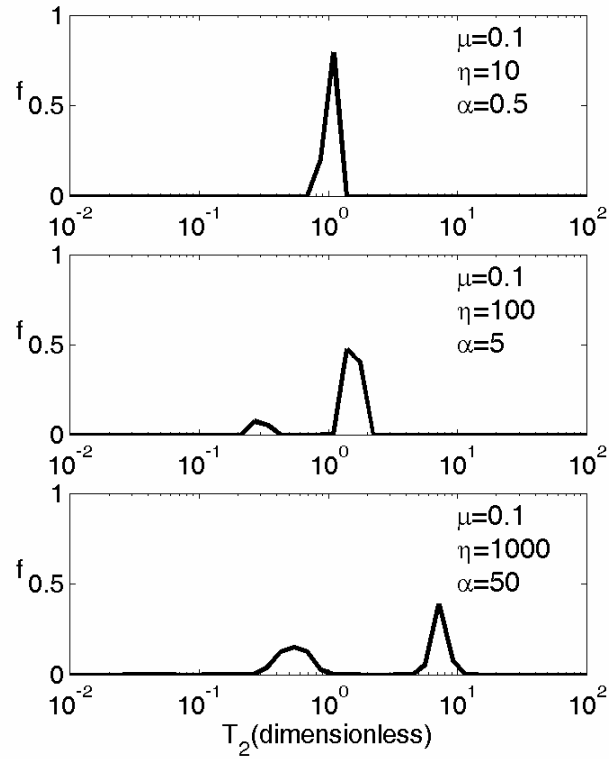


Figure 2.6: Simulated T_2 distributions of coupled pores with $\beta = 0.5$ and $\mu = 0.1$ and different values of η . The T_2 distributions transition from unimodal to bimodal distribution with increase in α even though μ remains same.

The relaxation of micro and macropore can be separately analyzed in terms of α as described below.

2.2.3.1. Micropore relaxation

The amplitude of the micropore peak (called ψ) in the T_2 distribution gives the magnitude of the fraction of the microporosity which is decoupled from the rest of the

pore. ψ , thus, serves as the criterion to quantify the extent of coupling between the micro and macropore. For totally coupled micro and macropore $\psi = 0$ while for decoupled pores $\psi = \beta$. A value of ψ between 0 and β indicates intermediate state of diffusional coupling. Figure 2.7 shows the plot of the ψ normalized by β (henceforth referred to as **independent microporosity fraction**) with α . The curves correspond to different β and span a range of η from 10 to 1000. The results show that depending on the value of α , micro and macropore can be in one of the three states of:

1. **Total coupling** ($\alpha < 1$) - For values of α less than 1, diffusion is much faster than relaxation of magnetization in the micropore. Thus, the micropore is totally coupled with the macropore and the entire pore relaxes with a single relaxation rate.
2. **Intermediate coupling** ($1 < \alpha < 250$) - In this case, diffusion is just fast enough to couple part of the micropore with the macropore. The T_2 distribution consists of distinct peaks for the two pore types but the amplitudes of the peaks are not proportional to the porosity fractions.
3. **Decoupled** ($\alpha > 250$) - The two pore types relax independently of each other and the T_2 spectrum consists of separate peaks with amplitudes representative of the porosity fractions (β and $1-\beta$ for micro and macroporosity respectively). Furthermore, the dimensionless relaxation time of the micropore peak reaches a value β (Appendix B) indicating complete independence of the two pores.

It can be seen that the independent microporosity fraction correlates more strongly with α than with μ (inset in Figure 2.7). This is because α has dependence on the length scale of

both the micro and macropore and thus, it provides a better measure to quantify the extent of coupling.

The sigmoidal character of the curves in Figure 2.7 suggests that a lognormal relationship can be established between the independent microporosity fraction and α . Mathematically, the relationship can be expressed as

$$\frac{\psi}{\beta} = \frac{1}{2} \left[1 + \operatorname{erf} \left(\frac{\log \alpha - 2.29}{0.89\sqrt{2}} \right) \right] \quad (2.25)$$

The choice of mean and standard deviation of the lognormal relationship is governed by experimental results, as shown later.

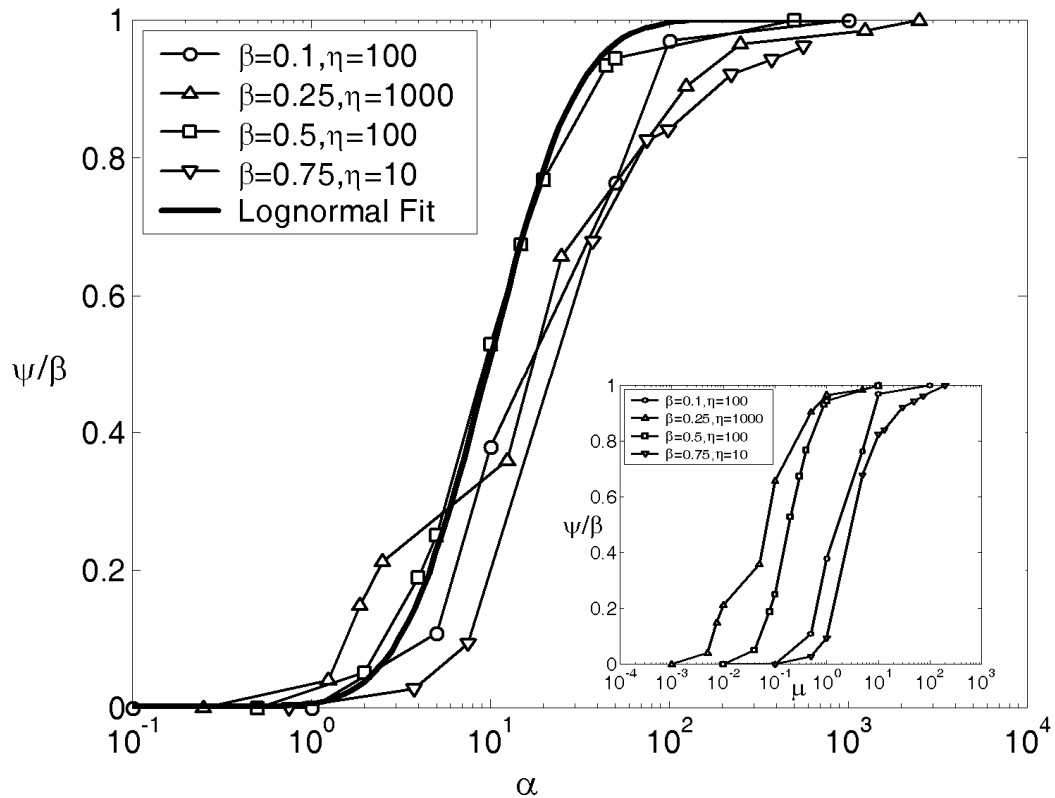


Figure 2.7: Plot of independent microporosity fraction (ψ/β) with α for different simulation parameters. The inset shows plot of (ψ/β) with μ for same simulation parameters.

2.2.3.2. Macropore relaxation

Since the relaxation of both micro and macropore is governed by the same Bloch Equation (2.11), relaxation time of the macropore is expected to also correlate with α . It is however, found that the macropore relaxation time correlates with the product of α and square of macroporosity fraction $(1-\beta)$. This is because the product $(1-\beta)^2\alpha$ represents the normalized diffusion time (t_d) within the macropore as described below

$$(1-\beta)^2\alpha = \frac{((1-\beta)L_2)^2/D}{L_1/\rho\beta} = \frac{t_d}{T_{2,c}} \quad (2.26)$$

Figure 2.8 shows the plot of the dimensionless relaxation time of the macropore with $\nu = (1-\beta)\sqrt{\alpha}$ for different parameter values. Here, the relaxation time is correlated with ν instead of its square because ν is proportional to the length scale, L_2 , of macropore (Equation 2.26). A cubic relationship between the dimensionless macropore relaxation time and ν can be established as shown in Equation (2.27). The cubic relationship provides a better statistical correlation with the experimental results than a quadratic one. The functional relationship, although fitted to experimental results for sandstones and grainstones as shown later, closely match the simulation results.

$$T_{2,\text{macro}}^* = 1 + 0.025\nu + 0.4\nu^2 - 0.009\nu^3 \quad (2.27)$$

where $10^{-1} < \nu < 10^1$.

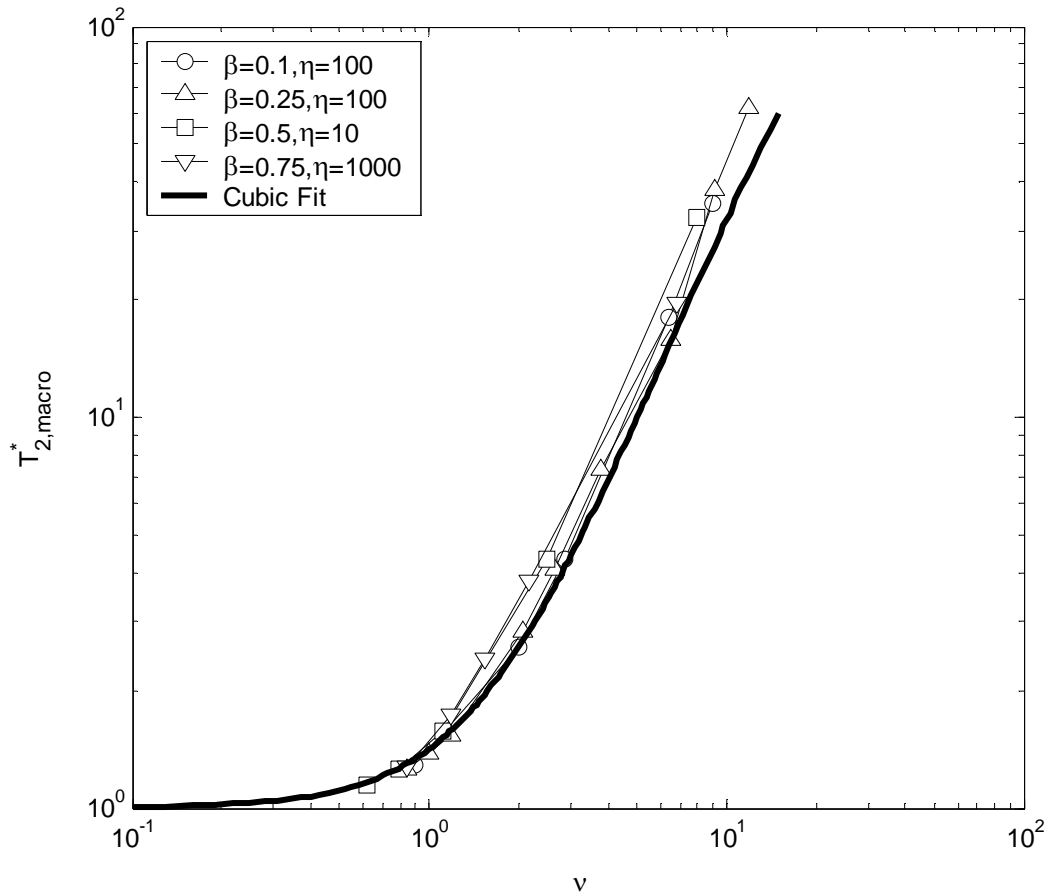


Figure 2.8: Plot of dimensionless relaxation time of macropore with $(1 - \beta)\sqrt{\alpha}$.

2.2.4. Estimation of irreducible water saturation and α

The sharp cutoff method for estimating irreducible water saturation ($S_{w,irr}$) employs a lithology-specific sharp $T_{2,cutoff}$ to partition the T_2 spectrum into free fluid and bound fluid saturations. For formations with diffusionally coupled micro and macropores, the use of a sharp cutoff may give incorrect estimates since in such cases the direct relationship between the pore size and the T_2 distribution no longer holds.

In case of pore coupling, the estimation of $S_{w,irr}$ amounts to the calculation of microporosity fraction (β) for a given T_1 or T_2 distribution at 100% water saturation. The

solution of this inverse problem is obtainable by making use of the correlations for independent microporosity fraction and normalized macropore relaxation time (Equations 2.25 and 2.27). Three parameters are required for the estimation: micropore peak amplitude (ψ), micropore relaxation time ($T_{2,\mu}$) and macropore relaxation time ($T_{2,\text{macro}}$). It is assumed that $T_{2,\mu}$ is known from laboratory core analysis and is same for the formation. This assumption is justified if the formation has similar relaxivity and micropore structure as the cores. From the T_2 spectrum at 100% water saturation, the values of ψ and $T_{2,\text{macro}}$ can be calculated as the area under the micropore peak and relaxation time of the mode of the macropore peak, respectively. Hence, for the calculated parameter values, the correlations can be simultaneously solved for the values of α and β . Graphically, the solution involves determining the intersection point of contours of ψ and $T_{2,\text{macro}}/T_{2,\mu}$ in the α and β parameter space as shown in Figure 2.9. The values of contour lines for $T_{2,\text{macro}}/T_{2,\mu}$ differ by a factor of 2 and those for ψ differ by 0.1. The coordinates of the intersection point of the contours for experimentally determined values of ψ and $T_{2,\text{macro}}/T_{2,\mu}$ estimates the value of α and β for the formation. For a unimodal distribution with $\psi = 0$ (total coupling regime), the microporosity fraction can be calculated from the ratio of the relaxation times of micro and macropore, i.e.

$$\beta = \left(\frac{T_{2,\mu}}{T_{2,\text{macro}}} \right), \psi = 0 \quad (2.28)$$

In this case, the value of α is indeterminate and can be anything less than 1. This is because as ψ approaches 0, the contours for $T_{2,\text{macro}}/T_{2,\mu}$ asymptote to the reciprocal β value independent of α . (Note $\psi = 0$ implies totally coupled micro and macropore and not necessarily the absence of microporosity). The inversion technique provides accurate

estimates of microporosity fraction for the experimental sandstone and grainstone systems as shown in later sections.

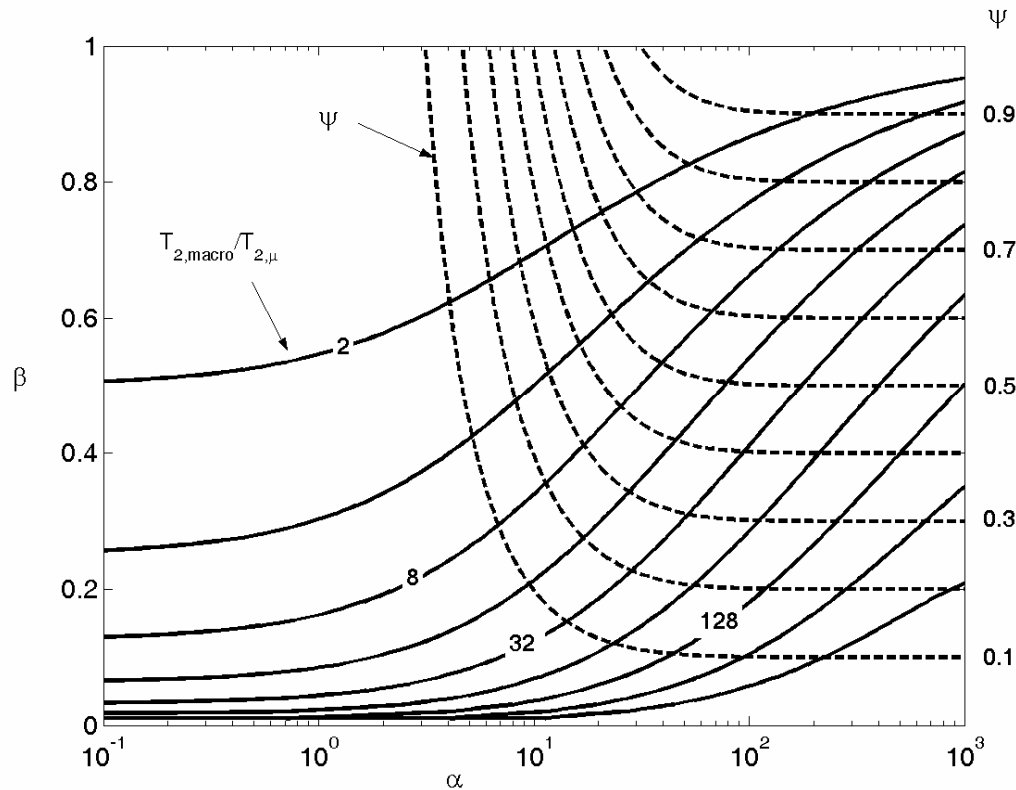


Figure 2.9: Contour plots of correlations for ψ and $T_{2,macro}/T_{2,\mu}$ in the α and β parameter space.

2.2.5. Unification of spectral and sharp $T_{2,cutoff}$ theory

The estimation of $S_{w,irr}$ using spectral or tapered $T_{2,cutoff}$ is based on the premise that each pore size has its own inherent irreducible water saturation (Coates et al., 1998; Kleinberg et al., 1997). An implicit assumption of the above-mentioned techniques is that the producible and irreducible fractions of each pore are totally coupled at 100% water saturation. However, the analysis of a single coupled pore shows that the micro and macropore can communicate through decoupled and intermediate coupling regimes as

well. Thus, in a general coupling scenario, the response of the pore shows distinct peaks for micro and macropore with amplitudes ψ and $(1-\psi)$, respectively. The amplitude ψ can vary from 0 to β depending on the coupling regime. Therefore, the portion of the microporosity coupled with the macropore divided by the macropore amplitude is given as

$$\Theta\left(\frac{T_{2,\text{macro}}}{T_{2,\mu}}, \alpha\right) = \frac{\beta - \psi}{1 - \psi} \quad (2.29)$$

Θ is a function of the ratio of macropore relaxation time to micropore relaxation time ($T_{2,\text{macro}}/T_{2,\mu}$) and α which determines the microporosity portion coupled with the macropore response. As α increases, the extent of pore coupling decreases and thus, the microporosity fraction coupled with the macropore response also decreases. Figure 2.10 shows the plot of Θ with ($T_{2,\text{macro}}/T_{2,\mu}$) for different values of α . The procedure for estimating Θ as a function of ($T_{2,\text{macro}}/T_{2,\mu}$) is as follows. For a known value of α , Θ is calculated from Equation (2.29) for several values of β using Equation (2.25). Similarly, $T_{2,\text{macro}}/T_{2,\mu}$ is calculated for the known α and same values of β by substituting the expression of $T_{2,c}$ from Equation (2.16) in Equation (2.27)

$$\frac{T_{2,\text{macro}}}{T_{2,\mu}} = \frac{1 + 0.025\nu + 0.4\nu^2 - 0.009\nu^3}{\beta} \quad (2.30)$$

Thus, the values of Θ and ($T_{2,\text{macro}}/T_{2,\mu}$) for the same α and β can be cross-plotted as shown in Figure 2.10.

The curves in Figure 2.10 show that a spectral or tapered cutoff is required for the estimation of irreducible saturation in total or intermediate coupling regime. As α increases, Θ decreases for same $T_{2,\text{macro}}/T_{2,\mu}$ indicating lesser correction for diffusional

coupling is required for larger α . Once the pores are decoupled, a sharp cutoff is suitable for estimating irreducible fraction as illustrated by sharp fall of Θ curve to zero for $\alpha > 250$. This sharp decrease in Θ could also probably explain the suitability of a single lithology-specific $T_{2,\text{cutoff}}$ for estimating irreducible saturations when the formation is in decoupled regime irrespective of the properties. More experiments are however, needed to prove this postulate.

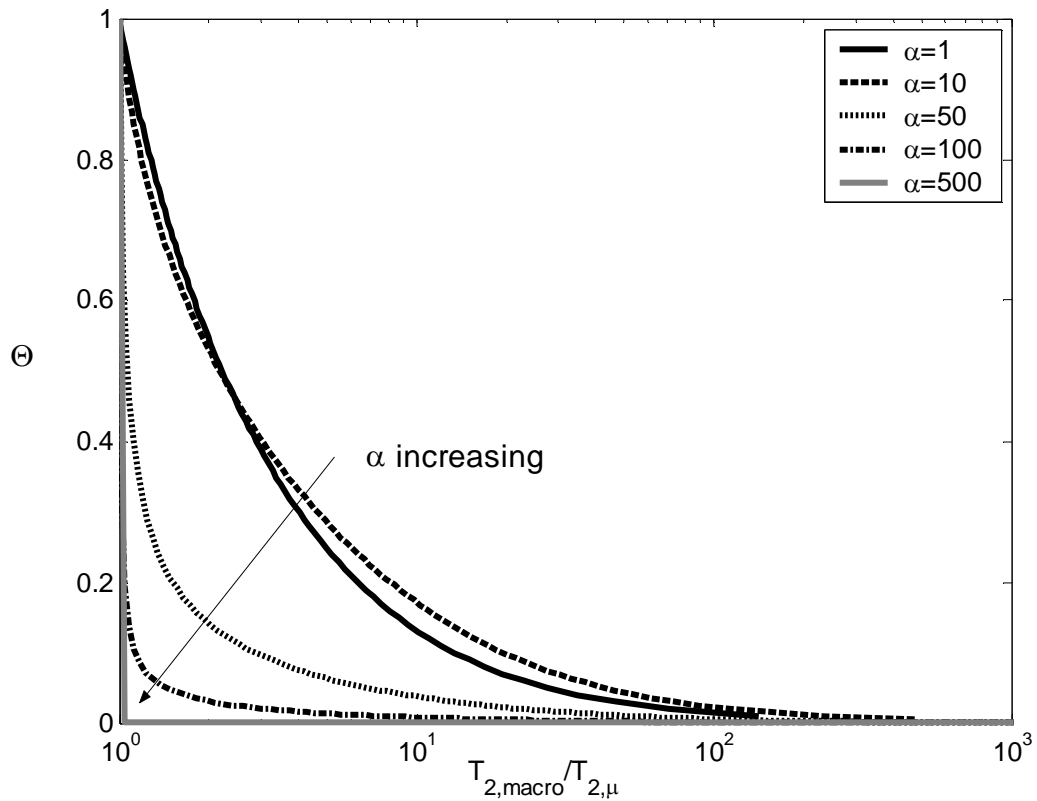


Figure 2.10: Plot of Θ vs. $T_{2,\text{macro}}/T_{2,\mu}$ for different α . A spectral or tapered cutoff is required for the estimation of irreducible saturation in the intermediate coupling regime. A sharp cutoff is applicable for the decoupled regime.

2.3. Diffusional coupling between pore lining clays and pore body

In this section, the theory developed in the previous section is applied to describe diffusional coupling in clay-lined pores in sandstones. Straley et al. (1995) modeled the clay flakes as forming microchannels perpendicular to the pore walls such that each micropore opens to a macropore (Figure 2.11a). The two dimensional structure of the clay-lined pore can be modeled as an array of rectangular flakes arranged along the wall of a macropore (Zhang et al., 2001; Zhang et al., 2003). Since the model is periodic, the relaxation process can be adequately modeled by considering only the symmetry element between two clay flakes. The model can be further simplified to the one described in Figure 2.2 by approximating the flakes to be needle shaped with negligible thickness as shown in Figure 2.11(b).

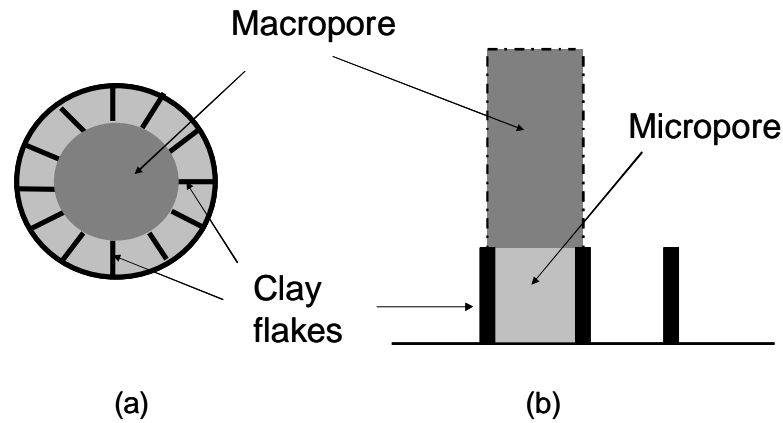


Figure 2.11: (a) Model of a clay-lined pore showing micropores opening to a macropore (Straley et al., 1995) (b) Simplified model with rectangular clays arranged along macropore wall.

2.3.1. Pore size distribution of North Burbank sandstone

To experimentally validate the theoretical model, NMR response of North Burbank (NB) sandstone with pores lined with chlorite flakes is simulated (Trantham and Clampitt, 1977). Analysis of the sandstone cores yielded an average porosity of 0.22 and air/brine permeability of 220 mD. The pore throat distribution obtained by mercury porosimetry for one of the cores is shown in Figure 2.12. The bimodal structure of the distribution arises due to the presence of pore-lining chlorite flakes. Mercury first invades the macropores giving rise to the peak at larger pore radii. The clay flakes, being closely spaced, are invaded by mercury at high capillary pressures which gives rise to the peak at smaller pore radii.

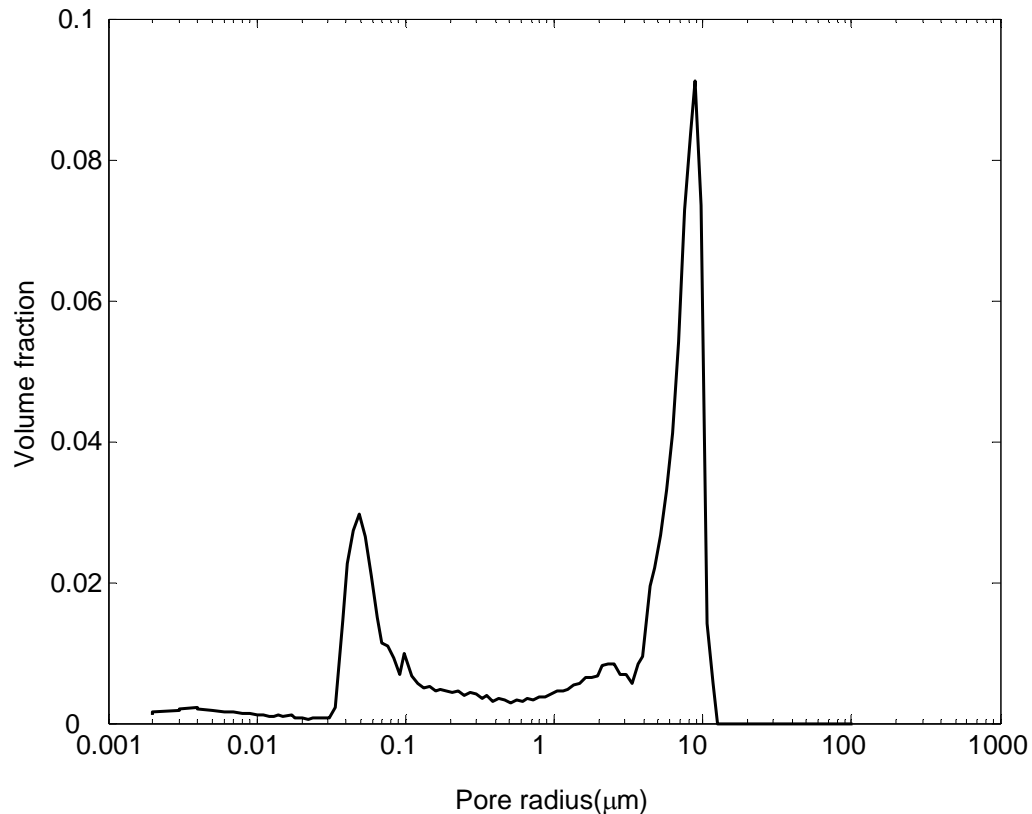


Figure 2.12: Pore throat distribution of the North Burbank sandstone obtained from mercury porosimetry. The bimodal distribution arises due to pore-lining chlorite.

A lognormal distribution with mean of 8 μm and standard deviation 0.135 is simulated to approximate the distribution of macropores (Figure 2.13). Since mercury porosimetry measures the distribution of pore throats, the distribution of pore bodies is obtained by assuming a fixed pore body to pore throat ratio of 3 (Lindquist et al., 2000). Thus, the most abundant pore has the pore radius (L_2) of 24 μm . Each pore is then modeled to be lined with clay flakes which are assumed to be of constant length and equally spaced in all pores. As a result, the flakes completely occupy the small pores and form just a thin rim on the surface of larger pores. The distance between the flakes (L_1) is given by the peak at smaller pore radius in the pore size distribution ($\approx 0.03 \mu\text{m}$).

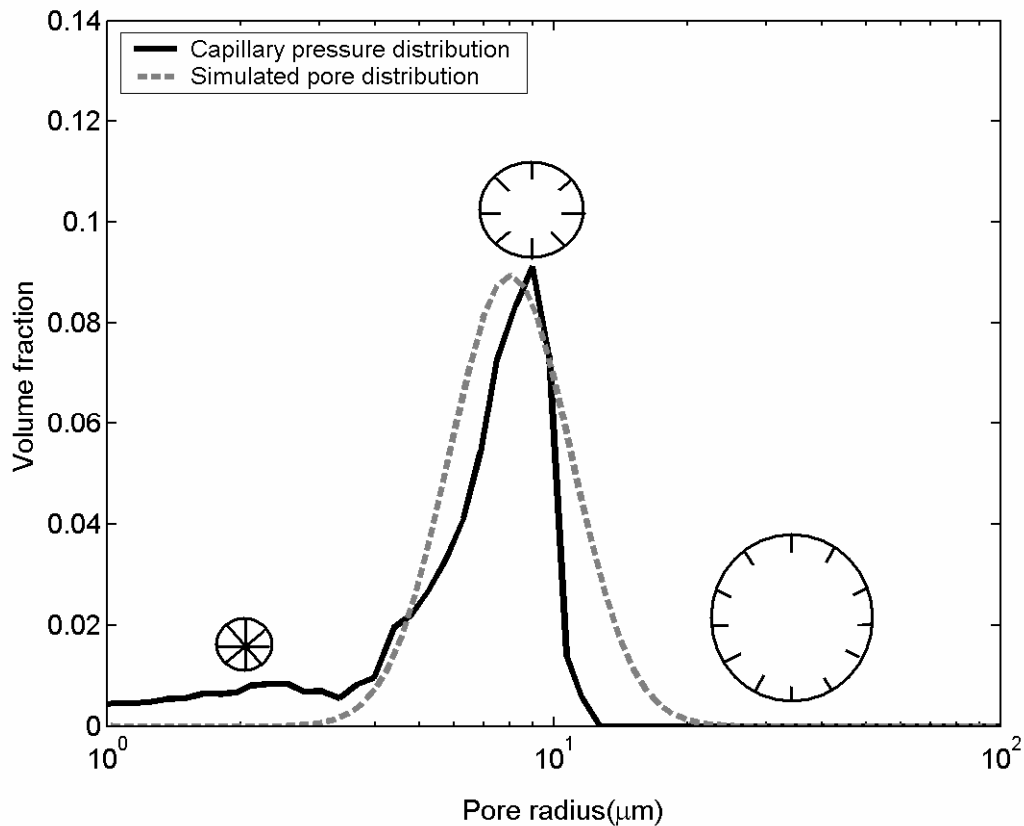


Figure 2.13: Lognormal pore size distribution simulated to approximate the distribution of macropores. Also shown are the pores with changing proportion of pore volume occupied by the clay flakes.

2.3.2. Numerical solution of Bloch equation in pore size distribution

In order to solve Equation (2.11) for the decay of magnetization in the i^{th} pore, three parameters are needed for each pore:

1. Microporosity fraction β_i
2. Aspect ratio $\eta_i = L_{2,i}/L_{1,i}$
3. Brownstein number $\mu_i = \rho L_{2,i}/D$

The parameters in different pores are, however, not totally independent of each other since they are constrained by the assumptions of constant length and equal spacing between clay flakes in all pores. Mathematically, the constraints imply

$$L_{1,i} = L_{1,c} = \text{const.} \quad (2.31)$$

$$\beta_i L_{2,i} = \beta_c L_{2,c} = \text{const.} \quad (2.32)$$

where the subscript “c” refers to the characteristic (most abundant) pore. Since the value of L_1 is constant (constraint 1), the aspect ratio of the i^{th} pore ($L_{2,i}/L_{1,i}$) is related to the aspect ratio of the characteristic pore as

$$\eta_i = \frac{L_{2,i}}{L_1} = \frac{L_{2,c}}{L_1} \frac{L_{2,i}}{L_{2,c}} = \eta_c \frac{L_{2,i}}{L_{2,c}} \quad (2.33)$$

Constraint 2 provides a similar relationship between microporosity fractions of the individual pores to the microporosity fraction for the characteristic pore (β_c),

$$(\beta L_2)_i = (\beta L_2)_c \quad (2.34)$$

$$\beta_i = \beta_c \frac{L_{2,c}}{L_{2,i}} \quad (2.35)$$

Further, assuming that the value of the clay surface relaxivity and the diffusion coefficient of the fluid remains constant in all the pores, the Brownstein number of the individual pore (μ_i) is also related to that of the characteristic pore as

$$\mu_i = \left(\frac{\rho L_{2,i}}{D} \right) = \left(\frac{\rho L_{2,c}}{D} \right) \cdot \left(\frac{L_{2,i}}{L_{2,c}} \right) = \mu_c \left(\frac{L_{2,i}}{L_{2,c}} \right) \quad (2.36)$$

Hence, the parameters for the only characteristic pore need to be specified and Equations (2.33-2.36) can be used to calculate the parameters for rest of the pores. Similar to the analysis of a single pore in the previous section, the governing Equations (2.11-2.13) for each pore are non-dimensionalized with respect to common characteristic parameters. Hence, the spatial and temporal variables are respectively normalized by the radius and characteristic relaxation time (Equation 2.14) of the most abundant pore.

The dimensionless diffusion equation (Equation A.1, Appendix A) is solved for the decay of magnetization in each pore individually. The magnetization in the entire pore structure is computed by linearly interpolating the individual magnetization values at some common values of time, and then integrating them over the entire pore volume. Interpolation is needed since the algorithm for computing magnetization in individual pores uses an adaptive time stepping to reduce the computational time and truncation errors (Appendix A). Hence, the magnetization in different pores is not known at same values of time. The decay times for the slowest relaxing pore, i.e. with smallest microporosity fraction, are taken as the common time values for interpolation. The total magnetization (M_t) in the pore size distribution is given as

$$M_t(t) = \sum_i^{N_p} V_{p,i} \cdot M_i(t) \quad (2.37)$$

where N_p is the number of pores, $V_{p,i}$ is the volume fraction of the i^{th} pore and M_i is the magnetization in the i^{th} pore at dimensionless time t . The T_2 distribution for the pore structure is obtained by fitting a multi-exponential fit to the total magnetization.

2.3.3. Simulated T_2 distributions

Since each pore in the lognormal pore size distribution has a different value of α , a volume averaged $\bar{\alpha}$ for the distribution can be defined as

$$\bar{\alpha} = \sum_i \alpha_i V_{p,i} \quad (2.38)$$

The simulated T_2 distributions for the pore size distribution with typical values of β_c and η_c ($\beta_c = 0.3$ and $\eta_c = 100$) are shown in Figure 2.14 as a function of $\bar{\alpha}$. It can be seen that the T_2 distribution changes from unimodal to bimodal with increase in $\bar{\alpha}$. This transition occurs because when $\bar{\alpha} < 1$, the pores are in total coupling regime and each pore relaxes single exponentially with the dimensionless relaxation time, $T_{2,i}$, given as

$$T_{2,i} = \frac{(V/\rho S)_i}{T_{2,c}} = \frac{\beta_c}{\beta_i} = \frac{L_{2,i}}{L_{2,c}} \quad (2.39)$$

Thus, for $\bar{\alpha} < 1$, the T_2 distribution exactly replicates the unimodal lognormal distribution of the pore radii. As the pores enter the intermediate coupling regime ($\bar{\alpha} > 1$), a fraction of micropores starts relaxing faster than the rate of diffusional mixing with the macropores, thereby giving the T_2 distributions a bimodal shape.

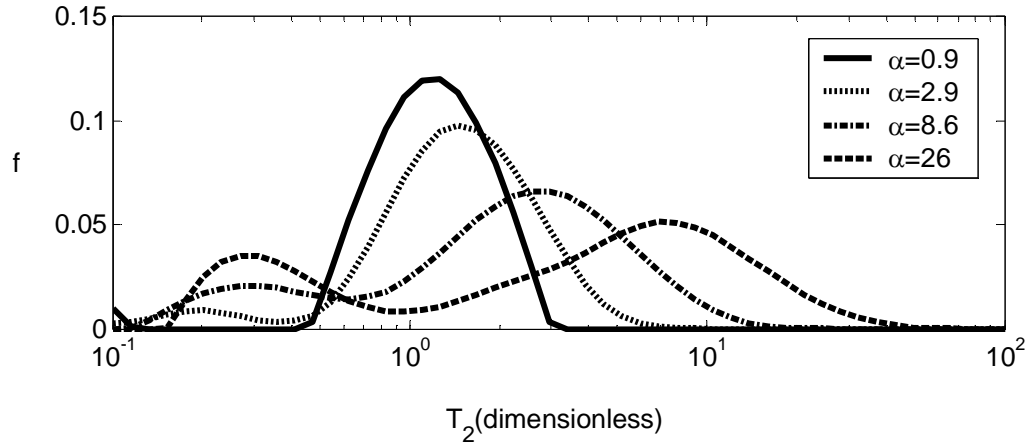


Figure 2.14: Simulated T_2 distributions for $\beta_c = 0.3$ and $\eta_c = 100$ showing transition from unimodal to bimodal distribution with increase in $\bar{\alpha}$.

2.3.4. Coupling regimes in North Burbank sandstone

The simulations with characteristic parameters (β_c, η_c, μ_c) representative of the core properties can be compared with the experimental results for North Burbank. Hence, the value of β_c is calculated such that the microporosity fraction of the simulated pore size distribution corresponds to the irreducible water saturation,

$$\sum_i^{N_p} \beta_i V_{p,i} = S_{w,irr} \quad (2.40)$$

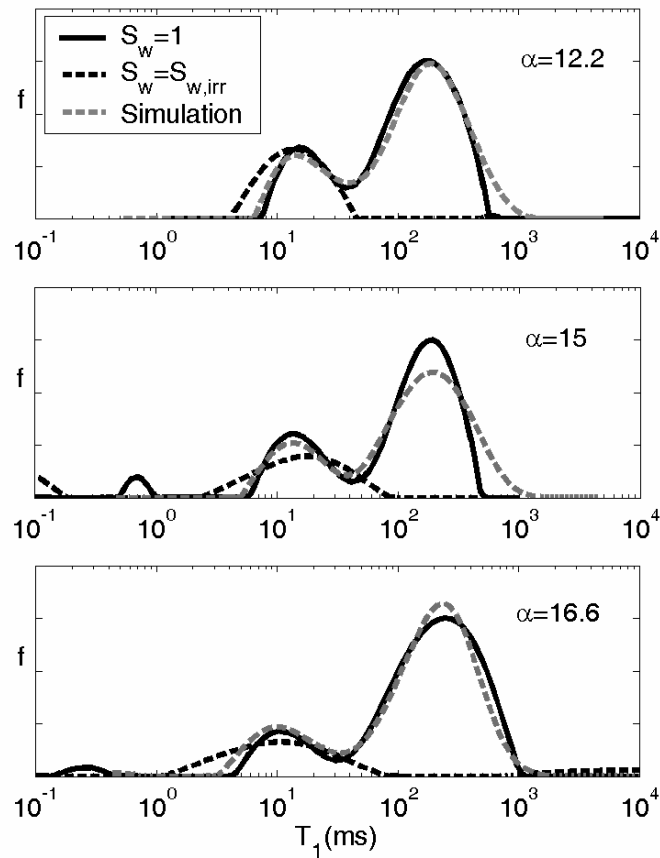
$$\Rightarrow \beta_c = \frac{S_{w,irr}}{L_{2,c} \sum_i^{N_p} \frac{V_{p,i}}{L_{2,i}}} \quad (2.41)$$

The aspect ratio η_c is calculated as the ratio of the macropore to micropore radius obtained from mercury porosimetry. The third parameter μ_c is specified such that the simulations best match with the experimental results.

Figure 2.15 shows the comparison of T_1 distributions of three water-saturated NB cores with the corresponding simulated distributions. Here, the comparison is made with the T_1 (instead of T_2) distributions since T_2 relaxation is additionally influenced by internal gradients induced by chlorite flakes (Zhang et al., 2001; Zhang et al., 2003). Diffusional coupling however, influences both T_1 and T_2 relaxation since it arises due to diffusion between pores of different surface-to-volume ratios. The characteristic parameters for the simulations are shown in Table 2.1. The dimensionless simulated distributions are dimensionalized by choosing $T_{2,c} = 50, 44$ and 40 ms respectively which gives the best overlay of the simulated and experimental distributions. The simulated distributions very well estimate the location as well as the amplitudes of the micro and macropore peaks. The values of $\bar{\alpha}$ ($=12.2, 15$ and 16.6) indicate that the two pore types are in intermediate coupling regime. This is also demonstrated in Figure 2.16 (a) which shows the plot of the amplitude of the micropore peak at 100% water saturation normalized with the total microporosity fraction with $\bar{\alpha}$ for the three cores. The measurements fall in the intermediate coupling regime of the lognormal relationship (Equation 2.25). Figure 2.16 (b) shows that the cubic relationship (Equation 2.27) for the normalized macropore relaxation time also holds for the three cores. In this figure, the relaxation time of the macropore is normalized by a characteristic relaxation time defined by Equation (2.16).

Table 2.1: Characteristic parameters for the simulations for three NB cores.

Core	β_c	η_c	μ_c	$\bar{\alpha}$
NB1	0.3	800	0.048	12.2
NB2	0.28	800	0.065	15
NB3	0.21	800	0.094	16.6

Figure 2.15: Comparison of simulated and experimental T_1 distributions for three water saturated North Burbank cores.

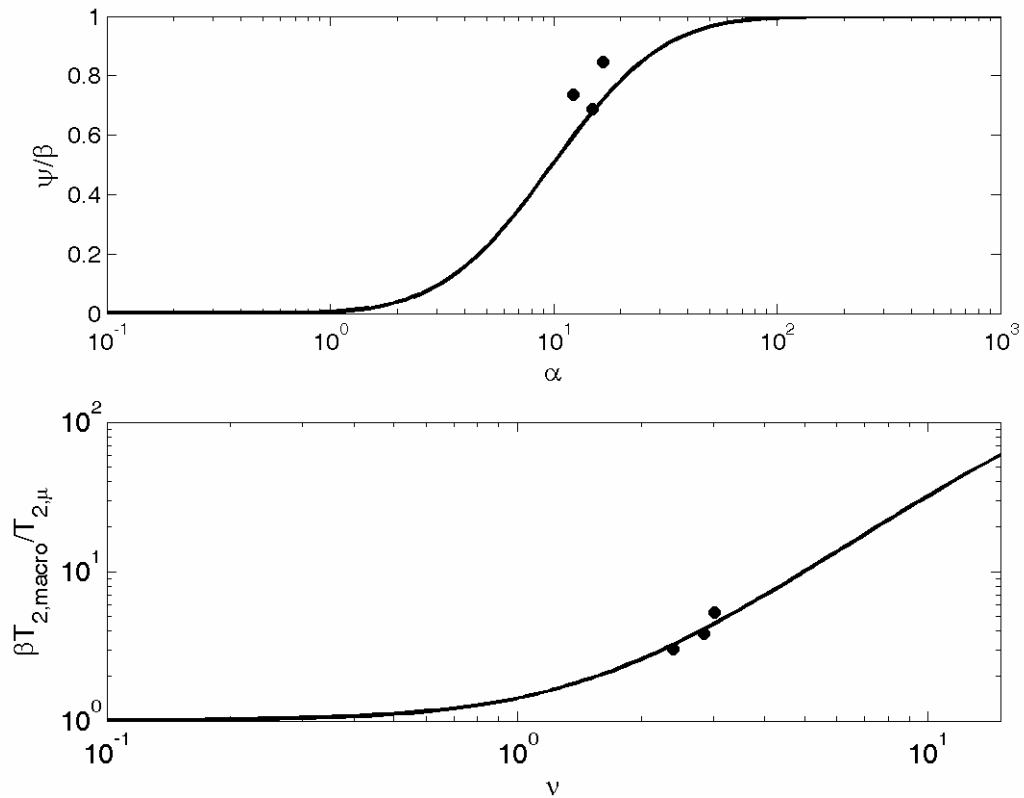


Figure 2.16: (a) Independent microporosity fraction agrees with the lognormal relationship (Equation 2.25) for the three North Burbank cores (b) Normalized macropore relaxation time also agrees with the cubic relationship (Equation 2.27).

To explore another coupling regime, measurements were done with dry cores saturated with hexane. Higher extent of coupling is expected with hexane than with water due to higher diffusivity and lower surface relaxivity for hexane. The lower surface relaxivity for hexane is due to intrinsic smaller hydrocarbon relaxivity of the sandstone surfaces (Chen et al., 2005). Figure 2.17 shows the T_1 distributions of cores NB1 and NB2 saturated with hexane and the corresponding simulated distributions. The dimensionless simulated distributions are dimensionalized by choosing $T_{2,c} = 450$ and 360 ms respectively. In this case, the T_1 distributions are unimodal implying the merger of the

micro and macropore peak. The smaller values of $\bar{\alpha}$ also suggest stronger coupling for hexane than for water.

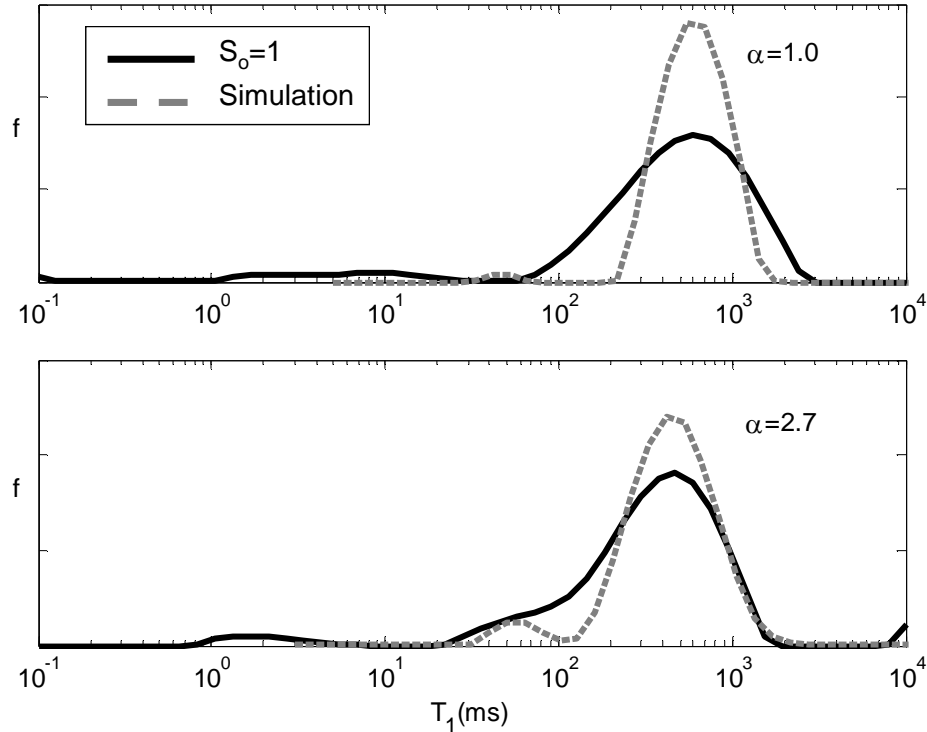


Figure 2.17: Comparison of simulated and experimental distributions for two hexane saturated North Burbank cores.

2.3.5. Estimation of surface relaxivity

The values of surface relaxivity for the North Burbank cores can be calculated from the corresponding values of $\bar{\alpha}$. For the values of parameters $L_{2,c} = 24 \mu\text{m}$, $L_1 = 0.03 \mu\text{m}$, diffusivity for water and hexane $D_W = 2.5 \cdot 10^{-5} \text{cm}^2/\text{s}$ and $D_H = 4.2 \cdot 10^{-5} \text{cm}^2/\text{s}$ (Reid et al., 1987), the average value of relaxivity is found to be $7.1 \mu\text{m}/\text{sec}$ for water and $1.6 \mu\text{m}/\text{sec}$ for hexane. The lower surface relaxivity of hexane is *not* due to water-wetness of the sandstone since hexane was in direct contact with the mineral surfaces and no water was present. Another estimate of relaxivity can be obtained by comparing the cumulative

pore size distributions obtained from T_1 relaxation and mercury porosimetry. However, the estimates from the latter method are about three times ($20 \mu\text{m}/\text{sec}$) as high as those calculated from simulations. This is because mercury porosimetry does not take into account the large surface area provided by the clay flakes in the estimation of relaxivity.

2.4. Effect of clay distribution on pore coupling

The previous section illustrated the applicability of α to quantify coupling between pore-lining clays and pore bodies in sandstones. This section demonstrates that the theory can also be applied to analyze the effect of clay distribution on pore coupling in shaly sands.

NMR well logging has evolved as a promising technology for the formation evaluation of shaly sands. Coates et al. (1994) proposed that the fast relaxing components of the T_2 spectrum in clayey rocks can be attributed to water adsorbed on clays. This idea was extended by Prammer et al. (1996) who found that clays in sandstones exhibited specific transverse relaxation times proportional to their surface area and cation exchange capacity (CEC). Thus, they postulated that the position of fast relaxing T_2 peak can be used for clay typing. This claim was disputed by Matteson et al. (2000) who found that relaxation time of clay-brine slurries is a function of compaction of clays. Since the degree of compaction of formation clays is usually not known, they argued that clay typing from T_2 measurements alone is not possible. In addition, they found that distinct peaks for clay-bound and free water were not visible for the clay-brine slurries.

In order to understand the phenomenological factors causing the apparent differences, a systematic study of the relaxation characteristics of clay-sand systems was undertaken. Two systems of model shaly sands consisting of fine sand and varying

amount of either kaolinite or bentonite clay were prepared. In the first system, the clays were uniformly dispersed (dispersed systems) with the sand such that the clays occupied the interstitial voids between the sand grains. For the second system, clays were present as a separate, discrete layer with the sand (laminated systems). NMR response of the systems was measured at 100% and irreducible water saturations.

2.4.1. Synthesis of model shaly sands with laminated and dispersed clays

Fine sand (grain radius 50 μm), kaolinite and bentonite clays were obtained from Sigma Aldrich. The physical properties of the materials are given in Table 2.2. The dispersed and laminated systems were prepared in four sets such that the clay (either kaolinite or bentonite) constituted 0, 2, 5 and 10% of the total solid content. For each set, the systems were prepared at total and irreducible water saturation separately. The details for the preparation of the systems are included below.

1. **Dispersed systems** - To prepare the dispersed system at 100% water saturation, 15 grams of fine sand was taken in a plastic centrifuge tube. The amount of either clay required to make the desired weight percentage content was added to the sand and the mixture was vigorously shaken to disperse the clay in the interstitial voids between the sand grains. 5 ml of 0.1M Calcium Chloride (CaCl_2) solution was added to the mixture to make thick slurries. The slurries were mixed with a glass rod to further homogenize the clays with the sand and then compacted at a relative centrifugal force (RCF) of 1500g. The small amount of supernatant water obtained after centrifuging was removed.

The dispersed systems at irreducible conditions were made by first preparing the water saturated slurries in a 1'' by 1'' Teflon sleeve. The base of the

sleeve was sealed with a covering of Teflon tape. 15 grams of sand and desired amount of either clay were mixed in the sleeve and the mixture was saturated with 5 ml of CaCl_2 solution. The slurries were then centrifuged in a Beckman rock core centrifuge at an air/water capillary pressure of 50 psi (which also approximately corresponds to 1500g RCF) for 3 hours to drain the free water. The Teflon base is permeable to water but prevents any grain loss during centrifugation.

2. **Laminated systems** – 15 grams of fine sand and 15ml CaCl_2 solution were taken in a centrifuge tube and compacted at 1500g RCF for half hour. The required amount of either clay was then added to the sand and centrifuged for 3 hours to compact the systems. Since the sand had already settled before the introduction of clay, there was no elutriation of the clay with sand. Clay thus, compacted as a laminated layer on top of the sand.

Laminated systems at irreducible conditions were prepared analogously to the dispersed systems at irreducible condition. 15 grams of sand was allowed to settle gravimetrically in 10 ml calcium chloride solution in a 1'' by 1'' sleeve with a sealed base. The required amount of either clay was added to the sand and the systems were centrifuged at 50 psi air/brine capillary pressure to drain the free water.

Table 2.2: Physical Properties of Fine Sand, Kaolinite and Bentonite clays.

	Sand	Kaolinite	Bentonite
Surface Area (m^2/gm)	0.2	19	38
Relaxivity ($\mu\text{m}/\text{sec}$)	4.7	1.4	9.2

2.4.2. T_2 Distributions of model shaly sands

Figures 2.18 and 2.19 show the T_2 distributions of the dispersed and laminated kaolinite systems at 100% water saturation. Figures 2.20 and 2.21 show the corresponding distributions for the dispersed and laminated bentonite systems. For each case, the distributions at irreducible conditions are also shown for comparison. Analysis of the T_2 distributions in Figures 2.18-2.21 shows that the systems exhibit different relaxation characteristics when the clays are dispersed or layered with sand. For the dispersed systems, the T_2 distributions at 100% water saturation show unimodal spectra. The laminated systems, on the other hand, show bimodal T_2 distributions at 100% water saturation. The fast and slow relaxing peaks in the bimodal distributions correspond to water in the clay and sand layer respectively. Note that the faster relaxation of water in bentonite (~ 4 ms) compared to that in kaolinite (~ 25 ms) is due to the large interlayer surface area in swelling bentonite clay (Prost et al., 1998).

Bimodal T_2 distributions of the laminated systems indicate that water populations in the clay and sand layer are decoupled. In contrast, unimodal T_2 distributions for the dispersed systems indicate that water in the interstitial pores between clay and sand is diffusionally coupled. Figure 2.22 shows that the relaxation rate of water in dispersed systems is linearly related to the clay content. Extrapolation of the linear relationship to zero clay fractions has an intercept close to the relaxation rate of water in sand-only system. Thus, the relaxation rate of water in the dispersed systems can be expressed as

$$\frac{1}{T_2} = \frac{\rho_{\text{sand}}S_{\text{sand}} + \rho_{\text{clay}}S_{\text{clay}}}{V_{\text{total}}} \quad (2.42)$$

where $\rho_{\text{sand}}S_{\text{sand}}$ and $\rho_{\text{clay}}S_{\text{clay}}$ are the products of relaxivity and surface area for sand and clay respectively and V_{total} is the total volume of water. Since the relaxation rate is

simultaneously influenced by both clay and sand surface areas, distinct peaks for irreducible and free water are not observed.

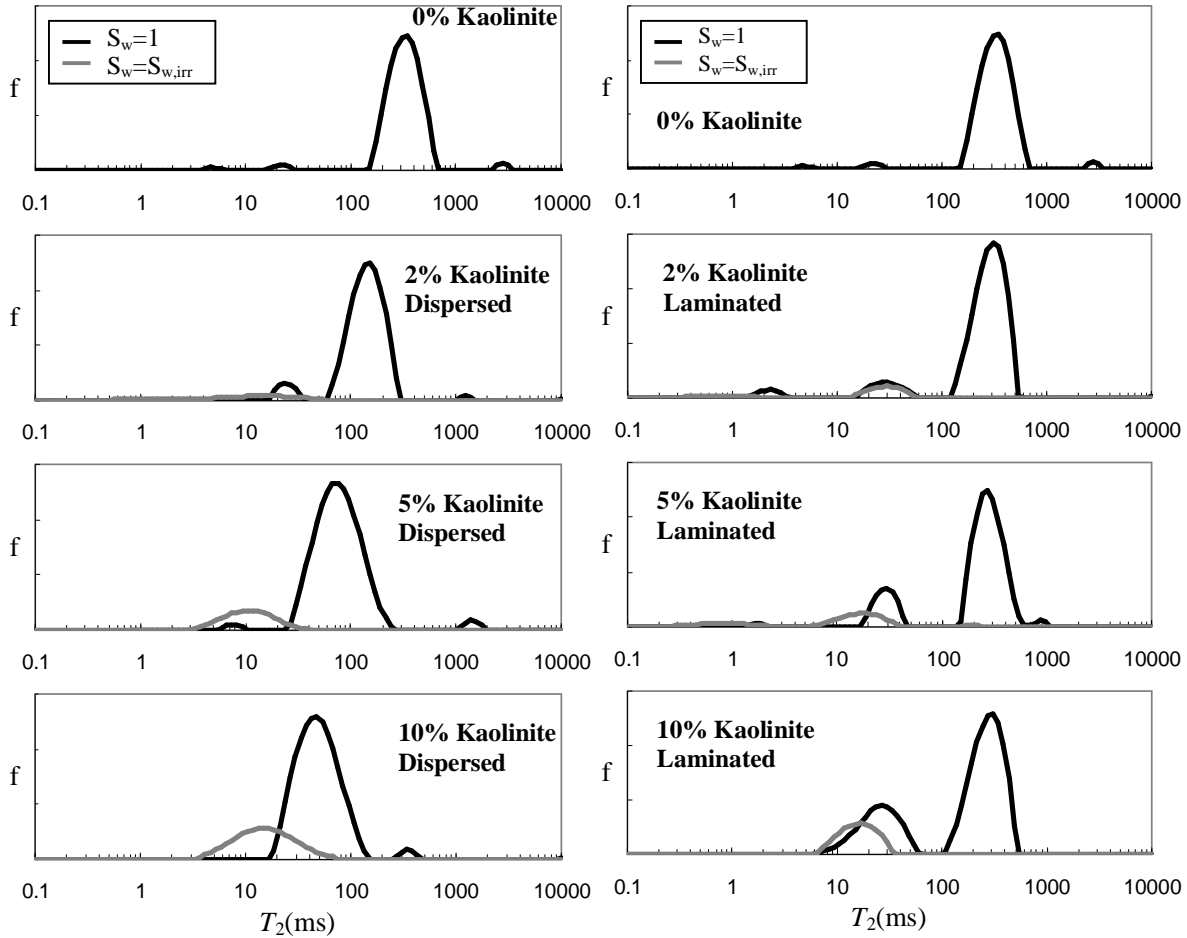


Figure 2.18: T_2 distributions of dispersed kaolinite-sand systems for different clay weight fractions.

Figure 2.19: T_2 distributions of laminated kaolinite-sand systems for different clay weight fractions.

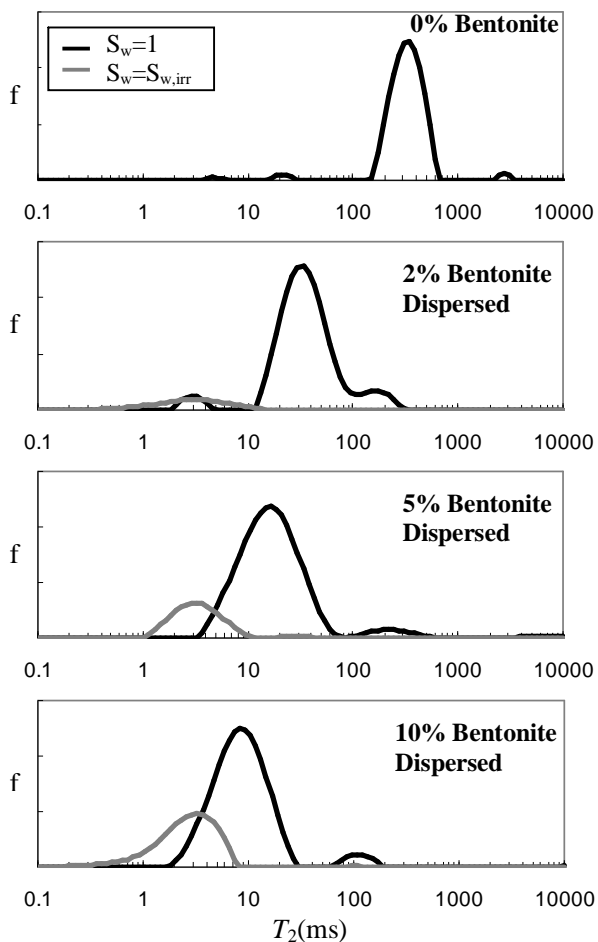


Figure 2.20: T_2 distributions of dispersed bentonite-sand systems for different clay weight fractions.

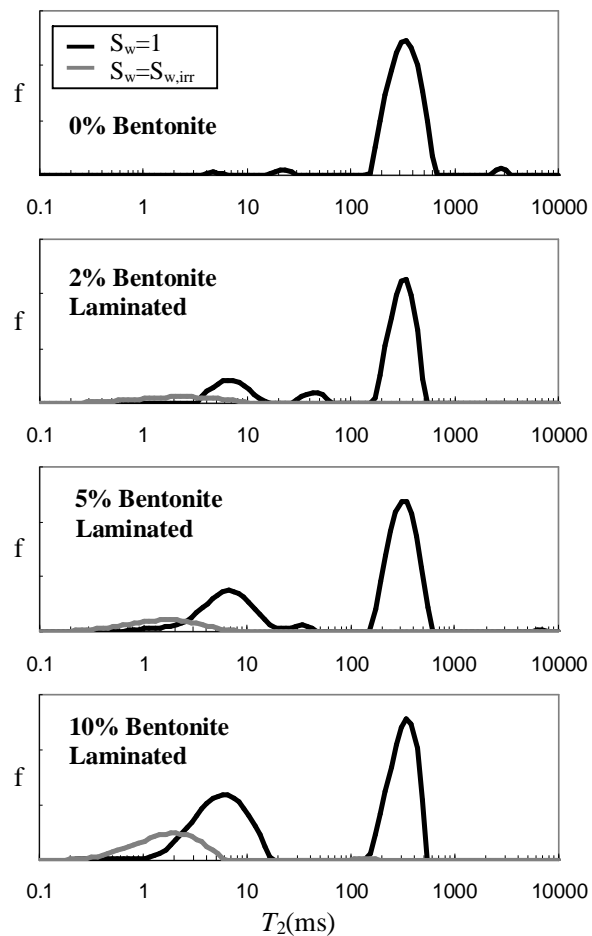


Figure 2.21: T_2 distributions of laminated bentonite-sand systems for different clay weight fractions.

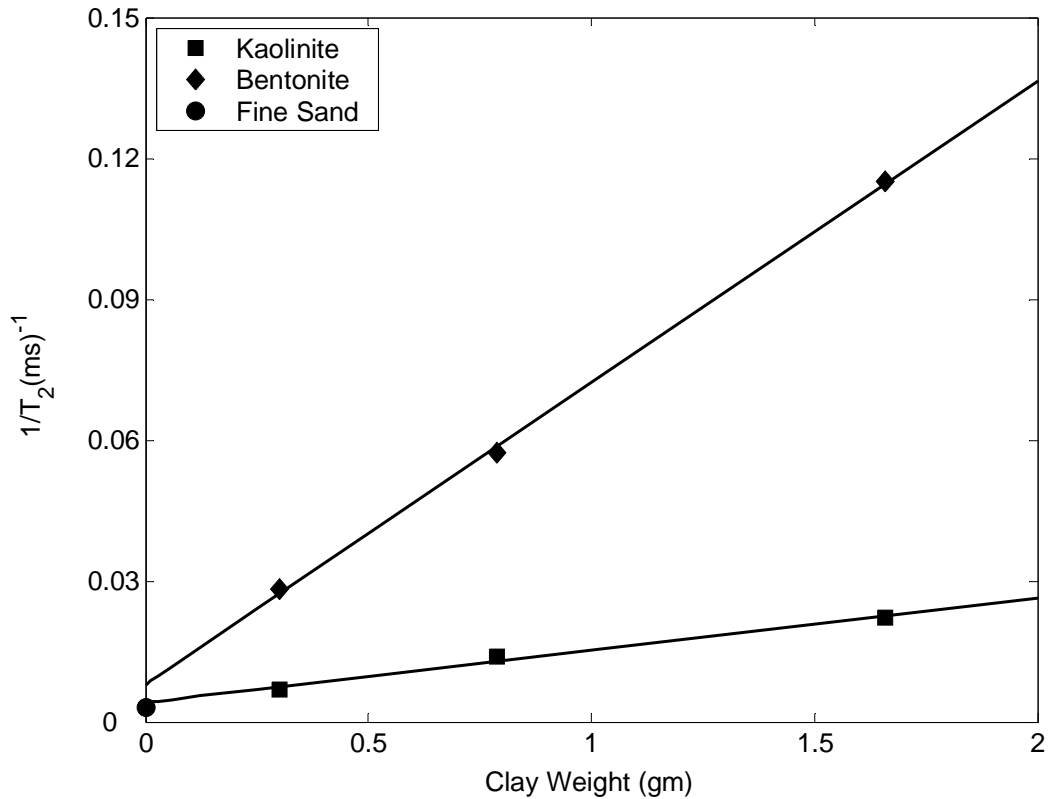


Figure 2.22: Linear dependence of the relaxation rates of dispersed clay-sand systems with the clay content.

A quantitative estimate of characteristic lengths required for the systems to be in coupled or decoupled regime can be obtained from the analysis of α . For coupled systems, α is given as (Equation 2.23)

$$\alpha = \frac{\rho S_{\text{active}}/V_{\text{total}}}{D/L_2^2} \quad (2.43)$$

Since the surface area of the sand is negligible compared to that of the clays, relaxation at the surface of the sand grains can be neglected in comparison to that at the clay surface

$$\rho S_{\text{active}} \approx \rho_{\text{clay}} S_{\text{clay}} \quad (2.44)$$

For totally coupled regime α is less than 1. Thus,

$$L_2 < \sqrt{\frac{DV_{\text{total}}}{\rho_{\text{clay}}S_{\text{clay}}}} \quad (2.45)$$

for totally coupled regime. For decoupled regime α is greater than 50 (based on $\psi/\beta = 0.97$ in Equation 2.25). Thus,

$$L_2 > \sqrt{\frac{50DV_{\text{total}}}{\rho_{\text{clay}}S_{\text{clay}}}} \quad (2.46)$$

for decoupled regime. From the values of relaxivity and surface area of the clays (Table 2.2), characteristic diffusion length for total coupling regime should be less than 15 μm and 5 μm for kaolinite and bentonite respectively. Since these values are of the order of the interstitial pores between the sand grains with grain radius of 50 μm , irreducible and free water in dispersed systems are coupled with each other. For the decoupled regime, the diffusion length should be greater than 110 μm and 35 μm for kaolinite and bentonite, respectively. Since the separation between clay and sand layer is of the order of two centimeters in the laminated systems, distinct peaks are observed for the irreducible and free water.

2.4.3. Estimation of irreducible water saturation in shaly sands

Irreducible water for the clay-sand systems consists of both clay-bound and capillary-bound water. The two populations are in close physical proximity and thus, relax at same rates due to fast diffusional exchange (Allen et al., 1998). If however, the distance between the irreducible and free water is large, the two populations can relax independently with distinct relaxation times. This was experimentally demonstrated for the laminated systems which showed separate peaks for clay and sand layers at 100% water saturation. Thus, for laminated systems a sharp cutoff is applicable to partition the

T_2 distributions into the irreducible and free water fractions. Note that in the model shaly sands considered in this study, there will be an overestimation of irreducible water if a sharp $T_{2,cutoff}$ is applied at the valley between the clay and sand peak. This is due to the additional compaction of the clays during centrifugation as the water squeezes out of the clay layer.

The dispersed systems in contrast, are in coupled regime and application of a sharp $T_{2,cutoff}$ to estimate the irreducible water would give wrong estimates. For example, application of conventional 33 ms cutoff would overestimate the irreducible saturation in the case of bentonite and underestimate in the case of kaolinite particularly for cases with high clay content. The coupled response necessitates the application of the inversion technique (Figure 2.9) for accurate estimation of the irreducible saturation. Since the systems are in totally coupled regime (unimodal T_2 distributions), the irreducible saturation is given by the ratio of modes of relaxation time peaks at irreducible saturation and at 100% water saturation (Equation 2.28)

$$S_{w,irr} = \left(\frac{T_{2,\mu}}{T_{2,macro}} \right)_{\alpha < 1} \quad (2.47)$$

Figure 2.23 shows the plot of the irreducible saturation obtained using Equation (2.47) with that obtained experimentally from NMR measurements at irreducible saturation. The estimates fall within 4% of the average absolute deviation proving the applicability of the technique. The higher irreducible saturation for bentonite systems than for kaolinite is due to the presence of interlayer water.

These experiments also resolve the apparent differences in the results reported by Matteson et al. (2000) and Prammer et al. (1996). The absence of a peak at short

relaxation time for the clay slurries which can be interpreted as the clay-bound water is due to fast diffusional exchange between the clay-bound and free water. However, when clays are present as laminated layers or as pore filling masses, the separation between irreducible water and free water is large enough to decouple the NMR responses. Thus, some sandstones can display distinct peaks for clay and free water with the clay response being proportional to the CEC of the clay, as was indeed observed by Prammer et al. (1996).

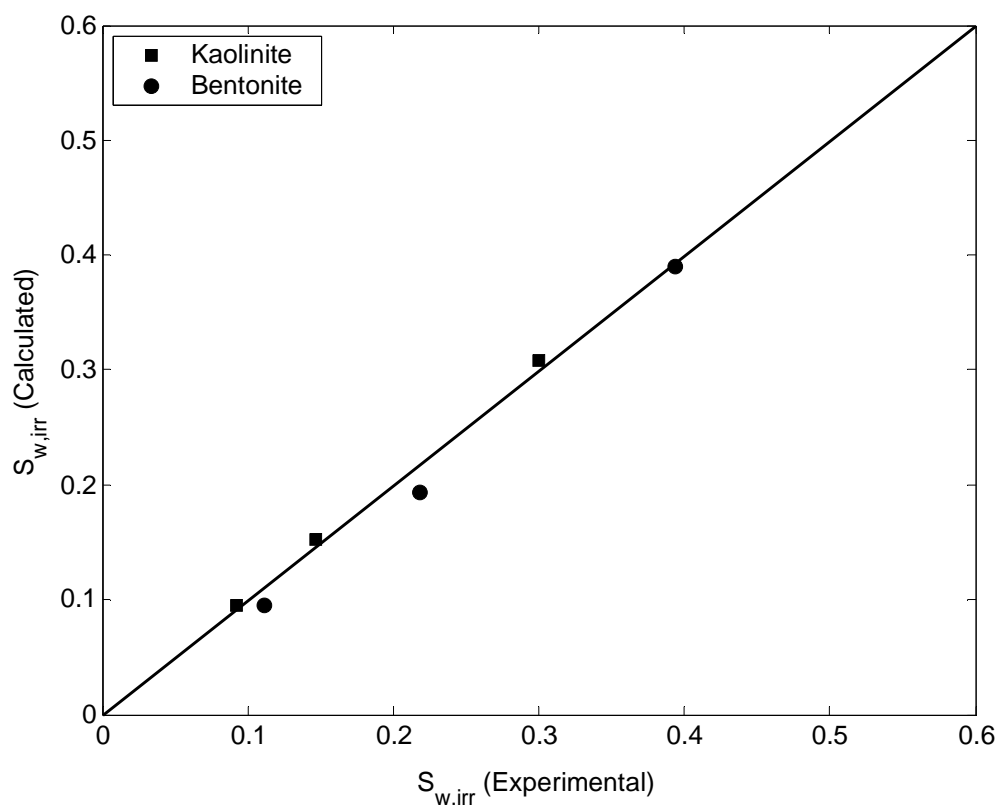


Figure 2.23: Comparison of the irreducible water saturation calculated using the inversion technique and measured experimentally for dispersed systems.

2.5. Diffusional coupling in microporous grainstones

The analysis of Section (2.2) can also be applied to describe pore coupling in grainstone carbonates. Ramakrishnan et al. (1999) modeled grainstones as microporous spherical grains surrounded by intergranular pores. This three dimensional model can be mapped into a two-dimensional model of periodic array of slab-like grains separated by intergranular macropores as shown in Figure 2.24. This model can be further transformed to the one in Figure 2.2 by neglecting the thickness of grain between the micropores and assuming the pores to be linear in shape. Note that in this model, relaxation at the outer surface of the grains is neglected. This assumption is justified if the surface-to-volume ratio of the micropore is much larger compared to external surface-to-volume ratio of the spherical grains.

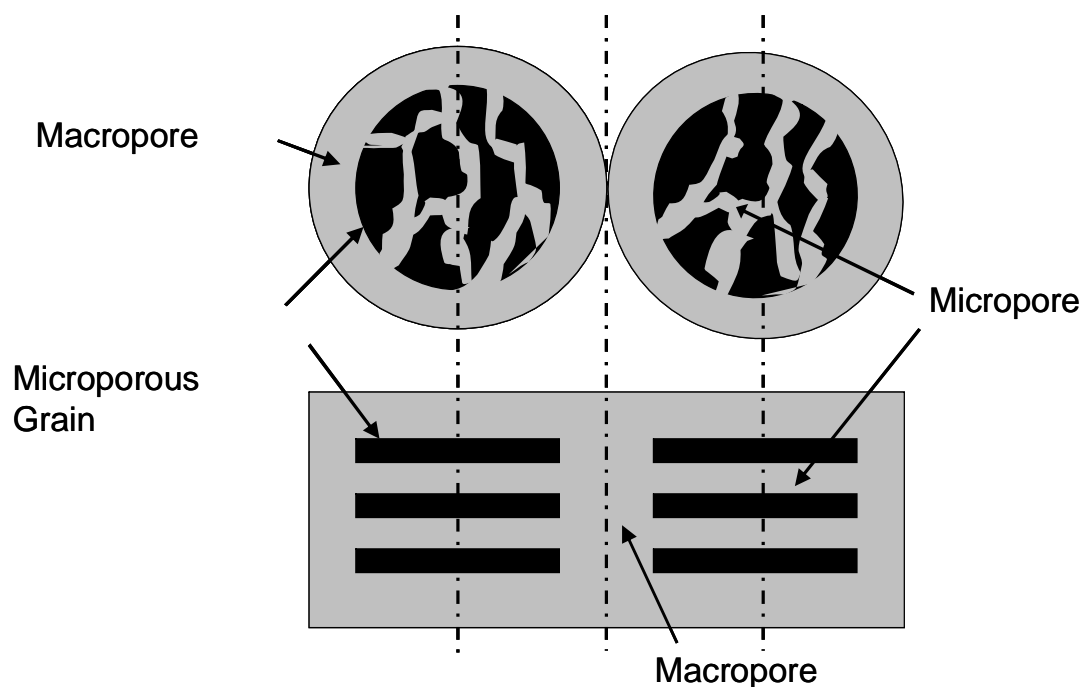


Figure 2.24: Pore coupling model in grainstone systems. The three-dimensional model (Ramakrishnan et al., 1999) can be mapped to a two-dimensional model of periodic array of microporous grains separated by macropores.

2.5.1. Coupling parameter for grainstones

The transformation of the spherical grain model to the 2-D model of Figure 2.2 helps to define a coupling parameter for grainstones through a mapping of characteristic parameters. In Figure 2.2, L_1 was defined to be the half-width of the micropore. Hence for microporous grains, L_1 corresponds to the radius of the micropore (R_μ) i.e.

$$L_1 = R_\mu \quad (2.48)$$

Also, as a first approximation, L_2 can be taken to be equal to the grain radius (R_g)

$$L_2 = R_g \quad (2.49)$$

Substituting Equations (2.48) and (2.49) in Equation (2.19), the definition of α for grainstones is given as

$$\alpha_{\text{grain}} = \frac{\rho\beta R_g^2}{DR_\mu} \quad (2.50)$$

α_{grain} , thus, shows a quadratic dependence on the grain radius and inverse dependence on the micropore radius. This relationship suggests that grainstones with large grain radius and/or small micropore radius are expected to show less effect of diffusional coupling.

The above definition of coupling parameter also helps to understand the analysis of grainstone model developed by Ramakrishnan et al. (1999). They suggested that in the case when the decay of magnetization in macropore occurs on a time scale much larger than that for the decay of magnetization in micropore, relaxation in the coupled geometry can be expressed as a bi-exponential decay.

$$M(t) = \phi_m \exp\left(-\frac{\rho_a t}{V_{sm}}\right) + (\phi - \phi_m) \exp\left(-\frac{t}{T_{2,\mu}}\right) \quad (2.51)$$

In the above equation, V_{sm} is the macropore volume-to-surface ratio, ϕ and ϕ_m are the total porosity and macroporosity respectively and ρ_a is the apparent relaxivity for the macropore. The bi-exponential model is valid when the diffusion length of magnetization within the microporous grain is much smaller than the grain radius i.e.

$$\sqrt{\frac{DT_{2,\mu}}{\phi_\mu F_\mu}} \ll R_g \quad (2.52)$$

where F_μ is the formation factor. The above condition can be explained by substituting the expressions for the parameters from the grainstone model as described below. The relaxation rate of micropore is related to the micropore radius, assuming cylindrical pores, as

$$\frac{1}{T_{2,\mu}} = \rho \left(\frac{S}{V} \right)_\mu = \frac{2\rho}{R_\mu} \quad (2.53)$$

Microporosity fraction (β) is equal to the product of grain fraction ($1-\phi_m$) and porosity of grains ϕ_μ normalized by total porosity ϕ ,

$$\beta = \frac{\phi_\mu(1-\phi_m)}{\phi} \quad (2.54)$$

Substituting the expressions for $1/T_{2,\mu}$ and ϕ_μ from Equations (2.53) and (2.54) in Equation (2.52), the following condition is obtained

$$\sqrt{\frac{DR_\mu(1-\phi_m)}{2\rho\beta\phi F_\mu}} \ll R_g \quad (2.55)$$

$$\Rightarrow \alpha_{\text{grain}} \equiv \frac{\rho\beta R_g^2}{DR_\mu} \gg \frac{(1-\phi_m)}{2\phi F_\mu} \quad (2.56)$$

The above condition implies that the micropore relaxes independently of the macropore for large values of α , which is the same condition for the decoupled regime obtained for the model in Figure 2.2. However, for typical values of grainstone parameters, the value of apparent relaxivity can be much larger than the micropore relaxivity (Ramakrishnan et al., 1999). Thus, even though the surface-to-volume ratio of macropore may be significantly smaller than that of micropore, diffusional coupling can result in the decay of macro and micropore at comparable time scales. For such cases, the pores are in intermediate coupling regime and the amplitudes of the bi-exponential fit are not representative of the actual micro and macroporosity fractions as was observed in the numerical simulations of Ramakrishnan et al. (1999).

2.5.2. Experimental validation of grain size dependence on pore coupling

In order to experimentally validate the grainstone model, NMR response of three systems -- microporous chalk, silica gels and alumino-silicate molecular sieves -- was studied as a function of grain radius. These systems with varying physical properties help to systematically analyze the effect of different governing parameters on pore coupling. The physical properties of the systems are listed in Table 2.3.

Table 2.3: Physical properties of the grainstone systems.

	Chalk	Silica Gels	Molecular Sieves
Surface Area (m ² /g)	4.1	300	20
Micropore Diameter (Å)	185	150	4
Surface Relaxivity (µm/sec)	0.27	0.06	0.04

1. **Chalk** - Crushed microporous chalk (Crayola) was sieved into five fractions with average grain radius of 335 μm , 200 μm , 112 μm , 56 μm and 11 μm . Known quantities of sorted fractions were water saturated in 1'' by 1'' Teflon sleeves whose bases were sealed with a covering of Teflon tape. After measuring the NMR response at 100% water saturation, the systems were centrifuged in a Beckman rock core centrifuge at an air/water capillary pressure of 100 psi for 3 hours to drain the macropores. The Teflon base is permeable to water but prevents any grain loss during centrifugation. Note that even though the sieve fractions are unconsolidated, they have irreducible microporosity which is not displaced on capillary drainage.

The T_2 distributions of the five fractions at 100% water saturation and the corresponding distributions at irreducible saturation are shown in Figure 2.25. The values of α_{grain} calculated using Equation (2.50) and $\mu_{\text{grain}} (= \rho R_g / D)$ are also mentioned for each sieve fraction. It can be seen that for the two coarsest fractions ($R_g = 335 \mu\text{m}$ and $200 \mu\text{m}$), the T_2 distributions show distinct peaks for micro and macropores and the area under the micropore peak is the same as that at irreducible conditions. This implies that the systems are in the decoupled regime which is verified by large values of α_{grain} . The effect of coupling becomes more pronounced for systems with $R_g = 112 \mu\text{m}$ and $56 \mu\text{m}$, which show a build-up of micropore peak amplitude at irreducible saturation. This build-up of amplitude is observed because at irreducible condition, there is no diffusional exchange of the fluid in micro and macropores and hence, the fluid relaxes with the surface-to-volume ratio of the micropores. However, at 100% saturation part of the fluid in

micropores is exchanging with the macropores. Thus, the apparent volume of the fluid is larger in surface-to-volume ratio which decreases its relaxation time. This is the same explanation given by Coates et al. (1998) for the observed increase in amplitude of short T_2 components at irreducible saturation in sandstone cores. The values of α_{grain} for $R_g = 112 \mu\text{m}$ and $56 \mu\text{m}$ correspond to the intermediate coupling regime and thus, quantitatively supports the explanation. The unimodal T_2 distribution of the finest fraction ($R_g = 11 \mu\text{m}$) at 100% water saturation shows that the system is in total coupling regime ($\alpha_{\text{grain}} = 0.8 < 1$).

2. **Silica gels** - A homologous series of silica gels (provided by Sigma-Aldrich) with grain radii of $168 \mu\text{m}$, $55 \mu\text{m}$ and $28 \mu\text{m}$ constituted the second system. Figure 2.26 shows the T_2 distributions at 100% water saturation and at irreducible saturation for the three fractions. Similar to the response of chalk, the distributions change from being bimodal to unimodal with the decrease in particle radius indicating increased coupling. The values of α_{grain} suggest intermediate coupling regime for the two coarsest fractions ($R_g = 168 \mu\text{m}$ and $55 \mu\text{m}$) and total coupling regime for the finest fraction ($R_g = 28 \mu\text{m}$).

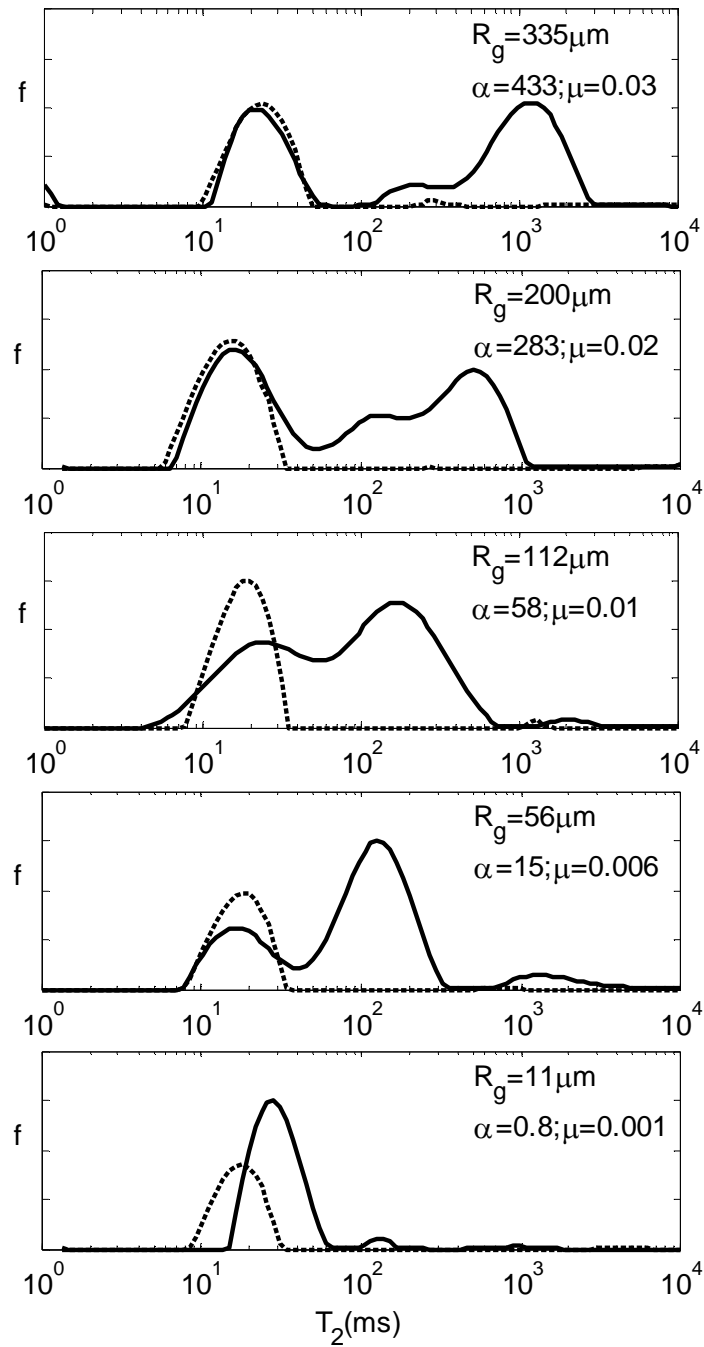


Figure 2.25: T_2 distributions of microporous chalk as a function of grain radius. The transition from decoupled ($R_g = 335 \mu\text{m}$) to total coupling regime ($R_g = 11 \mu\text{m}$) is predicted by the values of α .

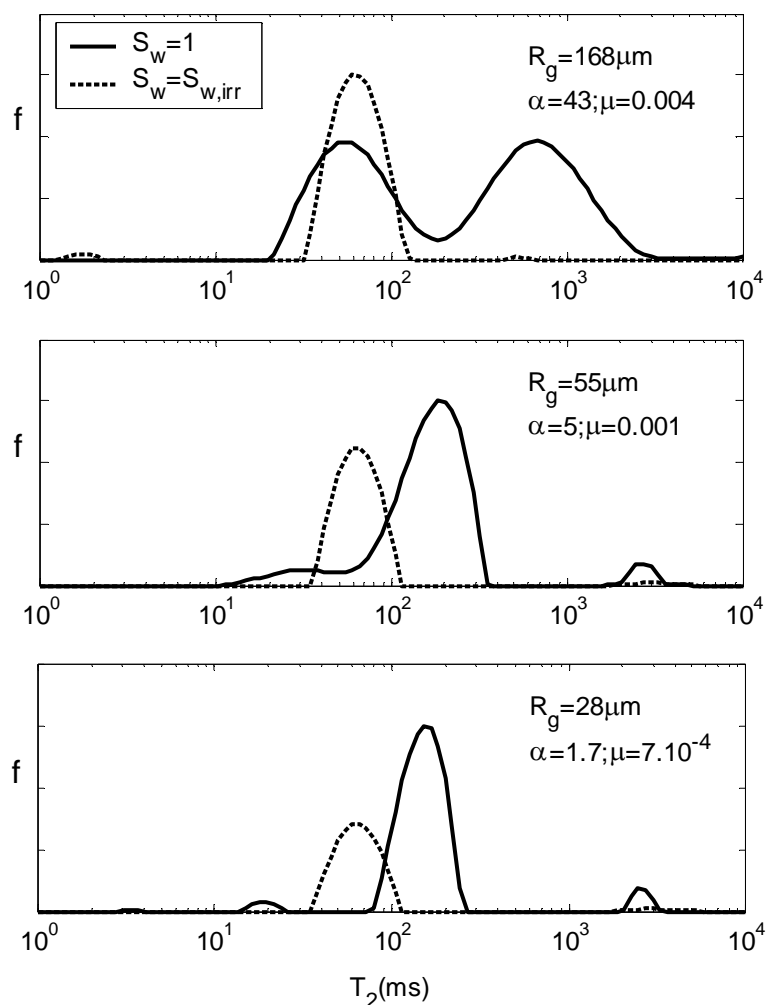


Figure 2.26: T_2 distributions of silica gels as a function of grain radius. The transition from almost decoupled ($R_g = 168 \mu\text{m}$) to total coupling regime ($R_g = 28 \mu\text{m}$) is predicted by the values of α .

3. **Molecular sieves** - Alumino-Silicate molecular sieves with nominal pore diameter of 4 \AA , supplied by Fisher Chemicals, was crushed and sieved into four fractions with average grain radius of $200 \mu\text{m}$, $112 \mu\text{m}$, $56 \mu\text{m}$ and $16 \mu\text{m}$. The T_2 distributions of the four fractions are shown in Figure 2.27 at 100% water saturation and at irreducible saturation. The response shows similar trend of narrowing T_2 distributions with decrease in grain diameter. An increase in

micropore peak amplitude at irreducible condition for fractions with $R_g = 56 \mu\text{m}$ and $16 \mu\text{m}$ is also observed. The values of α_{grain} for the respective fractions predict the transition of the coupling regimes.

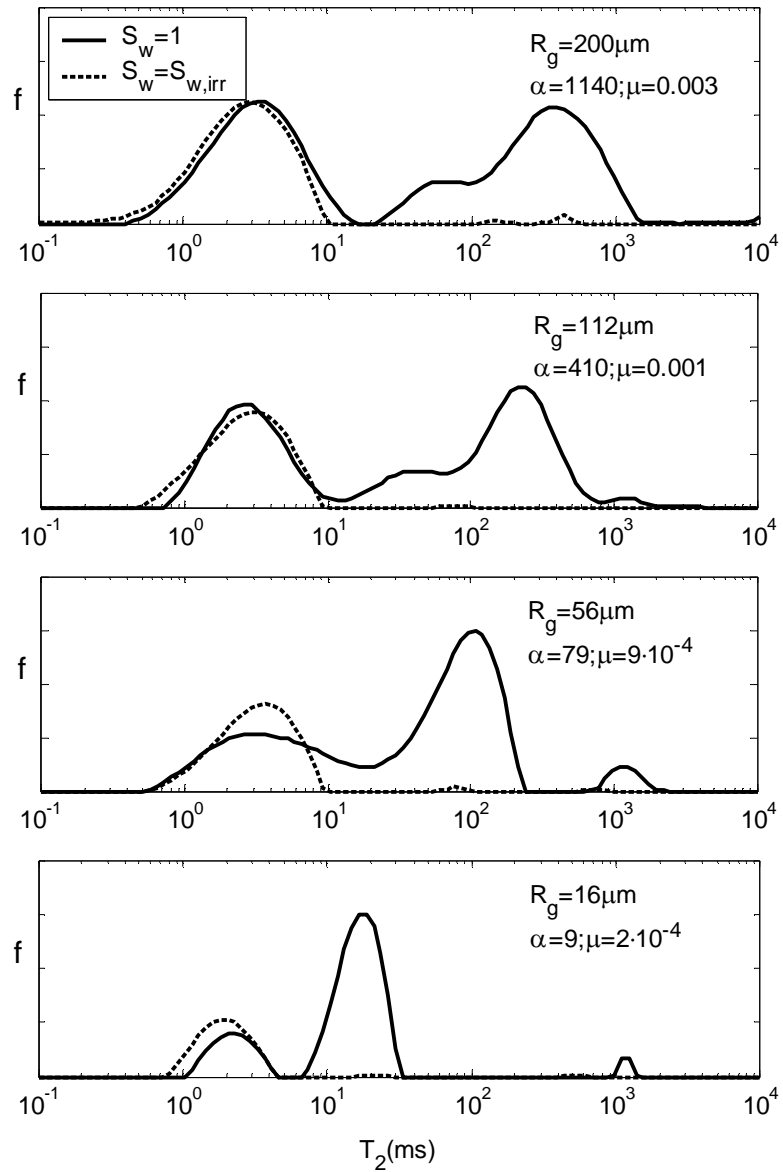


Figure 2.27: T_2 distributions of aluminosilicate molecular sieves as a function of grain radius.

Figure 2.28 shows that the lognormal and cubic relationships of Equations 2.25 and 2.27 also hold for the three systems establishing the validity of the grainstone model.

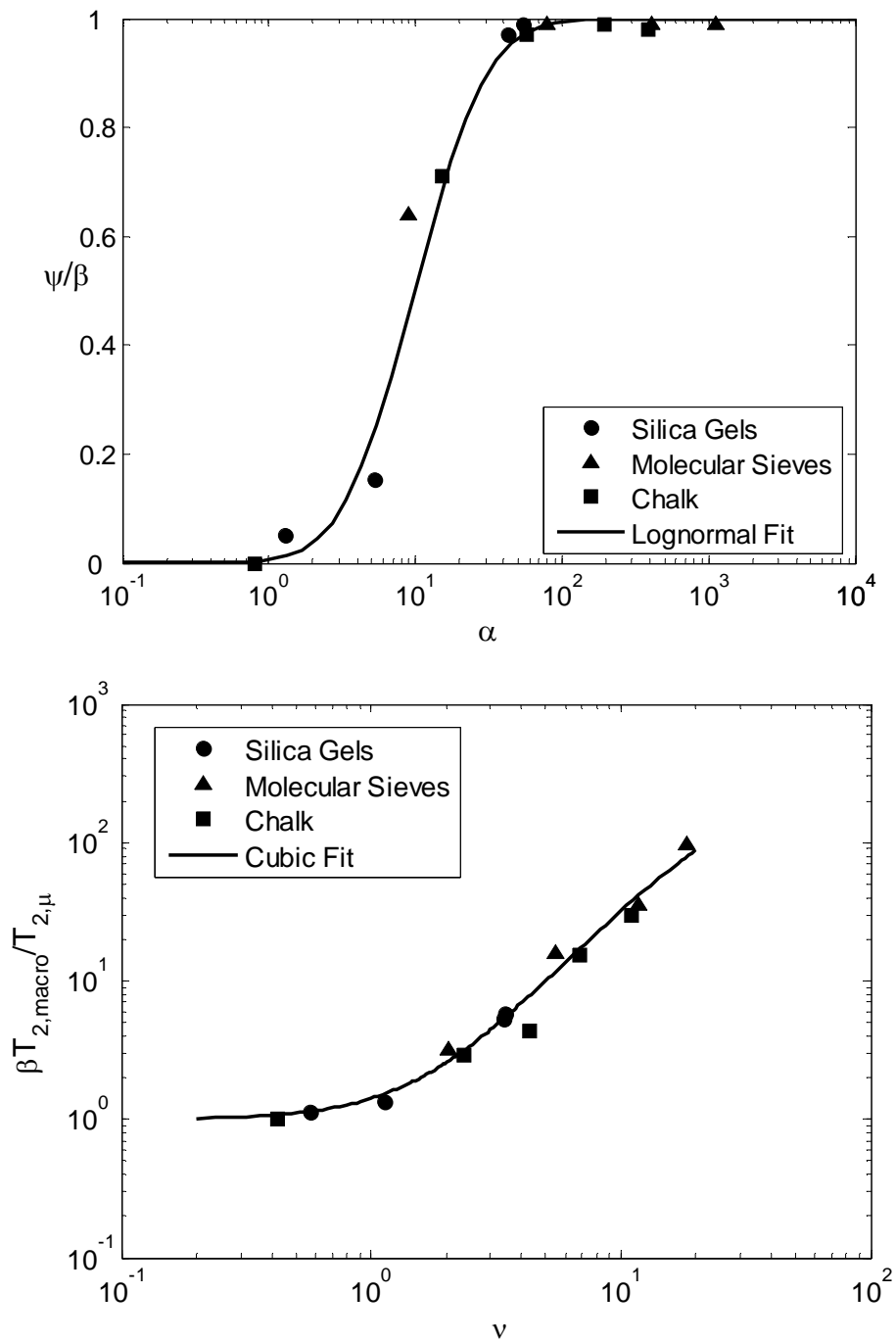


Figure 2.28: The lognormal and cubic relationships of Equations (2.25) and (2.27) hold for the grainstone systems.

2.5.3. Estimation of irreducible saturation for the sandstone and grainstone systems

The inversion technique developed in Section 2.2 can be applied to estimate irreducible saturation for the grainstone systems and North Burbank sandstone (section 2.3). The characteristic parameters (ψ , $T_{2,\mu}$, $T_{2,\text{macro}}$) required for the inversion technique are mentioned in Appendix C. Figures 2.29 and 2.30 show the comparison of the calculated values of β and α using inversion technique with the values determined experimentally for the two systems. An average value of $T_{2,\mu}$ obtained from the individual values for different sieve fractions or cores is used for calculations. The estimates lie within an average absolute deviation of 4% and 11% for β and α , respectively. This indicates that the technique is applicable to all the systems studied irrespective of the properties and coupling regimes.

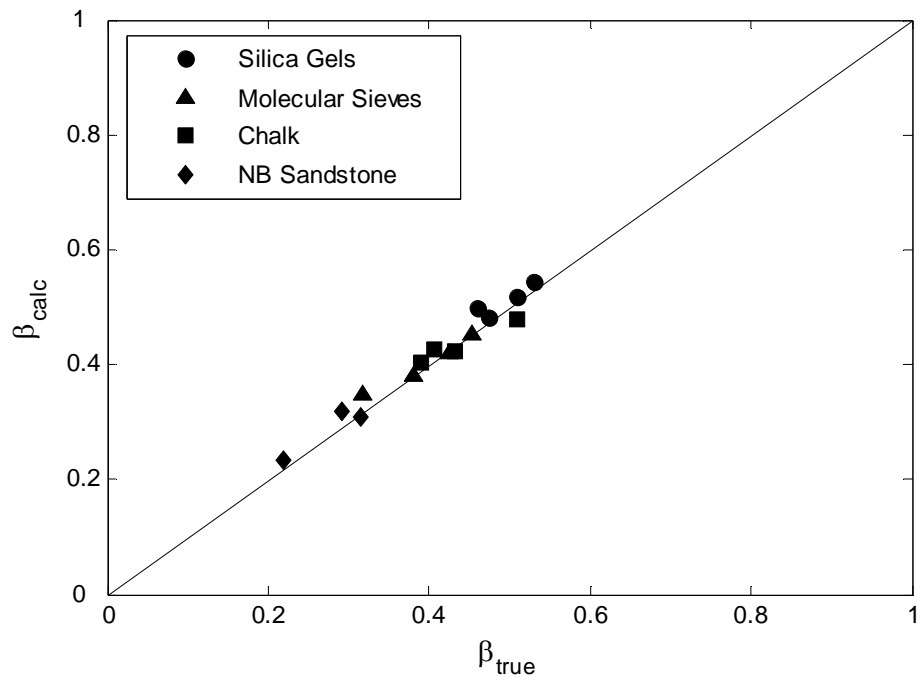


Figure 2.29: Comparison of calculated and experimentally measured values of microporosity fraction (β) for the grainstone and sandstone systems. The values are estimated within 4% average absolute error.

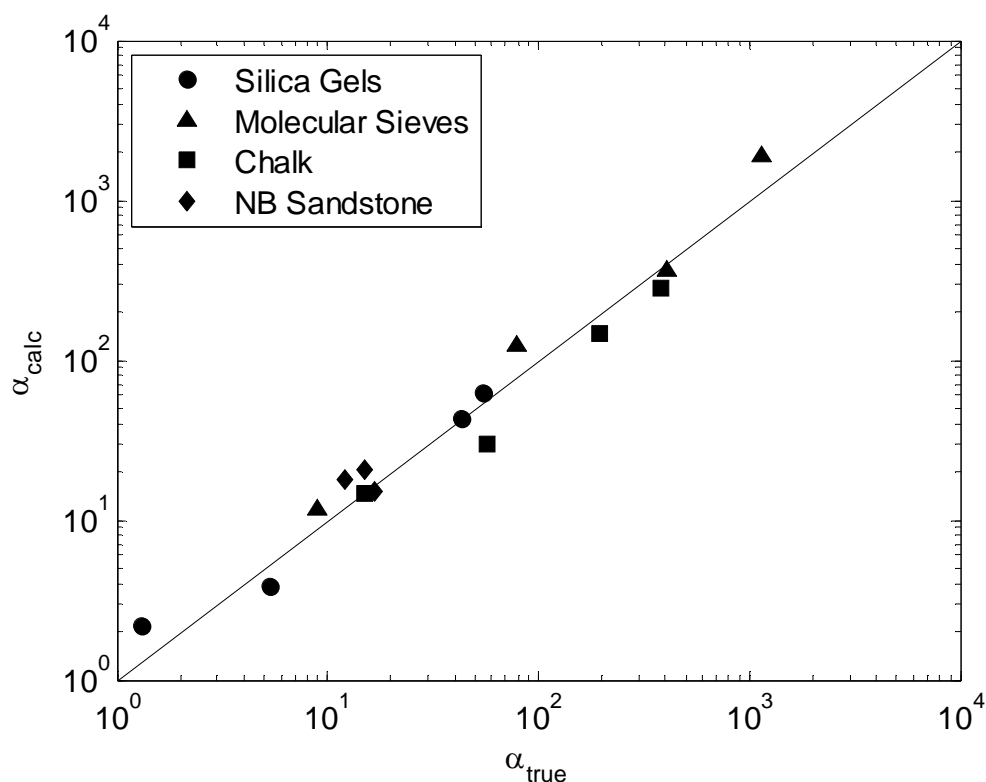


Figure 2.30: Comparison of calculated and experimentally measured values of α for the grainstone and sandstone systems. The values are estimated within 11% error for all coupling regimes.

2.6. Effect of temperature on diffusional coupling

Relaxation rates of bulk fluids are strongly temperature sensitive due to the thermal modulation of translational and rotational correlation times. For fluids in porous media, relaxation is usually dominated by surface relaxation which can be temperature dependent. In addition, diffusional coupling between pores of different sizes can also increase with temperature due to increased diffusional transport of fluid molecules. Thus, the interpretation of temperature effect on NMR measurements in porous media needs to take into account the temperature variation of both surface relaxation and diffusional coupling.

2.6.1. Temperature dependence of α

The effect of temperature on pore coupling can be quantified by incorporating the temperature dependence of surface relaxivity and diffusion coefficient in the functional relationship for α (Equation 2.19). Surface relaxation of fluid molecules in porous media is governed by two processes (Godefroy et al., 2001). First, translational motion of the fluid molecules near the paramagnetic sites at pore surface and second, exchange between surface and bulk molecules. The temperature dependence of surface relaxation arises from the thermal activation of the translational motion at the pore surface as well as increased exchange between surface and bulk fluid molecules. Quantitatively, the temperature dependence can be expressed as an Arrhenius relationship (Godefroy et al., 2001)

$$\rho = \rho_0 \exp\left(\frac{\Delta E}{RT}\right) \quad (2.57)$$

where ΔE is the effective activation energy and R is the universal gas constant. Self-diffusion of bulk fluids is also a thermally activated process and the diffusion coefficient usually shows Arrhenius dependence with temperature,

$$D = D_0 \exp\left(-\frac{E_a}{RT}\right) \quad (2.58)$$

In the above equation, E_a is the activation energy for the diffusion process and D_0 is the diffusion coefficient at infinite temperature. Substituting Equations (2.57) and (2.58) in the expression for α (Equation 2.19) and grouping variables, a temperature dependent functional relationship of α can be given as

$$\alpha = \alpha_0 \exp\left(\frac{E_a + \Delta E}{R} \left(\frac{1}{T} - \frac{1}{T_0}\right)\right) \quad (2.59)$$

where α_0 is the value of coupling parameter at a reference temperature T_0 . Thus, pore coupling can either increase or decrease with temperature if the difference in the activation energy for diffusion and relaxation process ($E_a + \Delta E$) is positive or negative, respectively.

2.6.2. Temperature dependence of T_2 distributions of silica gels and carbonate core

The effect of temperature on NMR diffusional coupling is experimentally illustrated for two systems of porous media. The first system consists of a homologous series of microporous silica gels with varying grain radii. The second system consists of a reservoir carbonate core with bimodal pore size distribution. For both systems NMR measurements are performed at 100% water saturation and irreducible water saturation as a function of temperature.

1. **Silica gels** - Silica gels with mean grain radii of 168 μm (Medium Coarse), 55 μm (Very Fine) and 28 μm (Silt size) were obtained from Sigma Aldrich. The physical properties of the gels have been mentioned previously in Table 2.3. Figure 2.31 shows the T_2 distributions at 100% water saturation for the three silica gels at 30, 50, 75 and 95°C. At each temperature, the distributions are normalized with the pore volume (area under the curve) to account for the Curie Law. Figure 2.32 shows the normalized T_2 distributions at irreducible condition for the medium coarse silica gel at the above mentioned temperatures. The NMR apparatus has a response around 1 ms at high temperatures which has been subtracted from the distributions.

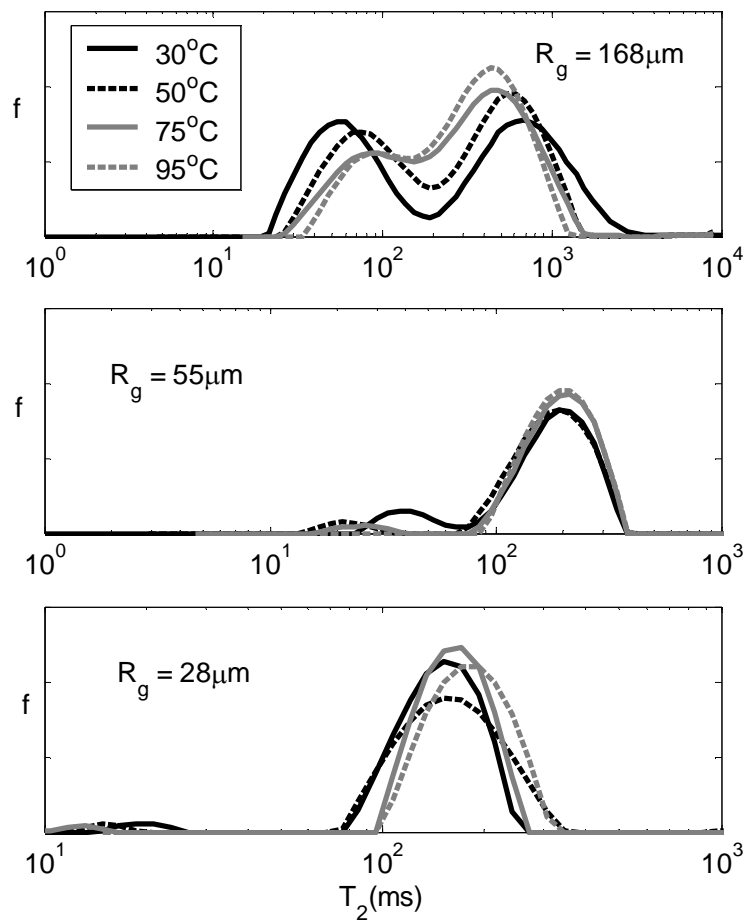


Figure 2.31: T_2 distributions of silica gels at 100% water saturation and at 30, 50, 75 and 95°C.

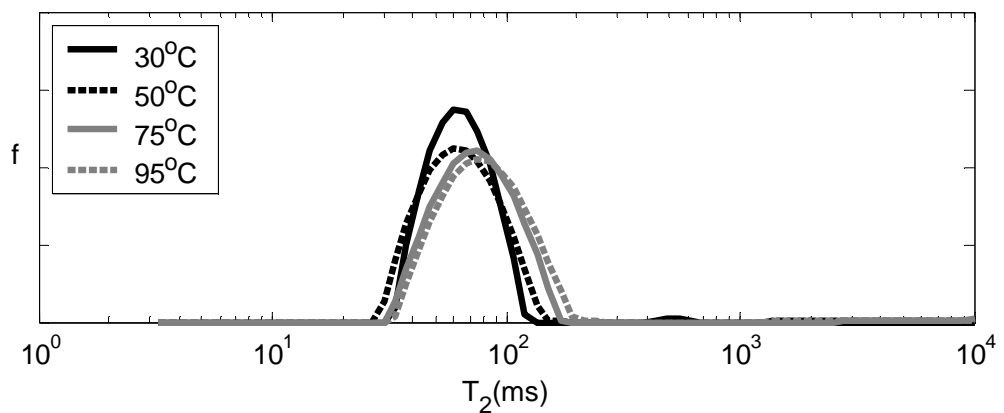


Figure 2.32: T_2 distribution of medium coarse silica gel at irreducible saturation and at 30, 50, 75 and 95°C.

The increase in relaxation time at irreducible condition with temperature (Figure 2.32) shows that the surface relaxivity decreases as the temperature is increased. This result is in agreement with those obtained by Ramakrishnan and Fordham et al. (1999) who saw a similar increase in the relaxation time of water-saturated systems with temperature. The temperature behavior at 100% water saturation can now be interpreted keeping in mind the negative dependence of relaxivity on temperature. Each of the three silica gels in Figure 2.31 represents a different coupling scenario. The medium coarse silica gel is almost in decoupled regime ($\psi/\beta = 0.97$) at 30°C. As the temperature is increased, surface relaxivity decreases and diffusivity of water increases. As a result, coupling between micro and macropores increases and the system transitions from almost decoupled to intermediate coupling regime. This transition is evidenced by the reduction in the amplitude of the micropore peak and decrease in the relaxation time of the macropore with temperature. Very fine silica gel is in intermediate coupling regime at 30°C ($\psi/\beta = 0.24$). Increasing the temperature increases coupling so that the T_2 distribution changes from bimodal at 30°C to unimodal at higher temperatures. However, the increase in relaxation rate of the macropore due to coupling is offset by the decrease in surface relaxation and thus, the position of macropore peak remains unchanged. Silt size silica gel has a unimodal T_2 distribution at 30°C suggesting that the system is in total coupling regime ($\psi/\beta \sim 0$). Increase in temperature has no further effect on coupling but the corresponding decrease in surface relaxivity leads to a shift of T_2 distribution to longer relaxation times. The results demonstrate that temperature can have

apparently different effects on the NMR response even though the systems may be governed by similar principles.

2. Reservoir carbonate core - The carbonate core studied is a Thamama reservoir carbonate with porosity 21.2% and water permeability of 13 mD. Analysis of lithology shows that the carbonate is a packstone/wackestone with mainly moldic macroporosity in leached areas. The microporosity is predominantly inside pellets and mud. Figure 2.33 shows the T_2 distributions of the core at 100% water saturation and at irreducible water saturation (oil saturated) for three temperatures of 25, 50 and 80°C (Fleury, 2006). As the temperature is increased, the amplitude of the micropore peak and relaxation time of the macropore decrease at 100% water saturation. These observations suggest that diffusional coupling between micro and macropores increases with temperature. Similar to the case for silica gels, the increase in pore coupling is due to increase in water diffusivity as well as decrease in surface relaxivity with temperature. The latter claim is based on the fact that the relaxation time of residual water in the micropores of oil-saturated core increases with temperature (lower panel of Figure 2.33). An important implication of the results is that application of a sharp $T_{2,cutoff}$ based on a laboratory calibration at room temperature for the estimation of irreducible saturation may not be suitable for high temperature formations.

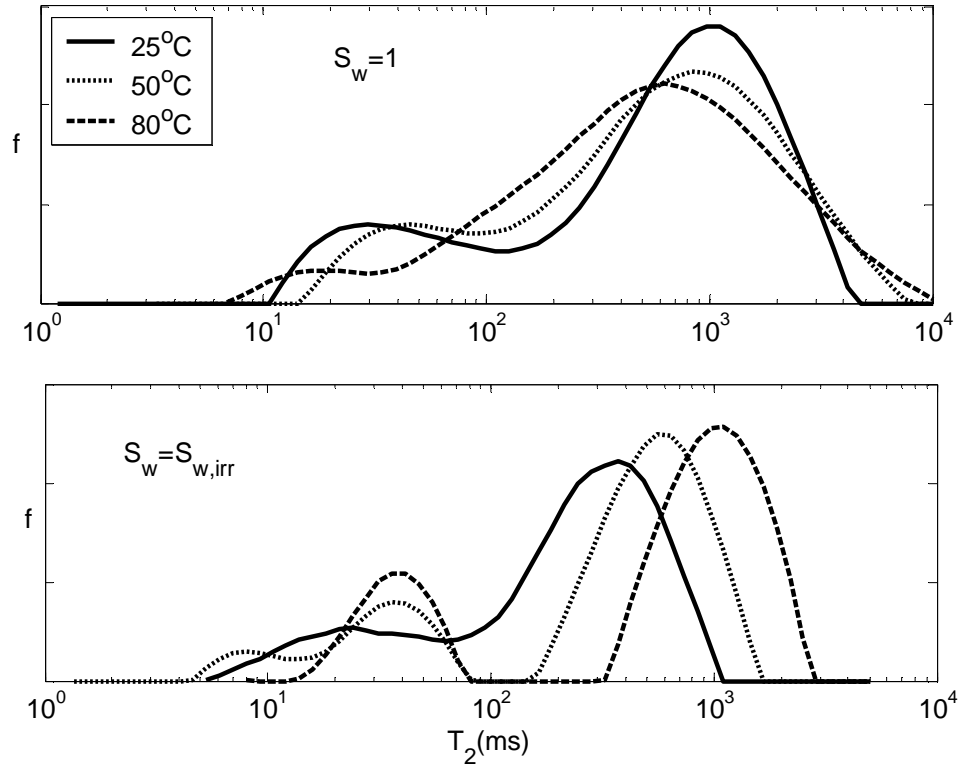


Figure 2.33: T_2 distributions of the Thamama formation carbonate core at 100% water (upper panel) and irreducible water saturation (lower panel) at 25, 50 and 80°C (Fleury, 2006).

2.6.3. Discussion

Effect of temperature on pore coupling for the two systems can be analyzed quantitatively from the temperature variation of α . For silica gels, α at different temperatures can be calculated by including the temperature dependence of surface relaxivity and diffusivity in the definition of α for grainstone systems (Equation 2.50)

$$\alpha_{\text{grain}}(T) = \frac{\rho(T)\beta R_g^2}{D(T)R_\mu} \quad (2.60)$$

Here R_g is the grain radius and R_μ is the micropore radius (75 Å for silica gels). The temperature variation of surface relaxivity is obtained from measurements at irreducible

saturation (Figure 2.32). The estimates of self-diffusion coefficient of water as a function of temperature are obtained from the experimental data of Holz et al. (2000). For the carbonate core, α is calculated using the inversion technique described earlier (Figure 2.9). The plot of the independent microporosity fraction (ψ/β) with α is shown in Figure 2.34 for the three silica gels and carbonate core. It can be seen that α accurately predicts the transition of the different coupling regimes with temperature as the systems move downward along the empirical relationship (Equation 2.25). The microporosity fraction, estimated using the inversion technique, agrees within 5% average absolute deviation as shown in Figure 2.35. Thus, the technique can prove useful in accurately estimating formation properties for reservoirs at elevated temperatures.

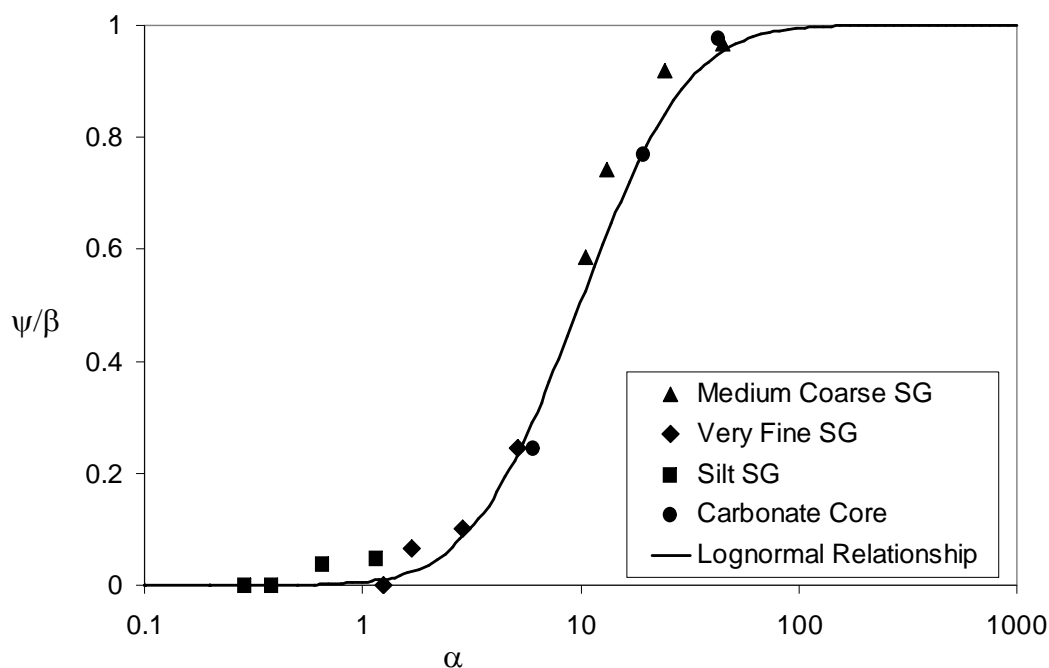


Figure 2.34: Plot of independent microporosity fraction (ψ/β) with α for grainstone systems and carbonate core.

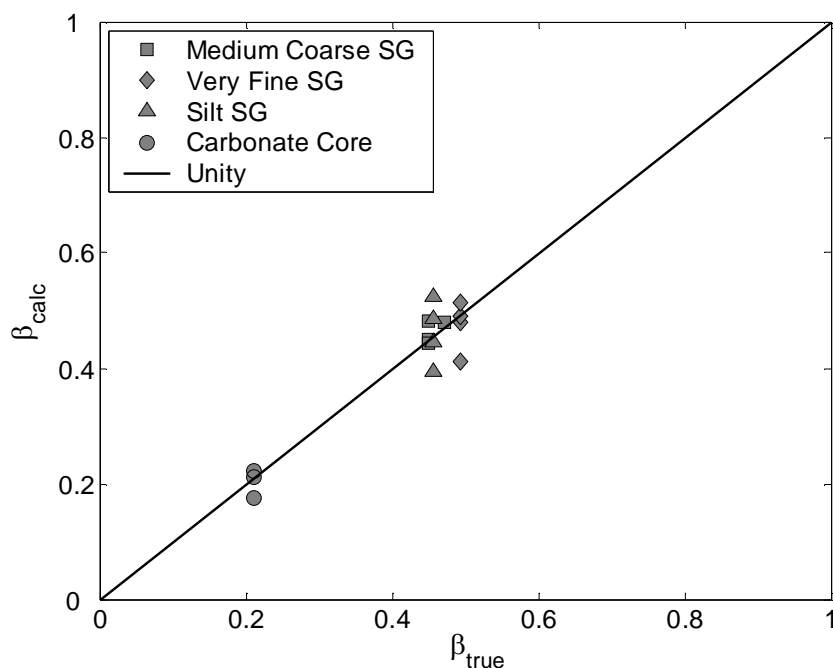


Figure 2.35: Comparison of the microporosity fraction calculated using the inversion technique and measured experimentally for silica gels and carbonate core.

2.7. Conclusions

A theoretical and experimental understanding of NMR relaxation in systems with diffusively coupled micro and macropores is provided. It is shown that the Brownstein number fails to characterize relaxation regimes in coupled pores due to its dependence on macropore length scale only. Instead, a coupling parameter (α) has been introduced which is defined as the ratio of the characteristic relaxation rate of the pore system to the rate of diffusional mixing of magnetization between micro and macropore. Depending on the value of α , the two pore types can communicate through total, intermediate or decoupled regimes. A technique for the estimation of microporosity fraction and α for formations with unknown geometrical parameters is also introduced. The required

parameters for the estimation are easily obtainable from laboratory core analysis and the T_2 (or T_1) spectrum at 100% water and irreducible saturation. It is assumed that the relaxation time of micropores is the same in the cores and in the field. Experiments with representative sandstone and grainstone systems prove the applicability of α to quantify the extent of coupling.

The effect of temperature on pore coupling is evaluated by incorporating the temperature dependence of surface relaxivity and fluid diffusivity in the definition of α . Experimental NMR measurements on reservoir carbonate rocks and model grainstone systems are performed at different temperatures. As temperature is increased, the T_2 spectrum for water-saturated systems progressively changes from bimodal to unimodal distribution. This enhanced pore coupling is caused by a combined effect of increase in water diffusivity and decrease in surface relaxivity with temperature. Extent of coupling at each temperature can be quantified by the values of α .

Chapter 3. Paramagnetic Relaxation in Sandstones: Generalized Relaxation Theory

3.1. Introduction and Literature Review

NMR relaxation measurements have become an important tool to estimate petrophysical properties of rocks. Relaxation of fluids in pores of sedimentary rocks is primarily governed by magnetic interactions of the fluid molecules with the paramagnetic sites at the pore surfaces. However, the relaxation mechanisms at pore surfaces are not understood completely. Kleinberg et al. (1993) studied the low field (2 MHz) NMR response of several sandstones and found that the T_1/T_2 ratio varied over a large range from 1 to 2.6. For most cases, no echo spacing dependence of the T_2 relaxation was observed. Based on these and other observations, Kleinberg et al. (1994) suggested that transverse relaxation is additionally influenced by scalar coupling between fluid molecules and surface paramagnetic sites and hence, the T_1/T_2 ratio is greater than unity. While scalar coupling is an important relaxation mechanism for paramagnetic Mn^{2+} ions, it is not so for ferric ions and the T_1/T_2 ratio of protons in ferric solutions is unity (Soloman, I., 1955; Morgan et al., 1959). Thus, scalar coupling alone can not explain the T_1/T_2 ratio of sandstones when the predominant paramagnetic mineral is iron.

In addition, several studies with fluid-saturated porous media have reported a strong dependence of transverse relaxation on echo spacing (Hürlimann et al., 1998; Appel et al., 1999; Dunn et al., 2001; Zhang et al., 2001; Fantazzini et al., 2003; Fantazzini et al., 2005). However, the dependence is not always quadratic as predicted by the classical expression (Carr et al., 1954). A theoretical and experimental understanding

of the principles governing the relaxation characteristics of the sedimentary rocks is, thus, needed for accurate interpretation of NMR measurements.

This study demonstrates that the observed range of T_1/T_2 ratio and echo spacing dependence of transverse relaxation in sandstones can arise due to diffusion in internal magnetic field inhomogeneities. In porous media, internal field inhomogeneities are often induced due to differences in magnetic susceptibility of pore fluids and paramagnetic minerals on pore surfaces (Glaser et al., 1974; Rothwell et al., 1985; Rueslåtten et al., 1998; Song et al., 2002; Sun et al., 2002). Figure 3.1 shows magnetic field lines in the presence of a paramagnetic sphere of unit radius with susceptibility 10^6 times that of the surrounding medium. The field lines concentrate in their passage through the paramagnetic sphere. Similarly, large field inhomogeneities can also occur around corners or sharp discontinuities in pore system (Brown et al., 1993, Zhang et al., 2003). Diffusion of fluid molecules in such inhomogeneous fields leads to additional relaxation of transverse magnetization due to dephasing. The additional relaxation is called “secular relaxation” (Gillis et al., 1987) and is defined as the difference in the transverse and longitudinal relaxation rates,

$$\frac{1}{T_{2,\text{sec}}} = \frac{1}{T_2} - \frac{1}{T_1} \quad (3.1)$$

Strictly speaking, secular relaxation refers to the residual transverse relaxation at high magnetic fields at which longitudinal relaxation rates are dispersed to zero (Gillis et al., 1987). However, in this study, secular relaxation is defined in Equation (3.1) as the additional transverse relaxation due to diffusion of spins in inhomogeneous fields.

At present, there is no exact theory which explains secular relaxation in porous media in a general inhomogeneous field. However, two ideal cases of relaxation in a constant

gradient and relaxation in an inhomogeneous field induced by paramagnetic spheres have been described analytically in the past. DeSwiet et al. (1994) described three length scales that characterize secular relaxation in a constant gradient g :

- 1) Pore structural length, L_s
- 2) Diffusion length, L_d , defined as

$$L_d = \sqrt{D\tau_E} \quad (3.2)$$

where τ_E is the echo spacing for CPMG pulse sequence, and

- 3) Dephasing length, L_g , defined as the distance over which the spins have to diffuse in order to dephase by 1 radian given as

$$L_g = \sqrt[3]{\frac{D}{\gamma g}} \quad (3.3)$$

where D is the diffusivity of the fluid and γ is the proton gyromagnetic ratio. Depending on the smallest length scale, secular relaxation can be characterized into three relaxation regimes of motionally averaging, free diffusion and localization. Similarly, secular relaxation in the field induced by paramagnetic spheres has been classified into regimes of motionally averaging, weak magnetization and strong magnetization depending on three characteristic time scales (Gillis et al., 1987, Brooks et al., 2001., Gillis et al., 2002). Analytical expressions for secular relaxation rates have been proposed for the different asymptotic regimes.

This study proposes a generalized relaxation theory which extends the definition of the asymptotic regimes defined for the ideal case of diffusion in constant gradient to general inhomogeneous fields. The regimes are determined by the shortest characteristic time scale (Brooks et al., 2001) which can be defined for a general inhomogeneous field

rather than the smallest length scale. The time scales also quantify the characteristics of the relaxation regimes such as the echo spacing dependence and T_1/T_2 ratio.

The chapter is organized as follows. In section 3.2, the generalized theory of relaxation regimes in inhomogeneous fields is provided. The theory is independent of the particular choice of inhomogeneous field distribution. The two cases of relaxation in constant gradient and relaxation by paramagnetic spheres are described for each regime to explain the correspondence between the characteristic parameters. Section 3.3 illustrates the dependence of characteristic time scales in sedimentary rocks on governing parameters such as the concentration and the size of paramagnetic particles. Section 3.4 describes random walk simulations of the secular relaxation in field induced by paramagnetic spheres to quantitatively explain the characteristics of the relaxation regimes.

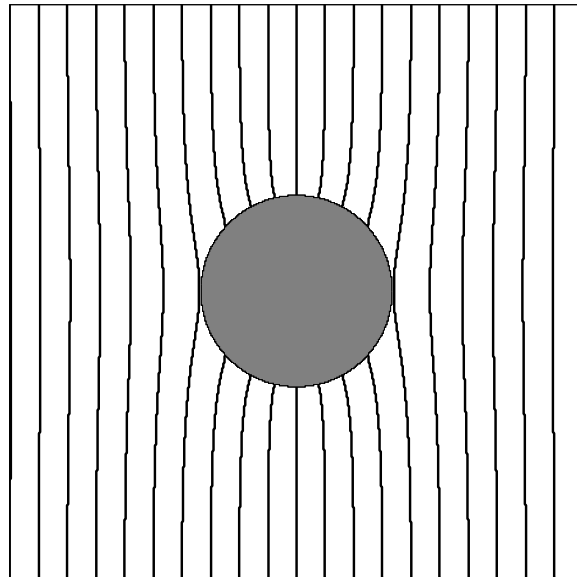


Figure 3.1: Magnetic field lines in the presence of a paramagnetic sphere with magnetic susceptibility 10^6 times that of the surrounding medium. The field lines concentrate in their passage through the sphere.

3.2. Generalized secular relaxation theory

3.2.1. Characteristic time scales for secular relaxation

Transverse relaxation due to dephasing in magnetic field inhomogeneities induced either internally due to susceptibility differences or externally due to applied gradients is characterized by three time scales (Brooks et al., 2001):

1) time taken for significant dephasing, τ_ω , defined as the inverse of the spread in Larmor frequencies ($\delta\omega$) existing in the system

$$\tau_\omega = \frac{1}{\delta\omega} \quad (3.4)$$

2) diffusional correlation time, τ_R , defined as the time taken to diffusively average the inhomogeneities

$$\tau_R = \frac{L^2}{D} \quad (3.5)$$

where L is the characteristic length of field inhomogeneity in the system, and

3) half echo spacing used in CPMG pulse sequence, τ_E , given as

$$\tau_E = \frac{TE}{2} \quad (3.6)$$

where TE is the echo spacing for the CPMG sequence.

The length scale of the field inhomogeneity (L) and spread in Larmor frequencies ($\delta\omega$) depend on particular system parameters. The characteristic time scales for the two ideal cases of relaxation in a constant gradient and in the field induced by paramagnetic spheres are described below.

3.2.1.1. Characteristic time scales for restricted diffusion in a constant gradient.

For the case of restricted diffusion in a constant gradient g in a pore, field inhomogeneity exists over the entire length of the pore. Thus, the length scale of the field inhomogeneity is equal to the structural length (L_s) of the pore i.e.

$$L=L_s \quad (3.7)$$

The diffusional correlation time is proportional to the square of the field inhomogeneity length scale (Equation 3.5). Thus,

$$\tau_R = \frac{L_s^2}{D} \quad (3.8)$$

using Equation (3.7). Furthermore, the spread in Larmor frequencies is equal to the frequency difference at the pore boundaries since the inhomogeneity exists over the entire pore length. Thus, the time for significant dephasing (τ_ω) is given as

$$\tau_\omega = \frac{1}{\delta\omega} = \frac{1}{\gamma g L_s} \quad (3.9)$$

3.2.1.2. Characteristic time scales for relaxation in the field induced by a paramagnetic sphere

A paramagnetic particle of magnetic susceptibility different from that of the surrounding medium induces internal magnetic field gradients when placed in an external magnetic field. Potential theory can be used to estimate the induced internal fields in idealized geometries. The field induced by a paramagnetic sphere of radius R_0 placed in an external magnetic field, \vec{B}_0 , is given as (Menzel, 1955)

$$\frac{\vec{B}_\delta}{|\vec{B}_0|} = \cos \theta \left(1 + \frac{2(k-1)R_0^3}{(k+2)r^3} \right) \vec{r} - \sin \theta \left(1 - \frac{(k-1)R_0^3}{(k+2)r^3} \right) \vec{\theta} \quad (3.10)$$

where $k = (1 + \chi_{\text{sphere}})/(1 + \chi_{\text{medium}})$, χ_{sphere} and χ_{medium} are the magnetic susceptibility of the sphere and medium respectively. θ is the azimuthal angle from the direction of \vec{B}_0 , and r is the radial distance from the centre of the paramagnetic sphere. $\vec{\theta}$ and \vec{r} are the unit vectors in the azimuthal and radial direction respectively. Thus, the component of the induced field along the direction of external field \vec{B}_0 is given as

$$B_{\delta z} = B_0 \left(\frac{k-1}{k+2} \right) (3 \cos^2 \theta - 1) \frac{R_0^3}{r^3} \quad (3.11)$$

The component of the internal field along the external magnetic field is considered since this component determines the precession frequency (Brown et al., 1993). Figure 3.2 shows the contour plots of the dimensionless internal magnetic field defined as

$$B_{\delta z}^* = \frac{B_{\delta z}}{[(k-1)/(k+2)]B_0} = \left(\frac{3 \cos^2 \theta - 1}{r^{*3}} \right) \quad (3.12)$$

where the radial distance r^* is normalized with respect to the radius of the paramagnetic sphere.

$$r^* = \frac{r}{R_0} \quad (3.13)$$

The internal field is maximum at the surface of the sphere (positive at poles and negative at equator) and falls as the cube of the radial distance from the center. Thus, the range of Larmor frequencies in the system is the difference in the polar and equatorial fields at the surface of the sphere

$$\delta\omega = \frac{3(k-1)}{(k+2)} \gamma B_0 \quad (3.14)$$

τ_ω is given by the reciprocal of $\delta\omega$. In addition, field inhomogeneity extends to distances proportional to the radius of the sphere. Thus, τ_R is given as

$$\tau_R = \frac{R_0^2}{D} \quad (3.15)$$

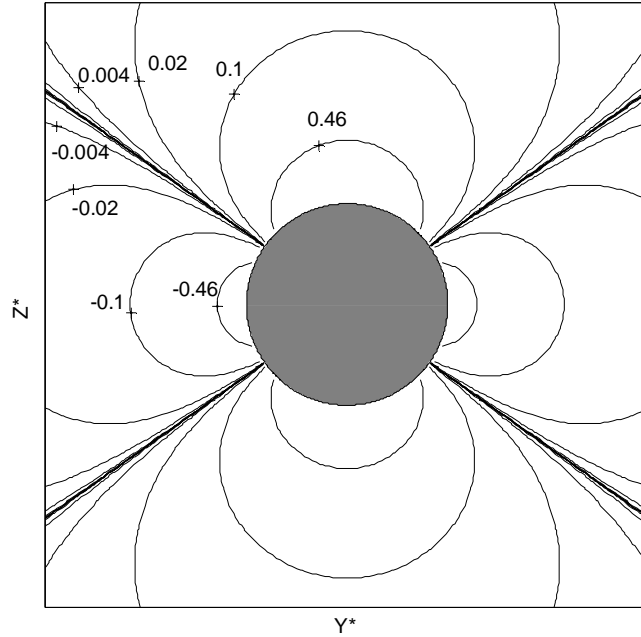


Figure 3.2: Contour plots of z component of internal magnetic field (dimensionless) induced by a unit paramagnetic sphere in a vertical plane passing through the center of the sphere. The external magnetic field is applied in the vertical z direction.

3.2.2. Asymptotic regimes of secular relaxation

Secular relaxation in inhomogeneous fields can be characterized by three regimes of motionally averaging, free diffusion and localization depending on the shortest characteristic time scale as described below. The particular cases of relaxation in a constant gradient and relaxation in the field induced by paramagnetic sphere are also described for each regime. For the case of relaxation in a constant gradient, the conditions for the relaxation regimes can be derived in terms of characteristic length scales (DeSwiet

et al., 1994) from the more general conditions in terms of the time scales. Thus, the time scales extends the classification of relaxation regimes to general inhomogeneous fields.

3.2.2.1. Motionally averaging regime

The motionally averaging regime is characterized by fast diffusion of protons such that the inhomogeneities in magnetic field are motionally averaged. This occurs when the diffusional correlation time is much shorter compared to the half echo spacing and the time taken for significant dephasing due to the presence of field inhomogeneities.

The conditions of motionally averaging regime are (Gillis et al., 1987)

$$\begin{aligned}\tau_R &\ll \tau_\omega \\ \tau_R &\ll \tau_E\end{aligned}\tag{3.16}$$

An important characteristic of the motionally averaging regime is that the secular relaxation rate is independent of the echo spacing. Since the diffusional correlation time is much shorter than the echo spacing, field inhomogeneities are motionally averaged in time much shorter compared to the echo spacing.

1. **Motionally averaging in a constant gradient** - The conditions for motionally averaging in constant gradient in a pore of length L_s can be obtained in terms of the characteristic length scales (Equations (3.2) and (3.3)) by substituting Equations (3.8) and (3.9) in Equation (3.16) given as

$$\begin{aligned}L_s &\ll L_g \\ L_s &\ll L_d\end{aligned}\tag{3.17}$$

Equations (3.17) imply that the motionally averaging regime is observed when the pore structural length is small compared to the diffusion length during time τ_E (L_d) and the dephasing length (L_g). Thus, the spins typically diffuse several times the

pore size during the measurement and any magnetic field inhomogeneities are motionally averaged by their motion.

Neumann (1974) derived the expression for the secular relaxation rate in the motionally averaging regime by assuming the distribution of phase shifts to be Gaussian given as

$$\frac{1}{T_{2,\text{sec}}} = \frac{L_s^4 \gamma^2 g^2}{120D} \quad (3.18a)$$

Using Equations (3.8) and (3.9), Equation (3.18a) can be expressed in terms of characteristic parameters as shown

$$\frac{1}{T_{2,\text{sec}}} = \frac{1}{120} (\delta\omega)^2 \tau_R \quad (3.18b)$$

Thus, the relaxation rate is independent of the echo spacing and shows a quadratic dependence on the field inhomogeneity ($\delta\omega$) in the motionally averaging regime. This quadratic dependence on field inhomogeneity was also derived for a non constant field gradient in one-dimensional restricted geometry by Tarczon et al. (1985).

2. Motionally averaging in internal fields induced by paramagnetic spheres-

The motionally averaging regime is observed for relaxation in fields induced by paramagnetic spheres when the diffusional correlation time (Equation 3.15) is the shortest characteristic time scale. Thus, the conditions for the motionally averaging regime in terms of system parameters are

$$\frac{R_0^2}{D} \ll \tau_\omega = \frac{1}{\overline{\delta\omega}} = \frac{(k+2)}{3(k-1)\gamma B_0} \quad (3.19)$$

$$\frac{R_0^2}{D} \ll \tau_E$$

The expression for $\delta\omega$ in Equation (3.19) is substituted from Equation (3.14). The quantum-mechanical outer sphere theory (Gillis et al., 1987) suggests that when conditions for motionally averaging are satisfied, the secular relaxation rate is given as

$$\frac{1}{T_{2,\text{sec}}} = \frac{4}{9} \Phi \left(\overline{\delta\omega} \right)^2 \tau_R = \frac{16}{45D} \Phi \left(\frac{(k-1)}{(k+2)} \gamma B_0 R_0 \right)^2 \quad (3.20)$$

where Φ is the volume fraction of the paramagnetic particles and $\overline{\delta\omega}$ is the root mean square frequency shift at the surface of the sphere given as

$$\overline{\delta\omega} = \sqrt{\frac{4}{5}} \frac{(k-1)}{(k+2)} \gamma B_0 \quad (3.21)$$

Equation (3.20) is derived by solving quantum mechanical equations for the “flip rates” of the protons using time dependent perturbation theory (Gillis et al., 1987). Note the similar functional form of the secular relaxation rate predicted by the outer sphere theory (Equation 3.20) and Equation (3.18b).

3.2.2.2. Free diffusion regime

The free diffusion regime is valid when half echo-spacing is the shortest characteristic time scale. The effect of restriction as well as large field inhomogeneities is not felt by the spins in the time of echo formation. Thus, the spins dephase as if diffusing in an unrestricted medium. The conditions for free diffusion regime are

$$\begin{aligned}\tau_E &\ll \tau_\omega \\ \tau_E &\ll \tau_R\end{aligned}\tag{3.22}$$

1. **Free diffusion in a constant gradient-** For the case of diffusion in a constant gradient in a pore, the free diffusion regime of transverse relaxation may arise for small echo spacing such that the spins do not experience the restriction effects in the time for echo formation. The conditions for free diffusion inside a pore of length L_s can be obtained in terms of the characteristic length scales (Equations (3.2) and (3.3)) by substituting Equations (3.8) and (3.9) in Equation (3.22) given as

$$\begin{aligned}L_d &\ll L_g \\ L_d &\ll L_s\end{aligned}\tag{3.23}$$

Thus, the free diffusion regime arises when the diffusion distance in τ_E is much shorter compared to the dephasing length and the pore length. In this regime, the secular relaxation rate is given by the classical expression derived by Carr and Purcell (1954) for unrestricted diffusion in a constant gradient

$$\frac{1}{T_{2,\text{sec}}} = \frac{\gamma^2 g^2 \tau_E^2 D}{3}\tag{3.24}$$

The relaxation rate thus shows a quadratic dependence on echo spacing as long as the conditions for free diffusion regime are satisfied.

2. **Free diffusion in internal fields induced by paramagnetic spheres -** The free diffusion regime has been described as the “weak magnetization regime ($\delta\omega \cdot \tau_E < 1$)” in the magnetic resonance imaging (MRI) literature mentioned below. The regime arises physically when weakly magnetized paramagnetic

particles are used as contrast agents for medical imaging or in biological tissues with iron rich cells or deoxygenated red blood cells (Jenson et al., 2000). Brooks et al. (2001) calculated the mean squared gradient of the magnetic field induced by a paramagnetic sphere (Equation 3.11) given as

$$\langle g^2 \rangle = \frac{9\Phi(\overline{\delta\omega})^2}{\gamma^2 R_0^2} \quad (3.25)$$

Substituting Equation (3.25) in the expression for the relaxation rate in unrestricted diffusion (Equation 3.24) and accounting for restriction from neighboring particles, the relaxation rate in the presence of weakly magnetized spheres is given as (Brooks et al., 2001)

$$\frac{1}{T_{2,\text{sec}}} = \frac{2.25\Phi(\overline{\delta\omega})^2 \tau_E^2}{\tau_R} = \frac{9}{5} \Phi \left[\frac{(k-1)}{(k+2)} \gamma B_0 \right]^2 \tau_E^2 \frac{D}{R_0^2} \quad (3.26)$$

The above expression (called the Mean Gradient Diffusion Theory, MGDT) shows the similar quadratic dependence of the secular relaxation rate on the echo spacing as the expression for unrestricted diffusion in the constant gradient (Equation 3.24). However, the relaxation rate shows an inverse squared dependence on the paramagnetic particle size which is opposite to that in the motionally averaging regime (Equation 3.20). This inverse dependence arises because the mean squared field gradient in Equation (3.25) decreases as the square of the particle size.

3.2.2.3. Localization regime

Localization regime of secular relaxation arises when the dephasing time is the shortest time scale. The conditions for the localization regime are

$$\begin{aligned}\tau_\omega &\ll \tau_R \\ \tau_\omega &\ll \tau_E\end{aligned}\tag{3.27}$$

1. **Localization regime in constant gradient-** Using Equations (3.8) and (3.9) for $\delta\omega$ and τ_R for restricted diffusion in constant gradient in a pore of length L_s , Equations (3.27) reduce to the following equations in special cases

$$\begin{aligned}L_g &\ll L_d \\ L_g &\ll L_s\end{aligned}\tag{3.28}$$

Thus, the dephasing length (L_g) is the smallest characteristic length in the localization regime. The spins typically dephase to such an extent during the measurement time that they do not contribute to the total magnetization. The signal comes primarily from the spins near the boundaries which see smaller change in the magnetic field due to reflection (Sen et al., 1999). Localization regime is most difficult to treat theoretically because of the presence of large gradients. DeSwiet et al. (1994) have shown that at long times, the echo amplitude decays as

$$\frac{M(g, \tau_E)}{M_0} = c \frac{L_g}{L_s} e^{-a_1(L_d/L_g)^2} = c \left(\frac{D}{\gamma g L_s^3} \right)^{1/3} e^{-a_1 D^{1/3} \gamma^{2/3} g^{2/3} \tau_E}\tag{3.29}$$

where $a_1 = 1.0188\dots$ and $c = 5.8841\dots$ for parallel plates. The exponent is independent of the pore geometry, but the prefactor is modified for other geometries (Hürlimann et al., 1995).

2. Localization regime in internal fields induced by paramagnetic spheres-

Secular relaxation in the localization regime has also been discussed in the MRI literature. The regime arises physically for relaxation in presence of strongly

magnetized contrast agents such as superparamagnetic particles for which $\delta\omega\tau_E > 1$. Gillis et al. (2002) proposed a semi-empirical model for decay in internal fields induced by strongly magnetized spheres. In their model, the region surrounding the paramagnetic particle is divided into two regions: an inner region with very strong internal gradients and an outer region with only weak gradients. The boundary radius (R') between the inner and outer region is related to the system parameters as (Gillis et al., 2002)

$$\frac{R'}{R_0} = \left(\frac{\overline{\delta\omega\tau_E}}{a + b\Phi\overline{\delta\omega\tau_E}} \right)^{1/3} \quad (3.30)$$

where a and b are model parameters. Since the gradients in the outer region ($r > R'$) are weak, Gillis et al. (2002) suggested that relaxation in the outer region can be described by theory for weakly magnetized particles. Thus, the relaxation rate in the outer region is given by Equation (3.26) with a modification to account for the excluded volume of the inner region as shown below

$$\frac{1}{T_{2,\text{sec}}} = \frac{2.25\Phi(\overline{\delta\omega})^2\tau_E^2}{\tau_R} \left(\frac{\overline{\delta\omega\tau_E}}{a + b\Phi\overline{\delta\omega\tau_E}} \right)^{-5/3} \quad (3.31)$$

The values of the parameters a ($=1.34$) and b ($=0.99$) were calculated by Gillis et al. (2002) by fitting Equation (3.31) to numerical simulations of transverse relaxation in the presence of strongly magnetized spheres.

In the inner region ($r < R'$), the spins experience strong gradients and dephase very rapidly. Due to rapid dephasing, they do not contribute much to the macroscopic relaxation rate; therefore Equation (3.31) can provide a good measure of relaxation rate in presence of strongly magnetized particles.

3.2.2. Parametric representation of asymptotic regimes

The asymptotic regimes of secular relaxation are schematically shown in Figure 3.3 as a function of two dimensionless parameters: $\delta\omega\tau_R$ and $\delta\omega\tau_E$. The boundaries between the asymptotic regimes are drawn at the equality between the characteristic time scales. Thus, the regimes are typically valid in the regions away from the boundaries.

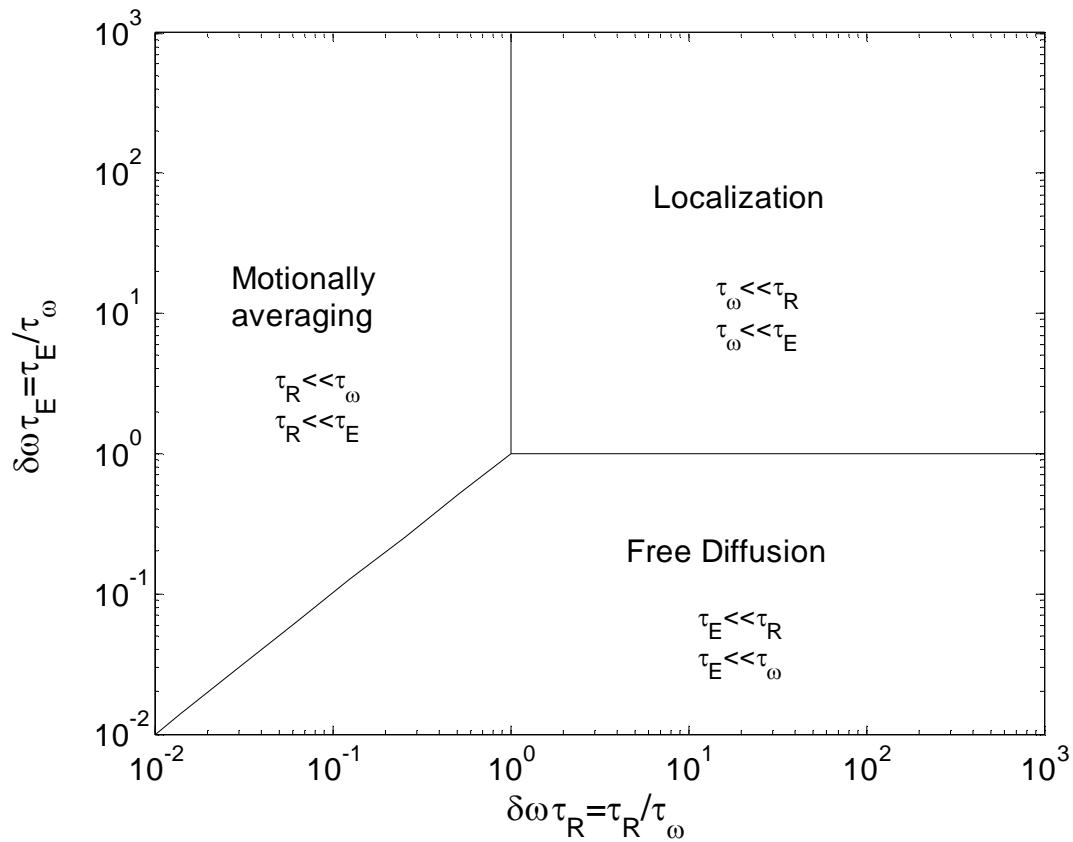


Figure 3.3: Schematic diagram of asymptotic relaxation regimes in $(\delta\omega\tau_R, \delta\omega\tau_E)$ parameter space.

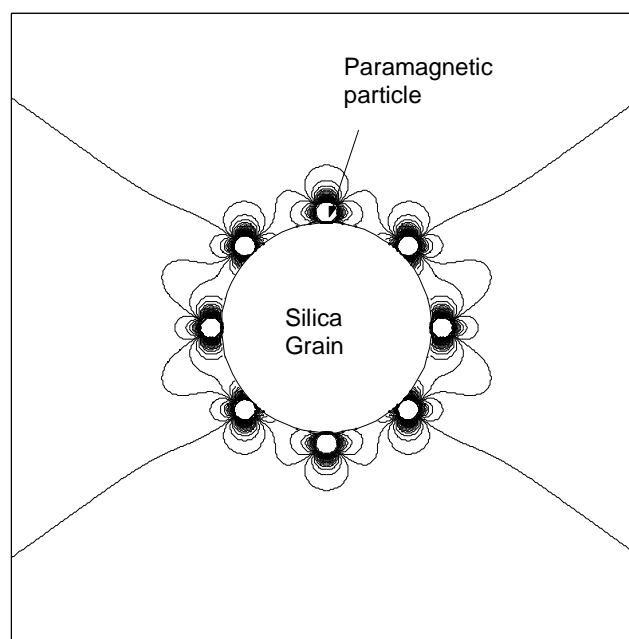
3.3. Relaxation regimes in sedimentary rocks

Sedimentary rocks usually contain paramagnetic minerals such as iron on the surfaces of silica grains (Foley et al., 1996). Thus, the relaxation of pore fluids can be influenced by field inhomogeneities induced due to the susceptibility difference between

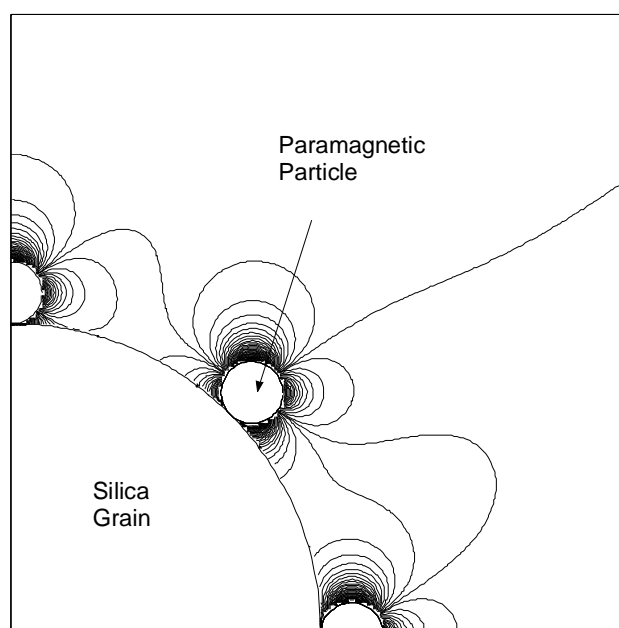
the paramagnetic minerals and the pore fluid. The asymptotic regimes of Figure 3.3 can provide useful insights for understanding the relaxation characteristics of sedimentary rocks such as the T_1/T_2 ratio and the echo spacing dependence. For the case of paramagnetic relaxation in sedimentary rocks, the characteristic time scales depend not only on the size and susceptibility of paramagnetic particles but also on the concentration of the particles and the size of silica grains. The two cases of dilute and high surface concentrations of paramagnetic particles are described below.

3.3.1. Paramagnetic particles at dilute surface concentration

At low concentrations of paramagnetic particles on silica surfaces, there is negligible superposition of the fields induced by individual particles. Figure 3.4 (a) shows the contour plots of z component of the dimensionless internal field (Equation 3.12) in the outer region of a silica grain coated with paramagnetic spheres at dilute concentration (Number of particles per unit area ~ 3). In the lower panel of the figure, the contour plots in a quadrant of the outer region are shown at higher magnification. The particles are separated far enough from each other such that the field induced by one particle is not significantly influenced by the fields induced by neighboring particles. Due to insignificant superposition, the protons in the outer region of the grain dephase as if diffusing in an internal field induced by a single particle. Thus, the asymptotic regimes mentioned for a single particle are applicable for describing secular relaxation in sandstones with dilute paramagnetic concentration. The spread in Larmor frequency ($\delta\omega$) and diffusional correlation time (τ_R) are given by Equations (3.14) and (3.15) defined for a single paramagnetic particle.



(a)



(b)

Figure 3.4: (a) Contour plots of dimensionless magnetic field (Equation 3.12) in the outer region of a silica grain coated with paramagnetic spheres at dilute concentrations (No. of particles per unit area ~ 3). The radial distance is normalized with respect to the radius of the grain. The ratio of radius of the silica grain to that of paramagnetic particles is 10. (b) Contour plots in a quadrant at higher magnification.

3.3.2. Paramagnetic particles at high surface concentration

At high surface concentrations of paramagnetic particles, the internal fields induced by individual particles overlap. Thus, the inhomogeneous field extends to larger distances than at lower surface concentrations due to superposition. Figure 3.5 shows the contour plots of the internal field (dimensionless) in the outer region of a grain coated with paramagnetic particles at high concentration (No. of particles per unit area ~ 30). The lower panel shows the contour plots in the quadrant at higher magnification. Strong field gradients are induced close to the surface of the particles. In addition, the fields induced by neighboring particles superpose and extend to length scales comparable to the size of the substrate silica grain. The field is similar to that of a single solid sphere shown in Figure 3.2.

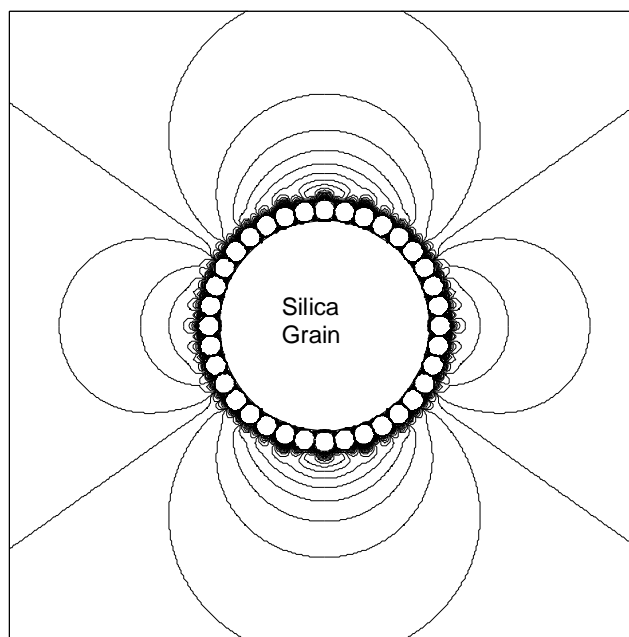
At high concentrations, the particles can be visualized as forming a paramagnetic “shell” around the silica grain. Consider a grain of radius R_g coated with a paramagnetic shell of thickness ε . The internal field induced by the paramagnetic shell can be calculated by subtracting the field induced by a sphere of radius R_g from the field induced by a concentric sphere of radius $R_g + \varepsilon$. Thus, the internal field contribution of only the spherical shell survives. Using Equation (3.11) for the field induced by a paramagnetic sphere, the field distribution for a paramagnetic shell is given as

$$\begin{aligned}
 B_\delta &= \frac{(k-1)B_0(3\cos^2\theta-1)}{(k+2)} \left[\frac{(R_g + \varepsilon)^3}{r^3} - \frac{R_g^3}{r^3} \right], & r > R_g + \varepsilon \\
 &\approx \frac{(k-1)B_0(3\cos^2\theta-1)}{(k+2)} \frac{3\varepsilon R_g^2}{r^3}, & \varepsilon \ll R_g
 \end{aligned}
 \tag{3.32}$$

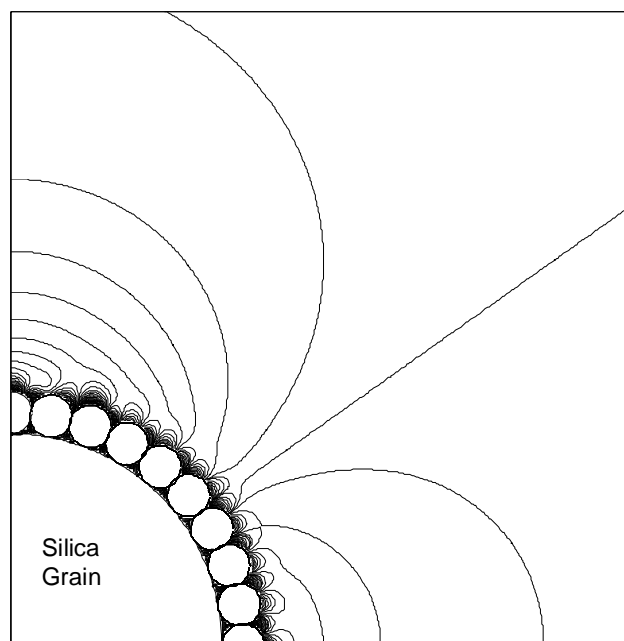
Similar to the field distribution of a solid sphere (Equation 3.11), the field is maximum at the surface of the shell (positive at poles and negative at equator) and falls as the cube of the radial distance. Thus, the range of Larmor frequencies is the difference in polar and equatorial frequencies at the surface given as

$$\delta\omega_{\text{shell}} \approx \frac{(k-1)\gamma B_0}{(k+2)} \frac{9\varepsilon}{R_g} \quad (3.33)$$

The frequency range ($\delta\omega_{\text{shell}}$) is proportional to the ratio of the thickness of paramagnetic shell to the radius of the silica grain. As a validation of this relationship, consider the limiting case of the field induced by an infinite paramagnetic sheet ($R_g \rightarrow \infty$). A paramagnetic sheet perpendicular to an externally applied field does not induce any field gradients since the field lines still remain parallel. This is also quantitatively verified by Equation (3.33) which shows $\delta\omega_{\text{shell}} \rightarrow 0$ as $R_g \rightarrow \infty$. Figure 3.6 shows the contour lines of the internal field induced by a paramagnetic shell around a sphere of unit radius. For comparison, the thickness of the shell is calculated such that the volume of the shell is equal to the total volume of paramagnetic particles on the silica surface in Figure 3.5. Good match between the contour lines in Figures 3.5 and 3.6 supports the claim that particles can be assumed as forming a paramagnetic shell around silica grains at high concentrations.



(a)



(b)

Figure 3.5: (a) Contour plots of dimensionless magnetic field (Equation 3.12) in the outer region of a silica grain coated with paramagnetic spheres at high concentrations (No. of particles per unit area ~ 30). The radial distance is normalized with respect to the radius of the grain. The ratio of radius of the silica grain to that of paramagnetic particles is 10. (b) Contour plots in a quadrant at higher magnification.

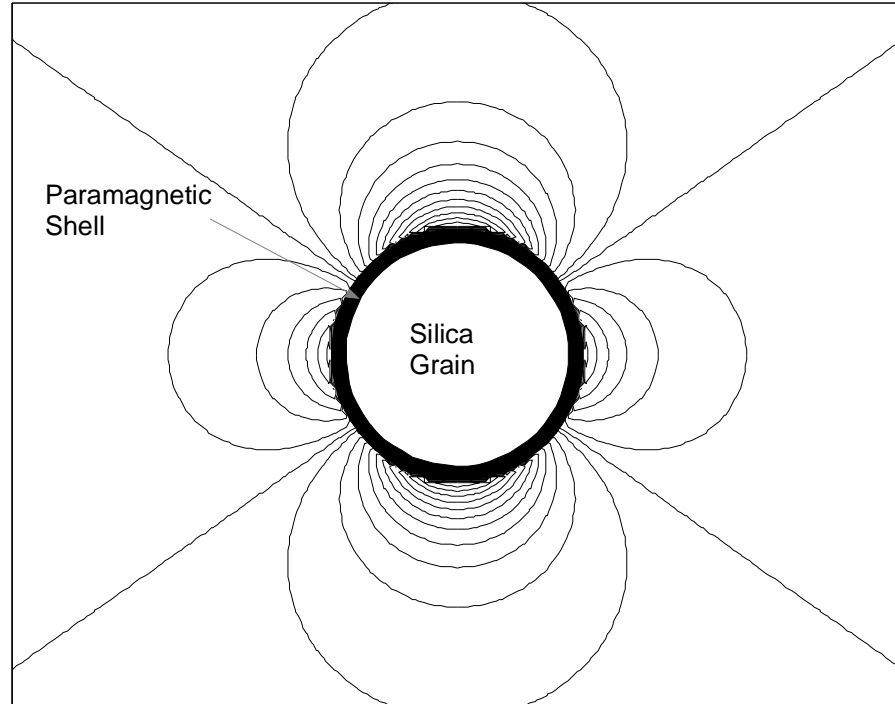


Figure 3.6: Contour plots of dimensionless magnetic field (Equation 3.12) in the outer region of a paramagnetic shell around a unit sphere. The thickness of the shell is calculated such the volume of the shell is same as the total volume of paramagnetic particles in Figure 3.5.

Equation (3.33) shows that the frequency range for a paramagnetic shell decreases by a factor $3\varepsilon/R_g$ in comparison to that for a single solid particle (Equation 3.14). Thus, the time for significant dephasing (τ_ω) increases by the same factor. In addition, the field inhomogeneity extends to a length scale comparable to the size of the substrate silica grain. Thus, for a close-packing structure of silica grains in sandstones, the length scale of field inhomogeneity (L) is given by the dimension of the interstitial pore between

grains as shown in Figure 3.7. The radius of the largest sphere that can fit in the interstitial pore is given as (Vainshtein et al., 2000)

$$L = 0.225R_g \quad (3.34)$$

Thus, the diffusional correlation time (τ_R) increases as the square of the silica grain radius rather than the paramagnetic particle radius. For sufficiently coarse grained sandstones, τ_R can become larger than τ_ω . Hence, the system can experience the localization regime (if $\tau_\omega < \tau_E$) or the free diffusion regime (if $\tau_E < \tau_\omega$) of secular relaxation even if silica grains are coated with fine-sized paramagnetic particles.

At the transition from an individual particle at low concentration to a paramagnetic shell at high concentration, the range of induced Larmor frequencies changes from that for a particle (Equation 3.14) to that for a shell (Equation 3.33). In addition, the paramagnetic volume fraction (Φ) also changes. At low concentrations, Φ is the ratio of the volume of the paramagnetic particles to the total volume. However, at high concentrations, Φ corresponds to the solid matrix volume fraction since the particles cover the surface of silica grains. The condition for transition from individual particle at low concentration to a paramagnetic shell at high concentration is that the product of the volume fraction and frequency range is the same for the particle and the shell.

$$\Rightarrow (\delta\omega\Phi)_{\text{particle}} = (\delta\omega\Phi)_{\text{shell}} \quad (3.35)$$

This condition ensures that the secular relaxation rates vary smoothly at the transition.

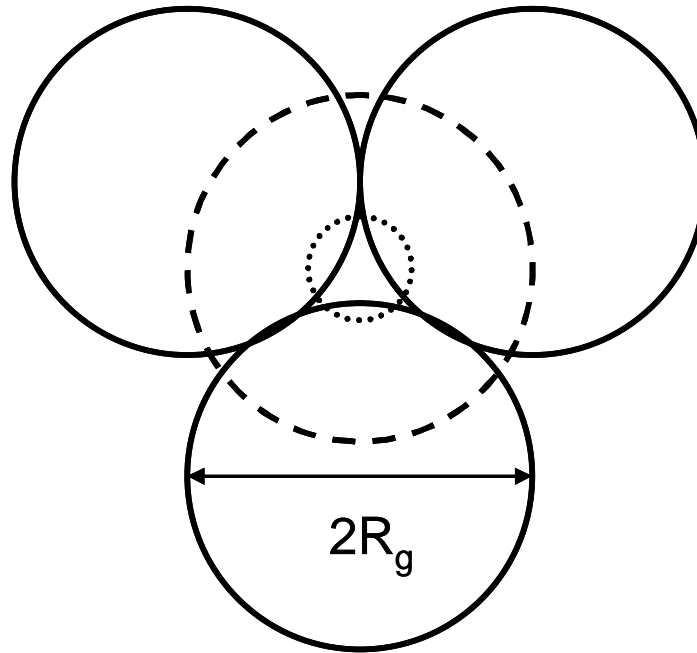


Figure 3.7 Schematic diagram of a tetrahedral pore between four touching silica grains of radius R_g . The length scale of field inhomogeneity is equal to the dimension of the tetrahedral pore when the paramagnetic particles are present at high concentration on the surface of the grains.

3.4. Random walk simulations

The decay of transverse relaxation due to diffusion in inhomogeneous fields is elucidated with the help of random walk simulations. The simulations provide a convenient method to quantitatively illustrate the characteristics of the asymptotic regimes in a general inhomogeneous field. Secular relaxation in the inhomogeneous field induced in the annular region of a paramagnetic sphere is modeled. Surface relaxation at the inner radius (R_0) and outer radius (R_e) of the annulus is neglected. It is also assumed that spin-echoes are measured by CPMG pulse sequence technique with ideal pulses.

3.4.1. Non-dimensionalization of Bloch equations

The relaxation of transverse magnetization (M) in an inhomogeneous field B_z after the application of first $\pi/2$ pulse is given by the Bloch-Torrey equation

$$\frac{\partial M}{\partial t} = -i\gamma B_z M - \frac{M}{T_{2,B}} + D\nabla^2 M \quad (3.36)$$

where D is the diffusivity of the fluid and $T_{2,B}$ is the bulk relaxation time. No surface relaxation at the inner and outer boundaries implies

$$\vec{n} \cdot \nabla M = 0 \text{ at } r = R_0. \quad (3.37)$$

$$\vec{n} \cdot \nabla M = 0 \text{ at } r = R_e. \quad (3.38)$$

Here r is the radial distance from the center and \vec{n} is the outward pointing normal. By

substituting $M = M_x + iM_y$ and $M = m \cdot e^{\left(-i\omega_0 t + \frac{-t}{T_{2B}}\right)}$ ($\omega_0 = \gamma B_0$), Equation (3.36) can be expressed as

$$\frac{\partial m}{\partial t} = -i\gamma B_{\delta z} m + D\nabla^2 m \quad (3.39)$$

Here $B_{\delta z}$ ($= B_z - B_0$) is the component of the internal field along the direction of the externally applied field. m represents the transverse magnetization with the precession at Larmor frequency (ω_0) and bulk relaxation factored out (Bergman et al., 1995).

The following dimensionless variables are introduced to normalize the governing equations

$$r^* = \frac{r}{R_e}, \quad t^* = \frac{t}{t_0}, \quad m^* = \frac{m}{M_0}$$

where t_0 is a characteristic time and M_0 is the initial magnetization. Substituting the dimensionless variables and Equation (3.11) for the field induced by a paramagnetic sphere in Equation (3.39), the following dimensionless equation is obtained

$$\frac{\partial m^*}{\partial t^*} = -i \frac{(3 \cos^2 \theta - 1)}{r^{*3}} \left(\frac{\gamma B_0 (k-1)}{(k+2)} \left(\frac{R_0}{R_e} \right)^3 t_0 \right) m^* + N_D \nabla^{*2} m^* \quad (3.40)$$

where dimensionless group N_D is defined as

$$N_D = \frac{Dt_0}{R_e^2} \quad (3.41)$$

The characteristic time t_0 is chosen such that the coefficient of the second term in Equation (3.40) is unity. Thus,

$$t_0 = \left[\frac{(k+2)}{\gamma B_0 (k-1)} \right] \frac{1}{\Phi} \quad (3.42)$$

where Φ is the volume fraction of the paramagnetic particle given as

$$\Phi = \left(\frac{R_0}{R_e} \right)^3 \quad (3.43)$$

Using Equation (3.14) for the frequency range ($\delta\omega$) of the inhomogeneous field induced by paramagnetic sphere, t_0 can also be expressed as

$$\Rightarrow t_0 = \frac{3}{\Phi \delta\omega} \quad (3.44)$$

Equation (3.44) is used to normalize secular relaxation rates for the experimental systems as described in Chapter 4. The dimensionless parameter, N_D , can be expressed in terms of system parameters by substituting Equation (3.42) in Equation (3.41)

$$N_D = \frac{Dt_0}{R_e^2} = \frac{(k+2)DR_e}{(k-1)\gamma B_0 R_0^3} = \frac{3}{(\delta\omega \tau_R) \Phi^{1/3}} \quad (3.45)$$

Equation (3.45) shows that N_D is *not* an independent dimensionless group but is specified if two dimensionless parameters $\delta\omega\tau_R$ and Φ are specified.

Thus, the governing Bloch equation in dimensionless form becomes

$$\frac{\partial m^*}{\partial t^*} = -i \frac{(3 \cos^2 \theta - 1)}{r^{*3}} m^* + N_D \nabla^{*2} m^* \quad (3.46)$$

The dimensionless boundary conditions are

$$\frac{\partial m^*}{\partial r^*} = 0 \quad \text{at} \quad r^* = 1 \quad (3.47)$$

$$\frac{\partial m^*}{\partial r^*} = 0 \quad \text{at} \quad r^* = \frac{R_0}{R_e} \quad (3.48)$$

In addition, the application of π pulse at dimensionless half echo spacing τ_E^* reverses the y component of the magnetization. Thus,

$$m^* |_{t^*_-} = \overline{m^*} |_{t^*_+} \quad \text{at} \quad t^* = \tau_E^*, 3\tau_E^*, 5\tau_E^* \dots \quad (3.49)$$

where the dimensionless half echo spacing, τ_E^* , is given as

$$\tau_E^* = \tau_E / t_0. \quad (3.50)$$

3.4.2. Algorithm

A continuous random walk algorithm (Weisskoff et al., 1994) is applied to model T_2 relaxation of spins (Equations 3.46-3.50) diffusing in an inhomogeneous internal field $B_{\delta z}(r, \theta)$. The random walkers are initially distributed uniformly in an annular region of the spherical paramagnetic particle. The outer radius is taken to be 20 times the radius of the concentric paramagnetic particle ($R_e = 20R_0$). Since the magnetic field falls as the cube of the radial distance, the field becomes negligible in the region greater than 10

times the inner radius. Thus, an outer radius of $20R_0$ is sufficient to avoid any boundary effects (Weisskoff et al., 2000).

The walkers start with a zero initial phase. In dimensionless time step dt^* , the n^{th} walker at a position (r^*, θ) accumulates a phase of $\Delta\phi_n = \omega^*(r^*, \theta)dt^*$. The dimensionless Larmor frequency ω^* is obtained by normalizing the Larmor frequency $\omega = \gamma B_{\delta z}$ (where $B_{\delta z}$ is given by Equation 3.11) with the characteristic rate $(1/t_0)$ as shown below

$$\omega^*(r^*, \theta) = \frac{\omega(r, \theta)}{1/t_0} = \frac{(3\cos^2\theta - 1)}{r^{*3}} \quad (3.51)$$

After every time step dt^* , the stochastic diffusion of a walker is simulated by choosing a random displacement with zero mean and standard deviation $\sqrt{2N_D dt^*}$ in the x, y and z directions in Cartesian coordinates. The clock is incremented by dt^* after every time step. At the time of the application of π pulses $t^* = \tau_E^*, 3\tau_E^*, 5\tau_E^*, \dots$, the phase of all random walkers is inverted. Perfect reflection at the inner and outer boundaries is simulated by returning the walker to the same position if the next displacement takes it outside the boundaries. The echo intensity at times $t^* = 2\tau_E^*, 4\tau_E^*, 6\tau_E^*, \dots$ is evaluated by averaging the phase of all walkers

$$M(t^*) = \frac{1}{N} \sum_{n=1}^N \exp(i\phi_n(t^*)) \quad (3.52)$$

where N is the number of walkers and $\phi_n(t^*)$ is the phase of the n^{th} walker at time t^* . The dimensionless relaxation rate is calculated from the slope of exponential fit to the simulated echo intensities. However, the magnetization decay is multi-exponential for simulations such that $\delta\omega\tau_R > 1000$. For such cases, the relaxation rate is calculated from the slowest component of the multi-exponential decay.

There are two simulation parameters which should be appropriately chosen to ensure the accuracy of the solution:

1. Number of walkers (N_w) – Number of walkers determines the statistical noise in the simulations. Simulations with different number of walkers show that $N=10,000$ gives a good accuracy (<1% average absolute deviation from the analytical solutions) and a reasonable amount of computational time.
2. Time step (dt^*) – The value of the time step should be chosen such that the dimensionless time step dt^* is less than the (normalized) characteristic time scales of the system

$$dt^* \ll \frac{\tau_R}{t_0}, \quad dt^* \ll \frac{\tau_\omega}{t_0}, \quad dt^* \ll \frac{\tau_E}{t_0} \quad (3.53)$$

3.4.3. Validation of numerical solution

The random walk simulations are validated for unrestricted and restricted diffusion in a constant gradient by comparing the simulations with the known analytical expressions for the transverse relaxation in the two cases.

3.4.3.1. Unrestricted diffusion in a constant gradient

For unrestricted diffusion in a constant gradient g , echo attenuation due to diffusion follows an exponential decay with a time constant given by the Equation (3.24). Figure 3.8 shows the comparison between the analytical and the simulated echo decay for the case of $g = 100$ G/cm and $\tau_E = 2$ ms. The two solutions match within 0.1% absolute average deviation, thereby indicating the validity of the algorithm. The algorithm was validated for more cases and for each case the solutions matched within good agreement.

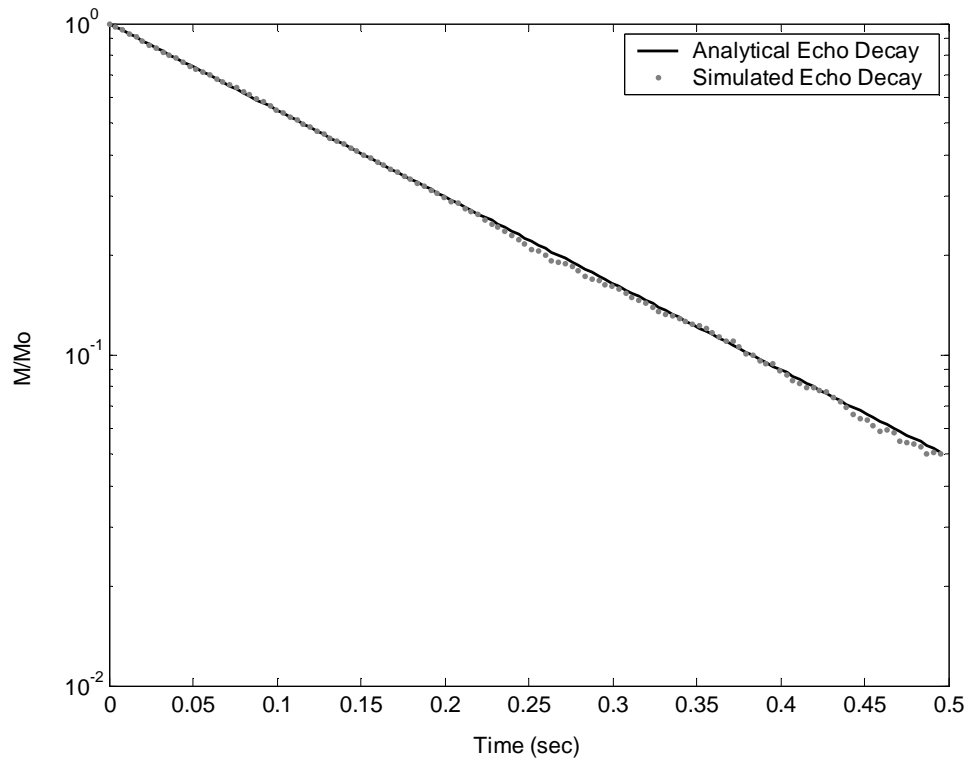


Figure 3.8: Comparison of analytical and simulated echo decay for **unrestricted diffusion in a constant gradient**. The parameters used in the simulations are $g = 100$ G/cm, $\tau_E = 2$ ms, $N_w = 10,000$ and $dt = 0.1$ μ s. The simulated echo decay matches within 0.1% of the analytical decay.

3.4.3.2. Restricted diffusion in constant gradient

For the case of restricted diffusion, random walk simulations are validated by comparing them with the analytical expression for transverse relaxation in constant gradient inside a sphere. In motionally averaging regime, relaxation due to diffusion in a constant gradient g in a sphere of radius R_s is given as (Neumann, 1974)

$$\frac{1}{T_2} = \frac{8R_s^4 \gamma^2 g^2}{175D} \quad (3.54)$$

Simulations are done in terms of dimensionless variables by normalizing the spatial variables with the radius of the sphere (R_s). Thus, the normalized characteristic lengths (Equations 3.2 and 3.3) are given as

$$L_g^* = \frac{L_g}{R_s} = \frac{1}{R_s} \sqrt[3]{\frac{D}{\gamma g}} \quad (3.55)$$

$$L_d^* = \frac{L_d}{R_s} = \frac{1}{R_s} \sqrt{D\tau_E} \quad (3.56)$$

The temporal variable is normalized with a characteristic time (t_c) defined as

$$t_c = \frac{1}{\gamma g R_s} \quad (3.57)$$

The characteristic time t_c defines the characteristic time for relaxation in constant gradient in contrast to t_0 (Equation 3.42) which was defined for relaxation in the presence of a paramagnetic sphere. The expression for t_c is derived by following the same procedure as is used to derive t_0 except that the inhomogeneous field ($B_{\delta z}$) is for a constant gradient given as

$$B_{\delta z} = gz \quad (3.58)$$

Secular relaxation due to diffusion in constant gradient with $L_g^* = 1.2$ and 1.5 is numerically simulated. For each case, two values of $L_d^* = 2$ and 3 (i.e two echo spacings) are chosen. The values of L_g^* and L_d^* are chosen greater than one so that the systems are in motionally averaging regime and relaxation rate is given by Equation (3.54) normalized by characteristic rate $1/t_c$. Figures 3.9 and 3.10 show the comparison between simulated and analytical echo decay for the two cases of $L_g^* = 1.2$ and 1.5 respectively. The two cases of $L_d^* = 2$ and 3 are shown in the upper and lower panel of the figures. The

simulated and analytical echo amplitudes match very well (<1% absolute average deviation) for all simulations, thereby indicating the validity of the numerical technique.

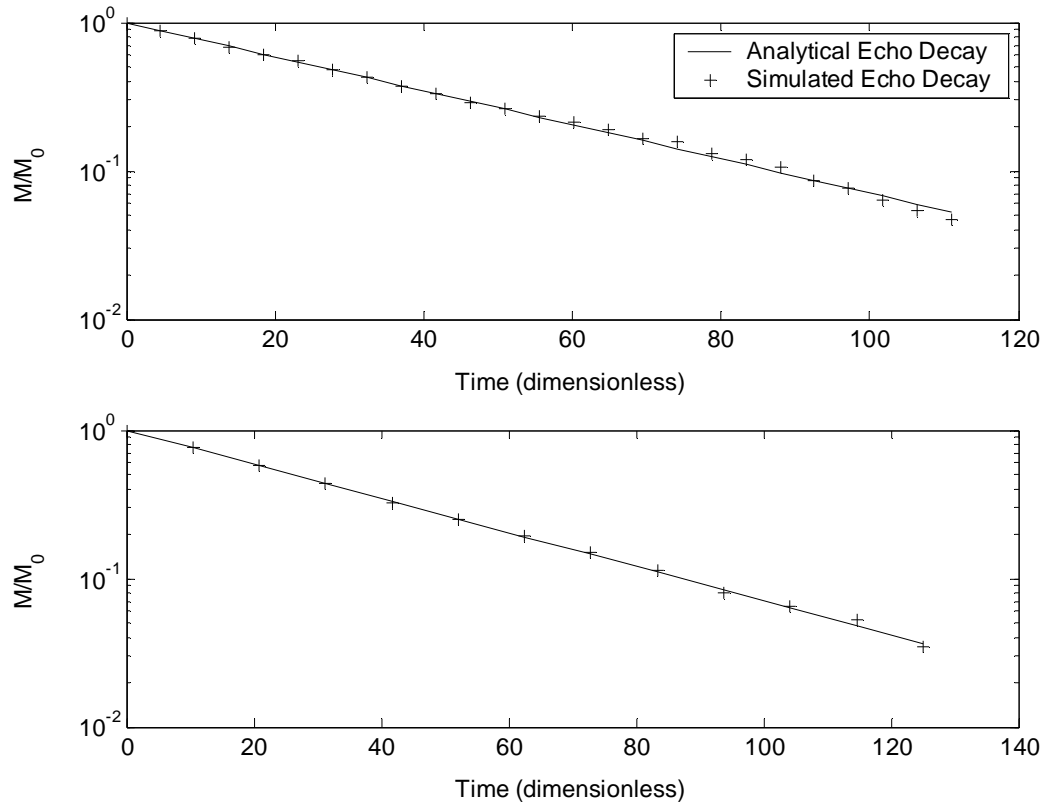


Figure 3.9: Comparison of simulated and analytical echo decays for **restricted diffusion in a sphere** with a constant gradient. The parameters used in the simulations are $L_g^* = 1.2$ and $L_d^* = 2$ (upper panel) and $L_d^* = 3$ (lower panel). Lesser number of points in the lower figure is due to smaller sampling rate with larger L_d^* . The analytical rate is given by Equation (3.54) normalized by $1/t_c$.

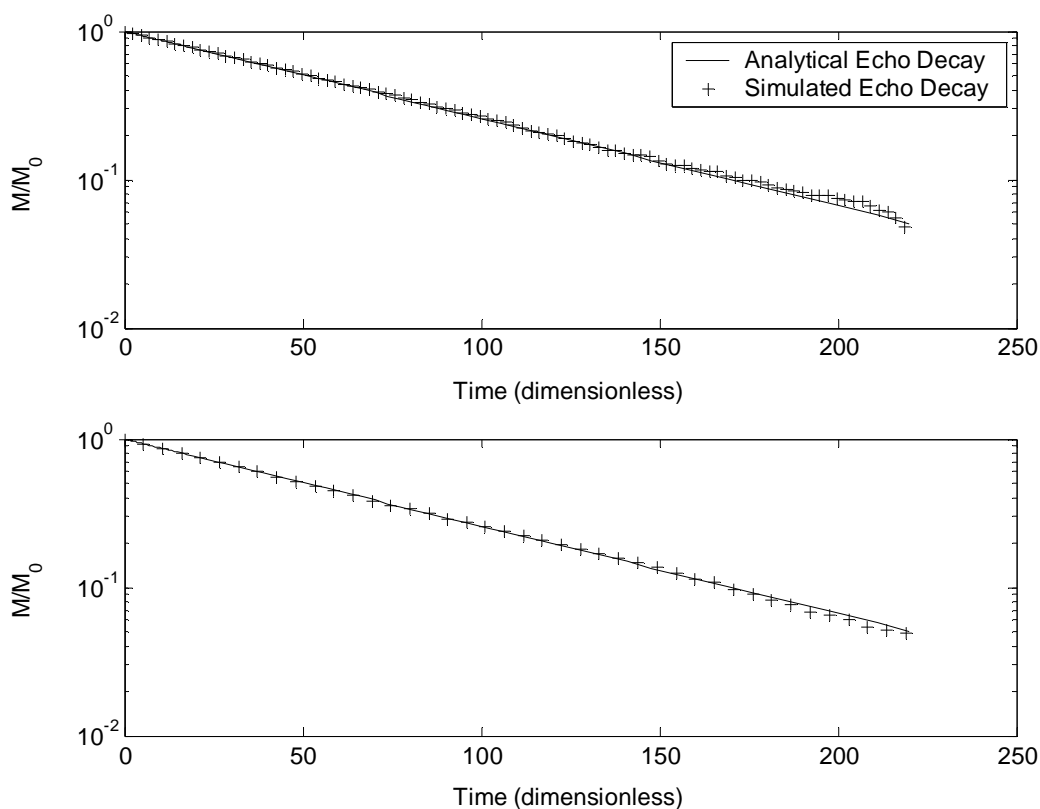


Figure 3.10: Comparison of simulated and analytical echo decays for **restricted diffusion in a sphere** with a constant gradient. The parameters used in the simulations are $L_g^* = 1.5$ and $L_d^* = 2$ (upper panel) and $L_d^* = 3$ (lower panel). Lesser number of points in the lower figure is due to smaller sampling rate with larger L_d^* . The analytical rate is given by Equation (3.54) normalized by $1/t_c$.

3.4.4. Results

The results for random walk simulations of secular relaxation in the presence of paramagnetic spheres are next described. The secular relaxation of protons in inhomogeneous field induced by a paramagnetic sphere of susceptibility 0.2 (SI units) surrounded by a medium of susceptibility $-0.8 \cdot 10^{-6}$ (SI units) is simulated. These values of susceptibilities are representative of magnetite and water respectively. The external magnetic field B_0 corresponds to a proton Larmor frequency of 2 MHz. The radius of

paramagnetic sphere is varied from 10 nm to 25 μm to change the diffusional correlation time (τ_R). For each particle size, simulations with several values of half echo spacing (τ_E) are performed to illustrate the echo spacing dependence of secular relaxation in different regimes. Thus, the simulations span the entire $(\delta\omega\tau_R, \delta\omega\tau_E)$ parameter space of Figure 3.3.

Figure 3.11 shows the plot of simulated dimensionless relaxation rates ($1/T_{2,\text{sec}}^D$) as a function of $\delta\omega\tau_R$ for different values of $\delta\omega\tau_E$. The superscript ‘‘D’’ refers to dimensionless relaxation rate. The relaxation rates can be made dimensional by using the following equation.

$$\frac{1}{T_{2,\text{sec}}} = \frac{1}{t_0 T_{2,\text{sec}}^D} = \left[\frac{(k+2)}{(k-1)\gamma B_0} \right] \frac{1}{\Phi T_{2,\text{sec}}^D} \quad (3.59)$$

$\delta\omega$ and τ_R are calculated from Equations (3.14) and (3.15) respectively for the specified values of radius and susceptibility of the paramagnetic sphere.

The plots of corresponding theoretical relaxation rates in the respective regimes are also shown for comparison. The solid black line is the plot of the theoretical relaxation rate (Equation 3.20) in the **motionally averaging regime** normalized by the characteristic rate $1/t_0$ (Brooks et al., 2001)

$$\frac{1}{T_{2,\text{sec}}^D} = \frac{t_0}{T_{2,\text{OS}}} = \frac{16}{135} \delta\omega\tau_R \quad (\tau_R \ll \tau_E, \tau_R \ll \tau_\omega) \quad (3.60)$$

The dotted lines are the normalized relaxation rate (Equation 3.26) given by mean gradient diffusion theory valid in the **free diffusion regime** (Brooks et al., 2001)

$$\frac{1}{T_{2,\text{sec}}^D} = \frac{t_0}{T_{2,\text{FD}}} = \frac{3(\delta\omega)\tau_E^2}{5\tau_R} = \frac{3(\delta\omega\tau_E)^2}{5\delta\omega\tau_R} \quad (\tau_E \ll \tau_R, \tau_E \ll \tau_\omega) \quad (3.61)$$

The dash-dotted lines are the plots of normalized relaxation rates (Equation 3.31) given by modified mean gradient diffusion theory (Gillis et al., 2002) valid in the **localization regime** given as

$$\frac{1}{T_{2,\text{sec}}^D} = \frac{t_0}{T_{2,\text{Loc}}} = \frac{3(\delta\omega\tau_E)^2}{5\delta\omega\tau_R} \left(\frac{\sqrt{4/45}\delta\omega\tau_E}{a + b\Phi\sqrt{4/45}\delta\omega\tau_E} \right)^{-5/3} \quad (\tau_\omega \ll \tau_E, \tau_\omega \ll \tau_R) \quad (3.62)$$

The dashed lines mark the boundaries $\delta\omega\tau_R = 1$ and $\delta\omega\tau_E = 1$ that delineate the asymptotic regimes.

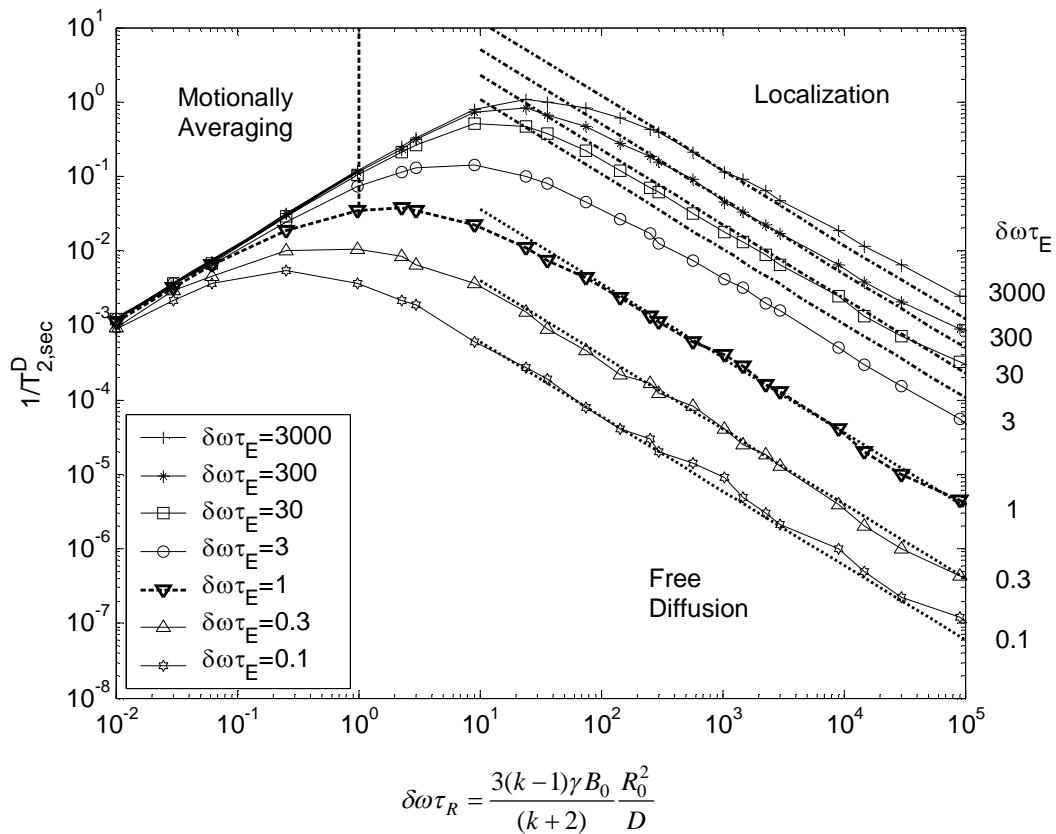


Figure 3.11: Plot of simulated secular relaxation rate (dimensionless) with $\delta\omega\tau_R$ as a function of $\delta\omega\tau_E$. The parameters used in the simulations are $\Phi = 1.25 \cdot 10^{-4}$, $k = 1.2$, $B_0 = 496$ Gauss. The solid, dotted and dash-dotted lines are the theoretically estimated secular relaxation rates according to the outer sphere theory (Equation 3.60), mean gradient diffusion theory (Equation 3.61) and modified mean gradient diffusion theory (Equation 3.62) plotted in the respective regimes of validity. The dashed lines are the boundaries $\delta\omega\tau_R = 1$ and $\delta\omega\tau_E = 1$ that delineate the asymptotic regimes.

The characteristics of the secular relaxation rate in Figure 3.11 can be described in terms of the three asymptotic regimes.

1. Motionally averaging regime: Motionally averaging regime exists for $\delta\omega\tau_R \ll 1$ and sufficiently large values of $\delta\omega\tau_E \gg 1$. In this regime, the secular relaxation rates are independent of the echo spacing because the field inhomogeneities are averaged in time much shorter compared to τ_E . In addition, the rates increase with diffusional correlation time and thus with particle size. A physical understanding of the increase in relaxation rate with τ_R can be obtained by considering the chemical exchange (CE) model of transverse relaxation (Gutowsky et al., 1953; Meiboom, 1961; Luz et al., 1963). The CE model consists of two sites A and B with a frequency shift ($\delta\omega$) between the two sites. The fraction of protons in the two sites is given by F_A and F_B respectively. When $F_B \ll 1$, the relaxation rate is given as (Meiboom, 1961)

$$\frac{1}{T_2} = F_B \tau_{ex} \frac{(\delta\omega)^2}{1 + (\delta\omega)^2 \tau_{ex}^2} \quad (3.63)$$

where τ_{ex} is the time to exchange between the two sites. In motionally averaging regime ($\delta\omega\tau_{ex} \ll 1$) of the CE model, Equation (3.63) reduces to

$$\frac{1}{T_2} \cong F_B \tau_{ex} (\delta\omega)^2 \quad (3.64)$$

Equation (3.64) shows that the relaxation rates increase with the exchange time τ_{ex} . In motionally averaging regime, exchange of protons between the two sites is fast compared to the dephasing rate ($\delta\omega \ll 1/\tau_{ex}$). Thus, the rate determining step is the amount of dephasing in the exchange time τ_{ex} . As τ_{ex} increases, the protons in the two sites are dephased by a larger amount and hence, the relaxation rates increase with τ_{ex} .

This CE model is analogous to the relaxation model in the outer region of a paramagnetic sphere (Gillis et al., 1987). The protons may be considered either near the sphere (site B) where there is frequency shift of order $\delta\omega$ or far away where there is no shift (site A). The exchange time from site B to site A is proportional to the diffusional correlation time which is the time to diffuse the length scale of field inhomogeneity. Thus, when diffusional exchange between the two sites is fast compared to the dephasing rate (i.e. motionally averaging, $\delta\omega\tau_R \ll 1$), relaxation rates increase with τ_R similar to the predictions of CE model.

2. Localization regime: The localization regime exists for $\delta\omega\tau_R \gg 1$ and large values of $\delta\omega\tau_E \gg 1$. The secular relaxation rates show strong dependence on echo spacing. Additionally, the dependence of the relaxation rate on the diffusional correlation time (and thus, the particle size) is inversed in contrast to that in the motionally averaging regime. The relaxation rates now decrease with the particle size. The CE model provides an explanation for the decrease in relaxation rates with particle size in the localization regime. When the condition $\delta\omega\tau_{ex} \gg 1$ holds, Equation (3.63) reduces to

$$\frac{1}{T_2} \cong \frac{F_B}{\tau_{ex}} \quad (3.65)$$

Thus, the relaxation rates are inversely proportional to τ_{ex} in contrast to Equation (3.64) for the motionally averaging regime. For $\delta\omega \gg 1/\tau_{ex}$, the dephasing rate is much larger compared to the rate at which protons exchange between sites A and B. Due to large dephasing, the protons are lost from the signal in a single exchange from site A to site B. In other words, site B acts like a ‘sink’ in which protons are dephased by a single visit (Brooks et al., 2002). Thus, the relaxation rate is determined by the rate at which protons

exchange between the two sites i.e. $1/\tau_{ex}$. For relaxation by paramagnetic spheres, a similar inverse dependence of relaxation rates on τ_R (which is analogous to τ_{ex}) is observed when $\delta\omega\tau_R \gg 1$.

The simulated relaxation rates in the localization regime of Figure 3.11 match well with the predictions of modified MGDT (Equation 3.62) except at large values of $\delta\omega\tau_E$ and $\delta\omega\tau_R$. This deviation is probably because at large values of parameters $\delta\omega\tau_E$ and $\delta\omega\tau_R$, the contribution of the inner region ($r < R'$) to the overall decay becomes substantial. Thus, the assumption that the decay is only governed by outer region in the derivation of Equation (3.62) may not be entirely valid.

3. Free diffusion regime: The free diffusion regime exists for small echo spacings such that $\delta\omega\tau_E \ll 1$ and $\delta\omega\tau_E \ll \delta\omega\tau_R$. Due to effective refocusing by π pulses in free diffusion regime, the simulated relaxation rates are significantly smaller than the ones in the localization or the motionally averaging regime. For $\delta\omega\tau_R > 1$, the relaxation rates show inverse dependence on the particle size similar to that in the localization regime. The simulated rates match well with the predictions of the mean gradient diffusion theory (Equation 3.61).

The above mentioned characteristics of the asymptotic regimes can be easily visualized in the $(\delta\omega\tau_R, \delta\omega\tau_E)$ parameter space. Figure 3.12 shows the contour plots (solid curves) of the simulated dimensionless relaxation rates in the $(\delta\omega\tau_R, \delta\omega\tau_E)$ domain. The contour plots differ by a factor of $\sqrt{10}$. Corresponding plots (dotted curves) for the theoretically predicted relaxation rates given by Equations (3.60), (3.61) and (3.62) are also shown in the respective regions of validity. The boundaries between the asymptotic regimes are shown by dashed lines. In the motionally averaging regime ($\delta\omega\tau_R \ll 1, \delta\omega\tau_E$

$\gg 1$), the contour plots are almost parallel to the $\delta\omega\tau_E$ axis implying that the relaxation rates are independent of the echo spacing. Also, the rates increase with $\delta\omega\tau_R$ showing that the secular relaxation increases with particle size. In localization and free diffusion regimes, the dependence of relaxation on $\delta\omega\tau_R$ is reversed and the rates decrease with particle size. In addition, the rates are echo spacing dependent in these regimes. The contours are more closely spaced and have lesser slope in the free diffusion regime than in the localization regime. Thus, the dependence of the relaxation rate on the echo spacing is higher in free diffusion than in the localization regime.

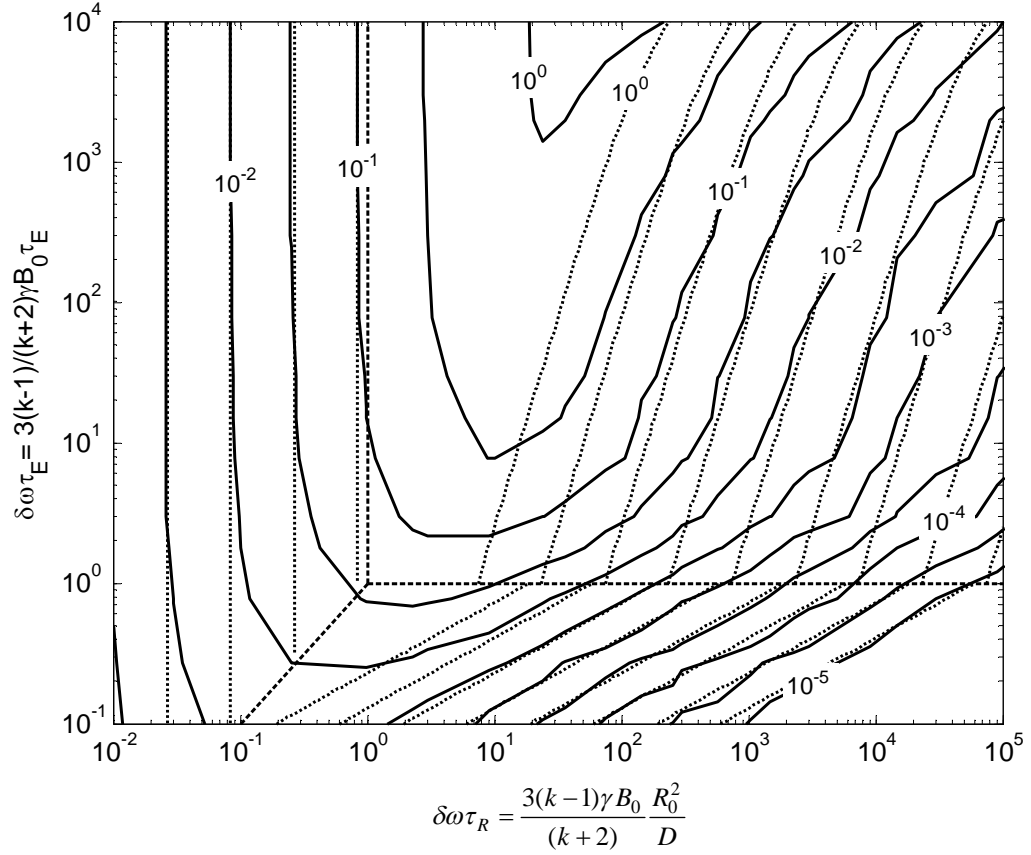


Figure 3.12: Contour plots of dimensionless secular relaxation rate in the $(\delta\omega\tau_R, \delta\omega\tau_E)$ parameter space. Contours differ by a factor of $\sqrt{10}$. The parameters used in the simulations are $\Phi = 1.25 \cdot 10^{-4}$, $k = 1.2$, $B_0 = 496$ Gauss. The dotted lines are the corresponding plots for the theoretically predicted relaxation rates given by Equations (3.60), (3.61) and (3.62). The bold dashed lines are the boundaries between asymptotic regimes. The contours are invariant for dilute volume fractions ($\Phi \leq 1.25 \cdot 10^{-4}$).

The echo spacing dependence of the simulated rates in the different regimes needs to be quantitatively studied. Figure 3.13 shows the plot of simulated relaxation rate with dimensionless echo spacing $\delta\omega\tau_E$ for cases in which $\delta\omega\tau_R \leq 1$. The dashed curve shows the boundary $\delta\omega\tau_E = \delta\omega\tau_R$ delineating free diffusion and motionally averaging regimes. In the motionally averaging regime, the relaxation rates increase with particle size in accordance to the predictions of outer sphere theory. In addition, the relaxation rates are

dependent on the echo spacing in the free diffusion regime while they are almost independent of the echo spacing in the motionally averaging regime.

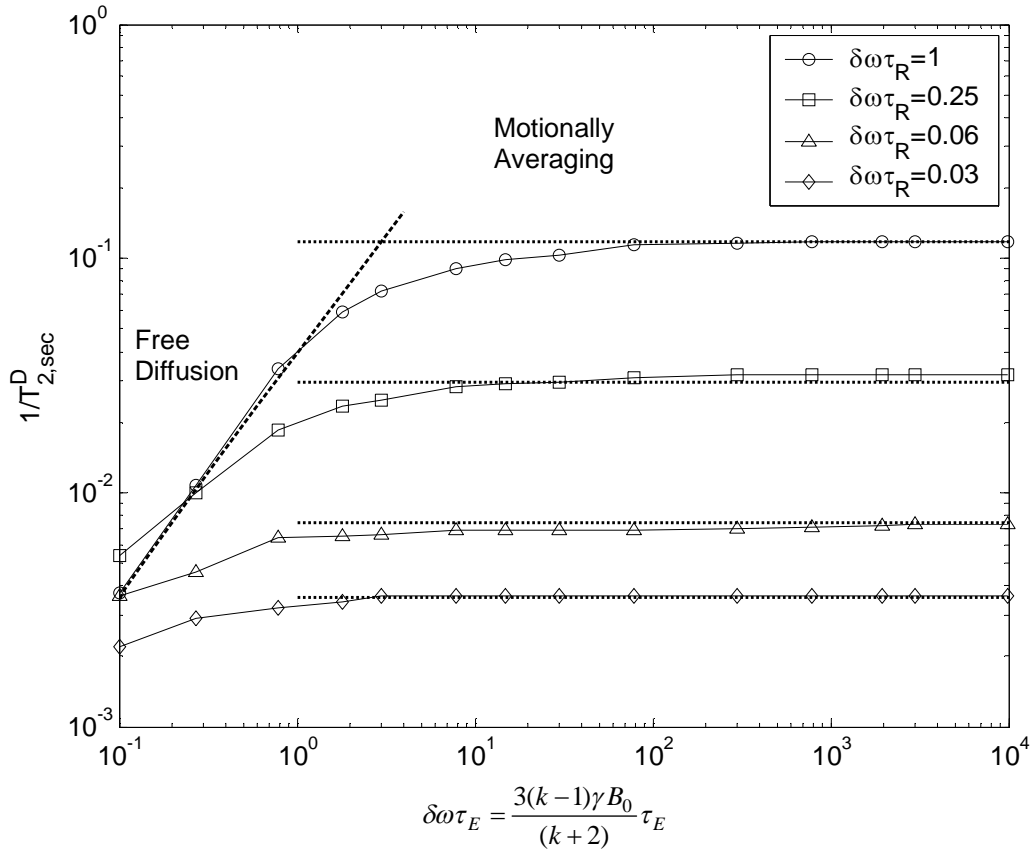


Figure 3.13: Plot of secular relaxation rates (dimensionless) with dimensionless echo spacing $\delta\omega\tau_E$ for $\delta\omega\tau_R \leq 1$. The parameters used in the simulations are $\Phi = 1.25 \cdot 10^{-4}$, $k = 1.2$, $B_0 = 496$ Gauss. The dotted lines are the plots of theoretically predicted relaxation rates in the motionally averaging regime given by Equation (3.60). The bold dashed line is the boundary $\delta\omega\tau_E = \delta\omega\tau_R$ delineating free diffusion and motionally averaging regimes. The relaxation rates are almost independent of echo spacing in the motionally averaging regime.

Figure 3.14 shows the plot of simulated relaxation rates with $\delta\omega\tau_E$ for cases in which $\delta\omega\tau_R \gg 1$. The dashed line shows the boundary $\delta\omega\tau_E = 1$ between free diffusion and localization regimes. The dotted and dash-dotted lines are the theoretically predicted relaxation rates in free diffusion and localization regimes given by Equations (3.61) and (3.62) respectively. Relaxation rates show quadratic dependence on the echo spacing in

the free diffusion regime as predicted by Equation (3.60). However, the slopes of relaxation rates decrease as the systems transition from the free diffusion to the localization regime. Power-law fits of relaxation rates with $\delta\omega\tau_E$ in the localization regime show that the exponent is approximately unity for low values of $\delta\omega\tau_E$ ($1 \leq \delta\omega\tau_E \leq 15$) and decreases to less than 0.6 for larger values of $\delta\omega\tau_E$ ($10^2 \leq \delta\omega\tau_E \leq 10^3$). These results are similar to the computations of Hardy et al. (1989) who found that the relaxation rates in presence of magnetic grains were proportional to $\tau_E^{0.6}$.

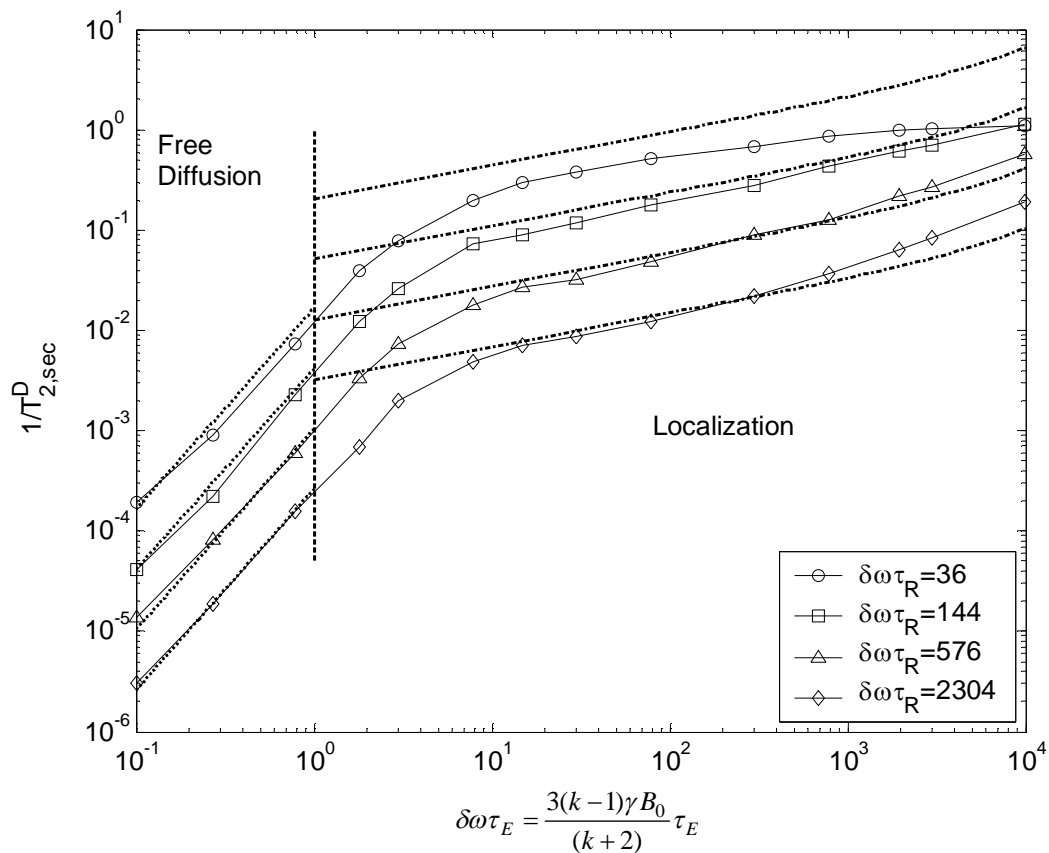


Figure 3.14: Plot of secular relaxation rates (dimensionless) with dimensionless echo spacing $\delta\omega\tau_E$ for $\delta\omega\tau_R \gg 1$. The parameters used in the simulations are $\Phi = 1.25 \cdot 10^{-4}$, $k = 1.2$, $B_0 = 496$ Gauss. The dotted and dash-dotted lines are the theoretically predicted relaxation rates in the free diffusion and the localization regime given by Equations (3.61) and (3.62) respectively. The bold dashed line is the boundary $\delta\omega\tau_E = 1$ delineating free diffusion and localization regimes. The dependence of the relaxation rates on echo spacing is less than quadratic in the localization regime.

Since the theory is presented in dimensionless terms, the plots of relaxation rates in Figures 3.11-3.14 are invariant under changes in parameters such as magnetic susceptibility of the paramagnetic spheres, diffusivity of the fluid, external magnetic field etc. However, the relaxation rates are invariant under changes in volume fraction for only dilute volume fractions ($\Phi \leq 1.25 \cdot 10^{-4}$). Figure 3.15 shows the contour plots of the simulated dimensionless relaxation rates in the $(\delta\omega\tau_R, \delta\omega\tau_E)$ space for $\Phi = 0.6$. This value of Φ corresponds to the paramagnetic volume fraction in a packing of very-well sorted sand grains coated with paramagnetic particles at high concentration. The field distribution ($B_{\delta z}$) for the simulations is specified by Equation (3.32) for a paramagnetic shell of susceptibility 0.2 (SI units) and assuming $3\varepsilon/R_g = 10^{-3}$. The contour plots differ by a factor of $\sqrt{10}$. Corresponding plots for the theoretically predicted relaxation rates are shown by the dotted curves in the respective regions of validity. The boundaries between the asymptotic regimes are shown by dashed lines.

Although the contours for $\Phi = 0.6$ and $1.25 \cdot 10^{-4}$ (Figures 3.15 and 3.12) have similar trends, there are quantitative as well as qualitative differences. First, the relaxation rates are typically larger for $\Phi = 0.6$ than for $\Phi = 1.25 \cdot 10^{-4}$. This deviation is because for $\Phi = 0.6$, the walkers experience larger field inhomogeneity due to the effect of enhanced restriction. Second, the relaxation rates for $\Phi = 0.6$ can be simulated for only small values of $\delta\omega\tau_E \leq 50$. For larger values of $\delta\omega\tau_E$, random walkers dephase even before the first few echoes can be formed. Third, the contours for $\Phi = 0.6$ in the localization regime have smaller slopes than those for $\Phi = 1.25 \cdot 10^{-4}$.

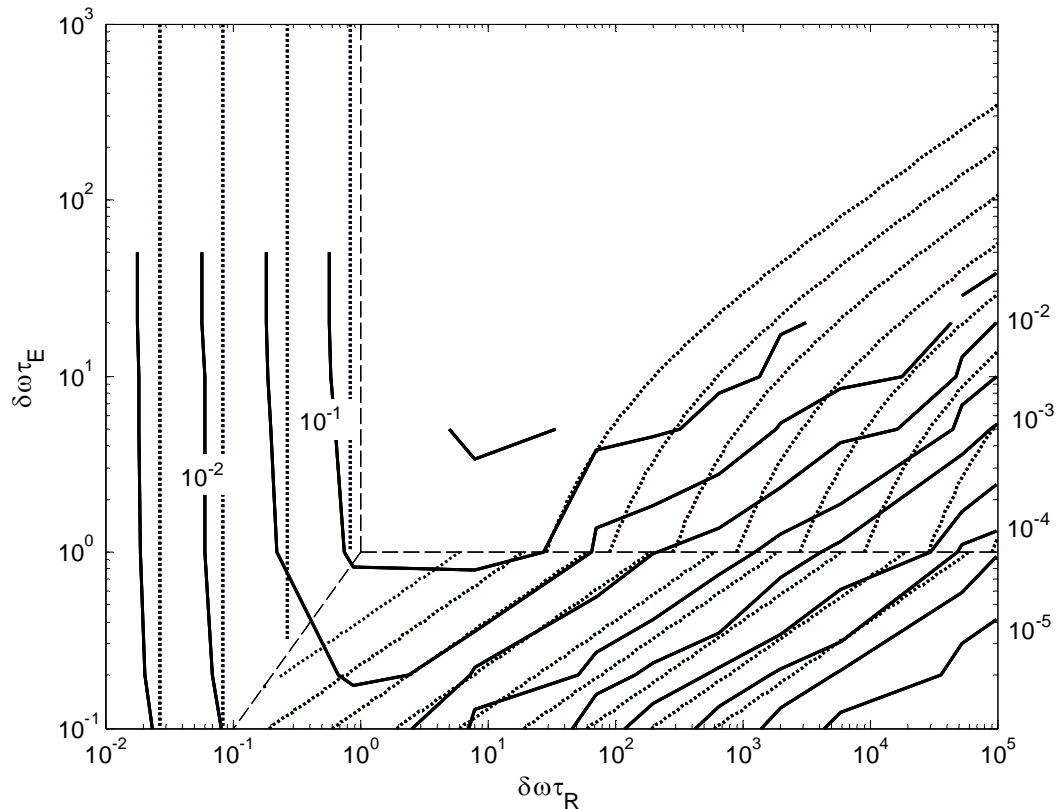


Figure 3:15: Contour plots of dimensionless secular relaxation rate in the $(\delta\omega\tau_R, \delta\omega\tau_E)$ parameter space for $\Phi = 0.6$. A paramagnetic shell with susceptibility 0.2 (SI units) and $3\varepsilon/R_g = 10^{-3}$ is assumed for the simulations. Contours differ by a factor of $\sqrt{10}$. The dotted lines are the corresponding plots for the theoretical relaxation rates given by Equations (3.60), (3.61) and (3.62). The bold dashed lines are the boundaries between asymptotic regimes.

Figure 3.16 shows the plot of average absolute deviation of simulations with higher volume fractions from the simulations with $\Phi = 1.25 \cdot 10^{-4}$. The deviations are less than 10% for $\Phi < 10^{-3}$ and greater than 50% for $\Phi = 0.6$.

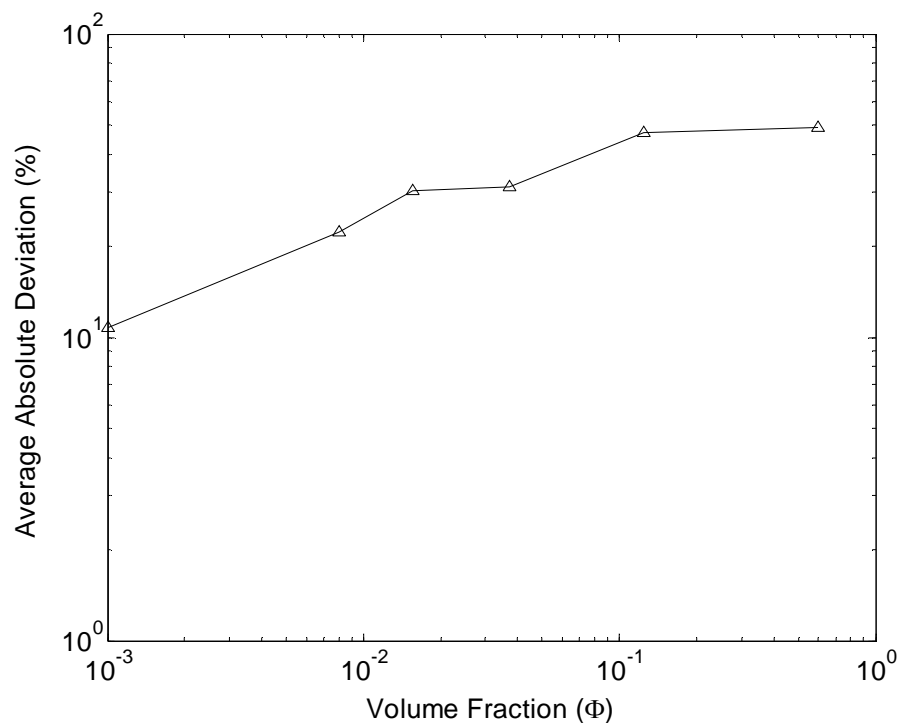


Figure 3.16: Plot of average absolute deviation (%) of simulations with higher volume fractions from the simulations with $\Phi = 1.25 \cdot 10^{-4}$. The deviation is less than 10% for $\Phi < 0.001$.

3.5. Conclusions

The loss of phase coherence between nuclear spins due to diffusion in magnetic field inhomogeneities leads to additional transverse relaxation called “secular” relaxation. A generalized relaxation theory is proposed which identifies three characteristic time scales governing secular relaxation: diffusional correlation time (τ_R), time for significant dephasing (τ_ω) and half echo spacing of the CPMG sequence (τ_E). The characteristic time scales can be defined for a general inhomogeneous field distribution. Depending on the shortest time scale, secular relaxation can be classified in three asymptotic regimes of motionally averaging, localization and free diffusion. These asymptotic regimes have been earlier identified by other authors for the particular case of restricted diffusion in

constant gradient. However, the generalized theory need not make assumption about the distribution of the inhomogeneous field.

The asymptotic regimes show different relaxation characteristics. In the motionally averaging regime, field inhomogeneities are averaged due to fast diffusion in time much shorter than τ_E . Thus, no echo spacing dependence of transverse relaxation is observed. Additionally, the relaxation rate increases with the length scale of field inhomogeneity. In the free diffusion regime, τ_E is the shortest characteristic time scale. Secular relaxation rates show quadratic dependence on echo spacing in this regime. The localization regime is characterized by τ_ω as being the shortest characteristic time scale. A sub-linear echo spacing dependence of secular relaxation rates is observed in localization regime. In contrast to motionally averaging regime, relaxation rates in free diffusion and localization regime are inversely dependent on the length scale of inhomogeneity. The dependence on field inhomogeneity length scale is reversed because when $\tau_R/\tau_\omega < 1$, the relaxation rate is determined by the amount of dephasing in diffusional correlation time. Thus, relaxation rates increase with τ_R (thus, with inhomogeneity length scale) in the motionally averaging regime. However, when $\tau_R/\tau_\omega > 1$, the relaxation rate is determined by the rate at which spins diffuse out of the region of field inhomogeneity. Thus, in localization and free diffusion regimes, relaxation rates are inversely proportional to the field inhomogeneity length scale. The characteristics of the relaxation regimes can be demonstrated in a single contour map of dimensionless relaxation rates in $(\tau_R/\tau_\omega, \tau_E/\tau_\omega)$ parameter space.

Chapter 4. Paramagnetic Relaxation in Sandstones: Experiments

In the previous chapter, generalized theory of T_2 relaxation due to diffusion in inhomogeneous fields was developed. This chapter experimentally analyzes the characteristics of the secular relaxation in porous media. Model sandstones are synthesized by coating silica grains with paramagnetic particles of known sizes and concentrations. These model systems simulate secular relaxation in sedimentary rocks in which field inhomogeneities are often induced due to presence of paramagnetic minerals and clays. The chapter is organized in four sections. In the first section, NMR measurements with aqueous dispersions of paramagnetic particles of various sizes are detailed. These experiments help to quantitatively estimate the characteristic time scales for relaxation in field inhomogeneities induced by paramagnetic particles. In the second section, proton relaxation measurements with model sandstones are described. A conceptual understanding of T_2 relaxation due to diffusion in internal field gradients in sandstones is developed in the third and fourth sections based on theoretical and experimental results.

4.1. Paramagnetic particles in aqueous dispersions

4.1.1. Ferric ion

The smallest paramagnetic particle studied was ferric ion (hydrated ionic diameter = 0.12 nm, Vainshtein et al., 2000). Solutions of ferric chloride were prepared at various solute concentrations in 0.1N Hydrochloric acid. Acidic pH of the solutions prevents the formation of ferric hydroxide. Proton longitudinal and transverse relaxation of the solutions was measured at 2 MHz and 30°C.

Figure 4.1 shows the T_1 and T_2 relaxation rates of the aqueous solution of ferric ions as a function of the solution concentration. The relaxation rates of the solutions increase linearly with the concentration. Furthermore, the T_1/T_2 ratio is unity and no echo spacing dependence of the transverse relaxation is observed. T_1/T_2 ratio of unity suggests that the secular relaxation does not contribute significantly to the transverse relaxation for ferric ion solutions. This hypothesis is validated by the calculation of characteristic time scales shown in the interpretation section later.

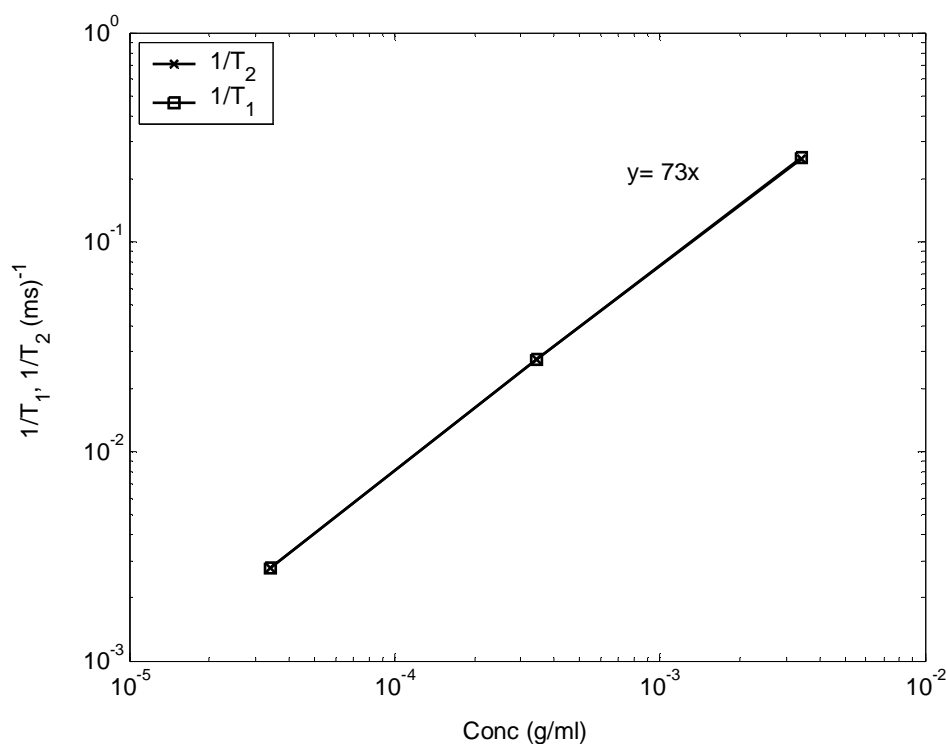


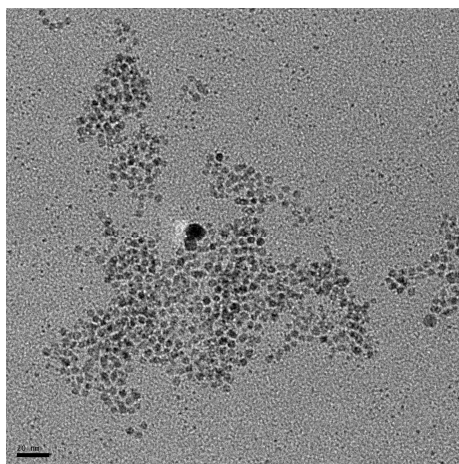
Figure 4.1: Longitudinal and transverse relaxation rates ($\tau_E = 0.2$ ms) of ferric chloride solutions as a function of the concentration of the solution. No echo spacing dependence of T_2 relaxation is observed and T_1/T_2 ratio is equal to unity.

4.1.2. Polymer-coated magnetite nanoparticles

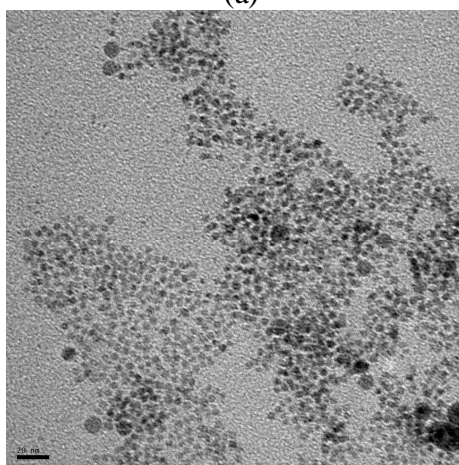
To explore a larger length scale of field inhomogeneity, NMR relaxation of the aqueous dispersions of magnetite nanoparticles was studied. Aqueous dispersions of

nanoparticles of various sizes were obtained from Dr. V.L. Colvin's Lab in Chemistry Department at Rice University. The nanoparticles were synthesized by the pyrolysis of iron carboxylate salts in an organic solvent and subsequently dispersing the nanoparticles in water (Yu et al., 2004). Particles were then coated with a layer of a polymer which prevents agglomeration of the particles in external magnetic field due to interparticle dipole attraction. The size of the particles was controlled by changing the time of reaction. Figure 4.2 shows the TEM images of 4 nm, 9 nm and 16 nm magnetite particles (Agarwal, 2007) used in this study. The hydrodynamic diameters of the particles, measured using dynamic light scattering, are equal to 10 nm, 12 nm and 22 nm respectively.

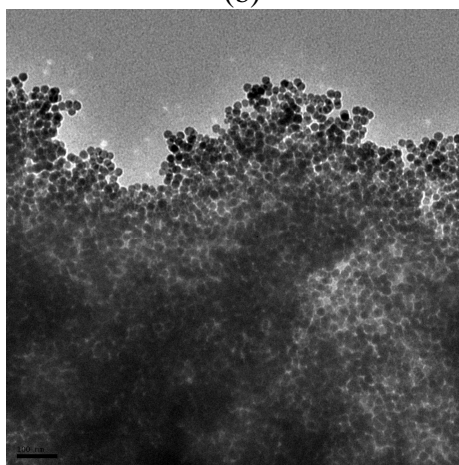
Proton relaxation rates of the aqueous dispersions were measured as a function of the concentration of the dispersion. Figure 4.3 shows the plots of longitudinal, transverse and secular relaxation rates with the concentration of the dispersion for the three particle sizes. The solid lines are the linear best fits of the experimental points. The relaxation rates increase linearly with the concentration of the paramagnetic particles. In addition, T_2 relaxation rates are independent of the echo spacing. This lack of echo spacing dependence is illustrated in Figure 4.4 which shows the T_1 and T_2 distributions of the dispersions at approximately same concentration ($C \sim 5 \cdot 10^{-5}$ g/ml) for the three particle sizes. Corresponding distributions for the ferric ion ($D_p = 0.12$ nm) solution are also shown for comparison. T_2 distributions with $\tau_E = 0.2$ ms and 2 ms overlay on each other for all cases. In contrast to the ferric ion solution however, the T_1/T_2 ratio for magnetite dispersions is greater than one and increase monotonically with the particle size (Figure 4.5).



(a)



(b)



(c)

Figure 4.2: TEM images of magnetite nanoparticles. (a) 4 nm magnetite (b) 9 nm magnetite (c) 16 nm magnetite (Agarwal, 2007).

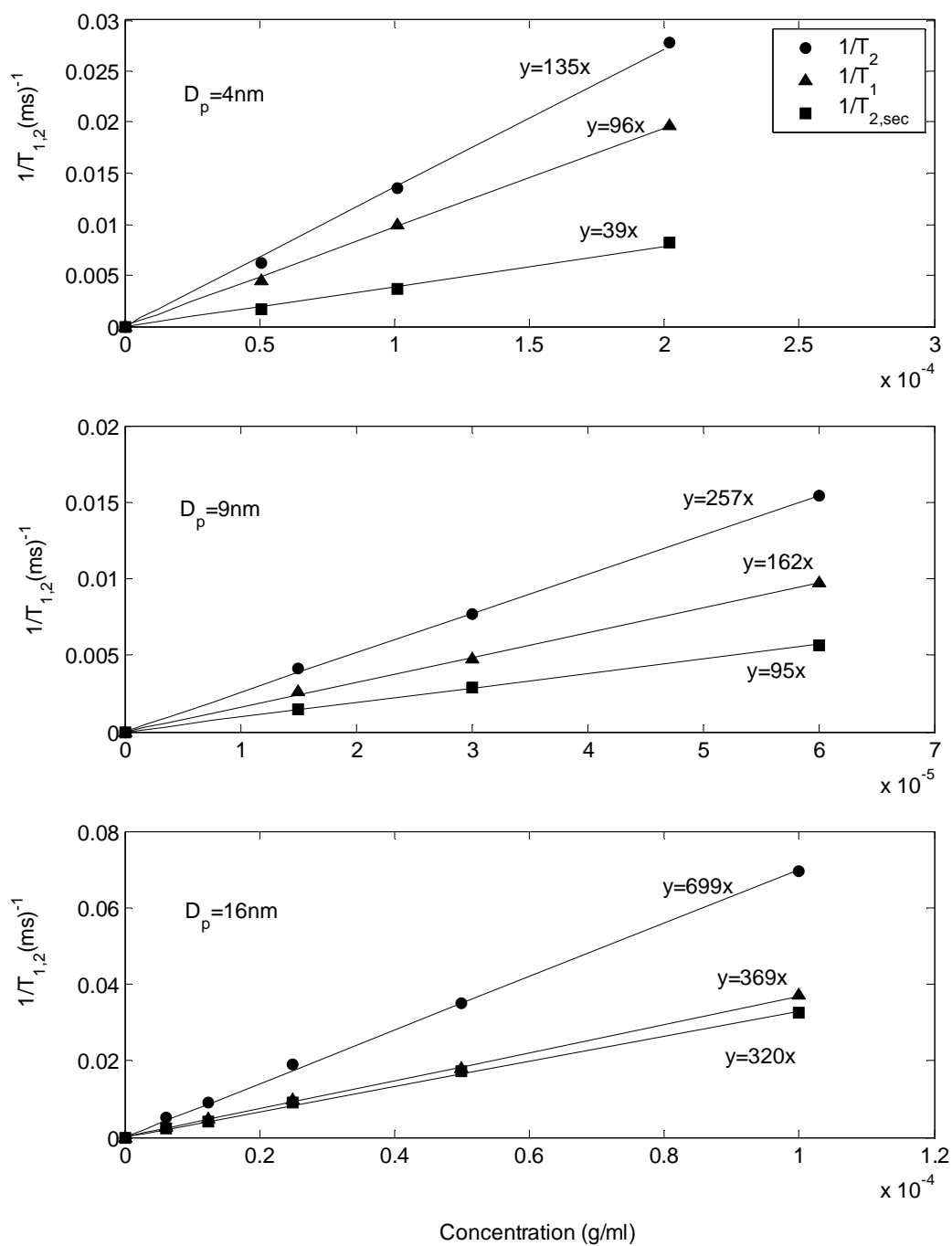


Figure 4.3: Plots of transverse, longitudinal and secular relaxation rates with the concentration of aqueous dispersions of polymer-coated nanoparticles of three different sizes. The average diameter of the nanoparticles (D_p) and slopes of the linear best fits are also mentioned.

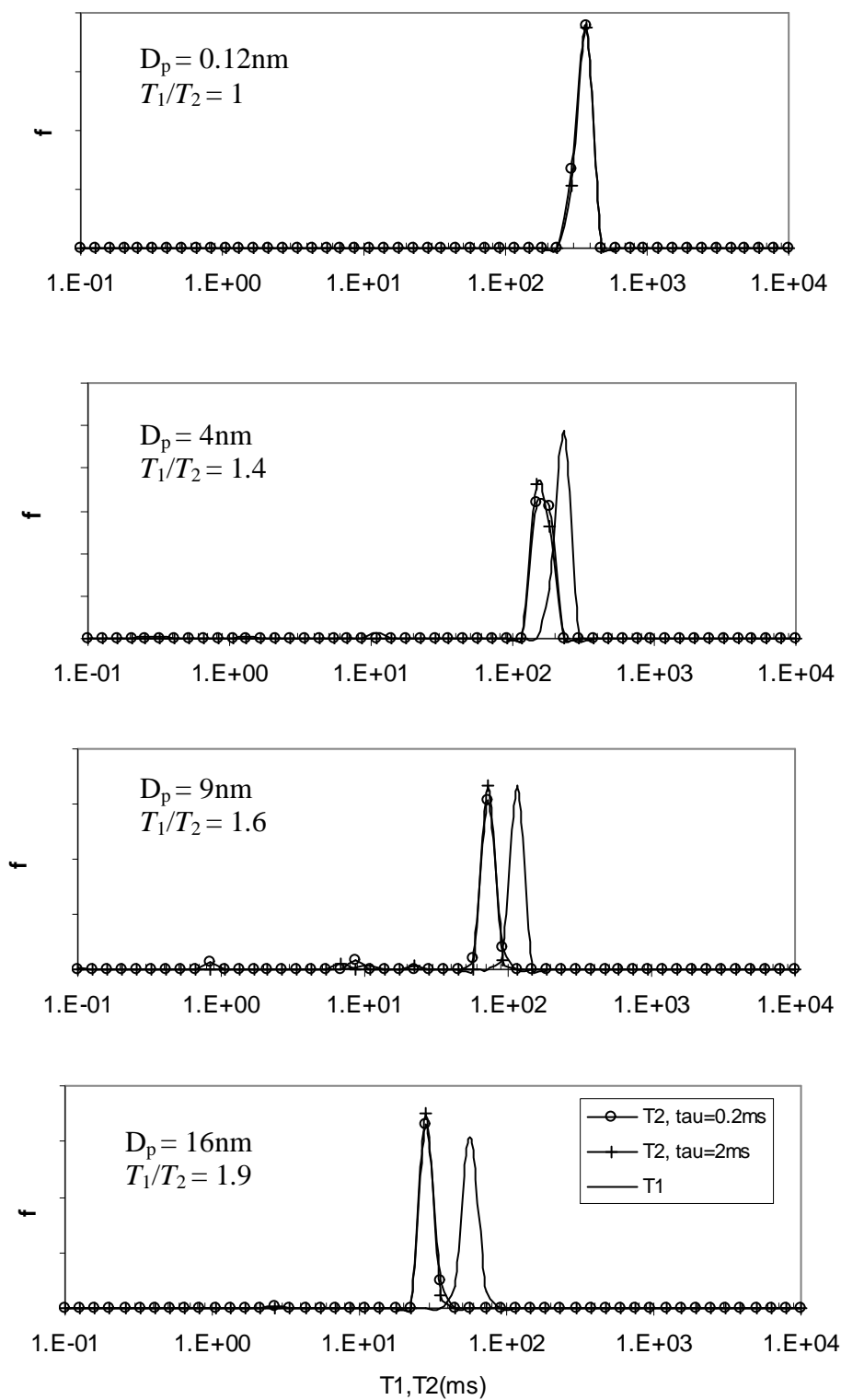


Figure 4.4: T_1 and T_2 distributions of aqueous dispersions of ferric ions and polymer coated magnetite nanoparticles. The T_2 distributions are independent of the echo spacing and T_1/T_2 ratio increases with the particle size.

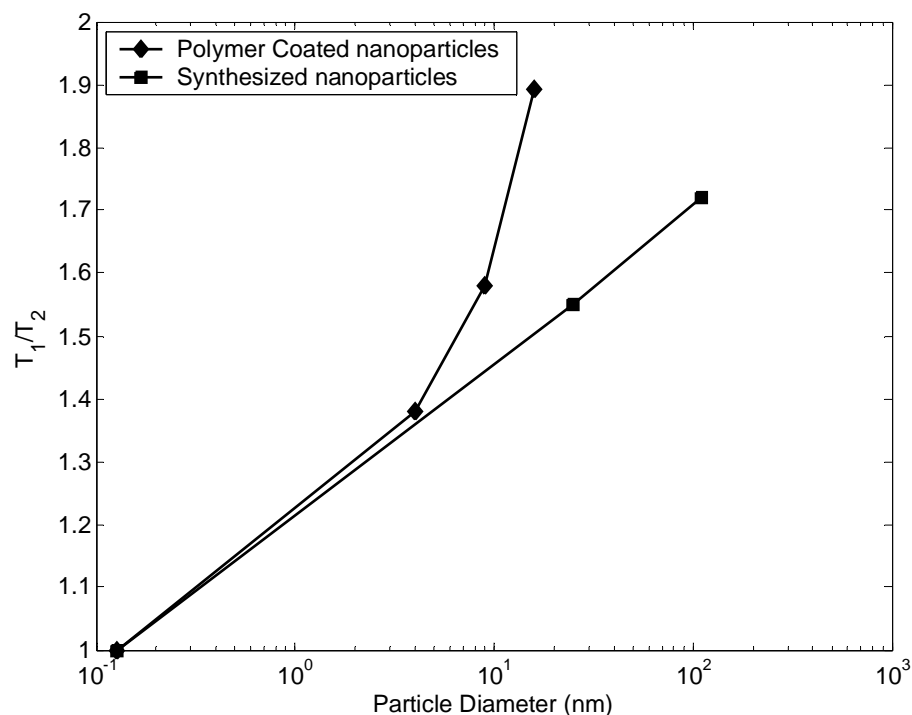


Figure 4.5: T_1/T_2 ratio of the aqueous dispersions of paramagnetic particles as a function of the particle size. The T_1/T_2 ratio increases with the particle size in the motionally averaging regime.

4.1.3. Magnetite nanoparticles coated with citrate ion

Positively charged magnetite nanoparticles of different sizes were synthesized in aqueous medium using Massart's Method (1981). The aim of synthesizing positively charged nanoparticles is to adsorb them on the negatively charged silica surface by coulombic attraction. Thus, relaxation characteristics of model sandstones with paramagnetic particles adsorbed at different concentrations can be studied. This is not possible for polymer-coated nanoparticles since the coating on the particles prevents them from adsorbing on the sand surface.

The following experimental procedure was used to synthesize aqueous dispersions of magnetite nanoparticles. Ammonia solution was added dropwise to an aqueous mixture of ferrous and ferric chloride till a gelatinous precipitate (magnetite) was obtained. The precipitated magnetite was washed with Perchloric acid which makes the particles positively charged due to surface adsorption of protons. The charged particles can then be peptized in excess of water (Massart, 1981). The size of the particles can be controlled by changing the temperature of the reaction. At higher temperature, larger sized particles were obtained due to Oswald ripening. Figure 4.6 shows the particle size distribution obtained by dynamic light scattering for two dispersions of nanoparticles. The average diameters of the particles for the two dispersions are 25 nm and 110 nm respectively. The 25 nm particles were synthesized at 10°C while 110 nm particles were synthesized at room temperature.

In absence of an external magnetic field, the positive charge of the particles prevents them from agglomeration due to interparticle dipole attractions. However, the weak columbic repulsion is not sufficient to prevent agglomeration in presence of the external field. Thus, the nanoparticles were stabilized by adding 1M Sodium Citrate in the volume ratio of 1%. Strong steric and columbic repulsion between the citrate-coated particles prevents them from agglomeration.

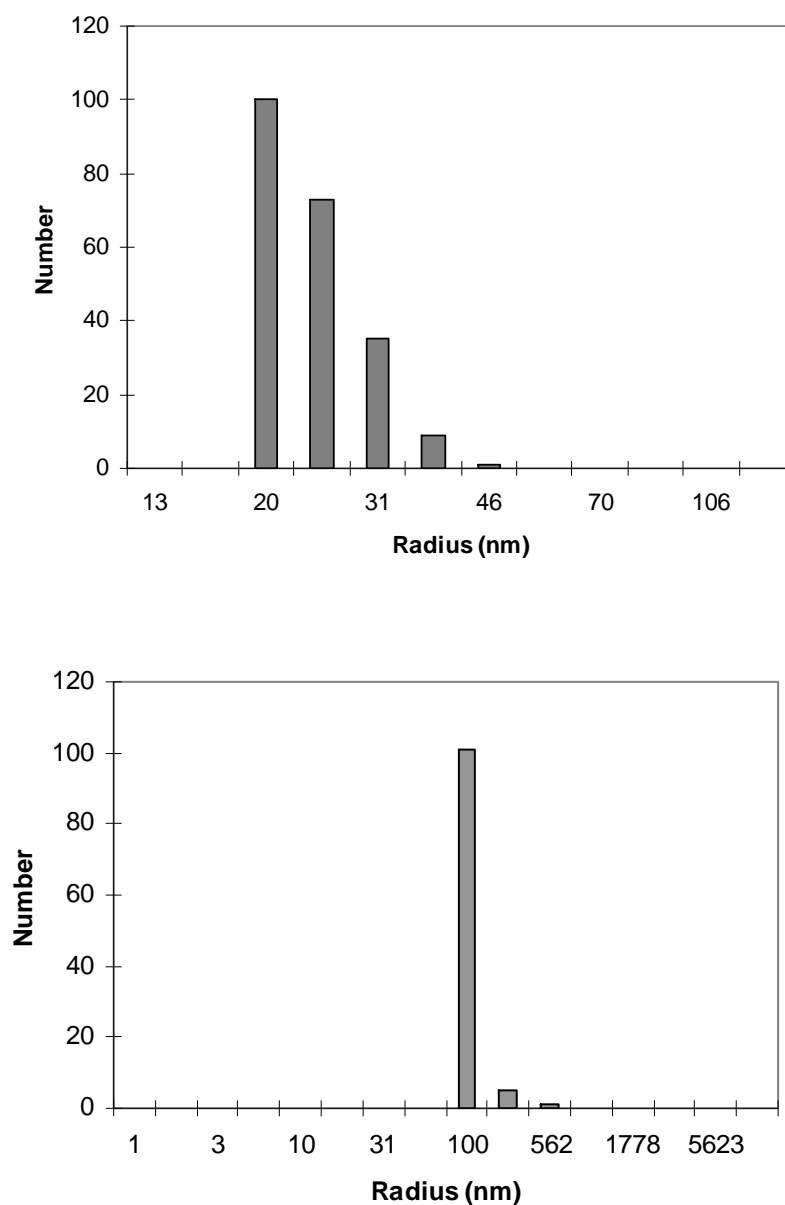


Figure 4.6: Particle size distribution of magnetite dispersions synthesized using Massart's method (1981). The average diameters of the particles are 25 nm (upper panel) and 110 nm (lower panel) respectively.

Proton relaxation rates of aqueous dispersions of the citrate-coated particles were measured as a function of the concentration. Figure 4.7 shows the plots of the longitudinal, transverse and secular relaxation rates with the concentration of the dispersion for the two particle sizes. The linear best fits of the experimental points and the corresponding slopes are also shown. Figure 4.8 shows the T_1 and T_2 distributions of

the dispersions of the nanoparticles at similar concentrations ($C \sim 5 \cdot 10^{-4}$ g/ml). T_2 distributions are shown as a function of the echo spacing. For comparison, the T_1 and T_2 distributions of ferric ion solution of similar concentration is also shown. The results are comparable to those for the aqueous dispersions of polymer-coated magnetite (Figures 4.3 and 4.4). Relaxation rates are linearly dependent on the concentration of the dispersion and no echo spacing dependence of T_2 relaxation rates is observed. Additionally, the T_1/T_2 ratio of magnetite dispersions is greater than one and increases with the particle size (Figure 4.5). NMR experiments with nanoparticles adsorbed on sand surface are detailed in a later section.

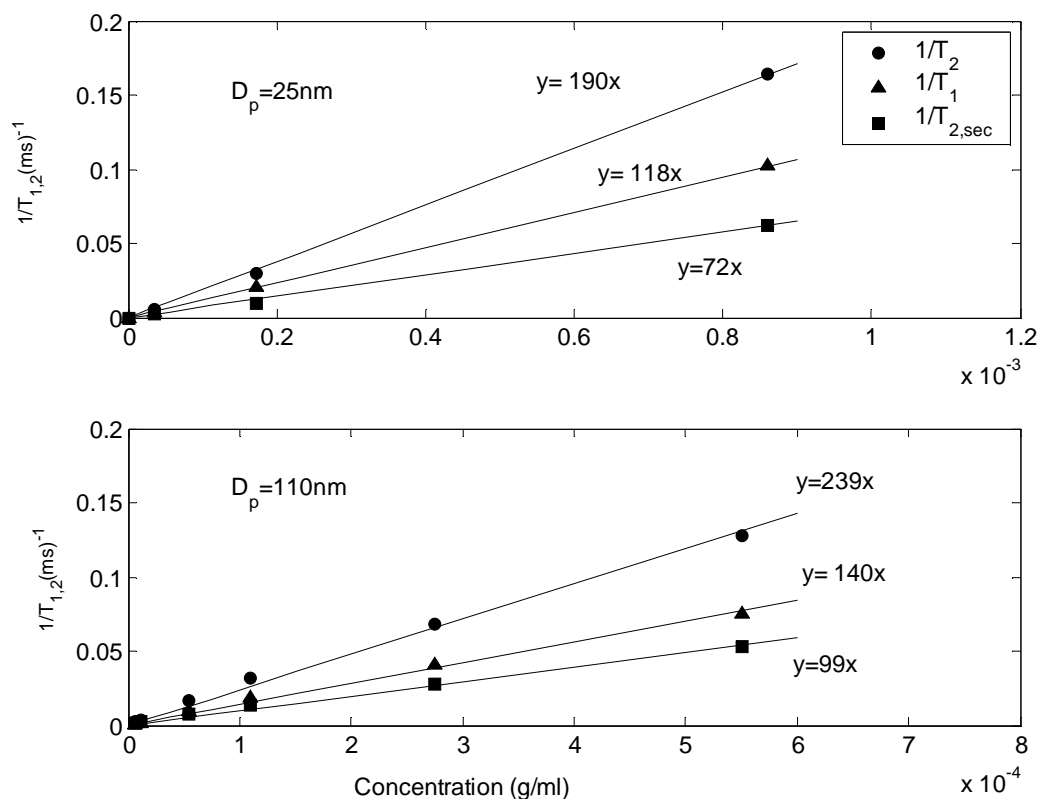


Figure 4.7: Plots of transverse, longitudinal and secular relaxation rates with the concentration of aqueous dispersions of magnetite nanoparticles synthesized using Massart's Method (1981). The average diameters of the nanoparticles (D_p) and slopes of the linear best fits are also mentioned.

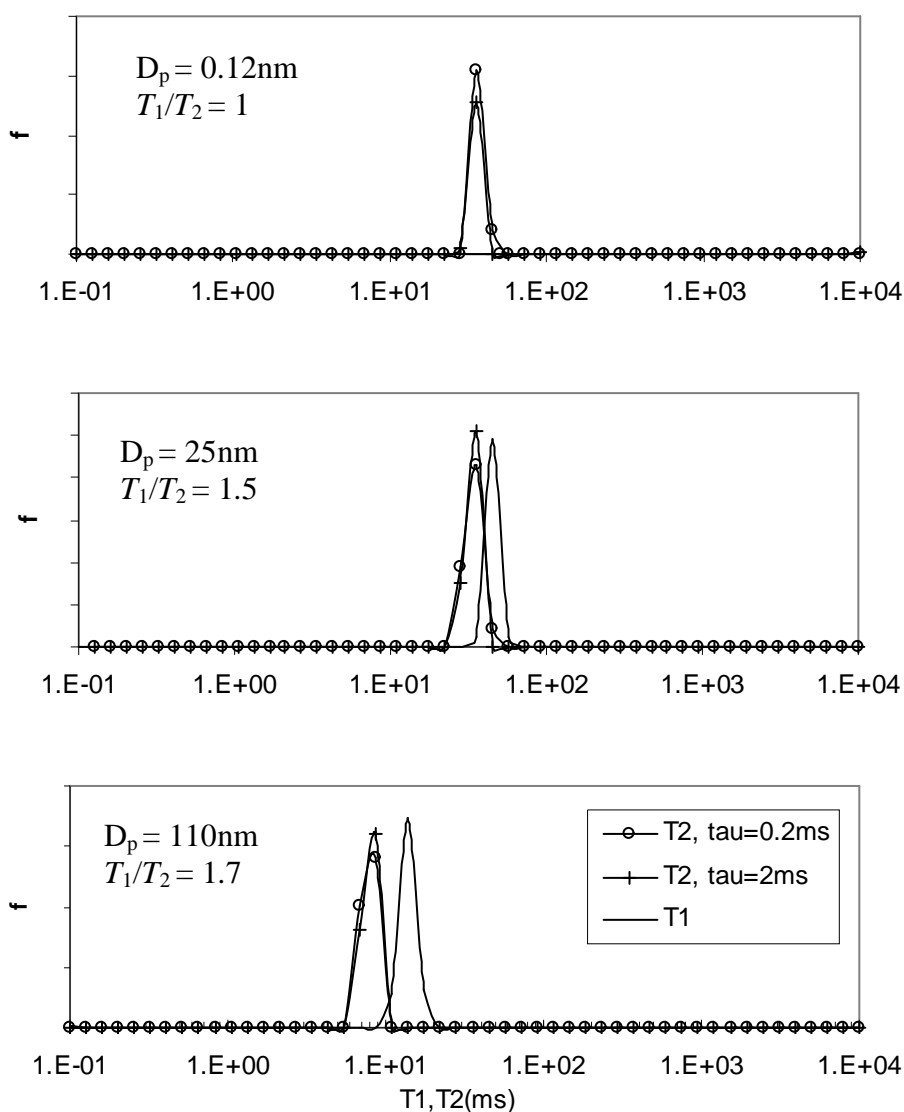


Figure 4.8: T_1 and T_2 distributions of aqueous dispersions of ferric ions and citrate coated magnetite nanoparticles. The T_2 distributions are independent of the echo spacing and T_1/T_2 ratio increases with the particle size.

4.1.4. Characteristic time scales for paramagnetic particles in dispersion

As was described in Chapter 3, secular relaxation can be characterized by three regimes depending on the smallest characteristic time scale. In motionally averaging regime, secular relaxation rate is independent of the echo spacing and increases with the particle size and concentration (Equation 3.20). Similar relaxation characteristics are also

observed for aqueous dispersions of submicron paramagnetic particles. No echo spacing of transverse relaxation is observed and the T_1/T_2 ratio increases with the particle size. Thus, it can be hypothesized that proton relaxation in aqueous dispersions of (submicron) paramagnetic particles experiences motionally averaging regime.

To prove the validity of the hypothesis, the characteristic time scales ($\tau_E, \tau_R, \tau_\omega$) need to be quantitatively evaluated. The value of half echo spacing (τ_E) is known from the experimental measurements. In this study, the smallest half echo spacing used was 0.2 ms. The diffusional correlation time (τ_R) can be calculated from the radius of the paramagnetic particle (R_0) and diffusivity of water at 30°C ($\sim 2.5 \cdot 10^{-5}$ cm²/sec) by using Equation (3.15). Under the assumption of motionally averaging regime, the expression for the secular relaxation rate (Equation 3.20) can be used to estimate $\delta\omega$ for the magnetite nanoparticles as shown below.

$$\frac{1}{T_{2,\text{sec}}} = \frac{4}{9} \Phi \overline{\delta\omega^2} \tau_R = \frac{16}{405} \Phi \delta\omega^2 \tau_R \quad (4.1)$$

$$\Rightarrow \frac{1}{T_{2,\text{sec}}} = \frac{16\delta\omega^2 \tau_R}{405d} C \quad (4.2)$$

Here C is the concentration of the dispersion, and d is magnetite density. Equation (4.2) shows that the slope (s) between secular relaxation rate and the concentration is proportional to $\delta\omega^2$. Thus, $\delta\omega$ for the various particle sizes can be evaluated from the slopes of the plots shown in Figures 4.3 and 4.6 as

$$\delta\omega = \sqrt{\frac{405sdD}{16R_0^2}} \quad (4.3)$$

τ_ω is obtained as the reciprocal of $\delta\omega$. Table 4.1 lists the characteristic time scales for the different particles. For all cases, $\tau_R < \tau_\omega$ and $\tau_R < \tau_E$ (except for 110 nm particle for which $\tau_R \sim \tau_\omega$) and thus, the earlier hypothesis of motionally averaging regime is justified. (Note that the characteristic time scales for polymer-coated nanoparticles are based on the hydrodynamic diameters mentioned earlier. For ferric ions, $\delta\omega$ is calculated from Equation (3.14) using $\chi_{\text{Fe}^{3+}} = 0.00046$ (Rosensweig, 1985) and $\gamma B_0 = 2$ MHz)

Table 4.1: Characteristic Time scales for the ferric ions and magnetite nanoparticles.

Time Scale (sec)	0.12 nm Fe ³⁺	4 nm Polymer coated	9 nm Polymer coated	16 nm Polymer coated	25 nm Citrate Stabilized	110 nm Citrate Stabilized
τ_R	$3 \cdot 10^{-11}$	$1 \cdot 10^{-8}$	$1.5 \cdot 10^{-8}$	$5 \cdot 10^{-8}$	$6 \cdot 10^{-8}$	10^{-6}
$\tau_{E,\text{minimum}}$	$2 \cdot 10^{-4}$	$2 \cdot 10^{-4}$	$2 \cdot 10^{-4}$	$2 \cdot 10^{-4}$	$2 \cdot 10^{-4}$	$2 \cdot 10^{-4}$
τ_ω	$2 \cdot 10^{-4}$	$8 \cdot 10^{-8}$	$6 \cdot 10^{-8}$	$6 \cdot 10^{-8}$	$8 \cdot 10^{-8}$	$3 \cdot 10^{-7}$

The condition $\tau_R < \tau_E$ implies that the magnetic field inhomogeneities are motionally averaged in time much shorter than τ_E . Thus, no dependence of T_2 relaxation on echo spacing is observed for the aqueous dispersions of ferric ions and magnetite nanoparticles. Additionally, secular relaxation rate is proportional to the square of the radius of the paramagnetic particle in motionally averaging regime (Equation 3.20). Due to very small size of the ferric ion, secular relaxation contributes negligibly to the transverse relaxation and thus, the T_1/T_2 ratio of ferric solutions is unity. Secular relaxation however, increases for the larger particles and contributes significantly to the

T_2 relaxation. Thus, the T_1/T_2 ratio of magnetite dispersions increases with the particle size as observed in Figure 4.5. The larger T_1/T_2 ratio for the polymer-coated nanoparticles is probably due to higher magnetic moment. The characteristic time scales help to quantitatively understand the asymptotic regimes in model sandstones described in the next section.

4.2. Paramagnetic particles on silica surface

NMR proton relaxation measurements with silica sand coated with paramagnetic particles are described in this section. Coated sand serves as a model to quantitatively understand the paramagnetic relaxation mechanisms in sandstones. Sand is coated with paramagnetic particles of various sizes and concentrations to illustrate the transition of the relaxation regimes with the length scale of field inhomogeneity.

4.2.1. Fine sand coated with ferric ions

The following experimental protocol was used to coat fine sand (Sigma Aldrich, grain radius 50 μm) with paramagnetic ferric ions. Fine sand was repeatedly washed with fresh batches of Hydrochloric acid to remove paramagnetic particles originally present on the grain surfaces. The sand was then washed with deionized water and dried. A known quantity of the dried sand was kept in contact with acidic (pH 1) solutions of ferric chloride of known concentrations for 24 hours in a plastic bottle. The solid to liquid ratio (gm sand/ml) of the slurries was kept at 1:10. Low pH ($\ll 7$) of the ferric solutions helps to prevent the precipitation of hydroxides on the sand surface. To ensure uniform coating, the slurries were constantly rotated which prevents the sand from settling at the bottom. After 24 hours, the supernatant was removed and the coated sand was repeatedly washed

with deionized water. This last step removes any remaining ferric ions in the pore liquid. Thus, the relaxation of the pore liquid can be attributed only to surface relaxation and diffusion in internal field gradients.

The surface concentration of the ferric ions can be estimated by measuring the quantity of ferric ions deposited on a known surface area of sand as described. BET surface area of sand ($0.2 \text{ m}^2/\text{g}$) was determined using N_2 adsorption at 77K. To estimate the deposited quantity of ferric ions, relaxation time of the supernatant was measured. Using the calibration between the concentration and relaxation rate of ferric chloride solution (Figure 4.1), the concentration of the supernatant can be determined. The difference in the concentration of the supernatant and the original coating solution multiplied by the volume of the solution gives the quantity of ferric ions deposited on the sand surface.

Figure 4.9 shows the T_1 and T_2 distributions of the sand coated with ferric ions at various surface concentrations expressed as surface area/ion. Table 4.2 lists the modes of the relaxation time distributions for the various cases. Both T_1 and T_2 relaxation times decrease as the surface concentration of Fe^{3+} ions increases. However, no echo spacing dependence of T_2 relaxation is observed and the T_1/T_2 ratio of coated sand is close to that of washed sand at all concentrations. Two important conclusions can be deduced from these observations:

1. Surface relaxation increases as the concentration of ferric ions on silica surface increases as shown by the corresponding decrease in T_1 and T_2 relaxation times.

This conclusion is also consistent with the observations that longitudinal and

transverse relaxivities of porous media increase with concentration of paramagnetic particles on pore surfaces (Foley et al., 1996, Chen et al., 2005).

2. T_2 relaxation due to dephasing in inhomogeneous field induced by Fe^{3+} ions is negligible. Secular relaxation is proportional to the square of the size of paramagnetic particle in motionally averaging regime (valid for Fe^{3+} , Table 4.1) and is negligible for angstrom size ferric ions.

These conclusions are however, contingent on the condition that paramagnetic particles are present in dilute surface concentrations. Kenyon et al. (1994) showed that surface relaxivities obtain asymptotic values at high concentration of paramagnetic particles. Similarly, secular relaxation can become significant at high concentration of particles due to superposition of fields induced by individual particles. The latter claim is experimentally validated for sand coated with magnetite nanoparticles shown in the next section.

Table 4.2: Longitudinal and transverse relaxation times of water-saturated fine sand coated with ferric ions at different surface concentrations (area/ferric ion).

Relaxation Time (ms)	Washed sand	$0.03\text{nm}^2/\text{Fe}^{3+}$	$0.09\text{nm}^2/\text{Fe}^{3+}$	$0.3\text{nm}^2/\text{Fe}^{3+}$
T_1	1587	294	372	471
T_2 ($\tau_E=0.2\text{ms}$)	1260	233	294	378
T_2 ($\tau_E=1\text{ms}$)	1260	233	294	378
T_1/T_2	1.26	1.26	1.26	1.25

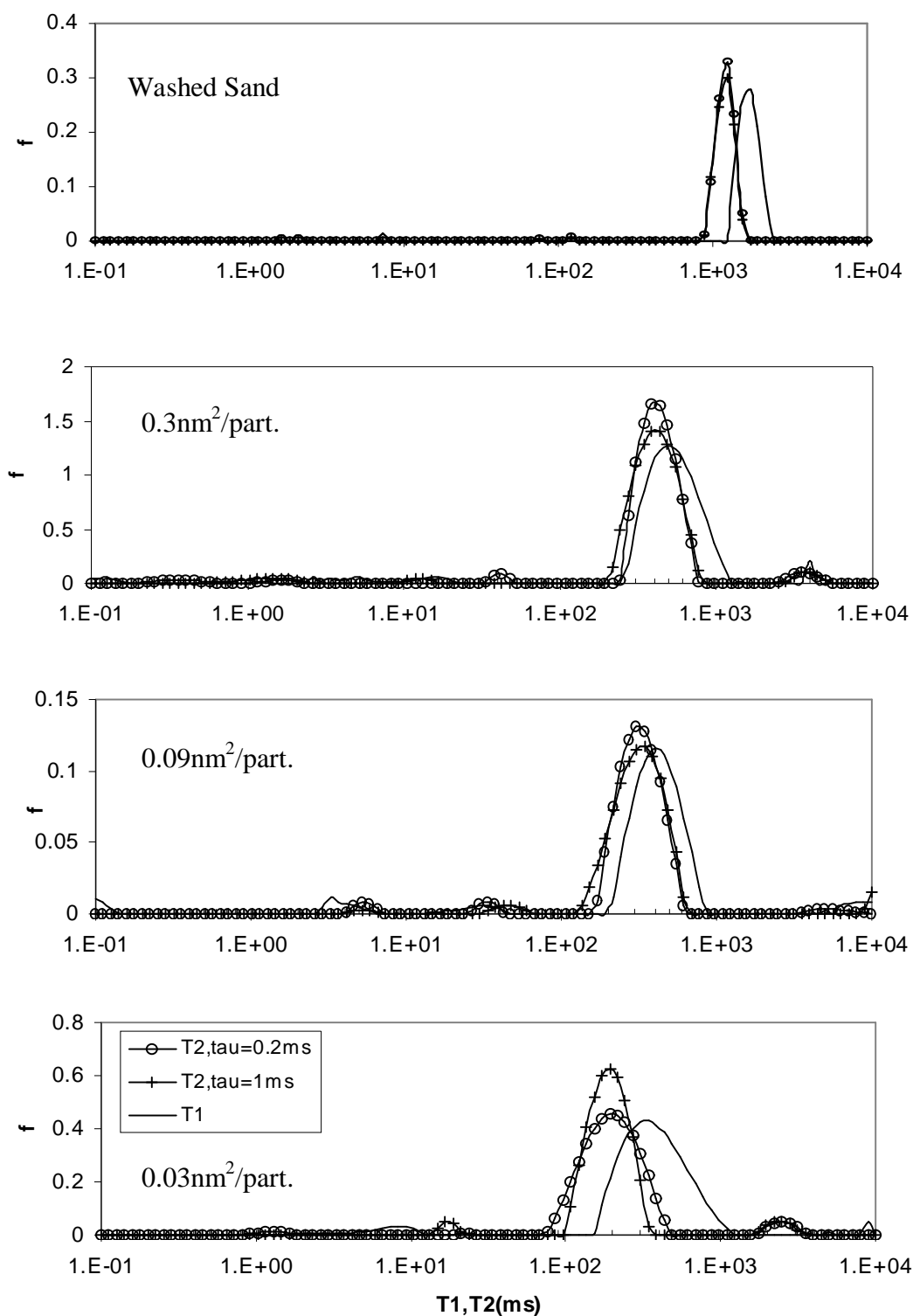


Figure 4.9: T_1 and T_2 distributions of fine sand coated with ferric ions at different surface concentrations.

4.2.2. Fine sand coated with magnetite nanoparticles

Known quantity of fine sand was coated with positively charged 25 nm and 110 nm magnetite particles by following the same procedure as that used for coating ferric ions. The concentrations of the coating dispersions were varied to obtain different surface concentrations of magnetite. Note that the coating is done with positively charged magnetite *not* coated with citrate ion. Figures 4.10 and 4.11 show T_1 and T_2 distributions of water-saturated fine sand coated with 25 nm and 110 nm magnetite at different surface concentrations. The modes of the relaxation time distributions for the different cases are listed in Tables 4.3 and 4.4.

At low surface concentrations of either 25 nm or 110 nm particles no echo spacing dependence of T_2 relaxation is observed. At high concentrations however, echo spacing dependence of T_2 relaxation is observed for both cases. This transition in echo spacing dependence can be understood in terms of the length scales of field inhomogeneity. Figure 3.4 shows that at low concentration, field inhomogeneity extends to length scale comparable to the size of paramagnetic particles. Thus, for submicron paramagnetic particles, field inhomogeneities are motionally averaged in time much smaller than τ_E ($\tau_R < \tau_E$, Table 4.1) and T_2 relaxation shows no echo spacing dependence. At high concentrations, the particles form a shell around silica grains such that the length scale of field inhomogeneity is comparable to the grain size (Figure 3.5). Due to large size of the substrate silica grain, field inhomogeneities are *not* motionally averaged and hence, echo spacing dependence of T_2 relaxation is observed. A quantitative calculation of the characteristic time scales is shown in the interpretation section to corroborate these assertions.

Table 4.3: Longitudinal and transverse relaxation times of water-saturated fine sand coated with 25 nm magnetite at different surface concentrations.

Concentration (Area/particle)	$3 \cdot 10^3 \text{ nm}^2/\text{part.}$	$7 \cdot 10^3 \text{ nm}^2/\text{part.}$	$10^4 \text{ nm}^2/\text{part.}$	$9 \cdot 10^4 \text{ nm}^2/\text{part.}$
T_1	22	24	42	343
T_2 ($\tau_E = 0.2\text{ms}$)	15	19	29	215
T_2 ($\tau_E = 0.5\text{ms}$)	11	16	29	215
T_2 ($\tau_E = 1\text{ms}$)	9	14	29	215
T_2 ($\tau_E = 2\text{ms}$)	5	9	29	215
T_1/T_2	1.47-4.4	1.3-2.6	1.45	1.6

Table 4.4: Longitudinal and transverse relaxation times of water-saturated fine sand coated with 110 nm magnetite at different surface concentrations.

Concentration (Area/particle)	$3 \cdot 10^5 \text{ nm}^2/\text{part.}$	$1.5 \cdot 10^6 \text{ nm}^2/\text{part.}$	$8 \cdot 10^6 \text{ nm}^2/\text{part.}$	$3 \cdot 10^7 \text{ nm}^2/\text{part.}$
T_1	24	38	95	613
T_2 ($\tau_E = 0.2\text{ms}$)	21	36	63	385
T_2 ($\tau_E = 0.5\text{ms}$)	20	30	63	385
T_2 ($\tau_E = 1\text{ms}$)	17	23	63	385
T_2 ($\tau_E = 2\text{ms}$)	14	21	63	385
T_1/T_2	1.2-1.7	1.2-1.8	1.50	1.60

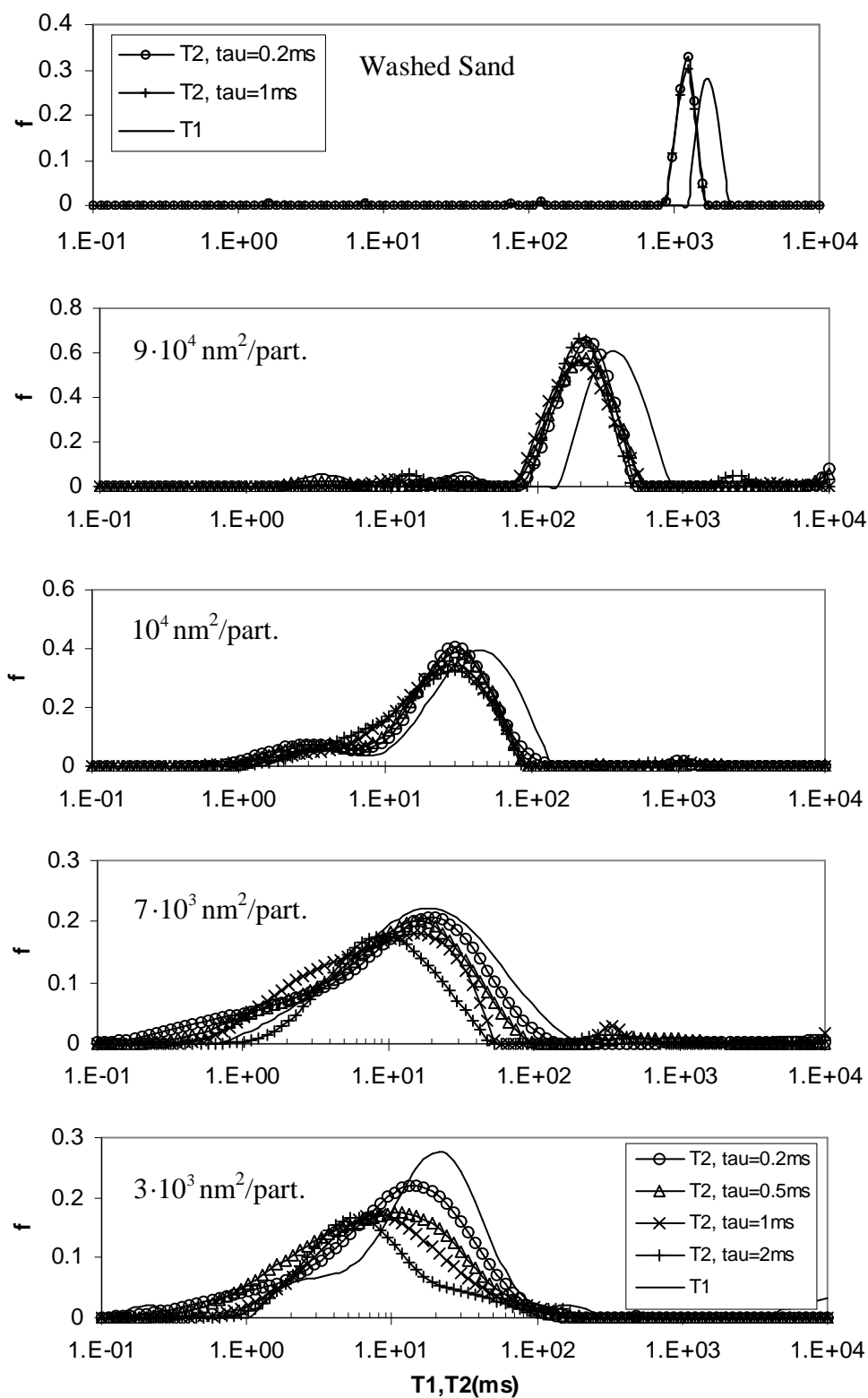


Figure 4.10: T_1 and T_2 distribution of water-saturated fine sand coated with 25 nm magnetite nanoparticles at various concentrations.

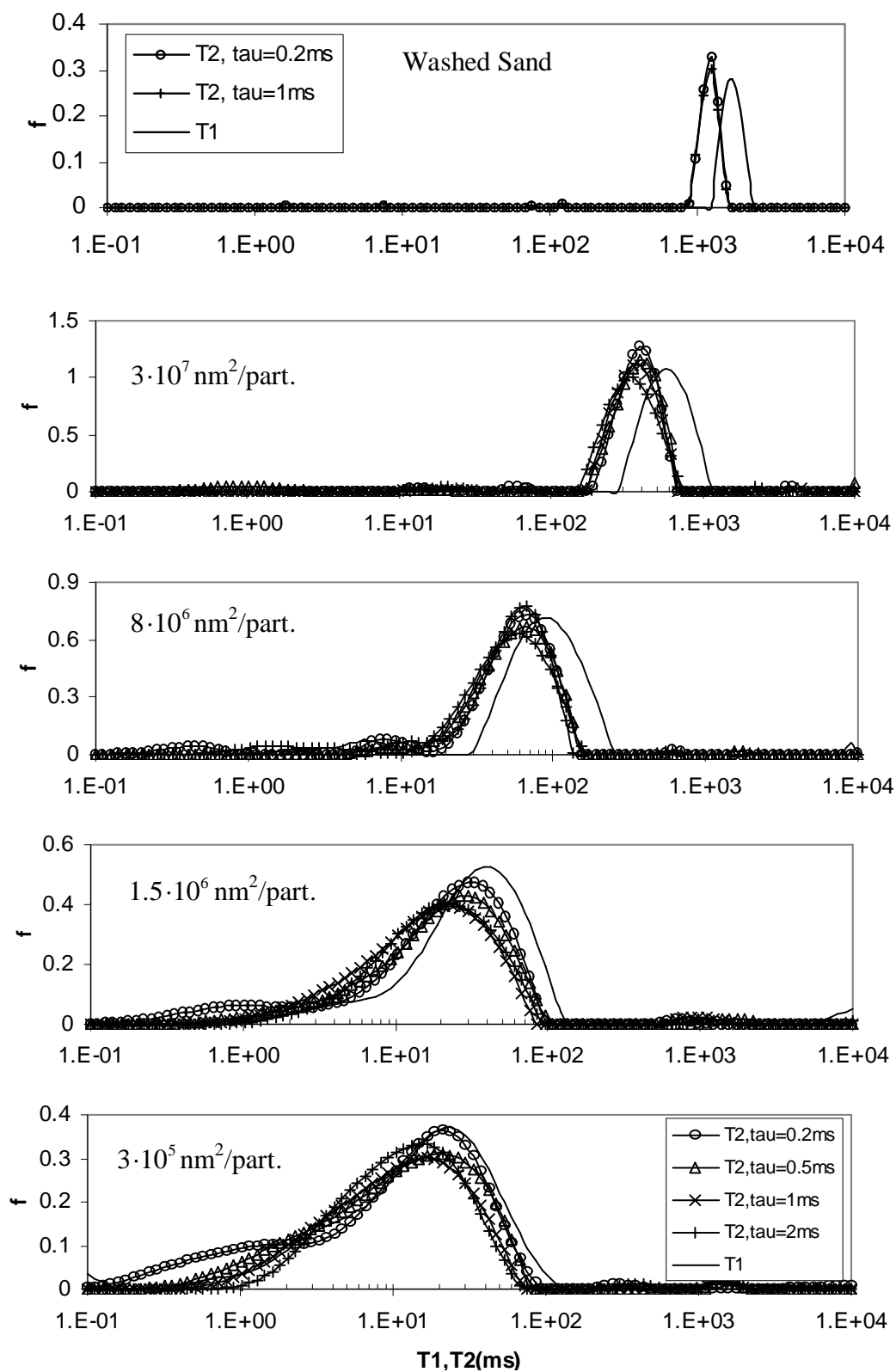


Figure 4.11: T_1 and T_2 distribution of water-saturated fine sand coated with 110 nm magnetite nanoparticles at various concentrations.

4.2.3. Fine sand with dispersed 2.4 μm magnetite

The length scale of field inhomogeneity can also be increased by increasing the size of the paramagnetic particle. Fine sand was dispersed with 2.4 μm magnetite (Fischer Scientific) dispersions of known concentrations. Figure 4.12 shows the T_1 and T_2 distribution of water-saturated fine sand with dispersed 2.4 μm magnetite at two concentrations. The corresponding modes of the relaxation time distributions for the two cases are listed in Table 4.5. A strong dependence of transverse relaxation on echo spacing is observed and the T_1/T_2 ratio is greater than 2. These observations are expected since the field inhomogeneity for micron size particles is not motionally averaged in the time for echo formation.

Table 4.5: Longitudinal and transverse relaxation times of water-saturated fine sand with dispersed 2.4 μm magnetite.

Concentration (Area/particle)	$9 \cdot 10^{13} \text{ nm}^2/\text{part.}$	$3 \cdot 10^{14} \text{ nm}^2/\text{part.}$
T_1	272	486
T_2 ($\tau_E = 0.2\text{ms}$)	76	215
T_2 ($\tau_E = 0.5\text{ms}$)	48	171
T_2 ($\tau_E = 1\text{ms}$)	38	135
T_2 ($\tau_E = 2\text{ms}$)	21	105
T_1/T_2	3.6-13	2.3-4.6

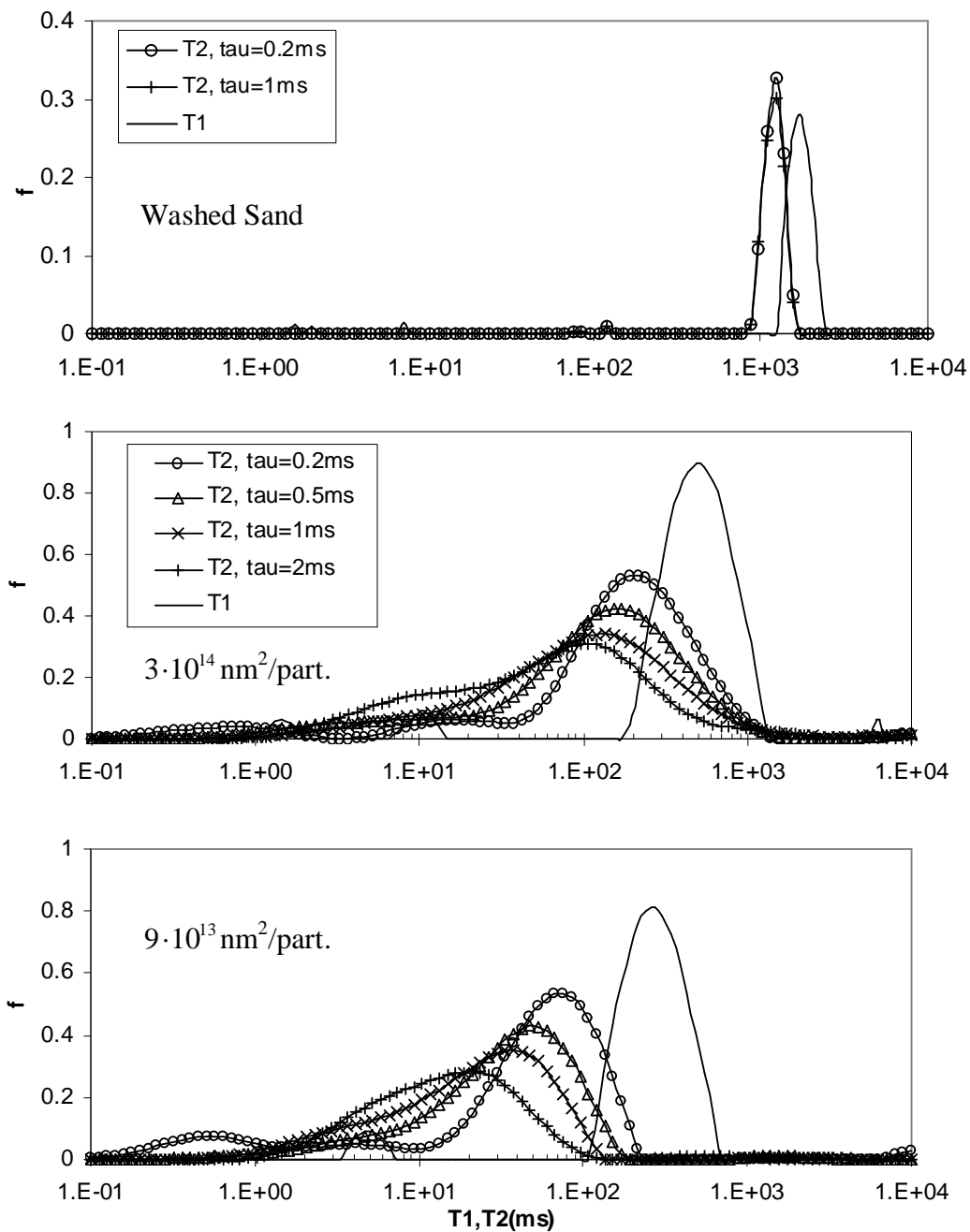


Figure 4.12: T_1 and T_2 distributions of fine sand with dispersed $2.4 \mu\text{m}$ magnetite at two concentrations. A large T_1/T_2 ratio and echo spacing dependence of transverse relaxation is observed.

4.2.4. Coarse sand coated with magnetite nanoparticles

Another set of NMR experiments were performed with coarse sand (Ottawa Sand 20/40 mesh) coated with magnetite nanoparticles. At high surface concentration of paramagnetic particles, the range of Larmor frequencies ($\delta\omega_{\text{shell}}$) varies inversely with the radius of the substrate silica grain (Equation 3.33). Thus, the transition of relaxation regimes can also be quantitatively studied by changing the size of the silica grain.

Coarse sand was washed with Hydrochloric acid to remove any originally present paramagnetic minerals. Washed sand was then coated with 25 nm magnetite particles by following the same procedure as that used for coating fine sand. Figure 4.13 shows the T_1 and T_2 distributions of water-saturated coarse sand coated with 25 nm magnetite at different surface concentrations. Table 4.6 lists the modes of the corresponding relaxation time distributions for the different cases. The distributions show similar characteristics as that observed for coated fine sand. At the lowest concentration ($4 \cdot 10^3 \text{ nm}^2/\text{particle}$), no echo spacing dependence of the transverse relaxation is observed. However, at high concentration ($7 \cdot 10^2 \text{ nm}^2/\text{particle}$), echo spacing dependence of the transverse relaxation is observed. These results suggest that the system transitions from the motionally averaging at low concentration to either the localization or the free diffusion regime at higher concentrations.

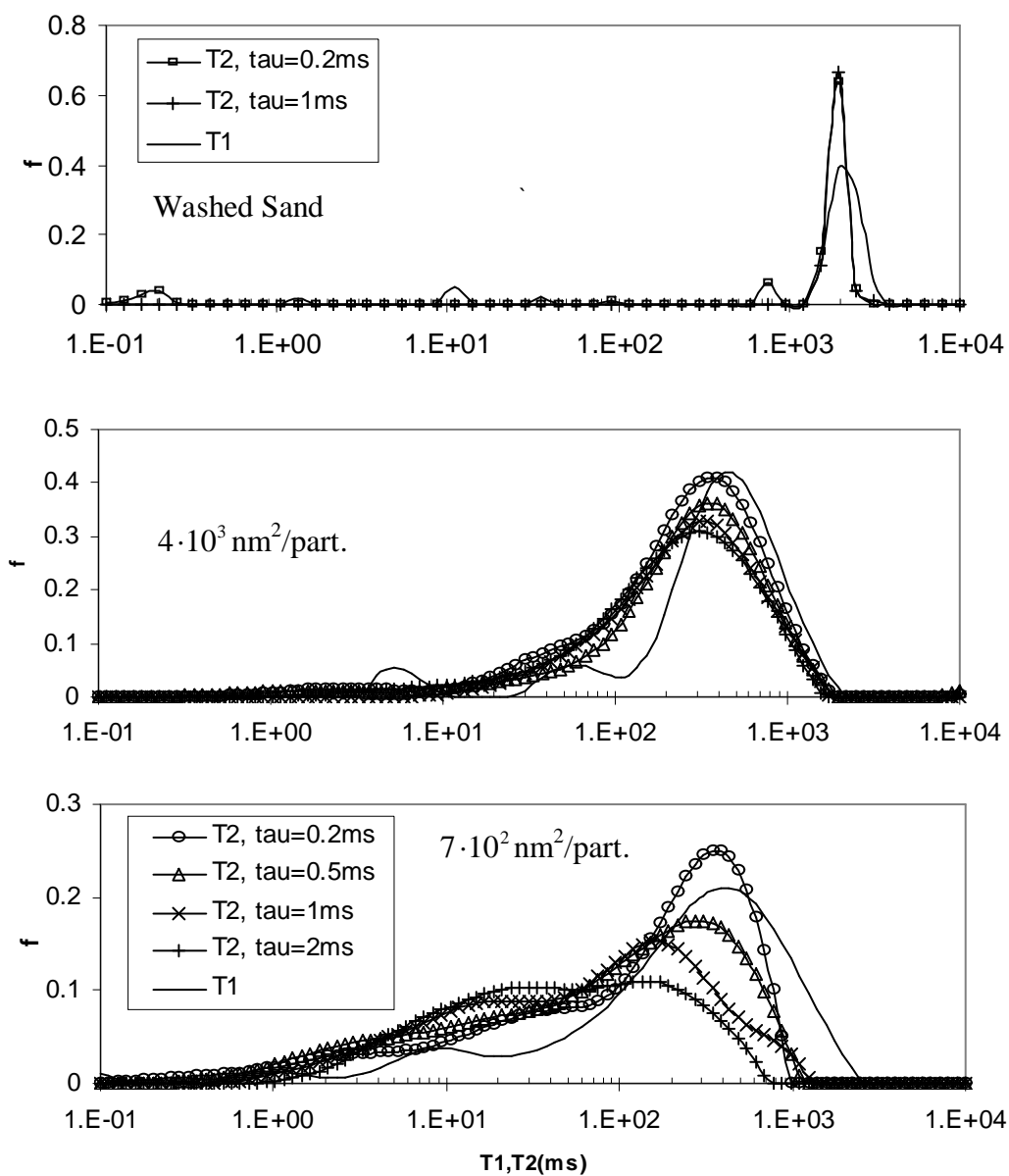


Figure 4.13: T_1 and T_2 distributions of coarse sand coated with 25 nm magnetite at different surface concentrations.

Table 4.6: Longitudinal and transverse relaxation times of water-saturated coarse sand coated with 25 nm magnetite at different surface concentrations

Concentration (Area/particle)	$7 \cdot 10^2 \text{ nm}^2/\text{part.}$	$4 \cdot 10^3 \text{ nm}^2/\text{part.}$
T_1	385	453
T_2 ($\tau_E = 0.2\text{ms}$)	364	303
T_2 ($\tau_E = 0.5\text{ms}$)	305	303
T_2 ($\tau_E = 1\text{ms}$)	171	303
T_2 ($\tau_E = 2\text{ms}$)	152	303
T_1/T_2	1.1-2.5	1.5

4.3. Paramagnetic relaxation in sandstones

The relaxation time distributions of model sandstones shown in Figures 4.9-4.13 illustrate the transition of asymptotic regimes with change in governing parameters such as the size and the concentration of paramagnetic particles. A quantitative interpretation of the experimental results in terms of the characteristic time scales and asymptotic regimes is explained below. The classification of the results in the asymptotic regimes also forms a basis for interpreting relaxation characteristics of real sandstones.

4.3.1 Motionally averaging regime

In motionally averaging regime, transverse relaxation is independent of the echo spacing since the field inhomogeneities are averaged in time much shorter than τ_E . This regime is experimentally observed for fine sand coated with ferric ions and for fine and coarse sand coated with 25 nm and 110 nm at low concentrations. For these cases, no echo spacing dependence of T_2 relaxation is observed and the T_1/T_2 ratio is higher than

that of washed sand (except for Fe^{3+} coated sand). At low surface concentrations, superposition of internal fields induced by individual particles is insignificant (Figure 3.4). Thus, protons in the pore fluid dephase as if diffusing in internal field induced by individual particles. Since τ_R is the smallest characteristic time for the submicron particles (Table 4.1), field inhomogeneities are motionally averaged and no echo spacing dependence is observed. The T_1/T_2 ratio is higher than that of washed sand due to additional contribution of the secular relaxation to T_2 relaxation.

These experimental results also explain the wide range of T_1/T_2 ratio in sandstones with no echo spacing dependence of T_2 relaxation (Kleinberg et al., 1993). In the motionally averaging regime, secular relaxation increases with the size and susceptibility of the paramagnetic particle (Equation 3.20). Thus, the presence of paramagnetic minerals of various sizes and susceptibilities on pore surfaces of sandstones can result in a range of T_1/T_2 ratio. Since the diffusional correlation time is much shorter than the time for echo formation in this regime, no echo spacing dependence of the T_2 relaxation would be observed. An important conclusion is that the lack of echo spacing dependence of the transverse relaxation does *not* necessarily imply that relaxation is not influenced by diffusion effects.

4.3.2. Free diffusion regime

Free diffusion regime of secular relaxation arises when half echo spacing is the shortest characteristic time compared to τ_R and τ_ω . The conditions for the free diffusion regime can be satisfied in sedimentary rocks at high surface concentration of paramagnetic particles on silica grains. At high surface concentrations, paramagnetic particles form a shell around silica grains such that the field inhomogeneity extends to

large distances proportional to the grain size (Figure 3.5). In addition, the range of Larmor frequencies is reduced (compared to that for a single particle) by a factor $3\varepsilon/R_g$ due to superposition of fields (Equation 3.33). Consequently, τ_R and τ_ω increase and may become larger than τ_E for appropriate system parameters.

Free diffusion regime is observed experimentally for fine sand coated with 110 nm magnetite and coarse sand coated with 25 nm magnetite at surface concentrations $1.5 \cdot 10^6 \text{ nm}^2/\text{particle}$ and $7 \cdot 10^2 \text{ nm}^2/\text{particle}$ respectively. Table 4.7 lists the characteristic time scales for the two cases. τ_ω is obtained from the reciprocal of $\delta\omega_{\text{shell}}$ (Equation 3.33) where the thickness of the shell is calculated such that the volume of the shell is the same as the total volume of particles deposited on a single silica grain. τ_R is calculated using Equation (3.5) where the length scale of inhomogeneity (L) is assumed to be the radius of the interstitial pore between silica grains (Equation 3.34).

Figure 4.14 shows the plot of secular relaxation rate (Equation 3.1) with τ_E for the two cases. The dashed vertical lines show the boundary $\delta\omega\tau_E = 1$ at which the systems transition from the free diffusion to the localization regime. The solid lines are the regression lines for the power-law fits in the two relaxation regimes. For both cases, the exponents of the power-law fits are close to 2 in the free diffusion regime and less than unity in the localization regime. Thus, the relaxation rates show quadratic dependence on echo spacing in the free diffusion regime and less than linear dependence in the localization regime. A change in slope is therefore observed as the systems transition from the free diffusion to the localization regime.

Table 4.7: Characteristic time scales for relaxation in coarse sand coated with 25nm ($7 \cdot 10^2 \text{ nm}^2/\text{particle}$) and fine sand coated with 110nm magnetite ($1.5 \cdot 10^6 \text{ nm}^2/\text{particle}$).

Time Scale (sec)	$7 \cdot 10^2 \text{ nm}^2/ 25 \text{ nm part.}$ Coarse Sand	$1.5 \cdot 10^6 \text{ nm}^2/110 \text{ nm part.}$ Fine Sand
τ_R	1.07	0.05
$\tau_{E,\text{minimum}}$	$2 \cdot 10^{-4}$	$2 \cdot 10^{-4}$
τ_ω	$9 \cdot 10^{-4}$	$1.3 \cdot 10^{-3}$

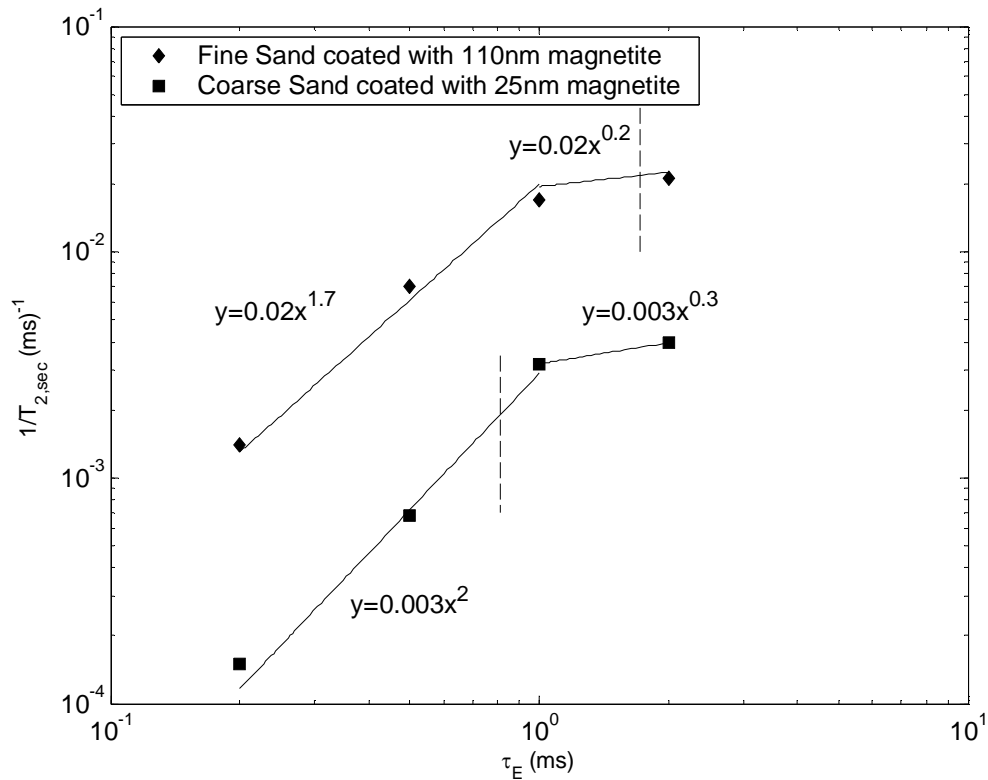


Figure 4.14: Plot of the secular relaxation rate of water-saturated coated sand with τ_E for cases in which free diffusion regime is observed. The surface concentrations are $1.5 \cdot 10^6 \text{ nm}^2/110 \text{ nm particle}$ (fine sand) and $7 \cdot 10^2 \text{ nm}^2/25 \text{ nm particle}$ (coarse sand) respectively. The vertical lines are the boundary $\delta\omega\tau_E = 1$ at which the two systems transition from free diffusion to localization regime. The solid lines are the regression lines for the power-law fits in the two relaxation regimes. Relaxation rates show almost quadratic dependence on echo spacing in the free diffusion regime and less than linear dependence in the localization regime.

4.3.3. Localization regime

Localization regime arises when time for significant dephasing (τ_ω) is the shortest characteristic time. This condition for the localization regime can also be satisfied at high surface concentrations of paramagnetic particles if the frequency range for the spherical shell is large such that τ_ω (reciprocal of $\delta\omega$) is small compared to τ_R and τ_E . This regime is experimentally observed for fine sand coated with 25 nm ($3 \cdot 10^3$ nm²/particle) and 110 nm ($3 \cdot 10^5$ nm²/particle) at the highest surface concentrations. Table 4.8 shows the characteristic time scales for the different cases. (Time scales τ_ω and τ_R are calculated using the same method as that used for the free diffusion regime). For both cases, the conditions for the localization regime ($\tau_\omega < \tau_R$ and $\tau_\omega < \tau_E$) are satisfied.

The localization regime can also be observed for relaxation in the presence of large paramagnetic particles with large diffusional correlation time. This is the case for relaxation in fine sand with dispersed 2.4 μm magnetite (Figure 4.12). The values of the characteristic times are mentioned in Table 4.9. ($\delta\omega$ is assumed to be same as that for 110 nm particles). The conditions for the localization regime are again satisfied and thus, echo spacing dependence of the transverse relaxation is observed.

Table 4.8: Characteristic time scales for relaxation in fine sand coated with 25 nm and 110 nm magnetite at high surface concentrations.

Time Scale (sec)	$3 \cdot 10^3 \text{ nm}^2/25 \text{ nm part.}$	$3 \cdot 10^5 \text{ nm}^2/110 \text{ nm part.}$
τ_R	0.05	0.05
$\tau_{E,\text{minimum}}$	$2 \cdot 10^{-4}$	$2 \cdot 10^{-4}$
τ_ω	$5.2 \cdot 10^{-5}$	$5 \cdot 10^{-5}$

Table 4.9: Characteristic time scales for relaxation in fine sand with dispersed 2.4 μm magnetite.

Time Scale (sec)	2.4 μm Magnetite
τ_R	$6 \cdot 10^{-4}$
$\tau_{E,\text{minimum}}$	$2 \cdot 10^{-4}$
τ_ω	$3 \cdot 10^{-7}$

An example of localization regime is transverse relaxation in North Burbank sandstone with macropores lined with chlorite clay flakes (Trantham and Clampitt, 1995). Zhang et al. (2003) modeled the gradients induced in a pore lined with clay flakes such that the flakes form micropores that open to a larger macropore. They found that large field gradients are concentrated around the sharp corners of the clay flakes and in the micropores between clay flakes. The gradients also extend considerably in the macropore although the strength is not as high as in the micropores. Fluid molecules in the micropores and macropores are, however, coupled by diffusion (Chapter 2). Thus, in general, the molecules experience gradients that are intermediate to those in the micro and macropores. Figure 4.15 shows the T_1 and T_2 distributions of two water-saturated North Burbank sandstone cores. The T_2 distributions are shown as a function of the echo

spacing. Once again, a large T_1/T_2 ratio is observed and the T_2 distributions show echo spacing dependence. The logmean longitudinal and transverse relaxation times for the cores are listed in Table 4.10.

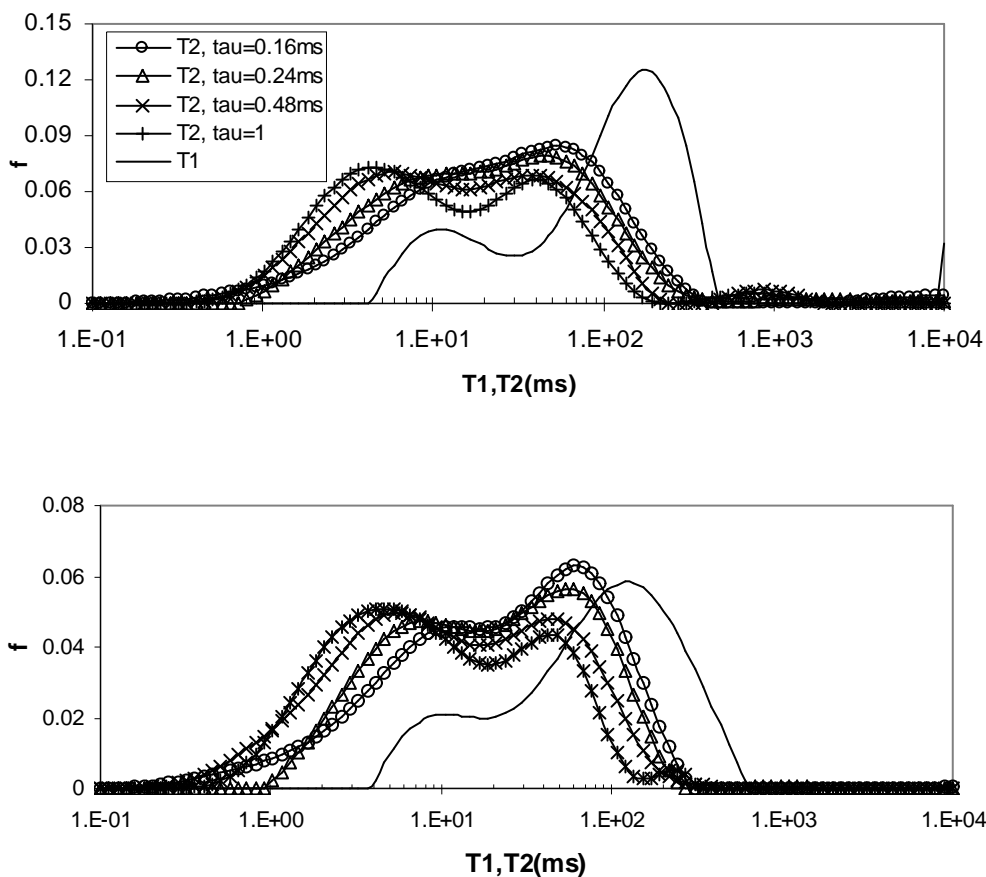


Figure 4.15: T_1 and T_2 distributions of water saturated North Burbank sandstone cores 1 and 2.

Table 4.10: Logmean longitudinal and transverse relaxation times of water saturated North Burbank cores.

Relaxation time (ms)	Core 1	Core 2
T_1	87	64
T_2 ($\tau_E = 0.16\text{ms}$)	24	20
T_2 ($\tau_E = 0.24\text{ms}$)	20	19
T_2 ($\tau_E = 0.48\text{ms}$)	14	11
T_2 ($\tau_E = 0.96\text{ms}$)	11	10
T_1/T_2	3.6-7.9	3.2-6.4

The values of characteristic time scales need to be evaluated to characterize the relaxation regime in North Burbank sandstone cores. The pore size distribution obtained from mercury porosimetry (Figure 2.12) shows that the average macropore radius is 24 μm assuming a pore-body to pore-throat ratio of 3. Since the inhomogeneous fields extend throughout the pore, diffusional correlation time is given as

$$\tau_R = \frac{R_0^2}{D} = \frac{(24 \cdot 10^{-4})^2}{2.5 \cdot 10^{-5}} \sim 0.2 \text{ sec} \quad (4.4)$$

According to Zhang (2001), the average gradient in the North-Burbank core is $g = 168$ G/cm. Thus, the range of frequencies in a pore of radius R_p is

$$\delta\omega \sim 2\gamma g R_p = 2.1 \cdot 10^4 \quad (4.5)$$

Thus, the characteristic dephasing time is

$$\tau_\omega = \frac{1}{\delta\omega} \sim 4.6 \cdot 10^{-5} \text{ sec} \quad (4.7)$$

Since $\tau_E \geq 2 \cdot 10^{-4} \text{ sec}$, $\tau_\omega \ll \tau_E$ and $\tau_\omega \ll \tau_R$ indicating that the cores are in localization regime.

Figure 4.16 shows the plot of the secular relaxation rates with half echo spacing for the several cases of the localization regime observed in Figures 4.10-4.12 and Figure 4.15. The solid lines are the regression lines for the power-law fits between the relaxation rates and the echo spacing. The exponents of the power-law fits range from 0.4 to 0.68 for the different cases. This less than linear dependence of the secular relaxation rates on τ_E in the localization regime was also illustrated in the numerical simulations of Chapter 3 (Figure 3.14). These results can also explain the linear echo spacing dependence of transverse relaxation rates in porous media for small values of τ_E observed by Brown et al. (1993) and Fantazzini et al. (2005). Power-Law fits between the simulated relaxation rates and $\delta\omega\tau_E$ in the localization regime of Figure 3.14 shows that the echo spacing dependence is nearly quadratic for small values of $\delta\omega\tau_E$ ($1 < \delta\omega\tau_E < 5$). However, the dependence is less than linear for higher values of $\delta\omega\tau_E$ ($10^2 < \delta\omega\tau_E < 10^3$). Therefore, a linear dependence on echo spacing can be observed for intermediate values of τ_E in the localization regime.

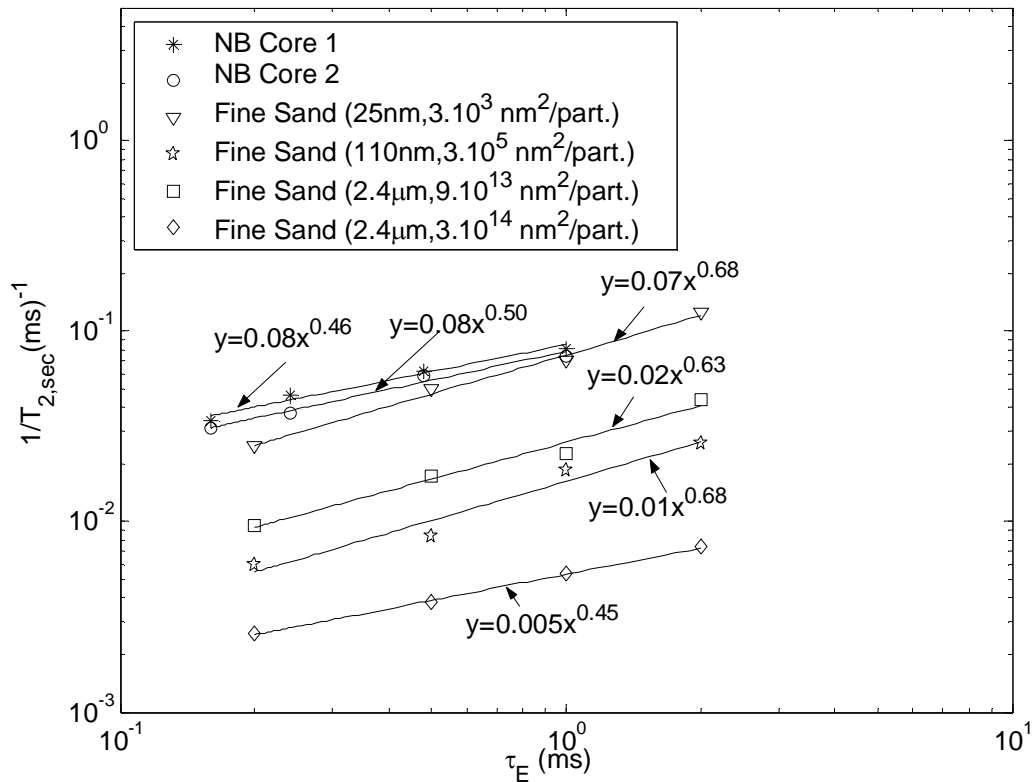


Figure 4.16: Plot of secular relaxation rate with half echo spacing for the several cases of the localization regime. The solid lines are the regression lines for the power-law fits to the data. The exponents of the power-law fits are less than unity for all cases.

4.4. Parametric representation of asymptotic regimes in experimental systems

The relaxation characteristics of the experimental systems can be summarized on the contour map of dimensionless secular relaxation rates in $(\delta\omega\tau_R, \delta\omega\tau_E)$ parameter space (Figure 3.12). The dimensionless rates for the experimental systems can be estimated by normalizing the dimensional secular relaxation rates (Equation 3.1) by the characteristic rate $(1/t_0)$ as shown

$$\frac{1}{T_{2,sec}^D} = \frac{1}{T_{2,sec}} \bigg/ \frac{1}{t_0} = \frac{1}{T_{2,sec}} \left(\frac{3}{\Phi\delta\omega} \right) \quad (4.9)$$

In Equation (4.9), the expression for characteristic rate ($1/t_0$) is substituted from Equation (3.44). Thus, three parameters (Φ , $\delta\omega$ and τ_R) are needed for calculation of dimensionless rates and the corresponding values of the coordinates ($\delta\omega\tau_R$, $\delta\omega\tau_E$). The values of τ_E are known from experiments. The procedure for estimating the characteristic parameters for the different experimental systems are discussed below.

1. **Paramagnetic particles in aqueous dispersion** – Φ is the volume fraction of paramagnetic particles. For the case of aqueous dispersions of the paramagnetic particles, Φ is given as

$$\Phi = \frac{C}{d} \quad (4.10)$$

where C is the concentration of the dispersion (g/ml) and d ($= 5.18 \text{ g/cm}^3$) is magnetite density (Lide et al., 1990). The values of $\delta\omega$ and τ_R are obtained from the calculations of characteristic times mentioned in Table 4.1 ($\delta\omega = 1/\tau_\omega$).

2. **Paramagnetic particles adsorbed on silica surface at low concentration** – Due to negligible superposition of fields induced by neighboring particles at low concentration, protons dephase as if diffusing in the internal field of a *single* particle (Figure 3.4). Thus, Φ is given by the volume of adsorbed paramagnetic particles normalized by the total volume. The values of $\delta\omega$ and τ_R are again given by calculations for a single particle in Table 4.1.
3. **Paramagnetic particles adsorbed on silica surface at high concentration** – At high concentration, paramagnetic particles cover the surface of the silica grains by forming a shell. Thus, in this case, Φ corresponds to the solid matrix volume

fraction (= 0.6 for very-well sorted grains). $\delta\omega_{\text{shell}}$ is calculated from Equation (3.33) where thickness (ε) is estimated such that the volume of the shell is the same as the volume of particles deposited on a silica grain. τ_R is calculated using Equation (3.5) and using radius of the interstitial pore as the length scale of field inhomogeneity (Equation 3.34). Thus, the coordinates ($\delta\omega\tau_R$, $\delta\omega\tau_E$) are given as

$$\begin{aligned}\delta\omega_{\text{shell}}\tau_R &= \delta\omega_{\text{particle}} \frac{3\varepsilon (0.225R_g)^2}{R_g D} = \delta\omega_{\text{particle}} \frac{0.15\varepsilon R_g}{D} \\ \delta\omega_{\text{shell}}\tau_E &= \delta\omega_{\text{particle}} \frac{3\varepsilon\tau_E}{R_g}\end{aligned}\tag{4.11}$$

$\delta\omega_{\text{particle}}$ is the frequency range for the respective paramagnetic particle given by the reciprocal of τ_0 in Table 4.1.

Figure 4.17 shows the dimensionless secular relaxation rates in the ($\delta\omega\tau_R$, $\delta\omega\tau_E$) parameter space for the various experimental systems studied. Experiments with the magnetite dispersions and silica sand coated with paramagnetic particles at low concentrations are compared with the contours for $\Phi \leq 1.25 \cdot 10^{-4}$ (upper panel). Experiments with sand coated with high concentrations of paramagnetic particles are compared with contours for $\Phi = 0.6$ (lower panel). The values of characteristic parameters used in the calculation are tabulated in Appendix D. A good quantitative agreement between the theoretically predicted rates and experimentally measured rates is observed for most cases.

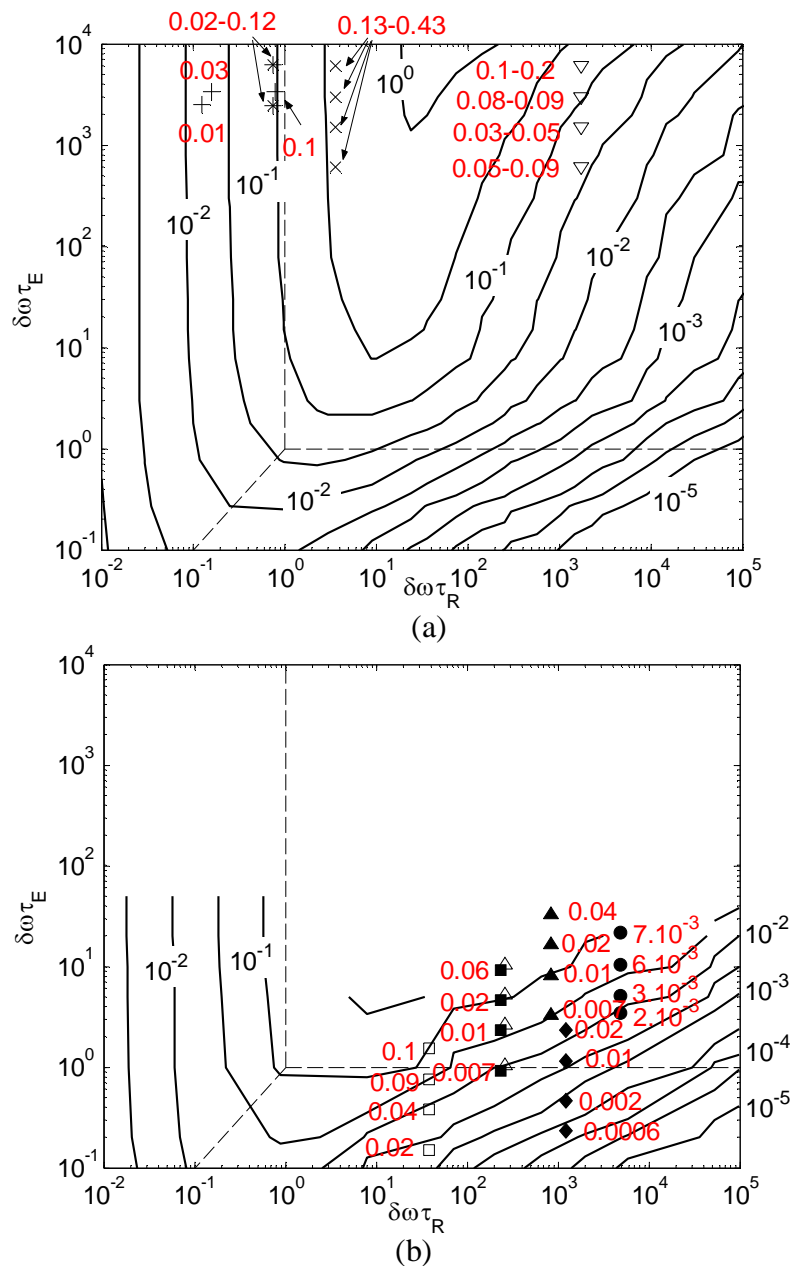


Figure 4.17: Parametric representation of dimensionless secular relaxation rates for experimental systems in the $(\delta\omega\tau_R, \delta\omega\tau_E)$ parameter space. The symbols are the experimental systems: (+) aqueous dispersion of 4nm, 9nm, 16nm particles, (*) fine and coarse sand coated with dilute concentrations of 25nm, (×) fine sand coated with dilute surface concentration of 110nm magnetite, (Δ) fine sand coated with 25nm magnetite Conc. = $7 \cdot 10^3 \text{ nm}^2/\text{part.}$, (\blacktriangle) fine sand coated with 25nm magnetite Conc. = $3 \cdot 10^3 \text{ nm}^2/\text{part.}$, (\blacklozenge) coarse sand coated with 25nm magnetite Conc. = $7 \cdot 10^2 \text{ nm}^2/\text{part.}$, (\square) fine sand coated with 110nm magnetite Conc. = $1.5 \cdot 10^6 \text{ nm}^2/\text{part.}$, (\blacksquare) fine sand coated with 110nm magnetite Conc. = $3 \cdot 10^5 \text{ nm}^2/\text{part.}$, (∇) fine sand with dispersed $2.4\mu\text{m}$ magnetite, (\bullet) North Burbank sandstone. (a) Comparison with contour plots for $\Phi \leq 1.25 \cdot 10^{-4}$ (b) Comparison with contours for $\Phi = 0.6$.

The relaxation characteristics of the experimental systems in Figure 4.17 can be explained in terms of the asymptotic regimes. The aqueous dispersions of nanoparticles (+ symbols) and fine and coarse sand coated with 25 nm low surface concentrations (* symbols) experience the motionally averaging regime. Thus, no echo spacing dependence is observed. Experiments with fine sand coated at high concentrations of 25 nm (open and closed triangles) and 110 nm (open and closed squares) lie in localization and free diffusion regimes. Similarly, coarse sand coated with 25 nm at high concentration (closed diamonds) lie in free diffusion and localization regimes. Thus, echo spacing dependence of the T_2 relaxation is observed for these cases. North Burbank sandstone (solid circles) and fine sand with dispersed 2.4 μm magnetite (inverted triangles) also fall in the localization regime and show an echo spacing dependence. The average absolute deviation between the experimental and simulated values is less than 80% which means that, on an average, the theory predicts the secular rates within the right order of magnitude.

Figure 4.18 summarizes the echo spacing dependence of the experimental systems in the free diffusion and/or the localization regime on the plot of the secular relaxation rates with $\delta\omega\tau_E$. The dashed line is the boundary $\delta\omega\tau_E = 1$ delineating the two regimes. The solid lines are the regression lines for the power-law fits between the relaxation rates and $\delta\omega\tau_E$. The exponents of the power-law fits are close to 2 in the free diffusion regime ($\delta\omega\tau_E \leq 1$). Thus, the relaxation rates show approximately quadratic dependence on $\delta\omega\tau_E$ in this regime. In contrast, the dependence of the relaxation rates on $\delta\omega\tau_E$ is less than linear in the localization regime ($\delta\omega\tau_E > 1$). Thus, these experiments demonstrate that the

T_2 relaxation rates in porous media can show quadratic as well as less than linear dependence on echo spacing.

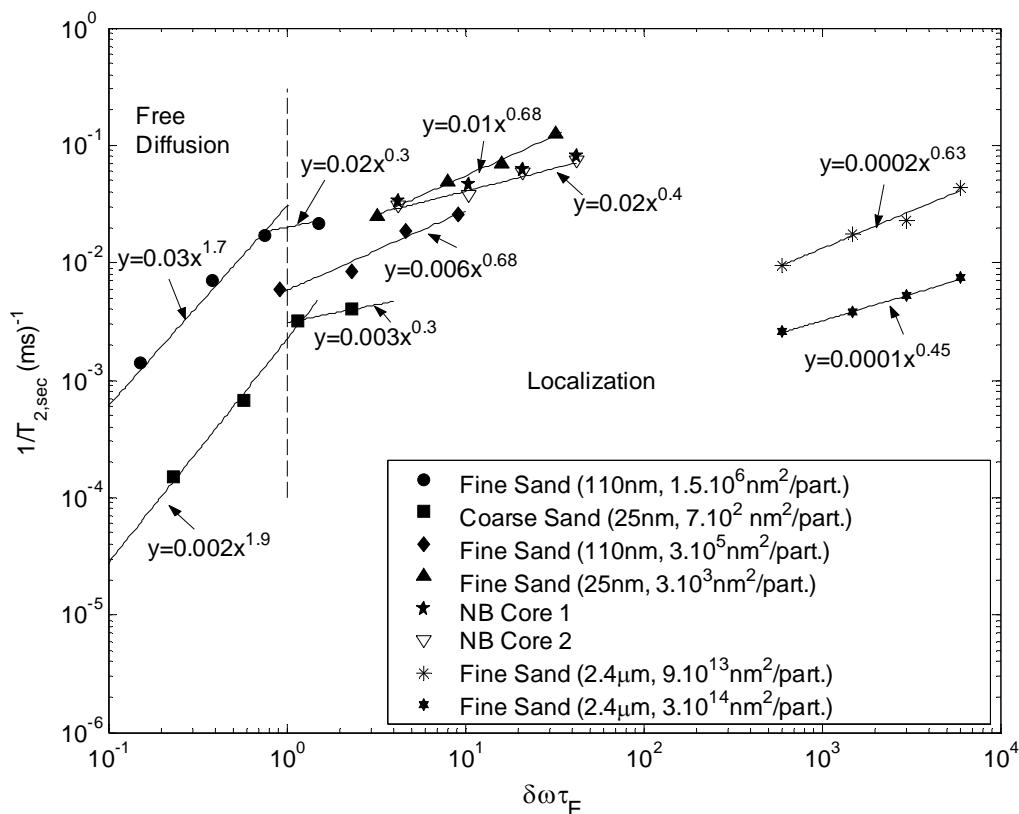


Figure 4.18: Plot of secular relaxation rates with $\delta\omega\tau_E$ for experimental systems in free diffusion and localization regimes. The relaxation rates show nearly quadratic dependence on echo spacing in the free diffusion regime and less than linear dependence in the localization regime.

Finally, Figure 4.19 shows the histogram of T_1/T_2 ratio for the experimental systems. The ratio ranges from 1.1 to 13 and is echo spacing dependent for several systems. Thus, T_1/T_2 ratio in sandstones can show a broad range as well as vary with echo spacing depending on the regime of secular relaxation.

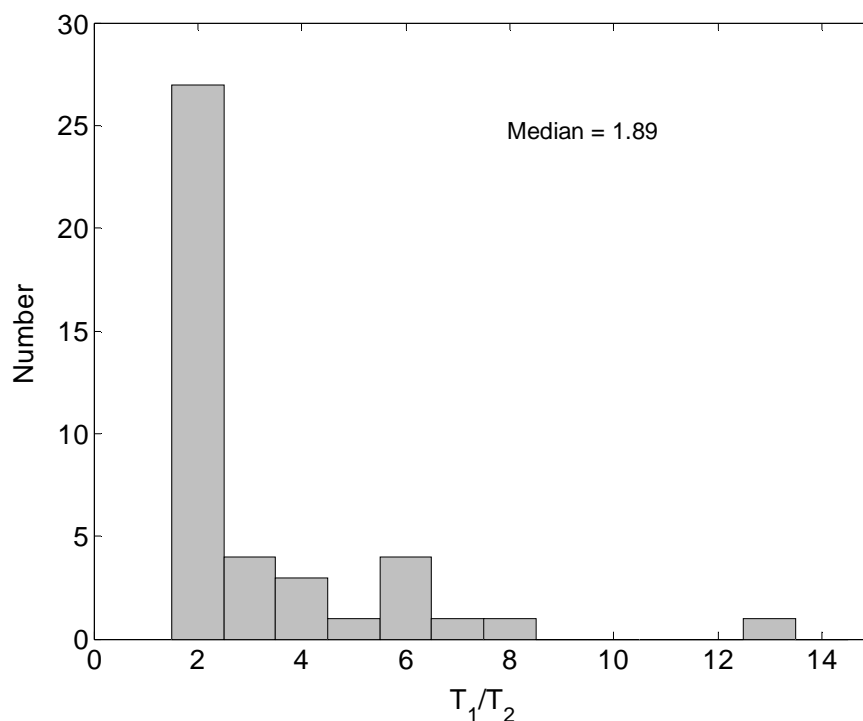


Figure 4.19: T_1/T_2 ratio for the experimental systems. The ratio ranges from 1.1 to 13 and is echo spacing dependent for several systems.

4.5. Conclusions

The classification of secular relaxation in asymptotic regimes provides conceptual understanding of relaxation characteristics of porous media. Experiments with sand coated with submicron paramagnetic particles show that the systems are in the motionally averaging regime at low surface concentration. Thus, no echo spacing dependence of T_2 relaxation is observed and the T_1/T_2 ratio increases with the paramagnetic particle size. Free diffusion or localization regimes are observed for paramagnetic particles with large diffusional correlation time *or* at large surface concentration of submicron particles. This transition in relaxation regimes occurs because the length scale of field inhomogeneity increases at large surface concentrations due to superposition of fields induced by

neighboring particles. The dependence of T_2 relaxation on echo spacing is quadratic in the free diffusion and sub-linear in the localization regime.

The relaxation characteristics of asymptotic regimes can also provide explanation for the diverse NMR characteristics observed in fluid-saturated sandstones. A large range of T_1/T_2 ratio in sandstones with no echo spacing dependence of T_2 relaxation observed by Kleinberg et al. (1993) can arise in the motionally averaging regime. The quasi-linear dependence of the T_2 relaxation on echo spacing shown in the experiments of Fantazzini et al. (2005) can arise in the localization regime. Thus, the estimation of characteristic time scales provides quantitative understanding of paramagnetic relaxation in sandstones.

Chapter 5. Conclusions

The concept of diffusional coupling between micro and macropores for NMR relaxation has been analyzed as a function of physical and geometrical parameters. Forward modeling of NMR relaxation in a coupled pore geometry shows that Brownstein number (μ) fails to quantify the extent of coupling since it is independent of the length scale of the micropore. A new coupling parameter (α) is introduced which is defined as the ratio of the characteristic relaxation rate of the coupled pore to the rate of diffusional mixing of magnetization between micro and macropores. Depending on the value of α , micro and macropores can communicate through total, intermediate or decoupled regimes.

An inversion technique for the estimation of microporosity fraction and α for formations with unknown parameters is also introduced. The required parameters for the estimation are obtainable from laboratory core analysis and the T_2 (or T_1) spectrum at 100% water and irreducible saturation. α also provides a quantitative basis for the application of spectral or sharp cutoffs.

The theory is applied to describe diffusional coupling in sandstones with distribution of macropores lined with clay flakes. Simulations are verified by comparing with experimental results for chlorite-coated, North Burbank sandstone. It is observed that the T_1 distribution shows a bimodal distribution at 100% water saturation but a unimodal distribution when saturated with hexane. This transition in the T_1 distributions occurs because the extent of coupling is higher for hexane than for water due to lower

relaxivity and higher diffusivity of hexane. The α values indicate intermediate coupling for water and strong coupling for hexane.

The model is also applied to explain pore coupling in grainstone carbonates with intra and intergranular porosity. In this case, α is found to have a quadratic dependence on the grain radius and inverse dependence on the micropore radius. The theory is experimentally validated on several systems with microporous particles of varying grain diameters and known microporosities. Here too, the T_2 distribution at 100% water saturation varies from bimodal for coarse-grained particles to unimodal for fine-grained particles. The transition from bimodal to unimodal distribution is predicted theoretically from the values of α .

The theoretical framework is extended for interpretation of the effects of temperature and clay-distribution on NMR measurements. The effect of temperature on pore coupling is quantified by proposing a temperature dependent functional relationship of α . This relationship takes into account the temperature dependence of surface relaxivity and fluid diffusivity. Experimental NMR measurements on reservoir carbonate rocks and model grainstone systems consisting of microporous silica gels of various grain sizes are performed at different temperatures. As temperature is increased, the T_2 spectrum for water-saturated systems progressively changes from bimodal to unimodal distribution. This enhanced pore coupling is caused by a combined effect of increase in water diffusivity and decrease in surface-relaxivity with temperature. Extent of coupling at each temperature can be quantified by the values of α . Thus, the theory can prove useful in interpreting log data for reservoirs at high temperatures.

Effect of clay distribution on pore coupling is illustrated for model shaly sands made with fine silica sand and bentonite or kaolinite clays. The NMR response is measured for two cases in which clay is either present as a separate, discrete layer or homogeneously distributed with the sand. For layered systems, T_2 spectrum shows separate peaks for clay and sand at 100% water saturation and a sharp $T_{2,cutoff}$ could be effectively applied for estimation of irreducible saturation. However, for dispersed systems a unimodal T_2 spectrum is observed and application of 33 ms $T_{2,cutoff}$ would underestimate the irreducible saturation in the case of kaolinite and overestimate in the case of bentonite. The inversion technique can still be applied to accurately estimate the irreducible saturation.

In addition to diffusional coupling, relaxation of fluids in porous media can also be influenced by field inhomogeneities induced due to susceptibility difference between solid matrix and pore fluids. Diffusion of pore fluids in such field inhomogeneities leads to additional transverse relaxation (called secular relaxation) due to dephasing. A generalized relaxation theory is developed which identifies three characteristic time scales governing secular relaxation: diffusional correlation time (τ_R), time for significant dephasing (τ_ω) and half echo spacing of the CPMG sequence (τ_E). Depending on the shortest time scale, secular relaxation can be classified in three asymptotic regimes of motionally averaging ($\tau_R \ll \tau_E$, $\tau_R \ll \tau_\omega$), localization ($\tau_\omega \ll \tau_E$, $\tau_\omega \ll \tau_R$) and free diffusion ($\tau_E \ll \tau_R$, $\tau_E \ll \tau_\omega$). The generalized relaxation theory is independent of the particular choice of spatial distribution of the field inhomogeneity.

Secular relaxation shows varying dependence on governing parameters in the three asymptotic regimes. In motionally averaging regime, no echo spacing dependence

of T_2 relaxation is observed. In contrast, quadratic and sub-linear echo spacing dependence is observed in the free diffusion and the localization regime respectively. The dependence of T_2 relaxation on the length scale of field inhomogeneity is also different in the three regimes. Relaxation rates increase with inhomogeneity length scale in the motionally averaging regime while the dependence is inverted in free diffusion and localization regimes. The dependence on inhomogeneity length scale is reversed because when $\tau_R/\tau_\omega < 1$, the relaxation rate is determined by amount of dephasing in diffusional correlation time. Thus, relaxation rates increase with τ_R (thus, with inhomogeneity length scale) in the motionally averaging regime. However, when $\tau_R/\tau_\omega > 1$, the relaxation rate is determined by the *rate* at which spins diffuse out of the region of field inhomogeneity. Thus, relaxation rates are inversely proportional to the field inhomogeneity length scale in localization and free diffusion regimes.

The relaxation characteristics of the asymptotic regimes provide a conceptual understanding of paramagnetic relaxation in porous media. NMR experiments with sand coated with submicron paramagnetic particles show that systems are in the motionally averaging regime at low surface concentrations. Thus, no echo spacing of T_2 relaxation is observed and T_1/T_2 ratio increases with paramagnetic particle size. However, the systems transition to the free diffusion or the localization regime at large surface concentration of paramagnetic particles. This transition in relaxation regimes occurs because at large concentrations, the length scale of field inhomogeneity increases due to superposition of fields induced by neighboring particles. Quadratic and sub-linear echo spacing dependence of T_2 relaxation is observed in the free diffusion and localization regimes respectively.

The relaxation characteristics of asymptotic regimes can also explain the diverse relaxation characteristics of fluid-saturated sandstones. A large range of T_1/T_2 ratio in sandstones with no echo spacing dependence of T_2 relaxation observed by Kleinberg et al. (1993) can arise in the motionally averaging regime. The lack of echo dependence of T_2 relaxation, thus, does *not* necessarily imply that relaxation is not influenced by diffusion in field inhomogeneities. The quasi-linear dependence of the T_2 relaxation on the echo spacing observed by Fantazzini et al. (2005) can arise in the localization regime. Thus, the generalized theory can aid in better interpretation of NMR measurements in porous media.

Chapter 6. Future Work

Several factors influence relaxation of fluids in porous media such as surface relaxation, diffusional coupling, internal field inhomogeneities etc. This study developed a theoretical framework for interpreting NMR measurements when the effects of diffusional coupling and field inhomogeneities are present separately. The next step in this direction is to develop interpretation models when the two effects are present concurrently in restricted pore geometries.

A pertinent example to study is relaxation in North Burbank sandstone with macropores lined with clay flakes. Relaxation in North Burbank sandstone is influenced not only by surface relaxation at clay surfaces but also by diffusional coupling and internal field inhomogeneities induced by clay flakes. A simplified model of clay-lined pores was developed which theoretically elucidated the effect of diffusional coupling on longitudinal relaxation. It is suggested to incorporate inhomogeneous field distribution of the clay-lined pore (Zhang et al., 2003) in the governing Bloch-Torrey equations for studying transverse relaxation. Important dimensionless groups based on ratios of characteristic time and length scales should be identified.

The presence of multi fluid phases should be next incorporated in the model of clay-lined pore. Numerical calculations of Zhang et al. (2003) show that the field inhomogeneities are present not only in the micropores but also extend to the macropores. The spatial penetration of field inhomogeneities would, thus, influence the relaxation of the non-wetting fluid present in the macropores. Understanding the effect of field inhomogeneities and restricted diffusion on the relaxation of non-wetting fluid is particularly useful for interpretation of two dimensional (2-D) NMR measurements. For

example, the interpretation of Diffusion Editing (Hürlimann et al., 2002) measurement assumes unrestricted diffusion of pore fluids in constant (externally applied) field gradients. Similarly, Magnetic Resonance Fluid (Freedman et al., 2002) characterization of oil saturation and viscosity assumes that relaxation of oil phase is not influenced by restricted diffusion or internal gradients. When these assumptions are not satisfied, departures from the existing correlations and expected results are observed. For example, diffusivity components are underestimated due to restricted diffusion and overestimated in the presence of internal field inhomogeneities. It is suggested that approaches to correcting the interpretation of 2-D measurements be developed.

Finally, it is expected that understanding of the relaxation mechanisms of pore fluids would enhance the general understanding of porous media. New concepts such as Decay due to Diffusion in Internal Fields (Song et al., 2000) use internal gradients induced in restricted pore geometries to gain information about the pore structure. Innovative ideas exploiting fluid-rock interactions measured by NMR relaxation could provide more useful information about porous media.

REFERENCES

1. Agarwal, S., 2007, "Use of magnetic nanoparticles for mixing in Microarrays and Microsystems", Ph.D. Thesis, Rice University.
2. Allen, D.F., Basan, P.B., Herron, M.M., Kenyon, W.E. and Matteston, A., 1998, "Petrophysical Significance of the Fast Components of the NMR T_2 spectrum in Shaly Sands and Shales", *SPE 49307, presented at SPE Annual Technical Conference and Exhibition*.
3. Appel., M., Freeman, J.J., Perkins, R.B. and Hofman, J.P., 1999, "Restricted Diffusion and Internal Field Gradient", Paper FF, in 40th Annual Logging Symposium Transactions, Society of Professional well Log Analysts.
4. Bergman, D.J. and Dunn, K-J, 1995, "NMR of diffusing atoms in a periodic porous medium in the presence of a nonuniform magnetic field", *Physical Review E*, Vol 52, No 6, P 6516-6535.
5. Bloch, F., 1946, "Nuclear Induction", *Physical Review*, Vol 70, Nos 7 and 8, p 460-474.
6. Brooks, R.A., Moyny, F. and Gillis, P., 2001, "On T_2 Shortening by Weakly Magnetized Particles: The Chemical Exchange Model", *Magnetic Resonance in Medicine*, Vol 45, p 1014-1020.
7. Brooks, R.A., 2002, " T_2 -Shortening by Strongly Magnetized Spheres: A Chemical Exchange Model", *Magnetic Resonance in Medicine*, Vol 47, p 388-391.
8. Brown, R.J.S. and Fantazzini, P., 1993, "Conditions for initial quasilinear T_2^{-1} versus τ for Carr-Purcell-Meiboom-Gill NMR with diffusion and susceptibility differences in porous media and tissues", *Physical Review B*, Vol 47, No 22, p 14823-14834.
9. Brownstein, K.R. and Tarr, C.E., 1979, "Importance of classical diffusion in NMR studies in water in biological cells", *Physical Review A*, Vol 19, p 2446-2453.
10. Carr, H.Y and Purcell, E.M., 1954, "Effects of Diffusion on Free Precession in Nuclear Magnetic Resonance Experiments", *Physical Review*, Vol 94, No 3, p 630-638.
11. Chen, J., 2005, "NMR Surface Relaxation, Wettability and OBM Drilling Fluids", Ph.D. Thesis, Rice University.
12. Chen, J., Hirasaki, G.J. and Flaum, M., 2006, "NMR wettability indices: Effect of OBM on wettability and NMR responses", *Journal of Petroleum Science and Engineering*, Vol 52, p 161-171.

13. Coates, G.R., Gardner, J.S. and Miller, D.L., 1994, "Applying Pulse Echo NMR to Shaly Sand Formation Evaluation", *Annual Logging Symposium Transactions, Society of Petrophysicists Well Log Analysts*.
14. Coates, G.R., Marschall, D., Mardon, D. and Galford, J., 1998, "A New Characterization of Bulk-Volume Irreducible Using Magnetic Resonance", *The Log Analyst*, Vol 39, No 1, p 51-63.
15. Coates G.R., Xiao L. and Prammer, M.G., 1999, "NMR Logging Principles and Applications", Halliburton Energy Services Publication.
16. DeSwiet, T.M and Sen, P.N, 1994, "Decay of nuclear magnetization by bounded diffusion in a constant field gradient", *Journal of Chemical Physics*, Vol 100, No 8, p 5597-5604.
17. Dunn, K.-J., LaTorraca, G.A., Warner, J.L. and Bergman, D.J., 1994, "On the Calculation and Interpretation of NMR Relaxation Time Distributions", *SPE 28367, presented at SPE Annual Technical Conference and Exhibition*.
18. Dunn, K.-J., Appel, M., Freeman, J.J., Gradner, J.S., Hirasaki, G.J., Shafer, J.L., and Zhang, G.Q., 2001, "Interpretation of restricted diffusion and internal field gradient in rock data", Paper AAA, in 42nd Annual Logging Symposium Transactions: Society of Professional Well Log Analysts.
19. Fantazzini, P. and Brown, R.J.S, 2005, "Initially linear echo-spacing dependence of $1/T_2$ measurements in many porous media with pore scale inhomogeneous fields", *Journal of Magnetic Resonance*, Vol 177, p 228-235.
20. Fantazzini, P., Salem A., Timellini, G., Tucci, A. and Viola, R., 2003, "Microstructure changes in fired ceramics quantified by magnetic resonance relaxation and imaging", *Journal of Applied Physics*, Vol 94, p 5337-5342.
21. Fleury, M., 2006, Personal Communication.
22. Foley, I., Farooqui, S.A. and Kleinberg, R.L., 1996, "Effect of Paramagnetic Ions on NMR Relaxation of Fluids at Solid Surface", *Journal of Magnetic Resonance, Series A*, Vol 123, p 95-104.
23. Freedman, R., Heaton, N. and Flaum, M., 2002, "Field applications of a New Nuclear Magnetic Resonance Fluid Characterization Method", *SPE 81197, presented at SPE Annual Technical Conference and Exhibition*.
24. Fukushima, E. and Roeder, S.B.W., 1981, "Experimental Pulse NMR: A nuts and Bolts Approach", Addison Wesley Publishing Company.
25. Gillis, P. and Koenig, S.H., 1987, "Transverse relaxation of Solvent Protons Induced by Magnetized Spheres: Application to Ferritin, Erythrocytes and Magnetite", *Magnetic Resonance in Medicine*, Vol 5, p 323-345.

26. Gillis, P., Moyny, F. and Brooks, R.A., 2002, "On T_2 -Shortening by Strongly Magnetized Spheres: A Partial Refocusing Model", *Magnetic Resonance in Medicine*, Vol 47, p 257-263.
27. Glasel, J.A. and Lee, K.H., 1974, "Interpretation of water nuclear magnetic resonance relaxation times in heterogeneous systems", *Journal of American Chemical Society*, Vol 96, No 4, p 970-978.
28. GodeFroy, S., Fleury, M., Deflandre, F. and Korb, J.-P., 2001, "Temperature effect on NMR Surface Relaxation", *SPE 71700, presented at SPE Annual Technical Conference and Exhibition*.
29. Gutowsky, H.S. and Satka, A., 1953, "Dissociation, Chemical Exchange, and the Proton Magnetic Resonance in Some Aqueous Electrolytes", *Journal of Chemical Physics*, Vol 21, p 1688-1694.
30. Hardy, P.A. and Henkelman, R.M., 1989, "Transverse relaxation rate enhancement caused by magnetic particulates", *Magnetic Resonance Imaging*, Vol 7, p 265-275.
31. Holz, M., Heil, S.R. and Sacco, A., 2000, "Temperature dependent self-diffusion coefficients of water and six selected molecular fluids for calibration in accurate ^1H NMR PFG measurements", *Physical Chemistry Chemical Physics*, Web Published, 3rd October.
32. Hürlimann, M.D., Kelmer, K.G., DeSwiet, T.M., Sen, P.N. and Sotak., C.H., 1995, "Spin Echoes in a Constant Gradient and in the Presence of Simple Restriction", *Journal of Magnetic Resonance Series A*, Vol 113, p 260-264.
33. Hürlimann, M.D., 1998, "Effective gradients in Porous Media Due to Susceptibility Differences", *Journal of Magnetic Resonance*, Vol 131, p 232-240.
34. Hürlimann, M.D. and Venkataramanan., L., 2002, "Quantitative Measurement of Two-Dimensional Distribution Functions of Diffusion and Relaxation in Grossly Inhomogeneous Field", *Journal of Magnetic Resonance*, Vol 157, p 31-42.
35. Jenson, J.H. and Chandra, R., 2000, "NMR Relaxation in Tissues with Weak Magnetic Inhomogeneities", *Magnetic Resonance in Medicine*, Vol 44, p 144-156.
36. Kenyon, W.E. and Kolleeny, J., 1994, "NMR Surface Relaxivity of Calcite with Adsorbed Mn^{2+} ", *Journal of Colloid and Interface Science*, Vol 170, p 502-514.
37. Kleinberg, R.L. and Farooqui, S.A., 1993, " T_1/T_2 Ratio and Frequency Dependence of NMR Relaxation in Porous Sedimentary Rocks", *Journal of Colloid and Interface Science*, Vol 158, p 195-198.

38. Kleinberg, R.L., Kenyon, W.E. and Mitra, P.P., 1994, "Mechanism of NMR Relaxation of Fluids in Rock", *Journal of Magnetic Resonance Series A*, Vol 108, p 206-214.
39. Kleinberg, R.L. and Boyd, A., 1997, "Tapered Cutoffs for Magnetic Resonance Bound Water Volume", *SPE 38737, presented at Annual Technical Conference and Exhibition Proceedings*.
40. Lindquist, W.B., Venkatarangan, A., Dundmuir, J. and Wong, T., 2000, "Pore and throat size distributions measured from synchrotron X-ray tomographic images of Fontainebleau sandstones", *Journal of Geophysical research*, Vol 105, No B9, p. 21509-21527.
41. Luz, Z. and Meiboom, S., 1963, "Nuclear Magnetic Resonance Study of the Protolysis of Triethylammonium Ion in Aqueous Solution – Order of the Reaction with Respect to Solvent", *Journal of Chemical Physics*, Vol 39, p 366-370.
42. Massart, R., 1981, "Preparation of Aqueous Magnetic Liquids in Alkaline and Acidic Media", *IEEE Transactions on Magnetics*, Vol 17, No 2, p 1247-1248.
43. Matteson, A., Tomanic, J.P., Herron, M.M., Allen, D.F. and Kenyon, W.E., 2000, "NMR Relaxation of Clay/Brine Mixtures", *SPE Reservoir Evaluation & Engineering*, Vol 3, No 5, p 408-413.
44. Meiboom, S. and Gill, D., 1958, "Modified Spin-Echo method for measuring Nuclear Relaxation Times", *Review of Scientific Instruments*, Vol 29, p 688-691.
45. Meiboom, S., 1961, "Nuclear Magnetic Resonance Study of the Proton Transfer in Water", *Journal of Chemical Physics*, Vol 34, p 375-388.
46. Menzel, D.A., 1955, "Fundamental Formulas of Physics", Prentice Hall, New York, NY.
47. Morgan, L.O. and Nolle, A.W., 1959, "Proton Spin Relaxation in Aqueous Solutions of Paramagnetic Ions II. Cr^{+++} , Mn^{++} , Ni^{++} , Cu^{++} and Gd^{+++} ", *Journal of Chemical Physics*, Vol 31, No 2, p 365-368.
48. Neuman, C.H., 1974, "Spin echo of spins diffusing in a bounded medium", *Journal of Chemical Physics*, Vol 60, p 4508-4511.
49. Peaceman, D.W. and Rachford, H.H., 1955, "The Numerical Solution of Parabolic and Elliptic Differential Equations", *Journal of the Society for Industrial and Applied Mathematics*, Vol 3, No 1, p. 28-41.
50. Prammer, M.G., Drack, E.D., Bouton, J.C. and Gardner, J.S., 1996, "Measurements of Clay-Bound Water and Total Porosity by Magnetic Resonance Logging", *The Log Analyst*, Vol 37, No 6, p 61-69.

51. Prost, R., Koutt, T., Benchara, A. and Huard, E., 1998, "State and Location of Water Adsorbed on Clay Minerals: Consequences of the Hydration and Swelling-Shrinkage Phenomena", *Clays and Clay Minerals*, Vol 46, No. 2, p 117-131.
52. Ramakrishnan, T.S., Fordham, E.J., Venkataramanan, L., Flaum, M. and Schwartz, L.M., 1999, "New Interpretation Methodology Based on Forward Models for Magnetic Resonance in Carbonates", Paper MMM, in *Annual Logging Symposium Transactions, Society of Petrophysicists Well Log Analysts*.
53. Ramakrishnan, T.S., Schwartz, L.M., Fordham, E.J., Kenyon, W.E. and Wilkinson, D.J., 1999, "Forward Models for Nuclear Magnetic Resonance in Carbonate Rocks", *The Log Analyst*, Vol 4, No 4, p 260-270.
54. Reid, R.C., Prausnitz, J.M. and Poling, B.E., 1987, "The Properties of Gases and Liquids", McGraw Hill.
55. Rosensweig, R.E., 1985, "Ferrohydrodynamics", Cambridge University Press.
56. Rothwell, W.P. and Vinegar, H.J. 1985, "Petrophysical applications of NMR Imaging", *Applied Optics*, Vol 24, p 3969-3972.
57. Rueslåtten, H., Eidesmo, T., Lehne, K.A. and Relling, O.M., 1998, "The use of NMR spectroscopy to validate NMR logs from deeply buried reservoir sandstones", *Journal of Petroleum Science and Engineering*, Vol 19, p 33-43.
58. Sen, P.N., André, A. and Axelrod, S., 1999, "Spins echoes of nuclear magnetization diffusing in a constant magnetic field gradient and in a restricted geometry", *Journal of Chemical Physics*, Vol 111, No. 14, p. 6548-6555.
59. Solomon, I., 1955, "Relaxation Processes in a System of Two Spins", *Physical Review*, Vol 99, No 2, p 559-565.
60. Song, Y.-Q., Ryu, S. and Sen, P.N., 2000, "Determining multiple length scales in rocks", *Nature*, Vol 406, p 178-181.
61. Song, Y.-Q., Lisitza, N.V., Allen, D.F. and Kenyon, W.E., 2002, "Pore Geometry and its Geological Evolution in Carbonate Rocks", *Petrophysics*, Vol 43, No 5, p 420-424.
62. Sun, B., and Dunn, K.-J., 2002, "Probing the internal field gradients of porous media", *Physical Review E*, Vol 65, p 051309(1) - 051309(7).
63. Straley, C., Morriss, C.E. and Kenyon, W.E. and Howard, J.J., 1995, "NMR in Partially Saturated Rocks: Laboratory Insights on Free fluid Index and Comparison with Borehole Logs", *The Log Analyst*, Vol 36, No 1, p. 40-56.

64. Tarczón, J.C. and Halerpin, W.P., 1985, "Interpretation of NMR diffusion measurements in uniform- and nonuniform-field gradients", *Physical Review B*, Vol 32, No 5, p 2798-2807.
65. Todd, M.R., O'Dell, P.M. and Hirasaki, G.J., 1972, "Methods of Increased Accuracy in Numerical Reservoir Simulators", *Society of Petroleum Engineers Journal*, Vol 12, No 6, p 515-530.
66. Toumelin, E., Torres-Verdin, C., Chen, S. and Fischer, D.M., 2003, "Reconciling NMR Measurements and Numerical Simulations: Assessment of Temperature and Diffusive Coupling Effects on Two-Phase Carbonate Samples", *Petrophysics*, Vol 44, No 2, p. 91-107.
67. Trantham, J.C. and Clampitt, R.L., 1977, "Determination of Oil Saturation after Waterflooding in Oil-Wet Reservoir- The North Burbank Unit, Tract 97 Project", *Journal of Petroleum Technology*, Vol 29, No 1, p. 491-500.
68. Vainshtein, B.K., Fridkin, V.M. and Indenbom, V.L., 2000, "Structure of Crystals," Third Edition, Springer.
69. Weisskoff, R.M., Zuo, C.S., Boxerman, J.L. and Rosen, B.R., 1994, "Microscopic Susceptibility Variation and Transverse Relaxation: Theory and Experiment", *Magnetic Resonance in Medicine*, Vol 31, p 601-610.
70. Yu, W.W., Joshua, C., Yavuz, C.T. and Colvin, V.L., 2004, "Synthesis of monodisperse iron oxide nanocrystals by thermal decomposition of iron carboxylate salts", *Chemical Communication*, web published on 2nd Sept 2004.
71. Zhang, Q., 2001, "NMR Formation Evaluation: Hydrogen Index, Wettability and Internal Field Gradients", Ph.D. Thesis, Rice University.
72. Zhang, G.Q., Hirasaki, G.J. and House, W.V., 2001, "Effect of Internal Field Gradients on NMR Measurements", *Petrophysics*, Vol 42, No 1, p 37-47.
73. Zhang, G.Q., Hirasaki, G.J. and House, W.V., 2003, "Internal Field Gradients in Porous Media", *Petrophysics*, Vol 44, No 6, p 422-434.

APPENDIX A. Numerical solution of Bloch equations in coupled pore model

The governing equations (2.11-2.13) in terms of dimensionless variables (with superscript $*$) are

$$\frac{\partial^2 M^*}{\partial x^{*2}} + \frac{\partial^2 M^*}{\partial y^{*2}} = \alpha \frac{\partial M^*}{\partial t^*} \quad (\text{A.1a})$$

$$\frac{\partial M^*}{\partial x^*} - \mu S(y) M^* = 0 \text{ at } x^* = 0, \quad 0 \leq y^* \leq 1 \quad (\text{A.1b})$$

$$\frac{\partial M^*}{\partial x^*} = 0 \text{ at } x^* = \eta^{-1}, \quad 0 \leq y^* \leq 1 \quad (\text{A.1c})$$

$$\frac{\partial M^*}{\partial y^*} = 0 \text{ at } y^* = 0 \text{ and } 1, \quad 0 \leq x^* \leq \eta^{-1} \quad (\text{A.1d})$$

$$M^* = 1 \text{ at } t^* = 0, \quad 0 \leq x^* \leq \eta^{-1}, \quad 0 \leq y^* \leq 1 \quad (\text{A.1e})$$

In the above system, the discontinuous boundary condition along the y -axis (Figure 2.2) is combined into a single equation by using the step function $S(y)$ defined as

$$S(y) = 1 \quad \text{for} \quad 0 \leq y^* \leq \beta \quad (\text{A.2a})$$

$$= 0 \quad \text{for} \quad \beta < y^* \leq 1 \quad (\text{A.2b})$$

Hereafter, the superscript ($*$) will be dropped from the dimensionless variables.

A.1. Finite difference approximation

Equation (A.1) represents a two-dimensional parabolic partial differential equation. The PDE is numerically solved by employing grid block centered finite difference approximations for the partial derivatives. The grid block formulation is closely related to the grid point formulation but is explicitly mass conserving.

The grid block finite difference approximation of the spatial derivative in x direction is

$$\Delta x_i \Delta y_j \left(\frac{\partial^2 M}{\partial x^2} \right) \approx \Delta y_j \left(\frac{(M_{i+1,j} - M_{i,j})}{1/2(\Delta x_{i+1} + \Delta x_i)} - \frac{(M_{i,j} - M_{i-1,j})}{1/2(\Delta x_i + \Delta x_{i-1})} \right) \quad (\text{A.3a})$$

$$= T_{x,i+1/2,j} (M_{i+1,j} - M_{i,j}) - T_{x,i-1/2,j} (M_{i,j} - M_{i-1,j}) \quad (\text{A.3b})$$

$$= \Delta_x (T_x \Delta_x M) \quad (\text{A.3c})$$

The derivatives with respect to y and t can be similarly approximated to yield the following difference equation at the $(n+1)^{\text{th}}$ time step

$$\Delta_x T_x \Delta M_{n+1} + \Delta_y T_y \Delta M_{n+1} = C (M_{n+1} - M_n) \quad (\text{A.4})$$

where $C = \frac{\alpha \Delta x_i \Delta y_j}{\Delta t}$, $T_{x,i+1/2,j} = \frac{\Delta y_j}{1/2(\Delta x_i + \Delta x_{i+1})}$ and $T_{y,i,j+1/2} = \frac{\Delta x_i}{1/2(\Delta y_j + \Delta y_{j+1})}$. The

coefficients T_x and T_y are the interblock transmissibility coefficients in x and y direction, respectively. The use of transmissibility coefficients helps to handle variable grid spacing and also makes the imposition of zero derivative boundary condition easier by making the coefficients zero along the boundary.

Equation (A.4) is solved iteratively using the ADI method (Peaceman and Rachford, 1955) in two steps shown in Equations (A.5a) and (A.5b). $M^{k+1/2}$ and M^{k+1} are iterated estimates to M_{n+1} after the x and y sweeps respectively and r^{k+1} is the iteration parameter at the $(k+1)$ th iteration.

$$(\Delta_x T_x \Delta - C - r^{k+1}) M^{k+1/2} + (\Delta_y T_y \Delta + r^{k+1}) M^k = -C M_n \quad (\text{A.5a})$$

$$(\Delta_x T_x \Delta + r^{k+1}) M^{k+1/2} + (\Delta_y T_y \Delta - C - r^{k+1}) M^{k+1} = -C M_n \quad (\text{A.5b})$$

The equations are written in residual form by expressing the unknown as the change in magnetization from the previous iteration.

$$\delta M^{k+1/2} = M^{k+1/2} - M^k \quad (\text{A.6a})$$

$$\delta M^{k+1} = M^{k+1} - M^{k+1/2} \quad (\text{A.6b})$$

Substituting the above incremental unknowns into Equations (A.5) and rearranging the terms, the following equations are obtained.

$$(\Delta_x T_x \Delta - C - r^{k+1}) \delta M^{k+1/2} = -(\Delta_x T_x \Delta + \Delta_y T_y \Delta) M^k + C(M^k - M_n) \quad (\text{A.7a})$$

$$(\Delta_y T_y \Delta - C - r^{k+1}) \delta M^{k+1} = -(\Delta_y T_y \Delta + r^{k+1}) \delta M^{k+1/2} \quad (\text{A.7b})$$

The right hand side of the Equation (A.7a) is similar to the original difference Equation (A.4). Hence the residual B^k , defined as

$$B^k = -(\Delta_x T_x \Delta + \Delta_y T_y \Delta) M^k + C(M^k - M_n), \quad (\text{A.8})$$

becomes zero when M^k is the solution of (A.4). The Equations (A.7a) and (A.7b) are solved repeatedly till the residual falls below the error tolerance.

The boundary conditions are also transformed into residual form by introducing the residual unknowns. Equation (A.9) shows the boundary condition (A.1b) transformed in terms of the residual variables

$$\frac{\partial M^{k+1/2}}{\partial x} - \mu S(y) M^{k+1/2} = \frac{\partial (\delta M^{k+1})}{\partial x} - \mu S(y) \delta M^{k+1} = 0 \quad (\text{A.9})$$

The finite difference approximation of Equation (A.9) is

$$\frac{\delta M_{1,j} - \delta M_{0,j}}{1/2(\Delta x_1 + \Delta x_0)} - \mu S(j) \delta M_{1/2,j} = 0 \quad (\text{A.10})$$

Since the value of magnetization is not known at the boundary, a second order approximation for $\delta M_{1/2,j}$ in terms of the values at the grid points $0,j$ and $1,j$ can be introduced as shown in Figure (A.1).

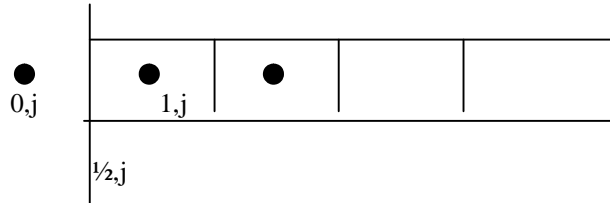


Figure A.1: Finite difference approximation scheme along the $x=0$ boundary.

The magnetization at the boundary is expressed in terms of the values at grid points 0 and 1.

$$\delta M_{1/2,j} = \frac{\delta M_{1,j} + \delta M_{0,j}}{2} \quad (\text{A.11})$$

Substitute Equation (A.11) in (A.10)

$$\delta M_{0,j} = \frac{T_{x,1/2,j} - \mu S(j)\Delta y_j / 2}{T_{x,1/2,j} + \mu S(j)\Delta y_j / 2} \delta M_{1,j} \quad (\text{A.12})$$

The expression for $\delta M_{0,j}$ can be substituted into the main difference equation to get the finite difference approximation for the boundary. The remaining reflection boundary conditions are managed by making the transmissibility coefficients zero along the boundaries.

A.2. Numerical solution

The finite difference equations described above are solved for the magnetization decay in a 2-D domain. The domain is divided into a grid system having N_x and N_y cells in x and y direction, respectively. At each time step, Equation (A.7a) is solved row at a

time for $\delta M^{k+1/2}$ and then Equation (A.7b) is solved for column at a time for δM^{k+1} using Thomas algorithm for inversion of a tridiagonal matrix. The values of magnetization at successive sweeps are updated by adding the residual unknowns to the magnetization value at the previous sweep as shown in Equations (A.13) and (A.14)

$$M^{k+1/2} = M^k + \delta M^{k+1/2} \quad (\text{A.13})$$

$$M^{k+1} = M^{k+1/2} + \delta M^{k+1} \quad (\text{A.14})$$

The residual, B^k , is updated after the two sweeps using Equation (A.8) and the iteration continued until the residual satisfies the tolerance criterion. The iteration parameters play the role similar to the reciprocal of the time step size for advancing the iteration. Thus, it is reasonable to start with larger iteration parameter and decrease the values with a geometric progression. A sequence of four parameters 0.75, 0.075, 0.0075, 0.00025 was found to be optimal in reducing the number of iterations per step. The cycle is repeated if the iteration does not converge during the sequence.

A.3. Automatic time step selection

All discrete approximations are subject to truncation error. A method of controlling the time truncation error is to limit the magnetization change per time step as shown (Todd et al., 1981)

$$\Delta t_{n+1} = \frac{DM_{\text{lim}}}{\max DM(i, j)} \Delta t_n \quad (\text{A.15})$$

where DM_{lim} is the maximum change in magnetization allowed at each time step. Hence, the Δt at the next time step is scaled by the ratio of maximum change in M desired to maximum change in M over the entire domain at the previous time step. The time

truncation errors are, thus, limited due to small Δt in the beginning of the simulation when the rate of change of M is large and large Δt towards the end.

The values of the parameters used in the simulation are shown in Table A.1. Depending on geometry, N_x and N_y were chosen so as to keep their product less than 25000 and the value of Δx same as Δy .

Table A.1: Model parameters for magnetization decay simulations.

Error tolerance	$\Delta t_{\text{initial}}$	DM_{lim}	M_{final}
10^{-8}	10^{-4}	10^{-2}	9×10^{-3}

A.4. Multi exponential fit

The magnetization decay curve is obtained by summing the magnetization values over the entire domain at each time step. Simulated decay data are sampled at the times corresponding to 0.5% change in the average magnetization and fitted to a multi-exponential distribution to obtain the T_2 distribution

$$\overline{M}(t_i) \approx \sum_j f_j \exp(-t_i / T_{2,j}) \quad (\text{A.16})$$

where $\overline{M}(t_j)$ is the average magnetization in the entire domain at discrete times (t_j). The coefficients f_j are obtained by minimizing the following objective function (Dunn et al., 1994).

$$\sum_i \left[\overline{M}(t_i) - \sum_j f_j \exp(-t_i / T_{2,j}) \right]^2 + \lambda \sum_j f_j^2 \quad (\text{A.17})$$

In the above expression, λ is the regularization parameter.

A.5. Validation

The magnetization simulation is validated by comparing the numerical solution with the analytical solution for the case of $\beta = 1$ (Brownstein et al., 1979) and different values of μ . For each case, the two solutions match within an accuracy of 0.1% (maximum relative error) indicating the correctness of the numerical solution. Additionally, simulations for different values of Δx , Δy and Δt show that the error between the analytical and numerical solutions varies proportional to the square of Δx and Δy and proportional to Δt in accordance with the second order approximation of the spatial derivatives and first order approximation of the time derivative.

APPENDIX B. Relaxation time of micropore in coupled pore model

Here, the issue of faster relaxation of micropore in the coupled case than in the decoupled case, observed in the simulations of Section (2.2) is resolved. For the case of no diffusional coupling, the dimensionless relaxation time of the micropore is inversely proportional to its surface-to-volume ratio i.e.

$$\lim_{\alpha \rightarrow \infty} T_{2,\mu}^* = \lim_{\alpha \rightarrow \infty} \frac{T_{2,\mu}}{T_{2,c}} = \frac{L_1/\rho}{L_1/\rho\beta} = \beta \quad (\text{B.1})$$

Hence, when coupling between micro and macropore is allowed, the micropore is expected to relax with a relaxation time larger than β . Figure B.1 shows the normalized relaxation time of micropore peak as a function of α for different simulation parameters. For the decoupled regime ($\alpha > 250$), the normalized micropore relaxation time tends to 1 as expected. However, for the intermediate coupling regime ($1 < \alpha < 250$), it appears that the micropore is relaxing faster than the decoupled rate i.e. $T_{2,\mu}^* < \beta$. This artifact of faster relaxation of micropore in the coupled case was also observed in Ramakrishnan's analysis (1999). No explanation was, however, offered in their paper.

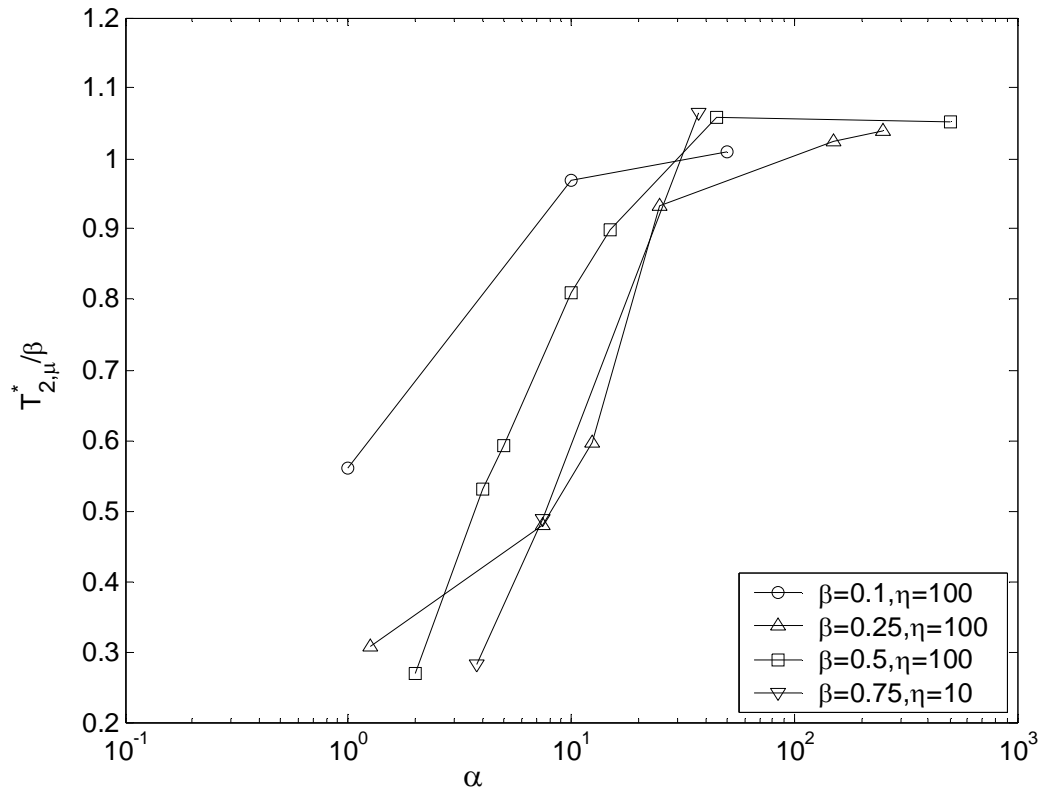


Figure B.1: Plot of micropore relaxation time with α for different simulation parameters. Micropore appears to relax faster when coupled with macropore.

The apparent contradiction can be resolved by studying the early relaxation data of the coupled pore. Analysis of the initial slope of the decay curve reveals that the system relaxes with a unit relaxation time. This is because at very short times, the fluids in micro and macropore do not have sufficient time to diffusively exchange with each other. Thus, the micropore decays with relaxation time of β (Equation B.1) while macropore relaxes with infinite relaxation time.

$$\begin{aligned}
M^* &= \beta \exp(-t/\beta) + (1-\beta) \exp(-t/\infty) \\
&\approx \beta(1-t/\beta) + (1-\beta) \quad (t \ll 1) \\
&= 1-t \\
&\approx \exp(-t)
\end{aligned}
\tag{B.2}$$

The derivation in Equation (B.2) shows that a unit relaxation time is observed at short times. However, at longer times, macropore relaxes with a finite relaxation time due to diffusional coupling with the micropore. This decrease in relaxation time of the macropore has an apparent effect of reducing the relaxation time of the micropore. Figure (B.2) shows the simulated relaxation data for the case of $\beta = 0.5$, $\eta = 100$ and $\mu = 0.2$ ($\alpha = 10$, intermediate coupling regime). The system initially relaxes with unit relaxation time as shown by the dashed line. However, a bi-exponential fit (solid line) to the data estimates the relaxation time of the micropore to be 0.4 which is less than the expected value of 0.5. The inconsistency arises due to decrease in relaxation time of the macropore from infinity at short times to 2.2 at longer times.

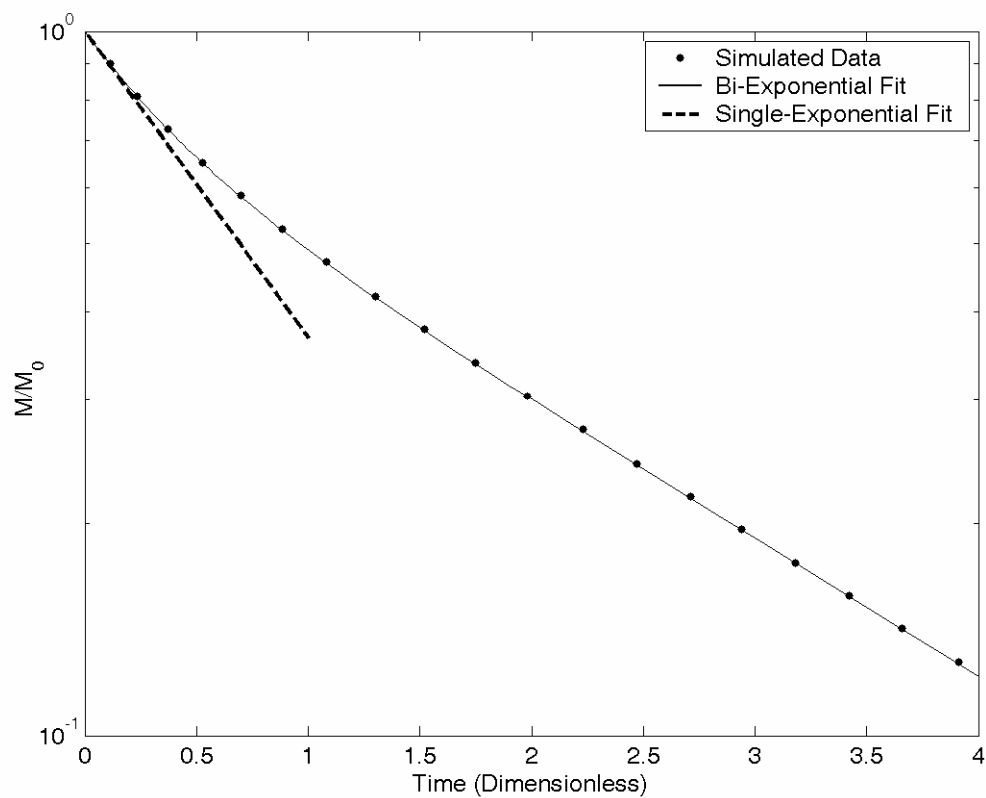


Figure B.2: Simulated relaxation data for $\alpha = 10$ ($\beta = 0.5, \eta = 100$ and $\mu = 0.2$). The black dashed line is an exponential decay with relaxation time of 1. The solid line is a bi-exponential fit ($0.26\exp(-t/0.4) + 0.74\exp(-t/2.2)$) of the data.

APPENDIX C. Characteristic parameters for the sandstones and grainstone systems

Table C.1: Characteristic parameters for North Burbank sandstone

Core	$T_{2,\mu}$ (ms)	$T_{2,\text{macro}}$ (ms)	ψ	β	α
NB1	14	180	0.23	0.32	12.2
NB2	15	191	0.25	0.3	15
NB3	10	242	0.15	0.22	16.6

Table C.2: Characteristic parameters for chalk

R_g (μm)	$T_{2,\mu}$ (ms)	$T_{2,\text{macro}}$ (ms)	ψ	β	α
335	17	1180	0.42	0.42	433
200	17	509	0.48	0.47	283
112	17	183	0.38	0.40	58
56	17	126	0.26	0.39	15
11	15	30	0	0.56	0.8

Table C.3: Characteristic parameters for silica gels

R_g (μm)	$T_{2,\mu}$ (ms)	$T_{2,\text{macro}}$ (ms)	ψ	β	α
168	61	669	0.46	0.47	43
55	61	201	0.24	0.49	5
28	61	148	0.02	0.46	1.7

Table C.4: Characteristic parameters for molecular sieves

R_g (μm)	$T_{2,\mu}$ (ms)	$T_{2,\text{macro}}$ (ms)	ψ	β	α
200	2.5	546	0.45	0.45	1140
112	2.5	215	0.42	0.42	410
56	2.5	107	0.38	0.38	79
16	2.5	19	0.21	0.32	9

Table C.5: Characteristic parameters for silica gels at 30, 50, 75 and 95°C

R_g (μm)	Temp. ($^{\circ}\text{C}$)	$T_{2,\mu}$ (ms)	$T_{2,\text{macro}}$ (ms)	ψ	β	α
168	30	60	669	0.46	0.47	43
168	50	67	546	0.42	0.47	28
168	75	75	486	0.31	0.47	16
168	95	76	433	0.21	0.47	12
55	30	61	201	0.24	0.49	5
55	50	67	184	0.05	0.49	3
55	75	75	184	0.03	0.49	2
55	95	76	184	0	0.49	1.5
28	30	61	148	0.02	0.46	1.7
28	50	67	152	0.01	0.46	0.7
28	75	75	170	0	0.46	0.45
28	95	76	192	0	0.46	0.34

Table C.6: Characteristic parameters for reservoir carbonate core at 25, 50, 80°C

Temp. ($^{\circ}\text{C}$)	$T_{2,\mu}$ (ms)	$T_{2,\text{macro}}$ (ms)	ψ	β	α
25	21	971	0.20	0.22	43
50	31	839	0.16	0.22	20
80	37	627	0.05	0.22	6

APPENDIX D: Characteristic parameters for the experimental systems of Chapter 4.

Table D.1: Characteristic parameters for fine sand coated with 25 nm magnetite at different surface concentrations. Φ and $1/T_{2,\text{sec}}^D$ are dimensionless.

Surface Concentration (nm ² /part.)	Φ	$\delta\omega$ (rad/sec)	τ_E (msec)	τ_R (sec)	$1/T_{2,\text{sec}}$ (sec ⁻¹)	$1/T_{2,\text{sec}}^D$	Regime
$9 \cdot 10^4$	$1.2 \cdot 10^{-5}$	$1.2 \cdot 10^7$	0.2-2	$6.3 \cdot 10^{-8}$	1.7	0.03	M.Av.
10^4	$2 \cdot 10^{-4}$	$1.2 \cdot 10^7$	0.2-2	$6.3 \cdot 10^{-8}$	10.7	0.02	M.Av.
$7 \cdot 10^3$	0.6	$5.2 \cdot 10^3$	0.2	0.2	11	0.01	Loc.
$7 \cdot 10^3$	0.6	$5.2 \cdot 10^3$	0.5	0.2	21	0.02	Loc.
$7 \cdot 10^3$	0.6	$5.2 \cdot 10^3$	1.0	0.2	30	0.03	Loc.
$7 \cdot 10^3$	0.6	$5.2 \cdot 10^3$	2.0	0.2	70	0.06	Loc.
$3 \cdot 10^3$	0.6	$1.6 \cdot 10^4$	0.2	0.2	25	0.007	Loc.
$3 \cdot 10^3$	0.6	$1.6 \cdot 10^4$	0.5	0.2	49	0.014	Loc.
$3 \cdot 10^3$	0.6	$1.6 \cdot 10^4$	1.0	0.2	69	0.021	Loc.
$3 \cdot 10^3$	0.6	$1.6 \cdot 10^4$	2.0	0.2	154	0.04	Loc.

Table D.2: Characteristic parameters for fine sand coated with 110 nm magnetite at different surface concentrations. Φ and $1/T_{2,\text{sec}}^D$ are dimensionless.

Surface Concentration (nm ² /part.)	Φ	$\delta\omega$ (rad/sec)	τ_E (msec)	τ_R (sec)	$1/T_{2,\text{sec}}$ (sec ⁻¹)	$1/T_{2,\text{sec}}^D$	Regime
$3 \cdot 10^7$	$2.2 \cdot 10^{-6}$	$3 \cdot 10^6$	0.2-2	$1.2 \cdot 10^{-6}$	1	0.43	M.Av.
$8 \cdot 10^6$	$4 \cdot 10^{-5}$	$3 \cdot 10^6$	0.2-2	$1.2 \cdot 10^{-6}$	5	0.13	M.Av.
$1.5 \cdot 10^6$	0.6	761	0.2	0.05	1.4	0.009	F.D.
$1.5 \cdot 10^6$	0.6	761	0.5	0.05	7	0.015	F.D.
$1.5 \cdot 10^6$	0.6	761	1.0	0.05	15	0.024	F.D.
$1.5 \cdot 10^6$	0.6	761	2.0	0.05	21	0.03	Loc.
$3 \cdot 10^5$	0.6	4626	0.2	0.05	6	0.007	Loc.
$3 \cdot 10^5$	0.6	4626	0.5	0.05	8	0.009	Loc.
$3 \cdot 10^5$	0.6	4626	1.0	0.05	18	0.02	Loc.
$3 \cdot 10^5$	0.6	4626	2.0	0.05	26	0.03	Loc.

Table D.3: Characteristic parameters for coarse sand coated with 25 nm magnetite at different surface concentrations. Φ and $1/T_{2,\text{sec}}^D$ are dimensionless.

Surface Concentration (nm ² /part.)	Φ	$\delta\omega$ (rad/sec)	τ_E (msec)	τ_R (sec)	$1/T_{2,\text{sec}}$ (sec ⁻¹)	$1/T_{2,\text{sec}}^D$	Regime
$4 \cdot 10^3$	$2.1 \cdot 10^{-6}$	$1.2 \cdot 10^7$	0.2-2	$6.3 \cdot 10^{-8}$	1	0.12	M.Av.
$7 \cdot 10^2$	0.6	1152	0.2	1.07	0.1	0.0006	F.D.
$7 \cdot 10^2$	0.6	1152	0.5	1.07	0.7	0.003	F.D.
$7 \cdot 10^2$	0.6	1152	1.0	1.07	3.2	0.01	Loc.
$7 \cdot 10^2$	0.6	1152	2.0	1.07	3.9	0.016	Loc.

Table D.4: Characteristic parameters for fine sand with dispersed 2.4 μm magnetite at different concentrations. Φ and $1/T_{2,\text{sec}}^D$ are dimensionless.

Surface Concentration (nm ² /part.)	Φ	$\delta\omega$ (rad/sec)	τ_E (msec)	τ_R (sec)	$1/T_{2,\text{sec}}$ (sec ⁻¹)	$1/T_{2,\text{sec}}^D$	Regime
$3 \cdot 10^{14}$	$6.5 \cdot 10^{-5}$	$3 \cdot 10^6$	0.2	$5.7 \cdot 10^{-4}$	2.6	0.03	Loc.
$3 \cdot 10^{14}$	$6.5 \cdot 10^{-5}$	$3 \cdot 10^6$	0.5	$5.7 \cdot 10^{-4}$	3.8	0.05	Loc.
$3 \cdot 10^{14}$	$6.5 \cdot 10^{-5}$	$3 \cdot 10^6$	1.0	$5.7 \cdot 10^{-4}$	5.3	0.08	Loc.
$3 \cdot 10^{14}$	$6.5 \cdot 10^{-5}$	$3 \cdot 10^6$	2.0	$5.7 \cdot 10^{-4}$	7.4	0.11	Loc.
$9 \cdot 10^{13}$	$1.9 \cdot 10^{-4}$	$3 \cdot 10^6$	0.2	$5.7 \cdot 10^{-4}$	9.5	0.05	Loc.
$9 \cdot 10^{13}$	$1.9 \cdot 10^{-4}$	$3 \cdot 10^6$	0.5	$5.7 \cdot 10^{-4}$	17	0.09	Loc.
$9 \cdot 10^{13}$	$1.9 \cdot 10^{-4}$	$3 \cdot 10^6$	1.0	$5.7 \cdot 10^{-4}$	22	0.12	Loc.
$9 \cdot 10^{13}$	$1.9 \cdot 10^{-4}$	$3 \cdot 10^6$	2.0	$5.7 \cdot 10^{-4}$	43	0.22	Loc.

Table D.5: Characteristic parameters for North Burbank sandstones. Φ and $1/T_{2,\text{sec}}^D$ are dimensionless.

Core	Φ	$\delta\omega$ (rad/sec)	τ_E (msec)	τ_R (sec)	$1/T_{2,\text{sec}}$ (sec ⁻¹)	$1/T_{2,\text{sec}}^D$	Regime
1	0.6	$2.1 \cdot 10^4$	0.16	0.2	27	$2.3 \cdot 10^{-3}$	Loc.
1	0.6	$2.1 \cdot 10^4$	0.24	0.2	38	$3.2 \cdot 10^{-4}$	Loc.
1	0.6	$2.1 \cdot 10^4$	0.48	0.2	60	$5 \cdot 10^{-3}$	Loc.
1	0.6	$2.1 \cdot 10^4$	0.96	0.2	79	$6.8 \cdot 10^{-3}$	Loc.
2	0.6	$2.1 \cdot 10^4$	0.16	0.2	33	$2.8 \cdot 10^{-3}$	Loc.
2	0.6	$2.1 \cdot 10^4$	0.24	0.2	37	$3 \cdot 10^{-3}$	Loc.
2	0.6	$2.1 \cdot 10^4$	0.48	0.2	72	$6.1 \cdot 10^{-3}$	Loc.
2	0.6	$2.1 \cdot 10^4$	0.96	0.2	80	$6.8 \cdot 10^{-3}$	Loc.